(10)

THE THERMAL EVOLUTION OF THE BITTERROOT METAMORPHIC CORE COMPLEX, IDAHO-MONTANA

by

Martha Ann House

B.S. University of Michigan
(1990)

Submitted to the Department of
Earth, Atmospheric, and Planetary Sciences
in Partial Fulfillment of the Requirements
for the Degree of

DOCTOR OF PHILOSOPHY

at the MASSACHUSETTS INSTITUTE OF TECHNOLOGY

February, 1995

Signature of Author_____
Department of Earth, Atmospheric, and Planetary Sciences
February, 1995

Certified by_____
Kip V. Hodges
Thesis Advisor

Accepted by_____
Thomas H. Jordan
Department Head

THE THERMAL EVOLUTION OF THE BITTERROOT METAMORPHIC CORE COMPLEX, IDAHO-MONTANA

by

Martha Ann House

Submitted to the Department of Earth, Atmospheric, and Planetary Sciences at the Massachusetts Institute of Technology in partial fulfillment of the requirements for the Degree of Doctor of Philosophy in Geology

ABSTRACT

Granitic rocks of the Bitterroot batholith and their high-grade metamorphic host-rocks are exposed in the footwall of the Bitterroot metamorphic core complex, Montana-Idaho. Upper-amphibolite facies metamorphism in the Bitterroot core complex was associated with granite emplacement during Late Cretaceous-Early Tertiary time. Quantitative thermobarometry in metapelitic rocks suggests peak metamorphic conditions of ~950 - 1000 K and 750 - 800 MPa (26 - 28 km). Amphibolite thermobarometry suggests a period of isothermal decompression associated with the late stages of peak metamorphism that may represent early unroofing accommodated by the core-bounding Bitterroot mylonite zone. Crystallization ages of metamorphic zircons from garnet amphibolites in the northeastern Bitterroot complex indicate that peak metamorphic temperatures persisted in core rocks until 48 Ma.

Extensional unroofing of core rocks initiated shortly after emplacement of mesozonal plutons in the northern Bitterroot Range at 55.8 Ma. The northwestern Bitterroot complex cooled through the hornblende, muscovite, biotite, and K-feldspar Ar-closure temperatures (800, 650, 620, and 450 K, respectively) between 55.6 - 48 Ma; cooling continued in the northeastern Bitterroot complex from 48 - 40 Ma. Crystallization ages of epizonal plutons in the western Bitterroot complex demonstrate that this region was at shallow levels by 49 Ma, whereas high-temperature conditions persisted in the eastern footwall rocks until 48 Ma. The data suggest that core rocks in the eastern and western portions of the Bitterroot complex were at different structural levels at 49 - 48 Ma and can be explained by multiple extensional structures or progressive unroofing by a single feature.

The northeastern Bitterroot complex cooled through muscovite, biotite, and K-feldspar closure temperatures > 3 m.y. after extension on the Bitterroot mylonite zone. A quantitative model of conductive cooling suggests that this time lag represents the thermal re-equilibration of footwall rocks following removal of ~19 km of overburden by extension on the Bitterroot mylonite zone. Continued cooling through the K-feldspar closure temperature may represent renewed unroofing via post-mylonitic brittle structures that may have removed an additional 3 - 8 km of overburden.

Thesis advisor: Kip V. Hodges, Professor of Geology

ACKNOWLEDGEMENTS

I have grown a lot at M.I.T., both academically and personally, and I am grateful for the opportunity to be a part of this institution. Professors D. K. Rea and B. A. van der Pluijm at the University of Michigan encouraged me in science and provided me with opportunities that made coming to M.I.T. possible. My thesis advisor, Kip Hodges, accepted me in spite of my scattered background and deserves acknowledgement for his support, scientific advice, and encouragement over the years. Someone should give him a big box of Kleenex to put in his office. Sam Bowring has taught me a lot about U-Pb geochronology, and in a more general sense, how to approach science. In the end, he has always been there for me. Leigh Royden is someone that I would have liked to have met sooner during my time at M.I.T.; in the past few months she has opened up a whole world of new ideas to me and I hope to continue to work with her. I would also like to acknowledge Clark Burchfiel for his amazing tectonics seminars and assistance during these last few months. Roger Burns taught me a tremendous amount about teaching mineralogy and I am sorry for his passing. Finally, I would like to thank Clark Burchfiel, Sam Bowring, Leigh Royden, and Pat Bickford (Syracuse University) for serving on my thesis committee.

One thing I am certain of is that I would never have made it through this place without the help of a legion of people. Meg Coleman, in particular deserves a bouquet of roses for reading my entire thesis and being a continual source of positive reinforcement to me over the years. Dawn Sumner has been a valued friend during my time at M.I.T.; I admire her self confidence and commitment to her science and I wish her all the best in her future pursuits. Fellow Kip-students Audrey Huerta, Anke Friedrich, and Jim van Ormon are fantastic furniture refinishers and should go into business on the side. I also want to thank C.J. Northrup for his enthusiasm and interest in talking science—I have learned a lot from him. Nancy Harris, Dave Hawkins, Bev Saylor, and Shane Pelechaty rounded out the sphere graduate students while I was at M.I.T. and I have had many interesting interactions with them, both academic and otherwise. Dave Applegate, Allison MacFarlane, Dave McCormick, and Cathy Summa shared the wisdom of their experiences with me while they were at M.I.T. and continue to do so today. Outside of EAPS, my friends Barbara Slater and Susanna Leveroni have been a source of inspiration to me in how to make your M.I.T. degree work for you. Dean Jackie Simonis has been an unending source of support and I thank her for her guidance over the past two years.

Mike Jercinovic and Neel Chatterjee provided technical support in the microprobe lab and held my hand while I got up to speed on the equipment. Clark Isachsen, and Drew Coleman have been invaluable sources of information and assistance in the U-Pb lab. Bill Olszewski has been a great source of knowledge in the CLAIR facility and I look forward to continuing to benefit from his technical skills in the upcoming months. Pat Walsh has been an administrative god-send, as well as a good friend—thank you Pat for everything! Anita Killian and Karen Campbell are two friends who helped me through the EAPS administration and library system early on and have now gone on to new opportunities. Dan Burns picked up where Anita left off and has been invaluable in helping me through the final stages of completing my thesis. I can't thank him enough.

My experiences with field assistants got off to a rough start during my first field season, but drastically improved with the late summer arrival of Brett Smith, snow-boarder extraordinaire. During my second year Ellen Dotson introduced me to the joys of backpacking in fog, hammocks, knitting, and Powerbars. Aimee (jerk magnet) Dolan-Laughlin, a fellow Michigan undergraduate, helped me during my final year in the field. In spite of snow, sleet, hail, and bears, Aimee kept her humor and mine; kvetch-on Aimee!

Above all the others at M.I.T., I want to thank Mark Simons for his incredible friendship and support for the past five years. He has been there for me throughout everything and has helped me to keep my perspective during rough times. My friendship with Mark is one of the two most valuable things that I will take with me as I leave M.I.T.. I wish Mark long life and happiness and all of the rock-climbing, travel, and good food that his heart desires (not to mention an endless supply of Patagucci!).

Finally, I want to thank my family for their love and encouragement. I really could not have completed this dissertation without their support; I am only sorry that my father could not have seen this happen as well.

To Nancy, Jody, and Scott House

and to my father,
James Phillip House
September 27, 1942 - October 10, 1993

TABLE OF CONTENTS

CHAPTER 1

INTRODUCTION: TECTONIC SETTING OF THE BITTERROOT METAMORPHIC CORE COMPLEX

INTRODUCTION

The tectonic significance of metamorphic core complexes has been the subject of intense debate since this term was first used ~ twenty years ago to describe exposures of mid-crustal metamorphic rocks in the hinterland of the Cordilleran thrust belt (Figure 1; Coney, 1974). These features typically consist of a high-grade crystalline core separated from a low-grade suprastructural cover by an intervening low-angle detachment fault. Early workers attributed these "windows into the middle crust" to be the product of compressional tectonics (e.g., Armstrong and Hansen, 1966). While metamorphic and deformational features preserved in core rocks do preserve evidence of Mesozoic crustal shortening, this early portion of their evolution is generally modified by unroofing along Tertiary extensional structures that initiated under ductile deformational conditions and were overprinted by progressively lower-temperature fabrics as exhumation proceeded. The mechanism driving this extension remains hotly debated however, and there have been a number of models put forth to explain the geographical variations in the timing of extensional denudation of these structures in the North American Cordillera (e.g., Coney and Harms, 1984; Sonder *et al.*, 1987). Metamorphic core complexes similar to those in the Cordillera have been identified in orogenic belts worldwide (e.g., Chen *et al.*, 1990; Baldwin *et al.*, 1993), suggesting that the processes leading to their development are not exclusive to the North American Cordillera. Rather, these structures are an ubiquitous part of orogenic terranes, and

resolving the mechanism, or mechanisms, for their development is an important part of understanding mountain-building processes.

A key factor in developing models of core complex formation is deriving constraints on the age of extensional detachments responsible for exhuming these structures. $^{40}Ar/^{39}Ar$ and U-Pb geochronology have been important tools in reconstructing the time-temperature evolution of rocks exposed in the footwalls of core complexes, which in turn can be related to the age and mechanism of unroofing (tectonic vs. erosional; Parrish *et al.*, 1988; Baldwin *et al.*, 1993). These data can then be combined with thermobarometric constraints on peak metamorphic conditions and structural analyses to place the pressure-temperature-time history of core rocks in the context of their deformational history. Questions which can be addressed are: What is the thermal structure of the crust prior to and during extension and how is it generated? How does the core-bounding detachment evolve over time? How do core rocks respond to rapid exhumation? Before geographic trends in Cordilleran core complex development can be understood, these issues must be resolved. This dissertation presents thermobarometric and geochronologic constraints on the unroofing history of the Bitterroot metamorphic core complex, ID-MT. While this study does not definitively resolve any of these issues, it provides important data on which to base future models.

LATE CRETACEOUS-EARLY TERTIARY TECTONICS OF THE NORTH AMERICAN CORDILLERA

Metamorphic core complexes are generally located in regions that have undergone prior crustal shortening. Therefore, the pre-extensional geometry of these regions is an important factor in controlling the locus and timing of subsequent extensional deformation. Within the North American Cordillera, the majority of metamorphic core complexes lie within the region of the orogen characterized by Mesozoic plutonism or within the western parts of the foreland fold and thrust belt

(Figure 1). The Cordilleran fold and thrust belt is the result of deformation beginning in the Jurassic and continuing through Eocene time (>120 m.y.; Allmendinger, 1991). This period in the evolution of the Cordillera is dominated by compressional deformation, with localized strike-slip motion and extension (Burchfiel *et al.*, 1991).

The timing and style of Sevier-Laramide crustal shortening varies along the length of the Cordillera, and the thrust belt can be divided into several segments (Allmendinger, 1991). In order to place the Bitterroot metamorphic complex in the appropriate tectonic context, we must consider the compressional history of the region of the Cordillera to the north of the Snake River Plain (Figure 2). The segment of the thrust belt that is bound by the Lewis and Clark line and latitude 49°N is dominated by the Lewis thrust, which emplaced Precambrian Belt Supergroup rocks eastward over Upper Cretaceous strata (Yin and Kelty, 1991). Throughout the Cordillera, Sevier-Laramide deformation generally became younger from west to east. In the northern Montana segment, the eastern-most limits of compressional deformation occurred between 72 - 46 Ma (Allmendinger, 1991). Immediately to the south, the southwestern Montana-Idaho segment of the thrust belt, which contains the Bitterroot metamorphic core complex, is less well-understood, although regional correlations have been attempted (e.g., Skipp, 1987). There is no evidence for thrusting younger than Late Cretaceous in age in this region (Wallace *et al.*, 1989). East-vergent thrusts exposed to the east of the Bitterroot complex are cut by 78-73 Ma granites of the Sapphire and Bitterroot batholiths, providing the best constraints on the lower limit of thrusting (Wallace *et al.*, 1989).

The driving force behind Sevier-Laramide crustal shortening was the east-directed subduction of the Kula-Farallon plate to the west (Burchfiel *et al.*, 1991). Arc magmatism associated with this interaction accompanied compressional tectonism in the region north of the Snake River Plain (Burchfiel *et al.*, 1991). Intrusive activity ceased in the Sierra Nevada by 85 - 75 Ma and gradually spread eastward, occurring as

late as Early Eocene time in some areas. In southern British Columbia and northern Idaho and Washington, magmatism progressed from ~75 - 60 Ma arc-related tonalites and granodiorites to 62 - 52 Ma granite plutons that are coeval with the onset of extension (Burchfiel *et al.*, 1991). Arc-derived tonalite and quartz diorite plutons in the Bitterroot batholith have been dated between ~100 - 75 Ma and are coeval with late stages of east-vergent Sevier-Laramide thrusting (Toth, 1987; Wallace *et al.*, 1989).

The onset of extension is diachronous along the length of the Cordillera, and the Snake River Plain marks an important geographic boundary, dividing the Cordillera into two regions that are characterized by very different extensional styles. Metamorphic core complexes in northern Idaho and Washington and southern British Columbia—the Omineca Extended Belt— were unroofed by extension on Early Eocene mylonitic detachments (Orr and Cheney, 1987; Rehrig *et al.*, 1987; Parrish *et al.*, 1988). These moderately dipping shear zones, with ages ranging from 56 - 45 Ma, were coeval with and slightly younger than the latest stages of compressional tectonism and associated magmatism (Parrish *et al.*, 1988; Harms and Price, 1992). Extension in this region is localized in a narrow corridor in the hinterland of the east-vergent thrusts and is associated with dextral strike-slip motion (Harms and Price, 1992). South of the Snake River Plain, extensional denudation of core complexes is generally Oligocene and younger, post-dating the latest stage of Laramide deformation by several millions of years (Wernicke *et al.*, 1987). The southern extensional corridor is much wider, and the magnitude of extension is greater than in the northern Cordillera (Wernicke *et al.*, 1987).

THE ROCKY MOUNTAIN BASIN AND RANGE

While similar tectonic processes appear to be operating throughout the Cordillera during Late Cretaceous-Early Tertiary times, the development of extensional terranes in the northern and southern regions are very different and we are left with a

complicated temporal pattern of extension for which we have no satisfactory explanation (Burchfiel *et al.*, 1991). The transition between well-studied regions to the north and south—known as the Rocky Mountain Basin and Range (Wernicke, 1991)—is an important link in developing a regional understanding of core complex development and extension in the North American Cordillera (Figure 1). There is a long history of work in this area (see below), but the complex nature of the rocks and the prolonged history of magmatism in this area make regional studies difficult. To date, two core complexes have been identified in this region: the Bitterroot metamorphic core complex and the Pioneer complex (Figure 2). Published accounts of the geology at Boehls Butte, northwest of the Bitterroot complex, are suggestive of a core complex setting, but little has been done to investigate this possibility (Grover *et al.*, 1992). Circumstantial evidence in the Bitterroot complex prompted some workers to call for Late Cretaceous extension, coeval with the late stages of Laramide compression (Hyndman, 1980); there may be a component of earlier extension in the Pioneer metamorphic core complex as well (Silverberg, 1990). Until recently, the majority of published geochronologic work in the Rocky Mountain Basin and Range has been interpreted to indicate Late Eocene extension (Garmezy, 1983; Garmezy and Sutter, 1983; Silverberg, 1990), but recent work in the Bitterroot complex has demonstrated that ductile deformation on the core-bounding Bitterroot mylonite zone occurred prior to ~46.4 Ma (Hodges and Applegate, 1993).

The Lewis and Clark fault zone links the Bitterroot complex and Boehls Butte to the Omineca Extended Belt, which includes the Priest River, Valhalla, Kettle, and Okanogan complexes (Figure 2). Several roles have been suggested for this series of strike-slip faults in the development of core complexes to the north and south (e.g., Wernicke, 1991; Doughty and Sheriff, 1992) but uncertainties in structural relationships and the timing of extension, particularly in the Bitterroot and Pioneer complexes, complicate these relationships. Therefore, refining existing constraints on the

unroofing age of the core complexes in the Rocky Mountain Basin and Range is vital to resolving the tectonic significance of the Lewis and Clark fault zone, and more generally, the nature of the variations of extensional styles from north to south. The Bitterroot metamorphic core complex lies immediately to the south of the Lewis and Clark fault zone and coincides with granite plutons associated with the Idaho Batholith. This core complex presents an excellent opportunity to correlate extensional trends across the Rocky Mountain Basin and Range, as well as to evaluate the thermal structure of core rocks prior and following extension.

THE DISSERTATION

This dissertation presents new geochronologic and petrologic data from the Bitterroot metamorphic core complex that document the unroofing history of footwall rocks and place quantitative limits on peak metamorphism prior to unroofing. This project originated as part of a larger study evaluating the evidence for Cretaceous extension in this region of the Cordillera (Hodges and Walker, 1992). The prime objective of this project was initially three-fold: 1) to constrain the age of the Bitterroot mylonite zone; 2) to quantify the metamorphic conditions of footwall rocks prior to unroofing; 3) to document the cooling history of footwall rocks in response to unroofing.

My work is only the most recent contribution to understanding the tectonic evolution of the Bitterroot metamorphic core complex. Due to the difficult terrain, absence of exploitable mineral resources, and lack of roads, much of the region has only been mapped in a reconnaissance fashion (e.g., Reid, 1987; Toth, 1987). The first report on the region was published in 1904 as part of a U.S.G.S. reconnaissance survey (Lindgren, 1904). Lindgren recognized the frontal zone gneiss, or Bitterroot mylonite zone, as a narrow zone of intense deformation associated with tectonic unroofing of high-grade rocks in the Bitterroot Range, and identified the Bitterroot Valley as the

hanging wall, suggesting that normal faulting accommodated by faults associated with the frontal zone gneiss was Late Cretaceous or younger. Ross (1952) diverged from the shear zone interpretation and considered the frontal zone gneiss a region of granitized sediment resulting from intrusion of the Bitterroot batholith, suggesting that the strong gneissic foliation reflected primary sedimentary bedding. Work by a series of students and faculty at the University of Montana during the 1960's and early 1970's focused on the petrologic and structural characteristics of the Bitterroot complex (Berg, 1968; Wehrenberg, 1972; Chase, 1973; Nold, 1974; Cheney, 1975).

The dissertation is presented in five chapters, in addition to the introduction and conclusion chapters, that were written as stand-alone papers intended for journal publication. Chapter 2 presents $^{40}Ar/^{39}Ar$ data for footwall and mylonitic rocks in the northeastern Bitterroot metamorphic core complex that demonstrate the temporal relationship between extensional unroofing and cooling of footwall rocks. Chapter 2 is slightly modified from a *Geology* article (House and Hodges, 1994). Chapter 3 represents the first attempt to quantitatively document the conditions and timing of peak metamorphism in Bitterroot core rocks and to place it in a regional context. This chapter also presents a modification of four published geobarometers based on garnet-hornblende reactions (Kohn and Spear, 1989; Kohn and Spear, 1990), with propagated uncertainties. These modifications will eventually be submitted for publication in *Contributions to Mineralogy and Petrology*. The thermobarometric and U-Pb results in Chapter 3 will be submitted to *Journal of Metamorphic Geology*. Chapter 4 presents the results of $^{40}Ar/^{39}Ar$ and U-Pb geochronology undertaken to determine the cooling history of the Bitterroot batholith as a whole, including the western portion of the Bitterroot metamorphic core complex. Progressive unroofing indicated by the data that are presented in Chapter 4 is consistent with models that have been developed for the development of low-angle detachments (e.g., Wernicke and Axen, 1988). Chapter 4 will be submitted to *GSA Bulletin* and will have Sam Bowring and Kip Hodges as co-

authors. Chapter 5 discusses the probable correlation of a shear zone exposed in the footwall of the Bitterroot complex with regionally extensive east-vergent thrust sheets mapped elsewhere in the Boehls Butte area and the southern Sapphire Range, and presents first-order estimates of the amount of Tertiary strike-slip motion accommodated by the Lewis and Clark fault zone, as well as the magnitude of Tertiary extension affecting the region. Chapter 5 will be submitted to *Geology*. Chapter 6 presents a simple one-dimensional thermal model for post-extensional cooling in footwall rocks and discusses the model in the context of the data presented in Chapter 2. This model has significant implications for the interpretation of $^{40}Ar/^{39}Ar$ cooling data from core complexes in general and will be submitted as an article to Geology, with Leigh Royden as a co-author. Chapter 7 summarizes the data presented for the Bitterroots and discusses the implications in a regional context.

Geologic field work was done during three field seasons in July and August of 1991, 1992, and 1993. Results of field mapping are presented in Plate 1, which uses the U.S.D.A. Forest Service Selway Bitterroot Wilderness 1:100 000 topographic sheet as a base map. Mapping presented in Plate 1 modifies published maps by Wehrenberg (1972), Nold (1974), Chase (1977), and Lewis *et al*.. (1992). The map area consists of the following 7.5 minute topographic sheets: Idaho—Ranger Peak, White Sand Lake; Montana—Lolo Hot Springs, West Fork Butte, Dick Creek, Carlton Lake, Florence, St. Joseph Peak, St. Mary Peak, Stevensville, Gash Point, Victor, Printz Ridge, Hamilton North. The U-Pb analyses were carried out with the help of Sam Bowring, Clark Isachsen, and Drew Coleman at the M.I.T. radiogenic isotope laboratory. The $^{40}Ar/^{39}Ar$ analyses were done at the Cambridge Laboratory for Argon Isotopic Research (CLAIR) at M.I.T. with the help of Kip Hodges and Bill Olszewski.

ACKNOWLEDGEMENT OF SUPPORT

My dissertation research has been supported by teaching assistantships at the Massachusetts Institute of Technology and by National Science Foundation grant EAR-9218721 awarded to Kip Hodges. Additional support from the Student Research Fund of the Department of Earth, Atmospheric, and Planetary Sciences at M.I.T. is also gratefully acknowledged.

REFERENCES

Allmendinger, R. W., 1991, Fold and thrust tectonics of the western United States, exclusive of the accreted terranes, *in* Burchfiel, B. C., ed., The Cordilleran Orogen: Conterminus United States: Geological Society of America, p. 583-608.

Armstrong, R. L. and Hansen, E., 1966, Cordilleran infrastructure in the eastern Great Basin: American Journal of Science, v. 254, p. 112-127.

Baldwin, S. L., Lister, G. S., Hill, E. J., Foster, D. A., and McDougall, I., 1993, Thermochronologic constraints on the tectonic evolution of active metamorphic core complexes, D'Entrecasteaux Islands, Papua New Guinea: Tectonics, v. 12, p. 611-628.

Berg, R. B., 1968, Petrology of anorthosites of the Bitterroot Range, Montana, *in* Isachsen, Y. W., ed., Origin of Anorthosite and Related Rocks: Albany, NY, New York State Museum and Science Service Memoir 18, p. 387-398.

Burchfiel, B. C., Cowan, D. S., and Davis, G. A., 1991, Tectonic overview of the Cordilleran orogen in the western United States, *in* Burchfiel, B. C., ed., The Cordilleran Orogen: Conterminus United States: Boulder, CO, Geological Society of America, p. 407-479.

Chase, R. B., 1973, Petrology of the northeastern border zone of the Idaho batholith, Bitterroot Range, Montana: Montana Bureau of Mines and Geology Memoir, v. 43, p. 1-28.

Chase, R. B., 1977, Structural evolution of the Bitterroot dome and zone of cataclasis, *in* Chase, R. B. and Hyndman, D. W., ed., Mylonite detachment zone, eastern flank of Idaho batholith: Geological Society of America Rocky Mountain section, p. 1-24.

Chen, Z., Liu, Y., Hodges, K. V., Burchfiel, B. C., Royden, L. H., and Deng, C., 1990, Structural evolution of the Kangmar dome: A metamorphic core complex in southern Xizang (Tibet): Science, v. 250, p. 1552-1556.

Cheney, J. T., 1975, Kyanite, sillimanite, phlogopite, cordierite layers in the Bass Creek anorthosites, Bitterroot Range, Montana: Northwest Geology, v. 4, p. 77-82.

Coney, P. J., 1974, Structural analysis of the Snake Range "decollement," east-central Nevada: Geological Society of America Bulletin, v. 85, p. 973-978.

Coney, P. J. and Harms, T. A., 1984, Cordilleran metamorphic core complexes: Cenozoic extensional relics of Mesozoic compression.: Geology, v. 12, p. 550-554.

Doughty, P. T. and Sheriff, S. D., 1992, Paleomagnetic evidence for en echelon extension and crustal rotations in western Montana and Idaho: Tectonics, v. 11, p. 663-671.

Garmezy, L., 1983, Geology and geochronology of the southeast border of the Bitterroot dome: Implications for the structural evolution of the mylonitic carapace [Ph.D.]: The Pennsylvania State University.

Garmezy, L. and Sutter, J. F., 1983, Mylonitization coincident with uplift in an extensional setting, Bitterroot Range, Montana-Idaho: Geological Society of America Abstracts with Programs, v. 15, p. 578.

Grover, T. W., Rice, J. M., and Carey, J. W., 1992, Petrology of aluminous schist in the Boehls Butte region of northern Idaho: Phase equilibria and P-T evolution: American Journal of Science, v. 292, p. 474-507.

Harms, T. A. and Price, R. A., 1992, The Newport fault: Eocene listric normal faulting, mylonitization, and crustal extension in northeast Washington and northwest Idaho: Geological Society of America Bulletin, v. 104, p. 745-761.

Hodges, K. V. and Applegate, J. D. R. A., 1993, Age of Tertiary extension in the Bitterroot metamorphic core complex, Montana and Idaho: Geology, v. 21, p. 161-164.

Hodges, K. V. and Walker, J. D., 1992, Extension in the Cretaceous Sevier Orogen, North American Cordillera: Geological Society of America Bulletin, v. 104, p. 560-569.

House, M. A. and Hodges, K. V., 1994, Limits on the tectonic significance of rapid cooling events in extensional setting: Insights from the Bitterroot metamorphic core complex, Idaho-Montana: Geology, v. 22, p. 1007-1010.

Hyndman, D. W., 1980, Bitterroot dome - Sapphire tectonic block, an example of a plutonic-core gneiss-dome complex with its detached suprastructure, *in* Crittenden, M. D., Coney, P. J., and Davis, G. H., ed., Cordilleran Metamorphic Core Complexes: Boulder, CO, Geological Society of America Memoir 153, p. 427-443.

Kohn, M. J. and Spear, F. S., 1989, Empirical calibration of geobarometers for the assemblage garnet + hornblende + plagioclase + quartz: American Mineralogist, v. 74, p. 77-84.

Kohn, M. J. and Spear, F. S., 1990, Two new geobarometers for garnet amphibolites, with applications to southeastern Vermont: American Mineralogist, v. 75, p. 89-96.

Lewis, R. S., Burmeister, R. F., Reynolds, R. W., Bennett, E. H., Myers, P. E., and Reid, R. R., 1992,Geologic map of the Lochsa River area, Northern Idaho, *in* : Moscow, ID: Idaho Geological Survey.

Lindgren, W., 1904, A geological reconnaissance across the Bitterroot Range and Clearwater Mountains in Montana and Idaho: U.S. Geological Survey Professional Paper, v. 27, p. 123.

Nold, J. L., 1974, Geology of the northeastern border zone of the Idaho batholith, Montana and Idaho: Northwest Geology, v. 3, p. 47-52.

Orr, K. E. and Cheney, E. S., 1987, Kettle and Okanogan domes, northeastern Washington and southern British Columbia: Washington Division of Geology and Earth Resources Bulletin 77, v. p. 55-70.

Parrish, R. R., Carr, S. D., and Parkinson, D. L., 1988, Eocene extensional tectonics and geochronology of the southern Omenica Belt, British Columbia and Washington: Tectonics, v. 7, p. 181-212.

Rehrig, W. A., Reynolds, S. J., and Armstrong, R. L., 1987, A tectonic and geochronologic overview of the Priest River crystalline complex, northeastern Washington and northern Idaho: Washington Division of Earth Sciences Bulletin 77, v. p. 1-14.

Reid, R., 1987, Structural geology and petrology of a part of the Bitterroot lobe of the Idaho batholith: U.S. Geological Survey Professional Paper, v. 1436, p. 37-58.

Ross, C. P., 1952, The eastern front of the Bitterroot Range, Montana: U.S. Geological Survey Bulletin, v. 974, p. 135-175.

Silverberg, D. S., 1990, The tectonic evolution of the Pioneer metamorphic core complex, south-central Idaho [Ph.D.]: Massachusetts Institute of Technology.

Skipp, B., 1987, Basement thrust sheets in the Clearwater orogenic zone, central Idaho and western Montana: Geology, v. 15, p. 220-224.

Sonder, L. J., England, P. C., Wernicke, B. P., and Christiansen, R. L., 1987, A physical model for Cenozoic extension of western North America., *in* Coward, M. P., Dewey, J. F., and Hancock, P. L., ed., Continental Extensional Tectonics: Oxford, Geological Society of London, p. 187-201.

Toth, M. I., 1987, Petrology and Origin of the Bitterroot Lobe of the Idaho batholith: U.S. Geological Survey Professional Paper, v. 1436, p. 9-37.

Wallace, C. A., Lidke, D. J., Waters, M. R., and Obradovich, J. D., 1989, Rocks and structure of the southern Sapphire mountains, Granite and Ravalli Counties, western Montana: U.S. Geological Survey Bulletin, v. 1824, p. 29.

Wehrenberg, J. P., 1972, Geology of the Lolo Peak area, northern Bitterroot Range, Montana: Northwest Geology, v. 1, p. 25-32.

Wernicke, B., 1991, Cenozoic extensional tectonics of the U.S. Cordillera, *in* Burchfiel, B. C., Lipman, P. W., and Zoback, M. L., ed., The Cordilleran Orogen: Conterminus United States: Boulder, CO, Geological Society of America, The Geology of North America, p. 553-582.

Wernicke, B. and Axen, G. J., 1988, On the role of isostacy in the evolution of normal fault systems: Geology, v. 16, p. 848-851.

Wernicke, B. P., Christiansen, R. L., England, P. C., and Sonder, L. J., 1987, Tectonomagmatic evolution of Cenozoic extension in the North American Cordillera., *in* Coward, M. P., Dewey, J. F., and Hancock, P. L., ed., Continental Extensional Tectonics: Oxford, Geological Society of London, p. 203-221.

Yin, A. and Kelty, T. K., 1991, Structural evolution of the Lewis plate in Glacier National Park, Montana: Implications for regional tectonic development: Geological Society of America Bulletin, v. 103, p. 1073-1089.

FIGURE CAPTIONS

Figure 1. Simplified geologic map illustrating the major tectonic elements of the Cordillera. After Hodges and Walker (1992).

Figure 2. General tectonic map of southwestern British Columbia, western Washington, northern Idaho, and western Montana, as modified from Parrish *et al.* (1988), Burchfiel *et al.* (1991), and Harms and Price (1991). Metamorphic core complexes and faults designated as follows: B, Bitterroot complex; BB, Boehls Butte complex; BM, Bitterroot mylonite; CRF, Columbia River fault; GF, Granby fault; GWF, Greenwood fault; HF, Hope fault; JJF, Jumpoff Joe fault; K, Kettle complex; KF, Kettle fault; M, Monashee complex; NF, Newport fault; O, Okanogan complex; OF, Okanogan fault; P, Pioneer complex; PR, Priest River complex; PTF, Purcell Trench fault; R, Republic Graben; SFC, Standfast Creek fault; SLC, Slocan Lake fault; V, Valhalla complex; VSZ, Valkyr shear zone.

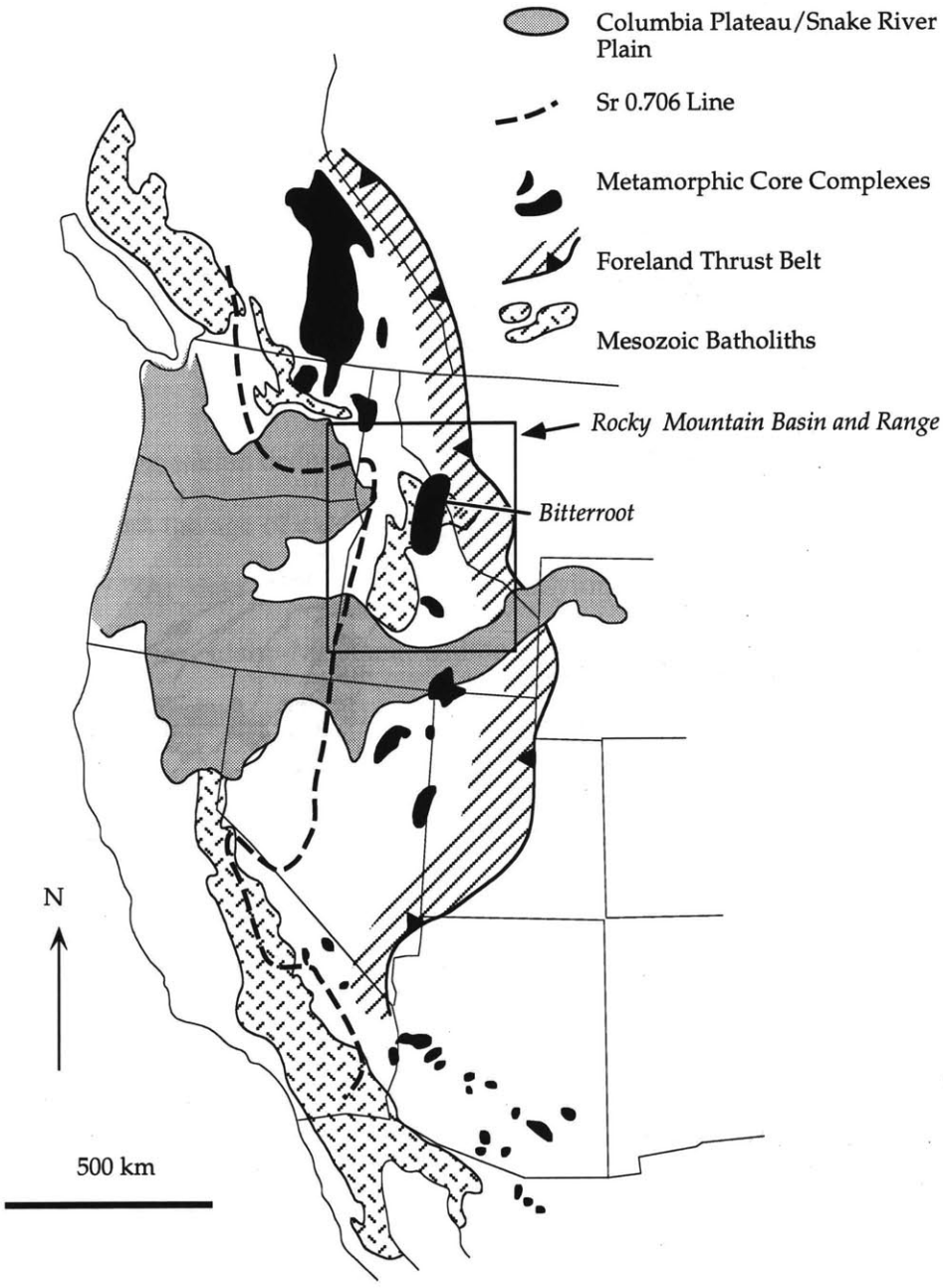
Columbia Plateau/Snake River Plain
Sr 0.706 Line
Metamorphic Core Complexes
Foreland Thrust Belt
Mesozoic Batholiths
Rocky Mountain Basin and Range
Bitterroot
N
500 km

Figure 1

Figure 2

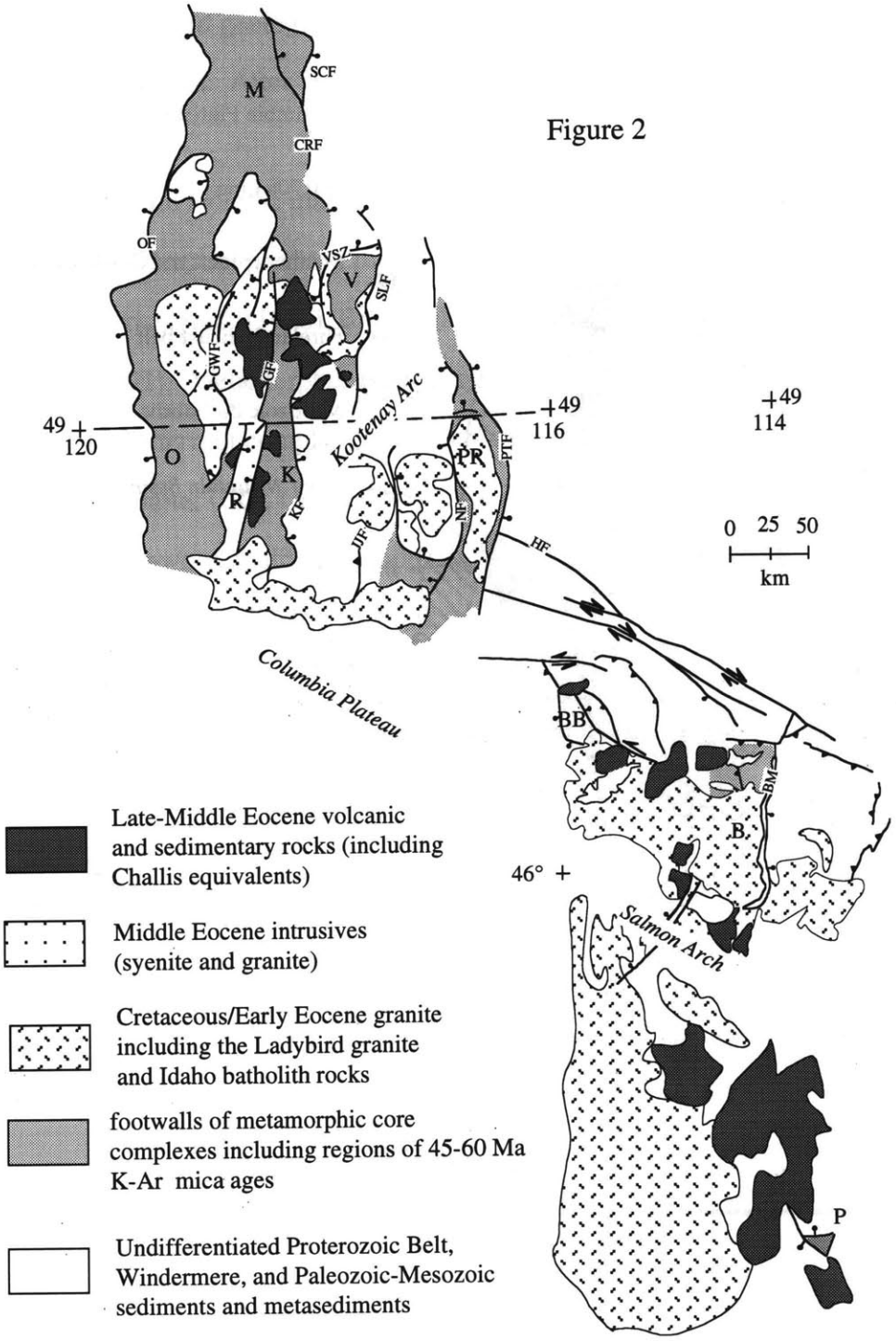
M
SCF
CRF
OF
VSZ
V
SLF
GWF
CF
Kootenay Arc
49 +
120
+49
116
+49
114
O
T
K
R
KF
UF
NF
PR
PTF
HF
0 25 50
km
Columbia Plateau
BB
BM
B
46° +
Salmon Arch
P
Late-Middle Eocene volcanic and sedimentary rocks (including Challis equivalents)
Middle Eocene intrusives (syenite and granite)
Cretaceous/Early Eocene granite including the Ladybird granite and Idaho batholith rocks
footwalls of metamorphic core complexes including regions of 45-60 Ma K-Ar mica ages
Undifferentiated Proterozoic Belt, Windermere, and Paleozoic-Mesozoic sediments and metasediments

CHAPTER 2

LIMITS ON THE TECTONIC SIGNIFICANCE OF RAPID COOLING EVENTS IN EXTENSIONAL SETTINGS: INSIGHTS FROM THE BITTERROOT METAMORPHIC CORE COMPLEX, IDAHO-MONTANA

ABSTRACT

Rapid cooling events deduced from thermochronologic data are often interpreted to be coincident with the age of extensional denudation in metamorphic core complexes. $^{40}Ar/^{39}Ar$ data for mylonitic and nonmylonitic footwall rocks from the Bitterroot core complex, Idaho-Montana, United States, challenge this view. Previous work brackets the age of the principal detachment in this area, the Bitterroot mylonite zone, between 48 ± 1 and 46.4 ± 0.8 Ma. Newly obtained hornblende $^{40}Ar/^{39}Ar$ cooling ages for samples collected from the mylonite zone are within this age range, consistent with mylonitization at amphibolite facies conditions. However, muscovite, biotite, and potassium feldspar $^{40}Ar/^{39}Ar$ ages of ~45 - 40 Ma for rocks from the same area define a rapid cooling event that is significantly younger than the Bitterroot mylonite zone. If the 45 - 40 Ma event is related to tectonic denudation by movement on the detachment, then we can infer a time lag of ~1-3 m.y. between the age of unroofing and the time of thermal re-equilibration. These data suggest caution in the use of $^{40}Ar/^{39}Ar$ data from the footwalls of metamorphic core complexes to suggest the precise age of tectonic denudation.

INTRODUCTION

Time-temperature histories based on geochronologic data from extensional terranes commonly indicate a brief interval of rapid cooling (e.g., Dokka *et al.*, 1986). Although alternative models have been advanced to explain these events in settings that have undergone synextensional plutonism (e.g., Lister and Baldwin, 1993), many researchers have attributed rapid cooling of the footwalls of major extensional shear zones to unroofing by movement on the shear zones themselves. This hypothesis has important tectonic implications; if it is correct, then the age of a cooling event provides some estimate of the age of the shear zone that is responsible. How good is this estimate? Many researchers have equated the onset of rapid cooling with the beginning of faulting and footwall denudation (e.g., Davis and Lister, 1988), despite the fact that theoretical models of the time-temperature history of extensional terranes suggest that rapid cooling generally postdates unroofing in such settings (e.g., Ruppel *et al.*, 1988). In this paper, we present $^{40}Ar/^{39}Ar$ data from the Bitterroot metamorphic core complex, Idaho-Montana, United States, that suggest a time lag of several million years between tectonic denudation and the onset of rapid cooling through mica and feldspar Ar closure temperatures. These findings substantiate the results of theoretical modeling and remind us that rapid cooling events defined by thermochronologic data from extensional terranes provide only minimum estimates of the absolute age of tectonic denudation.

GEOLOGY OF THE BITTERROOT RANGE

The Bitterroot core complex is a topographic high coinciding with the northeastern contact of the Idaho batholith with Proterozoic Belt Supergroup country rocks (Figure 1). Metasedimentary units in the core include pelitic, quartzofeldspathic, and calc-silicate schists and gneisses traditionally correlated with the Prichard Formation, Ravalli Group, and Wallace Formation of the Belt Supergroup, respectively (Wehrenberg, 1972). Amphibolite pods are scattered throughout the metasedimentary

rocks. The Belt sequence is intruded by unfoliated to foliated granites and granodiorites commonly assigned a Late Cretaceous age, although a large number have been dated as Paleocene to Eocene (e.g., Chase *et al.*, 1983). Intrusive activity led to regional-scale metamorphism of the Proterozoic country rocks. Metamorphic grade decreases from middle- or upper-amphibolite facies conditions adjacent to the batholith to greenschist facies in the essentially undeformed Belt units north of the core complex (Hyndman, 1980, and references therein). Eocene epizonal granitoids, characterized by hypabyssal textures, border the core complex, and broadly correlative Challis volcanic units unconformably overlie the core-bounding detachment in some places (Figure 1).

The principal structure responsible for unroofing of the core rocks is the Bitterroot mylonite zone, which flanks the eastern edge of the Bitterroot range (Figure 1). Exposure of the Bitterroot mylonite zone is continuous for a distance of ~100 km along strike. The mylonitic foliation strikes north-northeast and dips shallowly to the east; an associated mineral-stretching lineation plunges east-southeast. Asymmetric fabrics developed throughout the mylonite suggest a top-to-the-east, or normal, shear sense in the direction of the mylonitic lineation (Garmezy, 1983). Deformational features related to mylonitization decrease downward into the core rocks >1 km, and localized areas of high strain are found throughout the transitional zone between shear zone and footwall rocks (Chase, 1977; House, 1993, unpublished mapping).

The Bitterroot mylonite zone is interpreted to have been formed at relatively high temperatures (~775 K; Kerrich and Hyndman, 1986). Early high-grade deformational fabrics are overprinted by successively lower - temperature fabrics in many places. A chlorite breccia associated with later brittle deformation caps the Bitterroot mylonite zone in several locations, and high-angle, east-dipping normal faults truncate the earlier mylonitic foliation (Hyndman and Myers, 1988).

AGE OF THE BITTERROOT MYLONITE ZONE

The age of the Bitterroot mylonite zone has been the subject of considerable debate. The high-temperature nature of the mylonitic fabrics prompted Hyndman (1980) to argue for Late Cretaceous movement contemporaneous with the main phase of granitic plutonism. Subsequent U-Pb zircon geochronology of deformed granitoids within the mylonite zone indicates that deformation began after 48 ± 1 Ma (Figure 1; Chase *et al.*, 1983). Garmezy (1983) and Garmezy and Sutter (1983) documented rapid cooling of footwall rocks between 45.5 and 43.5 Ma on the basis of $^{40}Ar/^{39}Ar$ cooling ages for hornblende, muscovite, biotite, and potassium feldspar from mylonitic and undeformed footwall granitoids in the southern Bitterroot Range (Figure 1). They interpreted the data to indicate tectonic unroofing and inferred a ~45.5 Ma age for the beginning of movement on the Bitterroot mylonite zone.

Recent geochronologic studies in the Bitterroot complex complicate this interpretation, however, and suggest that the cooling event documented by Garmezy (1983) and Garmezy and Sutter (1983) actually postdates mylonitization. Hodges and Applegate (1993) reported a potassium feldspar $^{40}Ar/^{39}Ar$ cooling age of 46.4 ± 0.8 Ma from an undeformed rhyolite dike that crosscuts the Bitterroot mylonite zone (Figure 1), thereby limiting the minimum age for mylonitization in the southern part of the core complex. In addition, the suite of undeformed, epizonal granitic plutons that ring the Bitterroot complex were emplaced at shallow levels in country rocks originally metamorphosed at lower- to upper-amphibolite facies conditions, after unroofing of the metamorphic core (Rehn and Lund, 1981; Hyndman and Myers, 1988), and provide additional limits on the age of denudation. Recently obtained U-Pb zircon data indicate a crystallization age of 48.7 ± 0.3 Ma for one of the largest plutons, the undeformed Lolo Hot Springs batholith (Figure 1; House, unpublished data); these results refine an earlier published age of 49 ± 1 Ma (House *et al.*, 1993). The statistical agreement of the ages of the shallow-level, post-tectonic Lolo Hot Springs batholith and the mylonitized

granite dated by Chase *et al.* (1983) bracket the onset of mylonitization and unroofing between 48 and 49 Ma, significantly earlier than previously published estimates.

The currently available $^{40}Ar/^{39}Ar$ and U-Pb geochronologic data are clearly not consistent with the ~45.5 Ma formation age for the shear zone proposed by Garmezy and Sutter (1983) on the basis of $^{40}Ar/^{39}Ar$ thermochronology in the southern Bitterroot Range. To explore the significance of this discrepancy further, we analyzed mylonitic and nonmylonitic samples from the northern Bitterroot Range using the $^{40}Ar/^{39}Ar$ incremental heating technique.

SAMPLE DESCRIPTIONS

A suite of six samples consisting of pelitic and psammitic schists (NB16-1, NB16-4, and NB20-1), amphibolites (NB5-1 and NB17-1), and one granitoid (NB4-1) were selected for study (Table 1). This suite represents the gradual transition from highly sheared mylonitic rocks to core rocks that exhibit no mylonitic overprint. The samples exhibit no textural or petrologic evidence for subsequent hydrothermal alteration or brittle deformation. The structural relation of these samples to the mylonite zone is similar to that of the granitoids analyzed by Garmezy (1983) in the southern Bitterroot complex. Mylonitic schist samples NB16-1 and NB16-4 were collected near the base of the shear zone. The lithologically similar NB20-1 sample was collected from structurally lower, protomylonitic rocks ~8 km to the northwest. Amphibolite pods NB5-1 and NB17-1 are concordant with the surrounding mylonitic foliation, but they do not exhibit mylonitic fabrics. NB4-1, an unfoliated granitoid of probable Late Cretaceous age, is the structurally deepest sample examined as part of this study.

Microprobe analyses for dated minerals were obtained using the JEOL 733 electron microprobe at the Massachusetts Institute of Technology; compositional data is summarized in Table A of the appendix. Amphiboles from NB5-1 and NB17-1 contain

0.6 and 0.2 wt% K_2O, respectively, and can be classified as ferro-hornblende and actinolitic hornblende (Hawthorne, 1981). Muscovites show very slight compositional variability with K_2O = 9.8 - 10.8 wt%. Mg/(Mg+Fe) ratios in biotite vary from 0.36 to 0.54, with K_2O = 7.8 - 9.6 wt%. Potassium feldspar from the NB4-1 granitoid is essentially a binary K-Na solution (Or_{96}).

ARGON TECHNIQUES

Pure mineral separates were obtained by standard magnetic and heavy - liquid methods; hornblende from sample NB5-1 was hand - picked to obtain maximum purity. The separates were washed in water, acetone, and ethanol prior to packaging in individual aluminum foil packets for irradiation. Samples were irradiated at the Omega West reactor facility at Los Alamos National Laboratories, California, for 7 h with Cd shielding. Corrections for interfering reactions on Ca, K, and Cl were based on analyses of CaF_2, K_2SO_4, and KCl included in the irradiation package. Fast neutron flux was monitored by using MMhb-1 hornblende (520.4 Ma; Samson and Alexander, 1987) and Fish Canyon sanidine (27.8 Ma; Cebula *et al.*, 1986). Irradiated samples were analyzed on a resistance-furnace gas-extraction system and MAP 215-50 mass spectrometer at the Cambridge Laboratory for Argon Isotopic Research at MIT. A more detailed discussion of laboratory procedures is presented in Hodges *et al.* (1994).

Nominal closure temperatures commonly applied to hornblende, muscovite, and biotite are 800 ± 50, 650 ± 50, and 620 ± 50 K, respectively (McDougall and Harrison, 1988). Following methods outlined by Berger and York (1981), the closure temperature for NB4-1 K-feldspar (450 ± 50 K) was calculated by using diffusion data obtained from low-temperature increments during the step - heating experiment.

RESULTS

All of the analyzed samples exhibited straightforward behavior during step heating. Table 2 is a summary of the results. Representative inverse isotope correlation

diagrams are shown in Figure 2. Release spectra for all samples analyzed, as well as inverse isotope correlation diagrams for samples not shown in Figure 2 are presented in Figure A of the appendix. Analytical data are presented in Table B of the appendix. All age uncertainties are quoted at the 2σ level and reflect propagated errors in the J - value, reactor correction factors, flux values, signal measurements, and blank and fractionation corrections.

Both hornblende samples analyzed contained a considerable amount of unsupported (or "excess") argon; NB5-1 is shown as an example (Figure 2a). All release steps for NB5-1 define an isochron with an intercept age of 48 ± 1 Ma and an initial $^{40}Ar/^{36}Ar$ value of 800 ± 200. NB17-1 yielded an isochron corresponding to an intercept at 48 ± 1 Ma and an initial $^{40}Ar/^{36}Ar$ ratio of 410 ± 60. Although the initial $^{40}Ar/^{36}Ar$ ratios for the two hornblende separates are markedly different, the closure ages are equivalent within uncertainty. The data indicate that the NB5-1 and NB17-1 hornblendes cooled through ~800 K at roughly the same time, yet incorporated argon with different initial $^{40}Ar/^{36}Ar$ ratios.

Muscovites from samples NB16-1, NB16-4, and NB20-1 form linear arrays on inverse isotope correlation diagrams indicative of cooling ages between 44.7 ± 0.9 and 42.1 ± 0.8 Ma. NB20-1 exhibits typical behavior (Figure 2b). All ten release steps define an isochron corresponding to an age of 44.7 ± 0.9 Ma and an initial $^{40}Ar/^{36}Ar$ value of 300 ± 20. The initial ratios for all analyzed muscovite samples are within uncertainty of the present-day atmospheric value, indicating no significant incorporation of unsupported argon at the time of crystallization.

All biotite samples display well-defined isochrons, and there is no clear evidence for unsupported argon. Isochron ages range between 42.5 and 45 Ma. NB17-1 biotite (Figure 2c) yielded an isochron consisting of seven increments, representing 89% of the total ^{39}Ar released, with an intercept age of 44.3 ± 0.9 Ma. Individual steps for this and other analyzed biotites plot close to the horizontal axis on the isotope

correlation diagram and closely define the intercept age. The initial $^{40}Ar/^{36}Ar$ ratios for these samples are less well defined, but they are all within uncertainty of the present-day atmospheric value.

Only one potassium feldspar sample (NB4-1) was analyzed. With the exception of the first temperature step at 725 K, corresponding to <1% of the total ^{39}Ar released, the data for NB4-1 define an isochron age of 40.3 ± 0.8 Ma and an initial $^{40}Ar/^{36}Ar$ ratio of 750 ± 70 (Figure 2d). Because most release increments for this sample are highly radiogenic and plot close to the $^{39}Ar/^{40}Ar$ axis in Figure 2d, we do not place great confidence in the high initial ratio indicated by regression analysis. As a consequence, we interpret the data to indicate cooling through the closure temperature of the least-retentive Ar diffusion domain in this sample (~450 K) at ~41 - 40 Ma.

TECTONIC DENUDATION AND COOLING

Because the closure temperature for argon in hornblende is within the probable range of temperature conditions for the initial stages of mylonitization (Kerrich and Hyndman, 1986), we consider hornblende cooling ages of ~48 Ma from the mylonite zone to be reasonable estimates of the age of mylonitization in this shear zone. This interpretation is consistent with all available U-Pb data as well as the 46.4 Ma $^{40}Ar/^{39}Ar$ potassium feldspar age for a postmylonitic dike reported by Hodges and Applegate (1993). Mica and potassium feldspar cooling ages from the northern Bitterroot core complex are in agreement with those obtained by Garmezy (1983) and Garmezy and Sutter (1983) for the southern Bitterroot range. Together, the two suites of samples suggest that rapid cooling characterized the entire eastern Bitterroot complex over the 45.5-40.3 Ma interval. These data also demonstrate that this cooling event clearly postdates the age of shear zone formation as well as the minimum age of movement on the Bitterroot mylonite zone.

This discrepancy might be explained in several ways. It is possible that the $^{40}Ar/^{39}Ar$ mica systematics were disturbed by postmylonitization hydrothermal activity. We do not favor this hypothesis because the samples studied showed no petrographic evidence for alteration, and previous stable isotopic studies found no indication of hydrothermal exchange in the metasedimentary units making up the northeastern part of the complex (Kerrich and Hyndman, 1986). Similarly, there are no data to support the hypothesis that the 45.5 - 40.3 Ma cooling event was related to a pulse of post-mylonitization intrusive activity; no intrusive rocks of appropriate age have been identified. Noting that samples from higher structural levels yield ages older than those from lower levels, we suggest that rapid cooling in the Bitterroot core was most likely related to tectonic unroofing. In this scenario, the ~1 - 3 m.y. time lag between displacement and thermal re-equilibration of the footwall is indicative of the interval necessary for the cooling front related to unroofing to propagate downward to the structural levels represented by the analyzed samples. Theoretical studies have shown that a considerable amount of unroofing can occur before the thermal effects of the event are propagated through surrounding rocks, particularly in cases of rapid extension (Ruppel *et al.*, 1988). It remains to be determined, however, how much of this cooling is in direct response to mylonitization and how much is due to subsequent brittle extensional faulting. In any event, mica and feldspar cooling ages from footwall and mylonitic rocks do not reflect the age of mylonitization, as has been previously suggested.

Although $^{40}Ar/^{39}Ar$ geochronology is a valuable tool for reconstructing the thermal structure of metamorphic and igneous terranes, studies in areas such as the Bitterroot core complex illustrate the problems involved in interpreting the tectonic significance of thermochronologic data. If it can be demonstrated that a rapid cooling event in the footwall of an extensional shear zone is related to tectonic unroofing, then the time the cooling event began provides a minimum estimate for the age of shear-zone

development. In the Bitterroot example, this estimate is ~1 - 3 m.y. younger than the probable age of mylonitization. It is not difficult to imagine scenarios in which there is an even greater time lag between unroofing and thermal re-equilibration. These data serve to remind us that direct dating of synkinematic fabrics (Gromet, 1991) and high-precision dating of pre- and post-kinematic igneous rocks are the most desirable methods for determining the absolute age of extensional structures.

REFERENCES

Berger, G. W., and York, D., 1981, Geothermometry from $^{40}Ar/^{39}Ar$ dating experiments: Geochimica et Cosmochimica Acta, v. 45, p. 795-811.

Cebula, G. T., Kunk, M. J., Mehnert, H. H., Naeser, C. W., Obradovich, J. D., and Sutter, J. F., 1986, The Fish Canyon Tuff, a potential standard for the ^{40}Ar-^{39}Ar and fission-track methods: Terra Cognita, v. 6, p. 139-140.

Chase, R. B., 1977, Structural evolution of the Bitterroot dome and zone of cataclasis, in Chase, R. B., and Hyndman, D. W. eds., Mylonite detachment zone, eastern flank of Idaho batholith: Geological Society of America, Rocky Mountain Section, Field Guide 1, p. 1-24.

Chase, R. B., Bickford, M. E., and Arruda, E. C., 1983, Tectonic implications of Tertiary intrusion and shearing within the Bitterroot dome, northeastern Idaho batholith: Journal of Geology, v. 91, p. 462-470.

Davis, G. A., and Lister, G. S., 1988, Detachment faulting in continental extension; Perspectives from the Southwestern U.S. Cordillera, in Clark, S. P., *et al.*, eds., Processes in continental lithospheric deformation: Boulder, Colorado, Geological Society of America, Geology of North America, v. 218, p. 133-159.

Dokka, R. K., Mahaffie, M. J., and Snoke, A. W., 1986, Thermochronologic evidence of major tectonic denudation associated with detachment faulting, northern Ruby Mountains - East Humboldt Range, Nevada: Tectonics, v. 5, p. 995-1006.

Garmezy, L., 1983, Geology and geochronology of the southeast border of the Bitterroot dome: Implications for the structural evolution of the mylonitic carapace [Ph.D. thesis]: University Park, Pennsylvania State University, 276 p.

Garmezy, L., and Sutter, J. F., 1983, Mylonitization coincident with uplift in an extensional setting, Bitterroot Range, Montana-Idaho: Geological Society of America Abstracts with Programs, v. 15, p. 578.

Gromet, L. P., 1991, Direct dating of deformational fabrics, in Heaman, L., and Ludden, J. N., eds., Applications of radiogenic isotope systems to problems in geology: Toronto, Mineralogical Association of Canada, p. 167-189.

Hawthorne, F. C., 1981, Crystal chemistry of the amphiboles, in Veblen, D. R., ed., Amphiboles and other hydrous pyriboles-mineralogy: Mineralogical Society of America Reviews in Mineralogy, v. 9A, p. 1-102.

Hodges, K. V. and Applegate, J. D. R. A., 1993, Age of Tertiary extension in the Bitterroot metamorphic core complex, Montana and Idaho: Geology, v. 21, p. 161-164.

Hodges, K. V., Hames, W. E., Olszewski, W. J., Burchfiel, B. C., Royden, L. H., and Chen, Z., 1994, Thermobarometric and $^{40}Ar/^{39}Ar$ geochronologic constraints on Eohimalayan metamorphism in southern Tibet: Contributions to Mineralogy and Petrology, v.117, p. 151-163.

House, M. A., Isachsen, C. E., Hodges, K. V., and Bowring, S. A., 1993, Geochronologic evidence for a complex, post-extensional thermal structure in the Bitterroot dome metamorphic core complex, MT: Geological Society of America Abstracts with Programs, v. 25, no. 6, p. A411.

Hyndman, D. W., 1980, Bitterroot dome - Sapphire tectonic block, an example of a plutonic-core gneiss-dome complex with its detached suprastructure, in Crittenden, M. D., *et al.*, eds., Cordilleran metamorphic core complexes: Geological Society of America Memoir 153, p. 427-443.

Hyndman, D. W., and Myers, S. A., 1988, The transition from amphibolite-facies mylonite to chloritic breccia and role of the mylonite in formation of Eocene epizonal plutons, Bitterroot dome, Montana: Geologische Rundschau, v. 77, p. 211-226.

Kerrich, R., and Hyndman, D. W., 1986, Thermal and fluid regimes in the Bitterroot lobe - Sapphire block detachment zone, Montana: Evidence from $^{18}O/^{16}O$ and geologic relations: Geological Society of America Bulletin, v. 97, p. 147-155.

Lister, G. S., and Baldwin, S. L., 1993, Plutonism and the origin of metamorphic core complexes: Geology, v. 21, p. 607-610.

McDougall, I., and Harrison, T. M., 1988, Geochronology and thermochronology by the $^{40}Ar/^{39}Ar$ Method: New York, Oxford University Press, 212 p.

Rehn, W., and Lund, K., 1981, Eocene extensional plutonism in the Idaho batholith region: Geological Society of America Abstracts with Programs, v. 13, p. 536.

Ruppel, C., Royden, L., and Hodges, K. V., 1988, Thermal modeling of extensional tectonics: Application to pressure-temperature-time histories of metamorphic rocks: Tectonics, v. 7, p. 947-957.

Samson, S. D., and Alexander, E. C., 1987, Calibration of the interlaboratory $^{40}Ar/^{39}Ar$ dating standard, MMhb-1: Chemical Geology, v. 66, p. 27-34.

Wehrenberg, J. P., 1972, Geology of the Lolo Peak area, northern Bitterroot Range, Montana: Northwest Geology, v. 1, p. 25-32.

York, D., 1969, Least-squares fitting of a straight line with correlated errors: Earth and Planetary Science Letters, v. 5, p. 320-324.

APPENDIX

Table A.1
Hornblende microprobe analyses

	NB5-1 hornblende	NB17-1 hornblende
SiO_2	44.02(0.86)	51.47(0.99)
Al_2O_3	11.80(0.94)	5.08(1.09)
TiO_2	0.94(0.06)	0.34(0.05)
FeO	18.90(0.26)	12.40(0.37)
MgO	8.89(0.46)	15.38(0.42)
MnO	0.24(0.03)	0.20(0.02)
CaO	10.94(0.12)	11.92(0.11)
Na_2O	1.03(0.06)	0.56(0.16)
K_2O	0.63(0.07)	0.20(0.08)
F	-	0.00(0.01)
Cl	-	0.02(0.01)
Total	97.48	97.61
	Formula Basis 23 Oxygens	
Si	6.626	7.455
Al	2.094	0.816
Ti	0.107	0.035
Cr	0.011	0.004
Fe	2.379	1.479
Mg	1.994	3.347
Mn	0.031	0.025
Ca	1.764	1.846
Na	0.299	0.149
K	0.120	0.034
F	-	0.002
Cl	-	0.003
Total	15.424	15.194

Numbers in parentheses denote 1σ uncertainties in composition. Dashes indicate that the particular element was not analyzed.

Table A.2 Biotite and muscovite microprobe analyses

	NB4-1 biotite	NB5-1 biotite	NB16-4 biotite	NB17-1 biotite	NB20-1 biotite	NB16-1 muscovite	NB16-4 muscovite	NB20-1 muscovite
SiO_2	35.90(0.23)	36.32(0.18)	35.26(0.10)	36.85(0.27)	36.45(0.14)	46.47(0.32)	46.36(0.12)	47.13(0.23)
Al_2O_3	15.21(0.13)	16.3(0.61)	19.94(0.11)	15.7(0.10)	18.76(0.19)	34.32(0.57)	35.26(0.17)	32.99(0.58)
TiO_2	3.94(0.12)	2.86(0.06)	2.91(0.03)	3.52(0.07)	3.07(0.17)	0.74(0.07)	0.59(0.03)	1.02(0.06)
FeO	22.46(0.44)	21.2(0.65)	22.69(0.40)	18.57(0.70)	19.21(0.51)	1.21(0.21)	1.17(0.10)	1.44(0.10)
MgO	9.71(0.12)	9.83(0.12)	7.16(0.06)	12.43(0.62)	9.15(0.05)	0.72(0.13)	0.59(0.06)	1.22(0.14)
MnO	0.26(0.03)	0.12(0.02)	0.22(0.03)	0.08(0.01)	0.58(0.03)	0.03(0.02)	-	0.04(0.02)
CaO	0.03(0.01)	0.11(0.02)	0.01(0.01)	0.09(0.2)	-	0.04(0.03)	0.01(0.01)	0.01(0.01)
Na_2O	0.10(0.02)	0.11(0.02)	0.19(0.01)	0.12(0.04)	0.06(0.03)	0.90(0.04)	0.66(0.02)	0.42(0.01)
K_2O	9.40(0.12)	7.78(0.64)	9.11(0.01)	9.19(0.20)	9.57(0.12)	9.79(0.13)	10.4(0.06)	10.75(0.05)
F	0.19(0.03)	-	-	0.00(0.01)	-	-	-	-
Cl	0.04(0.01)	-	-	0.08(0.01)	-	-	-	-
Total	97.22	94.77	97.56	96.66	96.88	94.18	95.04	95.02
				Formula Basis 11 Oxygens				
Si	2.738	1.478	1.770	2.758	2.726	3.115	3.089	3.153
Al	1.367	0.165	0.165	1.385	1.654	2.714	2.769	2.602
Ti	0.226	0.165	0.165	0.198	0.173	0.037	0.030	0.051
Fe	1.437	1.358	1.429	1.163	1.201	0.069	0.065	0.080
Mg	1.104	1.122	0.804	1.387	1.021	0.072	0.058	0.122
Mn	0.017	0.008	0.014	0.005	0.037	0.002	0.000	0.002
Ca	0.002	0.009	0.001	0.007	0.000	0.003	0.001	0.001
Na	0.015	0.017	0.027	0.018	0.009	0.118	0.085	0.054
K	0.914	0.760	0.875	0.877	0.913	0.838	0.884	0.917
F	0.045	-	-	0.000	-	-	-	-
Cl	0.005	-	-	0.011	-	-	-	-
Total	7.864	7.702	7.746	7.809	7.735	6.969	6.981	6.981

Numbers in parentheses denote 1σ uncertainties in composition. Dashes indicate that the particular element was not analyzed.

Table A.3
K-feldspar microprobe analyses

	NB4-1 k-feldspar
SiO_2	64.03(0.22)
Al_2O_3	18.93(0.06)
FeO	0.02(0.02)
MgO	0.00(0.01)
CaO	0.03(0.01)
Na_2O	1.09(0.06)
K_2O	14.66(0.17)
Total	98.77
Formula Basis 8 Oxygens	
Si	2.978
Al	1.038
Fe	0.001
Mg	0.000
Ca	0.002
Na	0.098
K	0.870
Total	4.987

Numbers in parentheses denote 1σ uncertainties in composition.
Dashes indicate that the particular element was not analyzed.

Table B. 1 $^{40}Ar/^{39}Ar$ Analytical Data for NB20-1 Biotite

T(K)	$^{39}Ar/^{40}Ar$	$^{36}Ar/^{40}Ar$	$^{39}Ar(\%)$	$^{40}Ar^{*}(\%)$	K/Ca	Age ($\pm 2\sigma$)
900	0.1564	0.0010	34.7	69.5	1167.8	44.5 ± 0.9
950	0.2034	0.0003	44.1	89.9	1760.8	44.3 ± 0.9
1000	0.2002	0.0004	50.2	88.9	980.7	44.5 ± 0.9
1050	0.1944	0.0004	54.6	88.1	276.5	45.4 ± 0.9
1100	0.1946	0.0004	59.4	86.8	1480.7	44.7 ± 0.9
1150	0.1977	0.0004	68.4	88.4	1643.6	44.8 ± 0.9
1200	0.1987	0.0004	79.3	88.5	0.0	44.6 ± 0.9
1250	0.1964	0.0004	90.0	87.4	2098.0	44.6 ± 0.9
1350	0.1988	0.0004	97.3	89.5	1238.3	45.1 ± 0.9
1550	0.1931	0.0003	100.0	90.6	373.0	46.9 ± 0.9

J value: 0.00562 ± 0.0000562. Duration of each increment: 5 minutes. $^{39}Ar(\%)$ denotes the percentage of the total ^{39}Ar released in the experiment that was derived from the specified increment; $^{40}Ar^{*}(\%)$ indicates the percentage of radiogenic ^{40}Ar in the specified increment.

Table B.2 $^{40}Ar/^{39}Ar$ Analytical Data for NB20-1 Muscovite

T(K)	$^{39}Ar/^{40}Ar$	$^{36}Ar/^{40}Ar$	$^{39}Ar(\%)$	$^{40}Ar^{*}(\%)$	K/Ca	Age ($\pm 2\sigma$)
900	0.1613	0.0006	1.4	82.5	117.7	51.1 ± 1.0
950	0.1176	0.0015	5.4	55.8	362.2	47.4 ± 0.9
1000	0.1644	0.0009	28.3	73.6	3703.8	44.8 ± 0.9
1050	0.2052	0.0003	51.5	91.6	2216.1	44.7 ± 0.9
1100	0.1999	0.0004	66.6	89.3	1833.4	44.7 ± 0.9
1150	0.1805	0.0006	73.9	81.9	704.3	45.4 ± 0.9
1200	0.1692	0.0008	78.4	77.6	407.0	45.9 ± 0.9
1250	0.1801	0.0007	84.1	79.2	528.6	44.1 ± 0.9
1350	0.2010	0.0003	95.4	90.2	1220.2	44.9 ± 0.9
1550	0.2075	0.0001	100.0	96.2	529.9	46.4 ± 0.9

J value: 0.00562 ± 0.0000562. Duration of each increment: 5 minutes. $^{39}Ar(\%)$ denotes the percentage of the total ^{39}Ar released in the experiment that was derived from the specified increment; $^{40}Ar^{*}(\%)$ indicates the percentage of radiogenic ^{40}Ar in the specified increment.

Table B.3 $^{40}Ar/^{39}Ar$ Analytical Data for NB17-1 Biotite

T(K)	$^{39}Ar/^{40}Ar$	$^{36}Ar/^{40}Ar$	$^{39}Ar(\%)$	$^{40}Ar^{*}(\%)$	K/Ca	Age ($\pm 2\sigma$)
800	0.1853	0.0004	4.7	87.3	153.6	47.1 ± 0.9
850	0.1751	0.0003	5.8	92.2	59.1	52.3 ± 1.0
900	0.2010	0.0001	9.0	98.0	60.2	48.7 ± 1.0
950	0.2026	0.0003	11.1	91.8	42.7	45.3 ± 0.9
1000	0.2014	0.0003	23.1	90.5	34.6	44.9 ± 0.9
1050	0.2042	0.0003	32.6	91.5	25.6	44.8 ± 0.9
1100	0.1930	0.0004	39.1	88.0	13.2	45.6 ± 0.9
1150	0.1893	0.0005	48.8	86.5	8.1	45.7 ± 0.9
1200	0.1998	0.0003	62.2	90.6	3.6	45.3 ± 0.9
1250	0.2069	0.0002	75.7	94.2	4.7	45.5 ± 0.9
1300	0.2128	0.0002	91.5	95.2	5.1	44.7 ± 0.9
1400	0.2084	0.0002	98.2	93.6	3.9	44.9 ± 0.9
1550	0.1865	0.0001	100.0	98.0	5.5	52.4 ± 1.0

J value: 0.00561 ± 0.0000561. Duration of each increment: 5 minutes. $^{39}Ar(\%)$ denotes the percentage of the total ^{39}Ar released in the experiment that was derived from the specified increment; $^{40}Ar^{*}(\%)$ indicates the percentage of radiogenic ^{40}Ar in the specified increment.

Table B.4 $^{40}Ar/^{39}Ar$ Analytical Data for NB17-1 Hornblende

T(K)	$^{39}Ar/^{40}Ar$	$^{36}Ar/^{40}Ar$	$^{39}Ar(\%)$	$^{40}Ar^{*}(\%)$	K/Ca	Age ($\pm 2\sigma$)
1000	0.1303	0.0011	3.3	66.5	0.6	51.4 ± 1.0
1100	0.1221	0.0008	6.4	75.1	0.2	61.8 ± 1.2
1150	0.1002	0.0012	12.2	63.7	0.1	63.9 ± 1.3
1175	0.1066	0.0010	20.3	69.2	0.1	65.2 ± 1.3
1200	0.1087	0.0012	38.0	65.2	0.1	60.3 ± 1.2
1220	0.1221	0.0011	56.9	68.1	0.1	56.1 ± 1.1
1240	0.1484	0.0009	64.9	74.2	0.1	50.4 ± 1.0
1260	0.1606	0.0004	67.6	89.6	0.1	56.2 ± 1.1
1280	0.1443	0.0008	71.3	76.6	0.1	53.5 ± 1.1
1300	0.1378	0.0008	78.5	75.3	0.1	55.1 ± 1.1
1325	0.1383	0.0007	87.6	78.4	0.1	57.0 ± 1.1
1350	0.1363	0.0006	91.7	82.6	0.1	60.9 ± 1.2
1400	0.1348	0.0006	96.4	81.4	0.1	60.7 ± 1.2
1450	0.1341	0.0009	97.9	72.2	0.1	54.3 ± 1.1
1550	0.1282	0.0011	100.0	66.9	0.1	52.6 ± 1.0

J value: 0.00567 ± 0.0000567. Duration of each increment: 5 minutes. $^{39}Ar(\%)$ denotes the percentage of the total ^{39}Ar released in the experiment that was derived from the specified increment; $^{40}Ar^{*}(\%)$ indicates the percentage of radiogenic ^{40}Ar in the specified increment.

Table B.5 $^{40}Ar/^{39}Ar$ Analytical Data for NB16-4 Biotite

T(K)	$^{39}Ar/^{40}Ar$	$^{36}Ar/^{40}Ar$	$^{39}Ar(\%)$	$^{40}Ar^{*}(\%)$	K/Ca	Age ($\pm 2\sigma$)
900	0.1710	0.0008	42.4	76.4	0.0	44.3 ± 0.9
950	0.2069	0.0002	51.3	92.8	1110.9	44.4 ± 0.9
1000	0.2071	0.0002	57.7	93.7	754.9	44.8 ± 0.9
1050	0.2061	0.0002	62.4	94.8	515.9	45.5 ± 0.9
1100	0.2049	0.0003	67.7	90.9	489.8	43.9 ± 0.9
1150	0.2048	0.0003	78.5	90.4	1461.6	43.7 ± 0.9
1200	0.2023	0.0004	89.1	89.2	1401.3	43.7 ± 0.9
1250	0.2055	0.0003	97.3	91.1	1016.3	43.9 ± 0.9
1350	0.2038	0.0001	99.4	98.1	212.0	47.6 ± 0.9
1550	0.1863	0.0008	100.0	77.3	60.9	41.2 ± 0.8

J value: 0.00556 ± 0.0000556. Duration of each increment: 5 minutes. $^{39}Ar(\%)$ denotes the percentage of the total ^{39}Ar released in the experiment that was derived from the specified increment; $^{40}Ar^{*}(\%)$ indicates the percentage of radiogenic ^{40}Ar in the specified increment.

Table B.6 $^{40}Ar/^{39}Ar$ Analytical Data for NB16-4 Muscovite

T(K)	$^{39}Ar/^{40}Ar$	$^{36}Ar/^{40}Ar$	$^{39}Ar(\%)$	$^{40}Ar^{*}(\%)$	K/Ca	Age ($\pm 2\sigma$)
900	0.1384	0.0013	8.29	63.0	63.1	45.5 ± 0.9
950	0.1457	0.0010	12.51	69.1	314.1	47.4 ± 0.9
1000	0.1818	0.0007	31.74	78.2	558.2	43.0 ± 0.9
1050	0.2098	0.0003	51.99	90.2	463.2	43.0 ± 0.8
1100	0.2057	0.0003	62.63	89.8	254.7	43.7 ± 0.9
1150	0.1878	0.0007	68.49	80.5	81.3	42.9 ± 0.8
1200	0.1787	0.0008	72.93	75.7	123.1	42.4 ± 0.8
1250	0.1793	0.0007	78.11	79.2	393.0	44.1 ± 0.9
1350	0.1993	0.0005	92.73	85.5	173.4	42.9 ± 0.8
1550	0.2156	0.0002	100.00	93.3	53.5	43.3 ± 0.9

J value: 0.00561 ± 0.0000561. Duration of each increment: 5 minutes. $^{39}Ar(\%)$ denotes the percentage of the total ^{39}Ar released in the experiment that was derived from the specified increment; $^{40}Ar^{*}(\%)$ indicates the percentage of radiogenic ^{40}Ar in the specified increment.

Table B.7 $^{40}Ar/^{39}Ar$ Analytical Data for NB16-1 Muscovite

T(K)	$^{39}Ar/^{40}Ar$	$^{36}Ar/^{40}Ar$	$^{39}Ar(\%)$	$^{40}Ar^{*}(\%)$	K/Ca	Age ($\pm 2\sigma$)
800	0.1837	0.0004	0.49	88.1	26.4	47.5 ± 0.9
850	0.1730	0.0003	0.84	90.1	1196.9	51.6 ± 1.0
900	0.1708	0.0006	2.06	81.9	168.3	47.5 ± 0.9
950	0.1706	0.0007	4.91	78.0	87.0	45.4 ± 0.9
1000	0.1587	0.0010	11.95	70.5	185.9	44.1 ± 0.9
1050	0.1926	0.0005	38.85	84.3	660.4	43.4 ± 0.9
1100	0.2151	0.0003	55.62	92.4	442.0	42.7 ± 0.8
1150	0.2019	0.0004	64.08	87.8	463.7	43.2 ± 0.9
1200	0.1885	0.0007	69.03	79.2	192.4	41.8 ± 0.8
1250	0.1875	0.0006	73.82	82.3	754.5	43.6 ± 0.9
1300	0.1969	0.0005	82.63	85.7	363.9	43.2 ± 0.9
1350	0.2130	0.0003	93.16	91.4	435.3	42.6 ± 0.8
1500	0.2161	0.0002	100.00	93.5	265.5	43.0 ± 0.8

J value: 0.00561 ± 0.0000561. Duration of each increment: 5 minutes. $^{39}Ar(\%)$ denotes the percentage of the total ^{39}Ar released in the experiment that was derived from the specified increment; $^{40}Ar^{*}(\%)$ indicates the percentage of radiogenic ^{40}Ar in the specified increment.

Table B.8 $^{40}Ar/^{39}Ar$ Analytical Data for NB5-1 Hornblende

T(K)	$^{39}Ar/^{40}Ar$	$^{36}Ar/^{40}Ar$	$^{39}Ar(\%)$	$^{40}Ar^*(\%)$	K/Ca	Age ($\pm 2\sigma$)
1000	0.1242	0.0013	1.7	61.3	0.2	49.8 ± 1.0
1100	0.1050	0.0008	3.0	76.5	0.1	73.1 ± 1.4
1150	0.1230	0.0004	8.4	88.7	0.1	72.4 ± 1.4
1175	0.1904	0.0001	37.1	96.7	0.1	51.3 ± 1.0
1200	0.2002	0.0000	77.5	98.9	0.1	49.9 ± 1.0
1220	0.1786	0.0003	82.5	91.8	0.1	51.9 ± 1.0
1240	0.1557	0.0003	84.6	90.7	0.0	58.7 ± 1.2
1260	0.1562	0.0006	87.3	82.3	0.1	53.2 ± 1.0
1280	0.1574	0.0005	90.0	84.3	0.1	54.1 ± 1.1
1300	0.1663	0.0015	92.9	54.8	0.1	33.4 ± 0.7
1325	0.1761	0.0003	98.2	91.1	0.1	52.2 ± 1.0
1400	0.1350	0.0002	98.8	93.8	0.1	69.8 ± 1.4
1550	0.1478	0.0008	100.0	77.8	0.1	53.2 ± 1.0

J value: 0.00568 ± 0.0000568. Duration of each increment: 5 minutes. $^{39}Ar(\%)$ denotes the percentage of the total ^{39}Ar released in the experiment that was derived from the specified increment; $^{40}Ar^*(\%)$ indicates the percentage of radiogenic ^{40}Ar in the specified increment.

Table B.9 $^{40}Ar/^{39}Ar$ Analytical Data for NB5-1 Biotite

T(K)	$^{39}Ar/^{40}Ar$	$^{36}Ar/^{40}Ar$	$^{39}Ar(\%)$	$^{40}Ar^*(\%)$	K/Ca	Age ($\pm 2\sigma$)
800	0.0554	0.0031	1.3	9.0	4.2	16.4 ± 0.3
850	0.0806	0.0026	4.0	23.9	12.1	29.8 ± 0.6
900	0.1144	0.0017	8.0	50.7	26.3	44.3 ± 0.9
950	0.1650	0.0010	14.4	70.6	27.5	42.8 ± 0.8
1000	0.1756	0.0007	19.8	78.9	29.0	44.9 ± 0.9
1050	0.1731	0.0007	24.4	79.2	29.3	45.8 ± 0.9
1100	0.1779	0.0006	29.1	83.0	24.9	46.7 ± 0.9
1150	0.1740	0.0007	34.9	80.0	18.0	46.0 ± 0.9
1200	0.1874	0.0005	49.3	86.3	15.7	46.0 ± 0.9
1250	0.1990	0.0002	68.5	92.7	10.4	46.6 ± 0.9
1300	0.2061	0.0003	90.3	92.2	34.0	44.8 ± 0.9
1400	0.2041	0.0003	99.5	92.0	20.4	45.1 ± 0.9
1550	0.1522	0.0000	100.0	99.5	11.0	65.0 ± 1.3

J value: 0.005615 ± 0.00005615. Duration of each increment: 5 minutes. $^{39}Ar(\%)$ denotes the percentage of the total ^{39}Ar released in the experiment that was derived from the specified increment; $^{40}Ar^*(\%)$ indicates the percentage of radiogenic ^{40}Ar in the specified increment.

Table B.10 $^{40}Ar/^{39}Ar$ Analytical Data for NB4-1 Potassium Feldspar

T(K)	$^{39}Ar/^{40}Ar$	$^{36}Ar/^{40}Ar$	$^{39}Ar(\%)$	$^{40}Ar^{*}(\%)$	K/Ca	Age ($\pm 2\sigma$)
725	0.0289	0.0020	0.7	41.8	2.0	93.4 ± 1.8
750	0.1289	0.0003	1.1	91.5	0.9	46.5 ± 0.9
775	0.1394	0.0006	1.6	81.4	0.5	38.3 ± 0.8
800	0.1449	0.0001	2.2	97.8	1.8	44.3 ± 0.9
825	0.1355	0.0002	3.2	93.5	2.6	45.2 ± 0.9
850	0.1184	0.0007	4.4	79.5	3.2	44.0 ± 0.9
875	0.1336	0.0005	5.9	84.6	3.9	41.6 ± 0.8
900	0.1519	0.0002	8.0	95.0	24.4	41.0 ± 0.8
950	0.1548	0.0001	12.2	97.5	11.1	41.3 ± 0.8
1000	0.1558	0.0001	19.0	98.1	18.1	41.3 ± 0.8
1100	0.1569	0.0001	33.6	98.2	76.2	41.1 ± 0.8
1200	0.1557	0.0001	49.6	98.5	43.9	41.5 ± 0.8
1300	0.1495	0.0001	65.0	96.5	85.2	42.4 ± 0.8
1500	0.1356	0.0002	100.0	93.4	144.8	45.1 ± 0.9

J value: 0.00368 ± 0.0000368. Duration of each increment: 10 minutes. $^{39}Ar(\%)$ denotes the percentage of the total ^{39}Ar released in the experiment that was derived from the specified increment; $^{40}Ar^{*}(\%)$ indicates the percentage of radiogenic ^{40}Ar in the specified increment.

Table B.11 $^{40}Ar/^{39}Ar$ Analytical Data for NB4-1 Biotite

T(K)	$^{39}Ar/^{40}Ar$	$^{36}Ar/^{40}Ar$	$^{39}Ar(\%)$	$^{40}Ar^{*}(\%)$	K/Ca	Age ($\pm 2\sigma$)
900	0.1969	0.0006	8.6	84	97.0	42.4 ± 0.8
950	0.2164	0.0002	24.3	93	100.0	42.9 ± 0.8
1000	0.2178	0.0002	32.4	94	62.5	43.0 ± 0.8
1050	0.2142	0.0003	37.4	91	35.9	42.4 ± 0.8
1100	0.2079	0.0004	41.3	87	20.5	41.8 ± 0.8
1150	0.2098	0.0003	47.2	90	20.0	42.8 ± 0.8
1200	0.2188	0.0002	56.8	93	31.4	42.4 ± 0.8
1250	0.2192	0.0002	76.7	94	47.0	42.8 ± 0.8
1350	0.2161	0.0002	98.1	93	23.7	43.1 ± 0.9
1550	0.2003	0.0003	100.0	92	12.4	45.8 ± 0.9

J value: 0.00561 ± 0.0001122. Duration of each increment: 5 minutes. $^{39}Ar(\%)$ denotes the percentage of the total ^{39}Ar released in the experiment that was derived from the specified increment; $^{40}Ar^{*}(\%)$ indicates the percentage of radiogenic ^{40}Ar in the specified increment.

APPENDIX FIGURE CAPTIONS

Figure A. Supplementary release spectra and isotope correlation diagrams for samples referred to in Table 2 of House and Hodges (1994). For each sample, our interpretation of the best apparent age is the isochron age. Plateau ages were calculated following the method outlined by McDougall and Harrison (1988). Steps included in the plateau are shaded. Isochron ages were calculated using least-squares linear regression with correlated errors (York 2; York, 1969). The MSWD (mean squared weighted deviation) is shown for all regressions. Points excluded from the linear regression are indicated by the white circles. Uncertainties include propagated errors in the J - value, reactor correction factors, flux values, signal measurements, and blank and fractionation corrections and are quoted at the 2σ confidence level.

Appendix Figure A

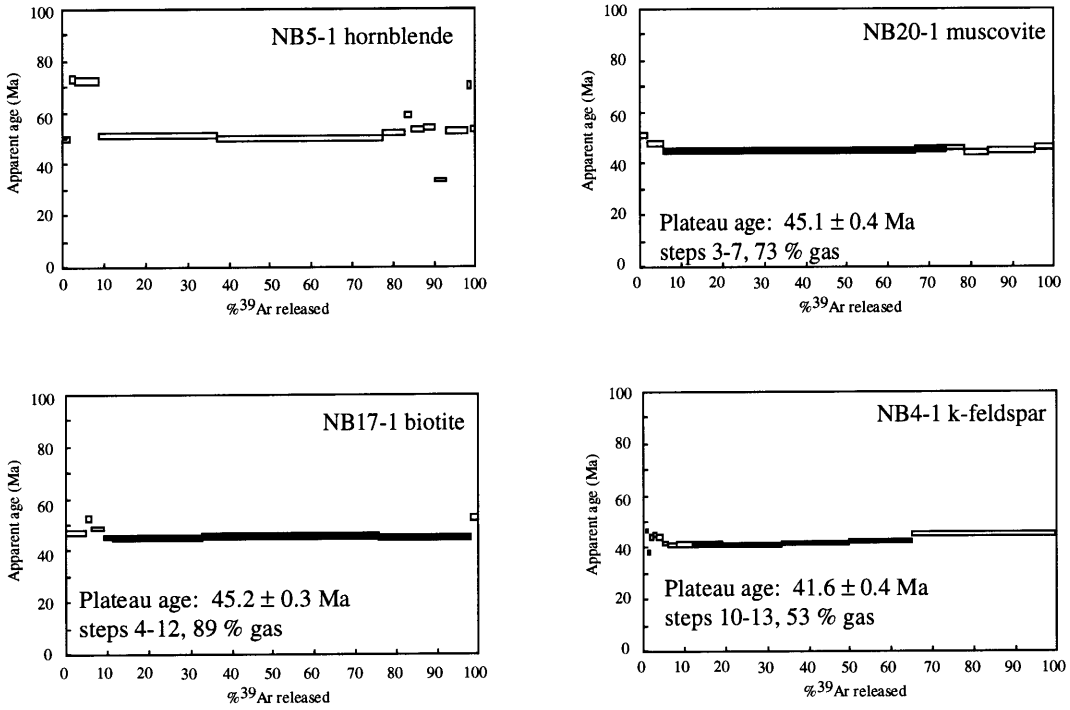

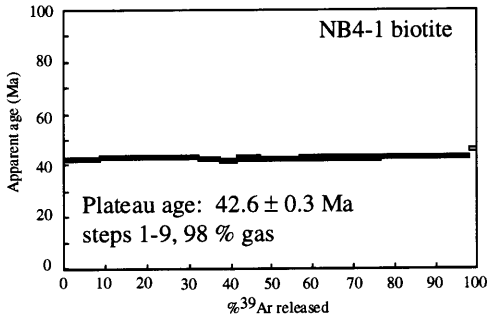
NB4-1 biotite
Plateau age: 42.6 ± 0.3 Ma
steps 1-9, 98 % gas
Apparent age (Ma)
%39Ar released

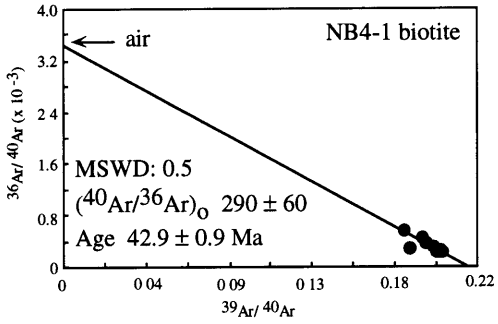
air
NB4-1 biotite
MSWD: 0.5
(40Ar/36Ar)o 290 ± 60
Age 42.9 ± 0.9 Ma
36Ar/40Ar (x 10-3)
39Ar/40Ar

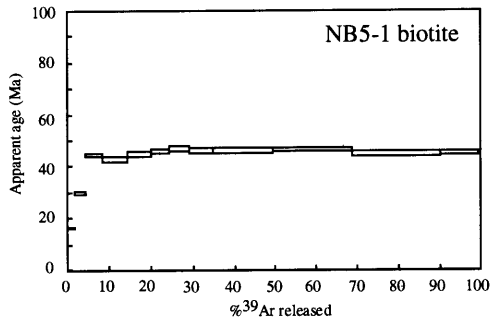
NB5-1 biotite
Apparent age (Ma)
%39Ar released

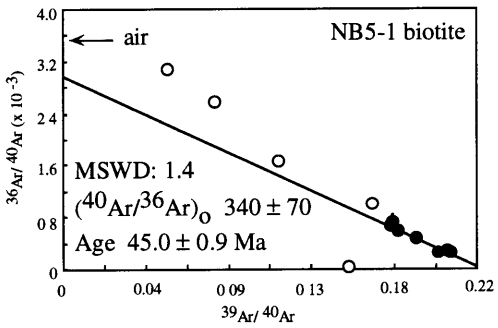
air
NB5-1 biotite
MSWD: 1.4
(40Ar/36Ar)o 340 ± 70
Age 45.0 ± 0.9 Ma
36Ar/40Ar (x 10-3)
39Ar/40Ar

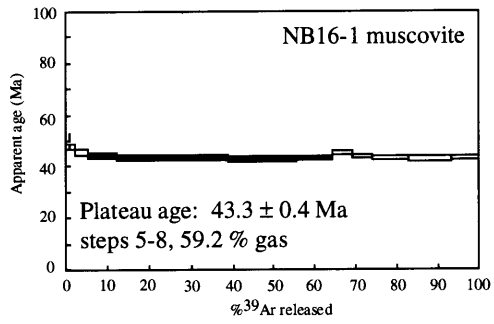
NB16-1 muscovite
Plateau age: 43.3 ± 0.4 Ma
steps 5-8, 59.2 % gas
Apparent age (Ma)
%39Ar released

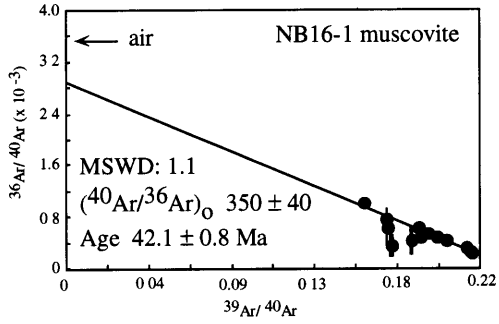
air
NB16-1 muscovite
MSWD: 1.1
(40Ar/36Ar)o 350 ± 40
Age 42.1 ± 0.8 Ma
36Ar/40Ar (x 10-3)
39Ar/40Ar

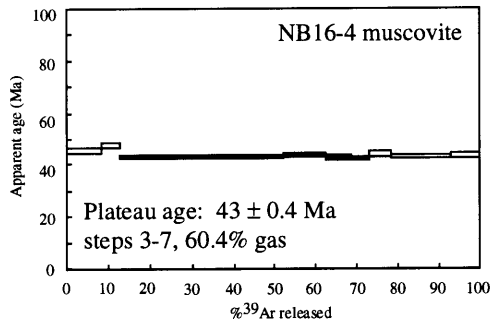
NB16-4 muscovite
Plateau age: 43 ± 0.4 Ma
steps 3-7, 60.4% gas
Apparent age (Ma)
%39Ar released

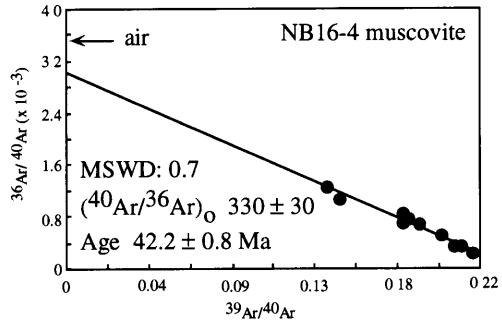
air
NB16-4 muscovite
MSWD: 0.7
(40Ar/36Ar)o 330 ± 30
Age 42.2 ± 0.8 Ma
36Ar/40Ar (x 10-3)
39Ar/40Ar

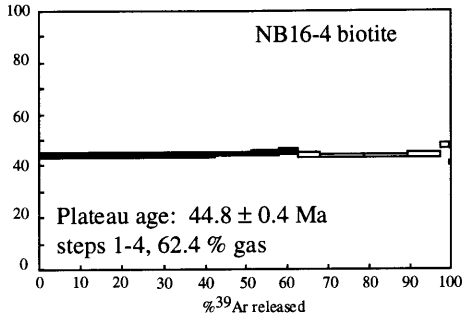
NB16-4 biotite
Plateau age: 44.8 ± 0.4 Ma
steps 1-4, 62.4 % gas
%39Ar released

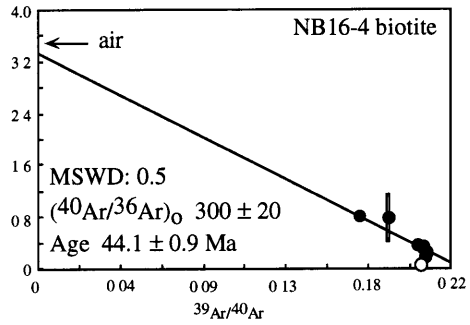
NB16-4 biotite
air
MSWD: 0.5
(40Ar/36Ar)o 300 ± 20
Age 44.1 ± 0.9 Ma
39Ar/40Ar

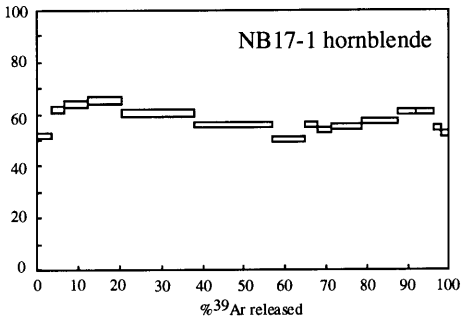
NB17-1 hornblende
%39Ar released

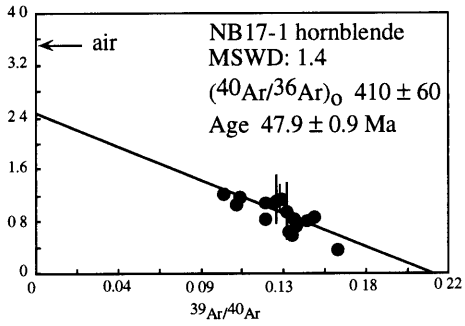
NB17-1 hornblende
air
MSWD: 1.4
(40Ar/36Ar)o 410 ± 60
Age 47.9 ± 0.9 Ma
39Ar/40Ar

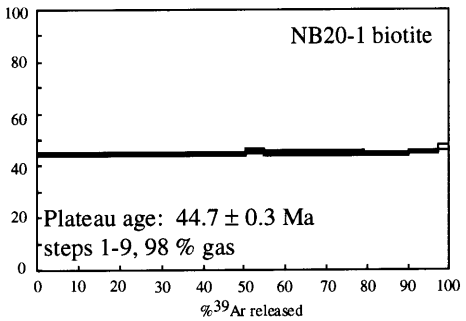
NB20-1 biotite
Plateau age: 44.7 ± 0.3 Ma
steps 1-9, 98 % gas
%39Ar released

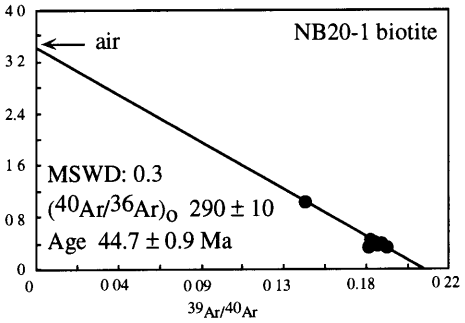
NB20-1 biotite
air
MSWD: 0.3
(40Ar/36Ar)o 290 ± 10
Age 44.7 ± 0.9 Ma
39Ar/40Ar

Table 1. Sample Locations

Sample	Latitude	Longitude
NB4 -1	46° 35' 00"	114° 11' 56"
NB5 -1	46° 30' 35"	114° 14' 23"
NB16 - 1	46° 37' 12"	114° 08' 37"
NB16 - 4	46° 37' 53"	114° 10' 34"
NB17 - 1	46° 38' 09"	114° 12' 56"
NB20 - 1	46° 41' 57"	114° 12' 05"

Table 2: Summary of $^{40}Ar/^{39}Ar$ Results

Sample	Mineral	Plateau age (Ma)	$^{39}Ar_p$ (%)	Isochron age (Ma)	$^{39}Ar_i$ (%)	$(^{40}Ar/^{36}Ar)_o$	MSWD
NB20-1	ms	45.1 ± 0.4	73	44.7 ± 0.9	100	300 ± 20	1.0
NB20-1	bt	44.7 ± 0.3	97	44.6 ± 0.9	98	290 ± 10	0.3
NB16-1	ms	43.3 ± 0.4	59	42.1 ± 0.8	99	350 ± 40	1.1
NB16-4	ms	43.0 ± 0.4	60	42.2 ± 0.8	100	330 ± 30	0.7
NB16-4	bt	44.8 ± 0.4	62	44.1 ± 0.9	98	300 ± 20	0.5
NB17-1	bt	45.2 ± 0.3	89	44.3 ± 0.9	95	400 ± 200	0.1
NB17-1	hbl	---	---	47.9 ± 0.9	100	410 ± 60	1.4
NB5-1	bt	---	---	45.0 ± 0.9	85	340 ± 70	1.4
NB5-1	hbl	---	---	48.4 ± 0.9	91	800 ± 200	1.1
NB4-1	ksp	41.6 ± 0.4	53	40.3 ± 0.8	98	750 ± 70	1.8
NB4-1	bt	42.6 ± 0.3	98	42.9 ± 0.8	98	290 ± 80	0.5

Note: For each sample, our interpretation of the best apparent age is the isochron age. Entries in the Plateau age column were calculated following the method outlined by McDougall and Harrison (1988), and the percentage of the total ^{39}Ar in the sample that was released in the heating steps included in the plateau are shown in the column labeled $^{39}Ar_p$. Isochron ages were calculated using least-squares linear regression with correlated errors (York, 1969). The column $^{39}Ar_i$ shows the percentage of total ^{39}Ar in the heating steps used for the regression. $(^{40}Ar/^{36}Ar)_o$ indicates the initial value for each sample. The MSWD (mean squared weighted deviation) is shown for all regressions. (See Appendix I for tables of analytical data.)

FIGURE CAPTIONS

Figure 1. Generalized geologic map of the Bitterroot complex, modified from Hyndman (1980), showing the locations of various geochronologic study sites mentioned in the text. a: this study; b: Hodges and Applegate (1993); c: Garmezy (1983); d: Chase *et al.* (1983).

Figure 2. Representative $^{40}Ar/^{39}Ar$ results for this study presented as inverse isotope correlation diagrams. Steps excluded from isochron regression are indicated by open circles. Error bars are shown at 2σ where they are larger than the circle representing the point. (See Appendix I for corresponding release spectra.)

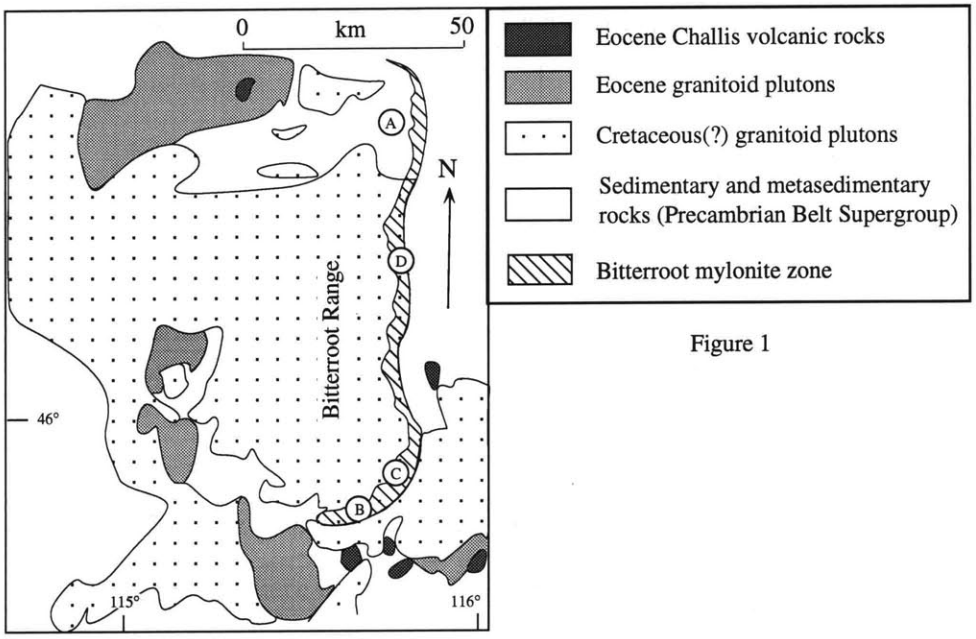
0
km
50
N
A
B
C
D
Bitterroot Range
46°
115°
116°
Eocene Challis volcanic rocks
Eocene granitoid plutons
Cretaceous(?) granitoid plutons
Sedimentary and metasedimentary rocks (Precambrian Belt Supergroup)
Bitterroot mylonite zone

Figure 1

Figure 2

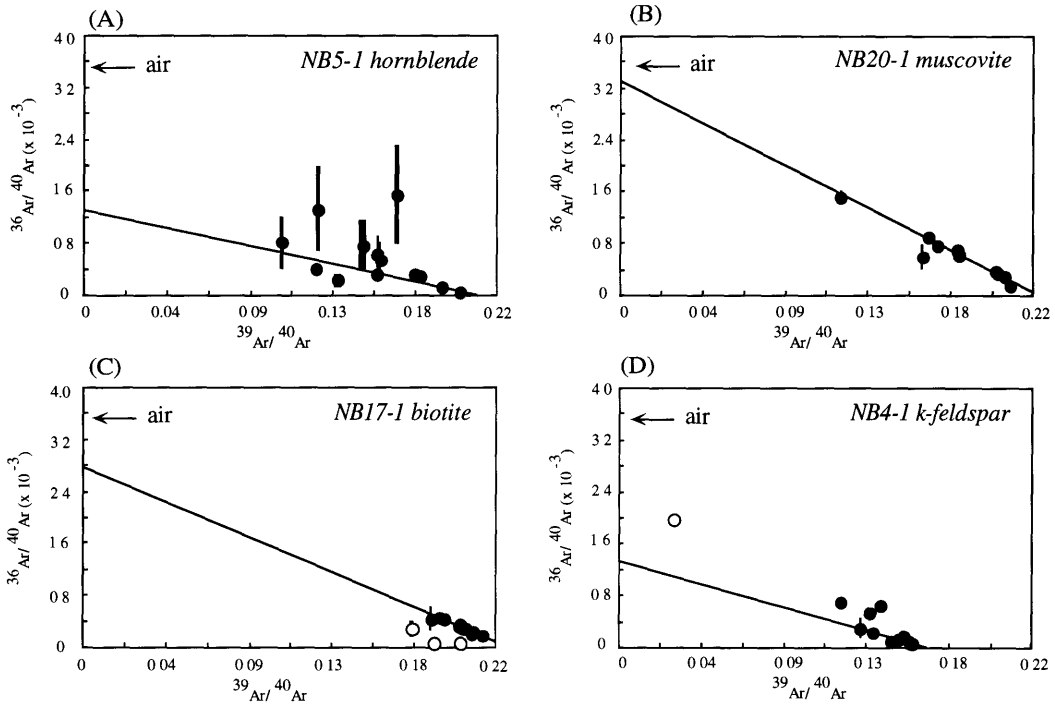
(A)
air
NB5-1 hornblende
(B)
air
NB20-1 muscovite
(C)
air
NB17-1 biotite
(D)
air
NB4-1 k-feldspar
$^{36}Ar/^{40}Ar$ (x 10^{-3})
$^{39}Ar/^{40}Ar$

CHAPTER 3

PETROLOGIC AND GEOCHRONOLOGIC CONSTRAINTS ON THE RELATIONSHIP BETWEEN MAGMATISM, METAMORPHISM, AND THE ONSET OF EXTENSION IN THE NORTHERN BITTERROOT METAMORPHIC CORE COMPLEX, IDAHO-MONTANA

ABSTRACT

Quantitative thermobarometry and U-Pb geochronology demonstrate that peak metamorphic temperatures persisted in the Bitterroot metamorphic core complex, Idaho-Montana, as late as middle Eocene times. Thermobarometric data place tighter constraints on peak metamorphic conditions in the core rocks than were available on the basis of petrogenetic relationships and provide insight into the regional thermal structure of rocks on the northern margins of the Bitterroot batholith during regional metamorphism related to batholith emplacement. Temperatures deduced from thermobarometry in pelitic schists and garnet amphibolites are internally consistent (~950 - 1000 K). Pressures of ~750 - 800 MPa for pelitic assemblages are higher than those for amphibolite assemblages (~550 - 750 MPa) suggesting that the amphibolites re-equilibrated during high-temperature decompression of footwall rocks. U-Pb direct-dating of metamorphic zircon from footwall garnet amphibolites indicates that temperature conditions resulting from upper-amphibolite facies metamorphism, generally considered to be late Mesozoic in age, persisted in footwall rocks as late as 48 Ma, coeval with late stages of granitoid plutonism in the northeastern Bitterroot batholith and the early stages of extension on the core-bounding Bitterroot mylonite zone. The thermal effects of these elevated temperatures may have been the catalyst for the initiation of extensional unroofing.

INTRODUCTION

The Bitterroot metamorphic core complex (BMCC) coincides with the northeastern margins of the Bitterroot batholith and provides an unique opportunity to address one of the key issues in Cordilleran metamorphic core complexes: the relationship between plutonic activity, metamorphism, and extensional denudation. Published constraints on peak metamorphic conditions and polymetamorphism in the BMCC are based on qualitative petrogenetic relationships. The metamorphic evolution of the BMCC appears to be tied to that of metamorphic rocks on the northwestern border of the Bitterroot batholith at Boehls Butte/Goat Mountain and at Snow Peak, ID, but little has been done to demonstrate this relationship.

This paper presents new thermobarometric results from the BMCC that place quantitative constraints on the pressure-temperature-time evolution of footwall rocks. U-Pb geochronology demonstrates that peak metamorphic conditions persisted in core rocks much later than previously thought and may have played a role in initiation of extensional unroofing of core rocks.

GEOLOGIC SETTING

High-grade metamorphic rocks of the BMCC, first recognized in the northern Bitterroot Range as early as 1904 (Lindgren, 1904), consist of pelitic, quartzofeldspathic, and calc-silicate schists and gneisses intruded by granitoids of the Bitterroot batholith (Plate 1; Figure 1). Stratigraphic relations within the BMCC are difficult to resolve because of poor exposure but field evidence and stratigraphic correlations elsewhere in the northern border zone of the Bitterroot batholith indicate that the rocks represent metamorphosed equivalents of the Middle Proterozoic Belt Supergroup (Hietanen, 1963a; Wehrenberg, 1972; Nold, 1974).

Pelitic schists and gneisses correlated with the Prichard Formation dominate the metamorphic core. Amphibolite pods, thought to be metamorphosed equivalents of

diabase dikes that are common in the Prichard Formation (Wehrenberg, 1972; Hyndman *et al.*, 1988) are scattered throughout the pelitic units and are concordant with the foliation in surrounding units. Several large anorthosite bodies found in the pelitic schist are of uncertain origin but may represent slivers of pre-Belt basement tectonically juxtaposed with Belt Supergroup units (Hietanen, 1963a; Berg, 1968; Cheney, 1972; Cheney, 1975).

The sequence of metasedimentary core rocks is intruded by unfoliated and foliated granitoids. Tonalite and quartz diorite plutons on the northeastern and western margins of the Bitterroot batholith represent early stages of magmatic activity between ~100 - 80 Ma (Toth, 1987). Mesozonal granodiorite and monzogranite plutons make up the bulk of the Bitterroot batholith. Most range in age from 66 - 57 Ma, but some mylonitized granites are as young as 52 - 48 Ma (Bickford *et al.*, 1981; Chase *et al.*, 1983). This emplacement episode was followed by intrusion of a suite of undeformed epizonal granitoids that range in age from ~51 - 46 Ma. (Nold, 1974; Toth, 1987; House and Hodges, 1994).

The principal structure responsible for unroofing of the core rocks is the Bitterroot mylonite zone, which flanks the eastern edge of the Bitterroot Range (Figure 1; Garmezy, 1983). Exposure of the shear zone is continuous for a distance of approximately 100 km along strike. The mylonitic foliation strikes north-northeast and dips shallowly to the east; an associated mineral-stretching lineation plunges east-southeast (Chase, 1977; Garmezy, 1983). Cross-cutting relationships suggest that extension accommodated by this structure was a Late Eocene phenomenon (House and Hodges, 1994) and was relatively short-lived (~2 m.y.).

POLYMETAMORPHISM ALONG THE NORTHWEST MARGIN OF THE BITTERROOT BATHOLITH

The metasedimentary and crystalline basement rocks exposed on the northwestern border of the Bitterroot batholith, in the regions of Boehls Butte/Goat Mountain, Idaho and at Snow Peak, Idaho, are correlative to core rocks in the BMCC and have a metamorphic history that is similar to that of the BMCC (Figure 1). Rocks at Boehls Butte/Goat Mountain consist primarily of pelitic and Mg-Al schists of the Boehls Butte Formation separated from the overlying pelitic schists and gneisses of the Prichard Formation by high-angle faults of unknown age (Hietanen, 1984). At Snow Peak, metasedimentary rocks of the Wallace Formation are juxtaposed with rocks of the Prichard Formation by northeast-vergent thrust faults (Lang and Rice, 1985b). Detailed petrography and thermobarometry has led to the identification of up to three metamorphic events for rocks on the northwestern border of the Bitterroot batholith. These events define a clockwise pressure-temperature loop (Figure 2) that is interpreted to be the metamorphic signature of regional thickening associated with east-vergent thrusting, followed by a thermal pulse related to emplacement of the Bitterroot batholith, and subsequent extensional unroofing (Hietanen, 1963a; Lang and Rice, 1985b; Grover *et al.*, 1992).

Petrographic evidence for the earliest metamorphic event (M1) is poorly preserved throughout the northwestern border zone (Lang and Rice, 1985b; Carey *et al.*, 1992; Grover *et al.*, 1992). In the metapelitic schists at Snow Peak, M1 reached middle-amphibolite facies conditions. Pseudomorphs of M1 staurolite, chloritoid, and kyanite porphyroblasts are locally present, and relic M1 staurolites form a nucleus on which M2 staurolite grew (Lang and Rice, 1985b) Few petrographic constraints are available for M1 at Boehls Butte/Goat Mountain, although Carey *et al.* (1992) and Grover *et al.* (1992) attribute inclusion-filled garnet cores to this event and suggest that M1 metamorphism occurred at ~775 K, and 500 - 600 MPa (Figure 2). The age of M1 metamorphism remains unknown, although M1 porphyroblast growth was syn- to post-

kinematic with ~100 - 50 Ma northeast-vergent thrusting in the region (Harrison *et al.*, 1980; Lang and Rice, 1985b).

Mineral isograds that are broadly concentric to the northern border of the Bitterroot batholith were developed during M2 metamorphism (Lang and Rice, 1985b; Grover *et al.*, 1992). At Snow Peak, coarse-grained M2 aggregates of Qtz + Ms + Ky [1] completely replace M1 porphyroblasts (Lang and Rice, 1985a). Metamorphic grade ranges from chlorite-biotite zone to kyanite zone conditions farther south; the highest grade assemblage is Ky + Grt + Bt + Ms + Qtz + Ilm + Pl + Gr. Based on model reactions, Lang and Rice (1985a) calculated peak M2 temperatures of ~740 K (chlorite-biotite zone) to ~835 K (kyanite zone), and pressures of ~600 MPa (Figure 2). At Boehls Butte/Goat Mountain, M2 assemblages reflect considerably higher pressures and temperatures, and completely obscure M1 assemblages (Carey *et al.*, 1992; Grover *et al.*, 1992). Hietanen (1963a, 1984) suggested that the M2 assemblage St + Ky + Sil at Boehls Butte/Goat Mountain reflects upper-amphibolite facies conditions (925 K, 600 MPa). More recently, quantitative pelite thermobarometric results imply peak conditions of 925 - 1100 K and 800 - 1100 MPa (Figure 2; Grover *et al.*, 1992). M2 was post-kinematic with respect to northeast-vergent thrusting at Snow Peak (Lang and Rice, 1985b) and may be as old as 105 Ma (Hyndman *et al.*, 1988) or as young as ~60 Ma based on K-Ar ages for early phases of the Bitterroot batholith (Armstrong, 1975; Hietanen, 1984; Carey *et al.*, 1992).

Low-pressure/high-temperature M3 mineral assemblages that include cordierite, hercynite, and andalusite are thought to reflect high-temperature isothermal decompression. M3 assemblages are well-developed in the Mg-Al schists exposed at Boehls Butte/Goat Mountain, but evidence of M3 is relatively minor at Snow Peak. Hietanen (1956) and Hyndman and Alt (1972) interpreted the occurrence of andalusite,

---

[1] **mineral abbreviations after Kretz (1983)**

kyanite, and sillimanite as an indication of final equilibration near the aluminum silicate triple point. More recently, Carey *et al.* (1992) and Grover *et al.* (1992) suggested that andalusite formed by polymorphic inversion of strained kyanite, while unstrained M2 kyanite and sillimanite remained unaffected by M3. Coronae of cordierite, cordierite + corundum, and cordierite + hercynite on aluminum silicate are additional evidence of recrystallization in response to post-M2 decompression. Reactions involving these phases suggest M3 conditions of equilibration at 925 - 1025 K, 400 - 600 MPa (Figure 2; Grover *et al.*, 1992). The absence of M3 assemblages at Snow Peak may be due to the distance of the region from the northern margins of the Bitterroot batholith; petrologic relationships indicate that this area never attained the peak temperature conditions seen at Boehls Butte/Goat Mountain, and did not experience the high-temperature isothermal decompression that affected the region nearer to the Bitterroot batholith (Lang and Rice, 1985b)

METAMORPHISM IN THE NORTHERN BMCC

Metamorphic rocks from the northwestern BMCC record a polymetamorphic history similar to that deduced for the Boehls Butte/Goat Mountain area. Evidence of the earliest phase of metamorphic mineral growth (M1) is preserved only by garnet textures: in many pelitic samples, garnets display distinctive cores, containing inclusions of quartz, plagioclase, and biotite, that are surrounded by inclusion-free rims. The lack of diagnostic mineral assemblages associated with M1 preludes estimation of pressure-temperature (P-T) conditions for that event. The dominant mineral assemblages in these rocks grew during M2, an amphibolite facies event that began prior to the development of high-strain fabrics related to the Bitterroot mylonite zone but persisted through the early stages of tectonic denudation of the footwall (Figure 3a).

The M2 peak metamorphic assemblage is characterized by Grt + Bt + Ms + Ky/Sil + Pl + Qtz in pelitic rocks and by Grt + Hb + Bt + Pl + Qtz in metabasic rocks.

Many samples display textures consistent with a period of high-temperature decompression in the latter stages of M2. Halos of Sil + Pl + Qtz surrounding garnets in pelitic samples suggest the decompressional reaction:

Grossular + Sillimanite + Quartz = Anorthite.

Garnets in amphibolite pods are mantled by Qtz + Pl, completely isolating the garnet from the surrounding hornblende matrix. In some samples garnets are euhedral, suggesting garnet growth at the expense of hornblende through a prograde reaction such as:

hornblende + plagioclase = garnet + plagioclase + quartz.

Some textures, however, suggest that this reaction operated in the opposite direction. Aggregates of Pl + Qtz ± Bt or euhedral hornblende and small fragments of garnet may represent almost total resorption of garnet. In one sample, single amphibole crystals appear to have replaced garnet entirely (Figure 3b). These textures suggest early garnet growth at the expense of amphibole, followed by subsequent decompressional resorption and reversal of the garnet-forming reaction. Alternatively, they may represent final equilibration at the upper stability limit of garnet. The garnet amphibolite textures, in conjunction with the absence of epidote and clinopyroxene, suggests equilibration at temperature conditions of ~975 - 1075 K (Spear, 1993).

Aluminum silicate phases also record evidence for changing pressure and temperature conditions. Kyanite, present in the northern BMCC, is commonly overgrown by prismatic sillimanite that parallels the regional foliation. Fibrolitic sillimanite, which is present throughout the footwall rocks, occurs as randomly oriented mats that overgrow biotite, muscovite, and plagioclase and often cross-cuts the dominant foliation. The aluminum silicate textures are multiply interpretable, but are consistent with high-temperature decompression.

Cordierite and andalusite, occurring in Mg-rich Al-schist layers of an anorthosite body within the pelitic schists of the BMCC, resemble M3 assemblages

described at Boehls Butte/Goat Mountain. Cheney (1972, 1975) and Chase (1973, 1977) suggested that these assemblages are the metamorphic signature of isothermal decompression related to extensional unroofing via the Bitterroot mylonite zone. The significance of these low-pressure assemblages is difficult to interpret because of their association exclusively with the anorthosite bodies. They are consistent with the other decompressional reaction textures found in the pelites and garnet amphibolites, although it is possible that they are relic features resulting from a much earlier metamorphic event.

Petrogenetic relationships demonstrate that M2 in the BMCC ranged from sillimanite-orthoclase zone conditions near the batholith to sillimanite-muscovite and kyanite zone conditions farther north (Wehrenberg, 1972; Chase, 1973). Mineral isograds are crudely concentric to the northern margins of the Bitterroot batholith, suggesting that this event is related to emplacement of the Bitterroot batholith (Wehrenberg, 1972; Chase, 1973). Migmatites containing Qtz + Ms ± Or + Bt + Sil suggest crystallization at ~20 - 25 km (570 - 710 MPa) and ~1000 K, consistent with emplacement of the batholith at these depths (Wehrenberg, 1972; Chase, 1973; Bittner, 1987; Hyndman *et al.*, 1988).

There is considerable unquantifiable uncertainty associated with published constraints on peak metamorphism in the BMCC that are based on petrogenetic relationships. Furthermore, estimates of the age of this event are broad (~100 - 60 Ma) and are based largely on K-Ar data, as well as Rb-Sr and Pb-alpha ages from within the Bitterroot batholith. There have been few attempts to directly date the metamorphic fabrics in the surrounding country rocks, although Bickford *et al.* (1981) obtained an U-Pb lower-intercept age of ~65 Ma for a multigrain monazite sample from a metasedimentary inclusion in granite and suggested that this age may reflect the timing of peak metamorphism. In order to refine these broad limits on the conditions and age of peak metamorphism in the BMCC, we collected a suite of pelitic schists and garnet

amphibolites from throughout the core-rocks for quantitative thermobarometry and U-Pb geochronology.

THERMOBAROMETRIC CONSTRAINTS ON M2 METAMORPHISM IN THE BMCC

Metapelites and garnet amphibolites were selected from the eastern portion of the BMCC based on their proximity to the northern margin of granitic rocks and structural position relative to the core-bounding mylonite zone (Plate 1; Table 1). Table 2 lists the mineral assemblage in each sample, and rim compositions used in calculating pressures and temperatures are presented in Table 3. Analytical and thermobarometric techniques are reviewed in Appendix I.

Thermobarometry of Metapelites

Metapelitic samples chosen for analysis contain the appropriate minerals for simultaneous solution of several well-calibrated thermobarometers (Table 4). Non-ideal solution behavior was modeled using the approaches of Berman (1990), Chatterjee and Froese (1975), and Elkins and Grove (1990) for garnet, muscovite, and plagioclase, respectively. Ideal mixing was assumed for biotite; sillimanite and quartz were treated as pure phases. Pressures and temperatures derived from solution of different thermobarometers are presented in Table 5 and ellipses corresponding to 2σ uncertainties resulting in solution of GARB/GMPP are shown in Figure 4.

CC273 was collected farthest from the northern margin of the Idaho batholith; it is not mylonitic, but displays a foliation that is generally northeast-dipping, concordant with the overlying mylonitic foliation. This sample comes from the boundary between the sillimanite and kyanite zones of Wehrenberg (1972) and contains the assemblage Qtz + Bt + Ms + Pl + Grt + Ky + Sil + Tur. Garnet porphyroblasts (2 mm diameter) contain abundant inclusions of quartz and plagioclase. Intensely strained kyanite porphyroblasts are rotated into parallelism with the dominant biotite foliation, and are

overgrown by prismatic sillimanite. Randomly oriented blades of fibrolitic sillimanite overgrow kyanite, prismatic sillimanite, and biotite, suggesting that this phase is the most recent polymorph to crystallize in this sample.

Simultaneous solution of GARB/GASP with sillimanite as the stable aluminum silicate yields a pressure and temperature in the kyanite stability field (929 ± 80 MPa, 950 ± 50 K), whereas incorporating kyanite as the stable aluminum-silicate results in slightly lower pressure conditions that are near the kyanite-sillimanite transition (Figure 4). These results suggest that kyanite was most likely the last stable aluminum silicate in equilibrium with Grt + Bt + Pl. Similar pressures and temperatures obtained from thermobarometer pairs which are independent of the aluminum silicate phase (GARB/GMPP and GMAP/GMPP) reinforce this interpretation (Table 5). Simultaneous solution of the GASP and GMPP barometers resulted in a pressure and temperature (830 ± 60 MPa, 960 ± 40 K) that is in agreement within uncertainty of those derived by solutions involving GARB.

Two samples of pelitic schist were collected from within the sillimanite zone of Wehrenberg (1972). Sample NB16-1 is mylonitic and contains the assemblage Bt + Qtz + Grt + Ms + Pl + Rt. NB16-4, containing the assemblage Grt + Bt + Qtz + Pl + Sil + Ms + Rt, comes from the base of the Bitterroot mylonite zone and is not mylonitic, but displays a foliation that is concordant to the mylonitic foliation. Garnets in both samples are ~1 - 1.5 mm in diameter and are pre-kinematic with respect to mylonitic fabrics. Biotite defines the dominant foliation in both samples and is locally altered to chlorite. Large muscovite crystals parallel the foliation and show some evidence of recrystallization at the margins. In sample NB16-4, fibrolitic sillimanite parallels the biotite foliation and also occurs as randomly oriented mats.

The GARB/GMPP and GMPP/GMAP thermobarometer pairs were applied to NB16-1 (Table 5; Figure 4). Considerable variation in garnet rim compositions in this sample resulted in a large uncertainty in the rim pressures and temperatures, but our

best estimate of the final equilibration conditions of this sample are ~1000 K and 800 MPa.

The presence of sillimanite in NB16-4 allows solution of a wide variety of thermobarometers. Solution of GARB/GMPP and GMPP/GMAP for NB16-4 suggest final equilibration at 750 ± 80 MPa, 950 ± 40 K and 790 ± 90 MPa, 1000 ± 50 K, respectively (Table 5; Figure 4). GARB/GASP results in a higher pressure (870 ± 90 MPa) that is statistically different from pressures obtained using GMAP or GMPP. Solution of GASP/GMPP results in an anomalously low pressure and temperature (540 ± 60 MPa, 730 ± 50 K). We interpret the results to indicate problems with the assumption of sillimanite stability in this sample and suggest that fibrolitic sillimanite post-dates the main assemblages in the pelites. Results for NB16-4 indicating final equilibration at ~800 MPa, 960 K are in statistical agreement with those obtained for NB16-1 (the same distance from the northern batholith contacts).

Thermobarometry of Amphibolites

The minimum amphibolite assemblage Grt + Hb + Pl + Qtz is ubiquitous in metamorphic terrains ranging from upper-greenschist to granulite facies (Spear, 1993); two empirically calibrated thermometers are available for garnet amphibolites containing this assemblage (Table 6; Graham and Powell, 1984; Holland and Blundy, 1994). These thermobarometers are considered to be more resistant than pelitic equilibria to the effects of retrogression and provide an independent test of the pressure-temperature estimates derived from the pelitic assemblages.

Like all empirical thermobarometers, the Kohn and Spear (1989, 1990) equilibria are most reliable when applied to samples with mineral compositions similar to those of the samples used for calibration. This condition was met for most phases in the Bitterroot garnet amphibolites with the exception of plagioclase, which is much more calcic (An92 - An94) than the feldspars in the Kohn and Spear (1989, 1990) data

set (An15 - An70). Applying the barometers to samples with high-Ca plagioclases, even in the upper ranges of anorthite contents suggested by Kohn and Spear (1989, 1990), results in pressures that are ~200 - 400 MPa lower than pressures reported in Kohn and Spear (1989, 1990). The failure of these barometers for samples containing high-Ca plagioclase may be the result of the plagioclase solution model used by Kohn and Spear (1989, 1990) for their empirical calibrations. The Hodges and Royden (1984) model was derived specifically for use with Na-rich plagioclases found in pelitic rocks.

In order to evaluate the effect of the plagioclase solution model on the pressure estimates resulting from the barometers, and to determine whether these barometers might be applied to samples containing high-Ca plagioclase, we incorporated the more recent ternary plagioclase solution model of Elkins and Grove (1990) into the equilibrium constants. One important feature of empirical calibrations is that they are strongly dependent on the solution models used to describe non-ideal behavior in impure minerals of the calibration set (Applegate and Hodges, 1994); thus, it would not be appropriate simply to use the thermodynamic constants empirically determined by Kohn and Spear (1989, 1990) with the plagioclase activity formulations of Elkins and Grove (1990). In order to incorporate the new plagioclase model into amphibolite thermobarometric calculations, we recalibrated the Kohn and Spear (1989, 1990) reactions using the same sample set with the same assumed pressures and temperatures, and the same solution models for all impure minerals except plagioclase. The resulting fit parameters are statistically indistinguishable from those obtained by Kohn and Spear (1989, 1990), and our experiments with samples containing An15 - An70 plagioclase show that the original thermobarometers and our recalibrated versions yield virtually indistinguishable results. However, for samples with more calcic plagioclase, the new calibrations should provide more reliable pressure estimates.

Garnet amphibolite samples NB5-1 and NB17-6 were collected for analysis from within the sillimanite zone of Wehrenberg (1972; Plate 1, Table 1). NB5-1 was collected immediately to the north of the northern granitoid contact within a zone of weak mylonitization, and NB17-6 originates from core rocks farther to the north, well below the mylonitic front. NB5-1 is foliated and concordant with the mylonitic foliation but is not itself mylonitic. NB17-6 is discordant with the surrounding foliation and is encased in a granitized "bake zone" that is transitional with the surrounding pelites schists and gneisses.

The garnet amphibolites are dominated by amphiboles that are classified as "aluminoferrohornblende" (Table 3; Leake, 1978). Chemical zoning in the amphiboles is minimal and there is no evidence for a second amphibole phase in the rocks. Plagioclase is extremely anorthitic (An92 - An94) and contains inclusions of quartz. Biotite is a minor constituent in the garnet amphibolites, comprising ~3 - 15% of the matrix, and is most likely a retrograde phase. Large (~4 mm), anhedral garnet porphyroblasts are poikilitic and variably embayed. In both samples, the porphyroblasts are surrounded by a halo of Qtz + Pl. Inclusions of quartz, plagioclase, biotite, hornblende, and chlorite are localized in the garnet cores.

Applying the recalibrated geobarometers resulted in pressures that are slightly lower than those obtained for pelites. Pressures and temperatures (with propagated uncertainties) derived from the simultaneous solution of each barometer with the garnet-hornblende (GH) thermometer are reported in Table 7; error ellipses for the Fe-end-member reactions are shown in Figure 5. Temperatures derived from the HAl thermometer are presented in (Table 7). Analytic uncertainties were not determined for this thermometer due to the complex amphibole solution models on which it is based; therefore we assign nominal uncertainties of ± 50 K. Temperatures derived from the two different thermometers are internally consistent and suggest final equilibration of footwall rocks at ~1000 K. Pressures obtained from our calibrations are ~200 MPa

higher than those resulting from the original Kohn and Spear (1989, 1990) calibrations and span a range of ~200 MPa for each sample, with GH/FePrg[1] being the highest and GH/MgTsc the lowest. This effect occurs in the original calibrations, regardless of the plagioclase solution model employed, and may be due to the dependence of the amphibole activity models in these reactions on Fe- and Mg-partitioning in octahedral sites. In addition, the Mg-end-member equilibria consistently resulted in lower pressures than those obtained using the Fe-end-member equilibria which may reflect the ability of the barometers to model the highly complex behavior of amphiboles.

GARNET ZONING AND RE-EQUILIBRATION

Numerous workers have noted the pitfalls of quantitative thermobarometry in high-grade samples (Frost and Chacko, 1989; Florence and Spear, 1991; Spear, 1993). During slow cooling, diffusional modification of garnet compositions through volume diffusion such that conventional thermobarometry substantially underestimates actual peak conditions. In order to evaluate the effects of diffusional modification of our samples, we obtained zoning profiles in garnets from the pelitic schists. The major element zoning in the NB16-4 garnet is representative (Figure 6). Garnets in this sample are relatively small (1 mm) and demonstrate little evidence of major element zoning. The profile through the center is flat, with a slight increase in Fe/(Fe + Mg) and decrease in almandine and pyrope at the rims. Spessartine sharply increases at rims and grossular remains largely unaffected. The absence of strong internal zoning suggests homogenization at high temperatures and is consistent with metamorphism at pressures and temperatures that we derive using metapelite and garnet amphibolite thermobarometry.

Relatively sharp increases in spessartine near the garnet rims are characteristic of post-metamorphic diffusion and rim resorption, suggesting that our rim thermobarometric calculations may underestimate peak conditions. We attempted to

evaluate the effect of rim re-equilibration by calculating pressures and temperatures from the reaction pairs GARB/GASP, GARB/GMPP, and GASP/GMPP using garnet core compositions and matrix compositions for biotite, muscovite, and plagioclase (Table 8). The results are close to those obtained using rim data, suggesting that the effects of rim retrogression and resorption are limited.

The internal consistency among the metapelite results also argues that our pressure and temperature estimates are reasonably robust. Results for reaction pairs involving GARB, an exchange reaction relatively sensitive to diffusive modification, are statistically indistinguishable. Furthermore, the temperatures derived from metapelite thermobarometry are consistent with the temperature estimates resulting from the amphibolite thermobarometer pairs. Thus, we consider the rim conditions that we obtain for metapelites to be close estimates of the peak pressures and temperatures experienced during M2 metamorphism.

AGE OF METAMORPHISM

Petrographic examination of metamorphic rocks from the northeastern BMCC revealed the presence of several accessory minerals that could be dated using the U-Pb method (Heaman and Parrish, 1991). We have found that zircon populations in metapelitic samples contain a large inherited component of Proterozoic age. Although geochronologic studies of monazites from these rocks are ongoing, our best current estimate of the age of M2 metamorphism comes from metamorphic zircon in an amphibolite sample (NB17-1; Plate 1; Table 1). Collected from an unfoliated amphibolite pod that is concordant with surrounding weakly mylonitic pelitic gneiss, this sample contains relatively small (~50 - 100 μm), clear zircons that generally occur within Pl + Qtz lenses. There is no isotopic or petrographic evidence of more than one population of zircons in this sample and the separated zircons are interpreted to be of metamorphic origin. Two 10 - 20 crystal fractions were analyzed using methods

outlined in Appendix II and explained in detail in Bowring *et al.* (1993). Both fractions give concordant results, with $^{206}Pb/^{238}U$ ages of 48.0 ± 0.1 Ma and 48.1 ± 0.1 Ma (Table 9; Figure 7).

U-Pb monazite ages from the northwestern BMCC demonstrate that migmatites associated with satellite plutons of the Bitterroot batholith crystallized at 55.8 ± 0.1 Ma (House, Chapter 4). These data demonstrate that high-temperature conditions associated with batholith emplacement existed in the northern BMCC at that time. Because the U-Pb closure temperature of zircon is thought to be relatively high (~1025 K; Heaman and Parrish, 1991), the ~48 Ma ages from the eastern BMCC suggest that high-temperature conditions persisted until much later than in the western BMCC, possibly due to progressive unroofing (House, Chapter 4). We therefore interpret the NB17-1 zircon ages as indicative of the timing of the late stages of M2 metamorphism. Beyond these constraints, we have no independent limits on the initial time or duration of M2. Future studies of metamorphic accessory minerals from this area should further improve our understanding of the age of M2 metamorphism.

METAMORPHIC HISTORY OF THE NORTHERN BMCC

Peak metamorphic pressures and temperatures determined from metapelite and amphibolite thermobarometry are internally consistent and in agreement with previously reported petrogenetic constraints on peak metamorphism in the BMCC (Figure 8). Peak temperatures are 950 - 1000 K throughout the footwall, with higher temperatures indicated near the Bitterroot batholith margins. Pressures of ~720 - 870 MPa, corresponding to depths of ~25 - 30 km indicated by metapelite thermobarometry are slightly higher than pressures derived from amphibolite barometers (530 - 740 MPa, or 19 - 26 km), but are in agreement. The metapelites and garnet amphibolites were collected from areas that contain abundant migmatites, and yield P-T estimates above, or within error of, the nominal water-saturated minimum melt curve for pelitic

compositions (Figure 8; Thompson, 1982). All three pelitic samples contain primary muscovite and provide rim temperatures below the water-saturated muscovite breakdown reaction, (Figure 8; Thompson and Tracy, 1979; Thompson, 1982). Amphibolite NB17-6 plots below the water-saturated muscovite breakdown reaction, consistent with its proximity to the pelitic schists. Amphibolite NB5-1 plots above the muscovite-out reaction, consistent with the occurrence of potassium feldspar in surrounding gneisses and reflecting its proximity to the northern extent of Idaho batholith-related plutonism.

Lower pressures indicated by the amphibolite barometers can be interpreted in two ways. They may reflect our inability to model solution behavior in samples containing high-Ca plagioclase. Introduction of an alternative plagioclase solution model had the effect of increasing apparent pressures but the remaining discrepancies may mean that we have not adequately modeled solution behavior. Alternatively, lower pressures obtained through amphibolite barometry may represent re-equilibration during decompression. Relatively little is known about the reaction kinetics of these recently developed empirical barometers. The response of the barometer reactions to changing pressures may be even more sluggish than the net-transfer reactions on which pelitic thermobarometry is based. The amphibolites may be "locking-in" a point on the decompressional path of the footwall and represent at different point in time than the pelite thermobarometry. The internal consistency between the predicted pressures and temperatures for the two amphibolites and the agreement with petrogenetic relationships suggests that the amphibolite data are geologically meaningful and provide an indication of the decompressional path of footwall rocks.

Peak M2 metamorphic conditions in the BMCC indicated by quantitative thermobarometry are similar to those reported for M2 metamorphism on the northwestern margin of the Bitterroot batholith at Boehls Butte/Goat Mountain, implying that the two events are the same. The distribution of prograde M2

assemblages is consistent with the association of this metamorphic event with emplacement of the Bitterroot batholith. If the inclusion-rich garnet cores in the BMCC, like their counterparts at Boehls Butte/Goat Mountain are relics of a staurolite-grade M1 event (Lang and Rice, 1985; Grover, *et al.*, 1992), it appears that M1 was largely obliterated by the M2 thermal effects of Bitterroot batholith intrusion. In regions farther to the north, M2 was less pronounced and samples preserve more evidence of their M1 history.

Pressures of ~21 - 30 km indicated for peak metamorphism in the BMCC and at Boehls Butte/Goat Mountain are not explained by simple stratigraphic overburden. Estimates of the thickness of the Belt Supergroup in this region are ~13 - 17 km (Hyndman, 1980; Winston, 1986) suggesting the presence of 4 - 17 km of additional overburden. East- to northeast-vergent thrusting, contemporaneous with M1 metamorphism and predating emplacement of the Bitterroot batholith, may have provided the additional overburden necessary to obtain pressures such as those indicated for M2 metamorphism at Boehls Butte/Goat Mountain and for the BMCC. Pressures are slightly higher at Boehls Butte/Goat Mountain than in the BMCC, consistent with thickening of the east-vergent thrust plates to the west.

Direct petrologic evidence for the low-pressure M3 event defined along the northwestern border of the batholith is lacking in the BMCC. There is, however, abundant evidence for decompression. Prismatic sillimanite overgrowths on kyanite may represent high-temperature decompression during the early stages of extensional mylonitization, with fibrolitic sillimanite forming in the late stages of high-temperature extension and continuing to grow after extension ceased. Decompressional reaction textures surrounding garnet the in amphibolites and in some metapelites also demonstrate evidence for a decompressional event. Furthermore, the pressures obtained by amphibolite thermobarometry are consistent with high-temperature decompression. Textural evidence suggests that peak metamorphism and decompression are actually a

protracted single metamorphic event and we note that the minimum amphibolite P-T estimates are similar to the inferred M3 pressure-temperature conditions at Boehls Butte/Goat Mountain (Figure 8; Grover *et al.*, 1992).

The proximity of decompressional assemblages to large extensional structures (the Bitterroot mylonite zone in the BMCC and high-angle faults bounding Boehls Butte/Goat Mountain) suggests that decompression is related to extensional unroofing of these high-grade terrains while still at relatively high temperatures. Evidence for high-temperature decompression may be absent at Snow Peak because these rocks never attained the temperature conditions of areas closer to the Bitterroot batholith, nor are these rocks associated with an overlying extensional structure.

The total age range for M2 along the northern border of the Bitterroot batholith remains poorly constrained. However, the ~48 Ma U-Pb zircon ages presented here demonstrate that amphibolite facies conditions persisted until at least Eocene time in the BMCC. This time also corresponds to the onset of tectonic denudation of the core complex by movement on the Bitterroot mylonite zone (Chase *et al.*, 1983; Hodges and Applegate, 1993; House and Hodges, 1994). Specifically, $^{40}Ar/^{39}Ar$ data for the same sample containing ~48 Ma zircons indicate extension-related cooling through the hornblende to biotite closure interval (800 - 620 K) over the 47.9 to 44.3 Ma period (House and Hodges, 1994). The initiation of extensional unroofing at upper-amphibolite facies M2 conditions is consistent with published stable isotopic and textural studies in the mylonite zone indicating that deformation began at temperatures greater than 775 K, coincident with the late stages of batholith intrusion (Kerrich and Hyndman, 1986; LaTour and Barnett, 1987).

CONCLUSIONS

Quantitative thermobarometry in pelites and garnet amphibolites from the Bitterroot metamorphic core complex, combined with direct U-Pb dating of

metamorphic zircon, provide new constraints on the P-T-t evolution of core rocks. These data indicate that peak metamorphic temperatures associated with emplacement of the Bitterroot batholith persisted in core rocks as late as 48 Ma. Extension in the Bitterroot complex initiated at elevated temperatures during the waning stages of peak metamorphism and granite plutonism, suggesting a genetic link between the high-temperature conditions of footwall rocks and the initiation of extension.

REFERENCES

Anderson, G. M., 1976, Error propagation by the Monte Carlo method in geochemical calculations: Geochimica et Cosmochimica Acta, v. 40, p. 1533-1538.

Applegate, J. D. R. and Hodges, K. V., 1994, Empirical evaluation of solution models for pelitic minerals and their application to thermobarometry: Contributions to Mineralogy and Petrology, v. 117, p. 56-65.

Armstrong, R. L., 1975, Precambrian (1500 m.y. old) rocks of central Idaho-The Salmon River arch and its role in Cordilleran sedimentation and tectonics: American Journal of Science, v. 275-A, p. 437-467.

Berg, R. B., 1968, Petrology of anorthosites of the Bitterroot Range, Montana, *in* Isachsen, Y. W., ed., Origin of Anorthosite and Related Rocks: Albany, NY, New York State Museum and Science Service Memoir 18, p. 387-398.

Berman, R. G., 1988, Internally-consistent thermodynamic data for minerals in the system Na_2O-K_2O-CaO-MgO-FeO-Fe_2O_3-Al_2O_3-SiO_2-TiO_2-H_2O-CO_2: Journal of Petrology, v. 29, p. 445-522.

Berman, R. G., 1990, Mixing properties of Ca-Mg-Fe-Mn garnets: American Mineralogist, v. 75, p. 328-344.

Bickford, M. E., Chase, R. B., Nelson, B. K., Schuster, R. D., and Arruda, E. C., 1981, U-Pb studies of zircon cores and overgrowths, and monazite: Implications for age and petrogenesis of the northeastern Idaho batholith: Journal of Geology, v. 89, p. 433-457.

Bittner, E., 1987, Migmatite zones in the Bitterroot lobe of the Idaho batholith: U.S. Geological Survey Professional Paper, v. 1436, p. 73-94.

Bowring, S. A., Grotzinger, J. P., Isachsen, C. E., Knoll, A. H., Pelechaty, S. M., and Kolosov, P., 1993, Calibrating rates of early Cambrian evolution: Science, v. 261, p. 1293-1298.

Carey, J. W., Rice, J. M., and Grover, T. W., 1992, Petrology of aluminous schist in the Boehls Butte region of northern Idaho: Geologic history and aluminum-silicate phase relations: American Journal of Science, v. 292, p. 455-473.

Chase, R. B., 1973, Petrology of the northeastern border zone of the Idaho batholith, Bitterroot Range, Montana: Montana Bureau of Mines and Geology Memoir, v. 43, p. 1-28.

Chase, R. B., 1977, Structural evolution of the Bitterroot dome and zone of cataclasis, *in* Chase, R. B. and Hyndman, D. W., ed., Mylonite detachment zone, eastern flank of Idaho batholith: Geological Society of America Rocky Mountain section, p. 1-24.

Chase, R. B., Bickford, M. E., and Arruda, E. C., 1983, Tectonic implications of Tertiary intrusion and shearing within the Bitterroot dome, northeastern Idaho batholith: Journal of Geology, v. 91, p. 462-470.

Chatterjee, N. D. and Froese, E., 1975, A thermodynamic study of the psuedobinary join muscovite–paragonite in the system $KAlSi_2O_8$–Al_2O_3–SiO_2–H_2O: American Mineralogist, v. 60, p. 985-993.

Cheney, J. T., 1972, Petrologic relationships of layered meta-anorthosites and associated rocks, Bass Creek, western Montana [M.A.]: University of Montana.

Cheney, J. T., 1975, Kyanite, sillimanite, phlogopite, cordierite layers in the Bass Creek anorthosites, Bitterroot Range, Montana: Northwest Geology, v. 4, p. 77-82.

Elkins, L. T. and Grove, T. L., 1990, Ternary feldspar experiments and thermodynamic models: American Mineralogist, v. 75, p. 544-559.

Ferry, J. M. and Spear, F. S., 1978, Experimental calibration of the partitioning of Fe and Mg between biotite and garnet: Contributions to Mineralogy and Petrology, v. 66, p. 113-117.

Florence, F. P. and Spear, F. S., 1991, Effects of diffusional modification of garnet growth zoning on P-T path calculations: Contributions to Mineralogy and Petrology, v. 107, p. 487-500.

Frost, B. R. and Chacko, T., 1989, The granulite uncertainty principle: limitations on thermobarometry in granulites: Journal of Geology, v. 97, p. 435-450.

Garmezy, L., 1983, Geology and geochronology of the southeast border of the Bitterroot dome: Implications for the structural evolution of the mylonitic carapace [Ph.D.]: The Pennsylvania State University.

Gasparik, T., 1984, Experimental study of the subsolidus phase relations and mixing properties of pyroxene in the system CaO-Al_2O_3-SiO_2: Geochimica et Cosmochimica Acta, v. 48, p. 2537-2545.

Goldsmith, J. R., 1980, Melting and breakdown reactions of anorthite at high pressures and temperatures: American Mineralogist, v. 65, p. 272-284.

Graham, C. M. and Powell, R., 1984, A garnet-hornblende geothermometer: Calibration, testing, and application to the Pelona Schist, southern California: Journal of Metamorphic Geology, v. 2, p. 13-31.

Grover, T. W., Rice, J. M., and Carey, J. W., 1992, Petrology of aluminous schist in the Boehls Butte region of northern Idaho: Phase equilibria and P-T evolution: American Journal of Science, v. 292, p. 474-507.

Hariya, Y. and Kennedy, G. C., 1968, Equilibrium study of anorthite under high temperature and high pressure: American Journal of Science, v. 266, p. 193-203.

Harrison, J. E., Kleinkopf, M. D., and Wells, J. D., 1980, Phanerozoic thrusting in Proterozoic Belt rocks, northwestern United States: Geology, v. 8, p. 407-411.

Hays, J. F., 1966, Lime-alumina-silica: Carnegie Institute of Washington Yearbook, v. 65, p. 234-239.

Heaman, L. and Parrish, R., 1991, U-Pb geochronology of accessory minerals, *in* Heaman, L. and Ludden, J. N., ed., Applications of Radiogenic Isotope Systems to Problems in Geology: Toronto, Mineralogical Association of Canada, p. 59-102.

Hemingway, B. S., Robie, R. A., Evans, H. T., and Kerrick, D. M., 1991, Heat capacities and entropies of sillimanite, fibrolite, andalusite, kyanite, and quartz and the Al_2SiO_5 phase diagram: American Mineralogist, v. 76, p. 1597-1613.

Hietanen, A., 1956, Kyanite, andalusite, and sillimanite in Boehls Butte Quadrangle, Idaho: American Mineralogist, v. 41, p. 1-27.

Hietanen, A., 1963a, Anorthosite and Associated Rocks in the Boehls Butte Quadrangle and Vicinity, Idaho: U.S. Geological Survey Professional Paper, v. 344-B, p. B1-B75.

Hietanen, A., 1963b, Metamorphism of the Belt series in the Elk River-Clarkia area, Idaho: U.S. Geologic Survey Professional Paper, v. 344-C, p. C1-C49.

Hietanen, A., 1984, Geology along the northwest border zone of the Idaho batholith, northern Idaho: U.S. Geological Survey Bulletin, v. 1608, p. 17.

Hodges, K. V. and Applegate, J. D. R. A., 1993, Age of Tertiary extension in the Bitterroot metamorphic core complex, Montana and Idaho: Geology, v. 21, p. 161-164.

Hodges, K. V., Burchfiel, B. C., Royden, L. H., Chen, Z., and Liu, Y., 1993, The metamorphic sigature of contemporaneous extension and shortening in the central Himalayan orogen: Data from the Nyalam transect, southern Tibet: Journal of Metamorphic Geology, v. 11, p. 721-737.

Hodges, K. V. and McKenna, L. W., 1987, Realistic propagation of uncertainties in geologic thermobarometry: American Mineralogist, v. 72, p. 671-680.

Hodges, K. V. and Royden, L. H., 1984, Geologic thermobarometry of retrograded metamorphic rocks: an indication of the uplift trajectory of a portion of the northern Scandinavian Caledonides: Journal of Geophysical Research, v. 89, p. 7077-7090.

Holland, T. and Blundy, J., 1994, Non-ideal interactions in calcic amphiboles and their bearing on amphibole-plagioclase thermometry: Contributions to Mineralogy and Petrology, v. 116, p. 433-447.

House, M. A. and Hodges, K. V., 1994, Limits on the tectonic significance of rapid cooling events in extensional setting: Insights from the Bitterroot metamorphic core complex, Idaho-Montana: Geology, v. 22, p. 1007-1010.

Hyndman, D. W., 1980, Bitterroot dome - Sapphire tectonic block, an example of a plutonic-core gneiss-dome complex with its detached suprastructure, *in* Crittenden, M. D., Coney, P. J., and Davis, G. H., ed., Cordilleran Metamorphic Core Complexes: Boulder, CO, Geological Society of America Memoir 153, p. 427-443.

Hyndman, D. W. and Alt, D., 1972, The kyanite-andalusite-sillimanite problem on Goat Mountain, Idaho: Northwest Geology, v. 1, p. 42-46.

Hyndman, D. W., Alt, D., and Sears, J. W., 1988, Post-Archean metamorphic and tectonic evolution of western Montana and northern Idaho, *in* Ernst, W. G., ed., Metamorphism and Crustal Evolution of the Western United States: Englewood Cliffs, NJ, Prentice Hall, p. 332-361.

Kerrich, R. and Hyndman, D., 1986, Thermal and fluid regimes in the Bitterroot lobe - Sapphire block detachment zone, Montana: Evidence from 18O/16O and geologic relations: Geological Society of America Bulletin, v. 97, p. 147-155.

Kohn, M. J. and Spear, F. S., 1989, Empirical calibration of geobarometers for the assemblage garnet + hornblende + plagioclase + quartz: American Mineralogist, v. 74, p. 77-84.

Kohn, M. J. and Spear, F. S., 1990, Two new geobarometers for garnet amphibolites, with applications to southeastern Vermont: American Mineralogist, v. 75, p. 89-96.

Koziol, A. M. and Newton, R. C., 1988, Redetermination of the anorthite breakdown reaction and improvement of the plagioclase-garnet-Al_2SiO_5-quartz geobarometer: American Mineralogist, v. 73, p. 216-223.

Kretz, R., 1983, Symbols for rock-forming minerals: American Mineralogist, v. 68, p. 277-279.

Krogh, T. E., 1982, Improved accuracy of U-Pb ages by the creation of more concordant systems using an air abrasion technique: Geochimica et Cosmochimica Acta, v. 46, p. 637-649.

Lang, H. M. and Rice, J. M., 1985a, Geothermometry, geobarometry and T-X(Fe-Mg) relations in metapelites, Snow Peak, northern Idaho: Journal of Petrology, v. 26, p. 889-924.

Lang, H. M. and Rice, J. M., 1985b, Metamorphism of pelitic rocks in the Snow Peak area, northern Idaho: Sequence of events and regional implications: GSA Bulletin, v. 96, p. 731-736.

LaTour, T. E. and Barnett, R. L., 1987, Mineralogical changes accompanying mylonitization in the Bitterroot dome of the Idaho Batholith: Implications for timing of deformation: Geological Society of America Bulletin, v. 98, p. 356-363.

Leake, B. E., 1978, Nomenclature of amphiboles: American Mineralogist, v. 63, p. 1023-1052.

Lindgren, W., 1904, A geological reconnaissance across the Bitterroot Range and Clearwater Mountains in Montana and Idaho: U.S. Geological Survey Professional Paper, v. 27, p. 123.

Ludwig, K. R., 1988, ISOPLOT for MS-DOS: a plotting and regression program for radiogenic-isotope data, for IBM-PC compatible computers: U.S. Geological Survey Open File Report, v. 88-557.

McKenna, L. W. and Hodges, K. V., 1988, Accuracy versus precision in locating reaction boundaries: Implications for the garnet-plagioclase-aluminum silicate-quartz geobarometer: American Mineralogist, v. 73, p. 1205-1208.

Nold, J. L., 1974, Geology of the northeastern border zone of the Idaho batholith, Montana and Idaho: Northwest Geology, v. 3, p. 47-52.

Spear, F. S., 1993, Metamorphic phase equilibria and pressure-temperature-time paths: Washington, D.C., Mineralogical Society of America, 799 p.

Spear, F. S. and Kimball, K. L., 1984, Recamp- A Fortran IV program for estimating Fe^{3+} contents in amphiboles: Computers and Geosciences, v. 10, p. 317-325.

Steiger, R. H. and Jäger, E., 1977, Subcommission on geochronology: convention on the use of decay constants in geo- and cosmochronology: Earth and Planetary Science Letters, v. 36, p. 359-362.

Stacey, J. S. and Kramers, J. D., 1975, Approximation of terrestrial isotope evolution by a two-stage model: Earth and Planetary Science Letters, v. 26, p. 207-221.

Thompson, A. B., 1982, Dehydration melting of pelitic rocks and the generation of H_2O-undersaturated granitic liquids: American Journal of Science, v. 282, p. 1567-1595.

Thompson, A. B. and Tracy, R. J., 1979, Model systems for anatexis of pelitic rocks: II. Facies series melting and reactions in the system CaO-$KAlO_2$-$NaAlO_2$-Al_2O_3-SiO_2-H_2O: Contributions to Mineralogy and Petrology, v. 70, p. 429-438.

Toth, M. I., 1987, Petrology and Origin of the Bitterroot Lobe of the Idaho batholith: U.S. Geological Survey Professional Paper, v. 1436, p. 9-37.

Wehrenberg, J. P., 1972, Geology of the Lolo Peak area, northern Bitterroot Range, Montana: Northwest Geology, v. 1, p. 25-32.

Winston, D., 1986, Belt Supergroup stratigraphic correlation sections showing general lithologies and history of formal usage: Montana Bureau of Mines and Geology Geologic Map Series, v. 40.

APPENDIX I: PETROLOGIC TECHNIQUES

Garnet, biotite, muscovite, plagioclase, and amphibole rim compositions are reported in Tables 3a-e. Compositions were obtained using the JEOL 733 electron microprobe at the Massachusetts Institute of Technology with a beam current of 10 nA and an accelerating voltage of 15 kV. The analytical procedure employed follows that of Hodges and McKenna (1987) such that each mineral composition reported in Table 4 represents the average of 10 - 20 spot measurements from at least two separate domains in each microprobe section. The reported uncertainties reflect compositional variations across the probe sections, as well as machine - specific analytical imprecision. Amphibole stoichiometries were recalculated with minimum Fe^{3+} (all FeO in these samples), following the technique of Spear and Kimball (1984).

Uncertainties in oxide weight percentages were propagated through thermobarometric calculations using a Monte Carlo approach (Anderson, 1976). Details of this approach are reported in Hodges *et al.* (1993). Uncertainties calculated in this manner correspond to the precision of thermobarometric calculations and do not reflect inaccuracies related to the calibration of end-member equilibria as thermobarometers. When possible, multiple thermometer-barometer pairs were employed in order to evaluate the internal consistency of the phase equilibria.

APPENDIX II: GEOCHRONOLOGIC TECHNIQUES

The U-Pb isotopic data were acquired in the radiogenic isotope lab at the Massachusetts Institute of Technology. Zircon was separated with the standard techniques of crushing, Wilfley table, magnetic separation, and heavy liquids and were selected on the basis of size, shape, color, and lack of inclusions. Zircon was then air-abraded (Krogh, 1982) to remove the outer portion of the grains and acid washed in 4N HNO_3 for one-half hour before dissolution in HF + HNO_3. Samples were spiked with a mixed ^{205}U - ^{233}U - ^{235}U spike before dissolution in Teflon bombs at 220 °C for 48

hours. Lead and uranium were separated using standard anion exchange chemistry. Total procedural blanks during the course of these analyses were 3.5 ± 2 pg for Pb and 1 ± 1 pg for U. Details of mass spectrometry are reported in Bowring *et al.* (1993). Errors in $^{206}Pb/^{238}U$, $^{207}Pb/^{235}U$, and $^{207}Pb/^{206}Pb$ were estimated using the method of Ludwig (1988) and all age uncertainties are quoted at the 2σ level (Table 9). Initial common Pb was determined using the method of Stacey and Kramers (1975).

Table 1. Sample Locations

Sample	Latitude	Longitude
CC273	46° 44' 34"	114° 10' 44"
NB5 -1	46° 30' 35"	114° 14' 23"
NB16-1	46° 37' 12"	114° 08' 37"
NB16-4	46° 37' 53"	114° 10' 34"
NB17-1	46° 38' 09"	114° 12' 56"
NB17-6	46° 41' 57"	114° 12' 05"

Table 2. Mineral Assemblages

Sample	Am	Bt	Chl	Ms	Qtz	Sil	Ky	Pl	Grt	oxides
pelites										
NB16-1		x		x	x			x	x (Pl, Bt,Qtz)	Rt
NB16-4		x	x[1]	x	x	x		x	x	Rt
CC273		x		x	x	x	x	x	x (Pl, Bt,Qtz)	Rt
amphibolites										
NB5-1	x	x	x[1]		x			x	x (Qtz, Pl)	Rt/Ilm
NB17-1	x	x	x[1]		x			x	x(Qtz, Pl)	Rt/Ilm
NB17-6	x	x	x[1]		x			x	x (Qtz, Pl)	Rt/Ilm

[1] retrograde mineral occuring in minor amounts (<2%). Minerals in parentheses in the garnet column indicate the presence of mineral inclusions.

Table 3a. Garnet rim analysis compositions (12 O basis).

	PELITES			AMPHIBOLITES	
	NB16-1	NB16-4	CC273	NB5-1	NB17-6
SiO_2	37.72(0.21)	37.79(0.22)	38.01(0.08)	38.22(0.48)	38.08(0.13)
TiO_2	0.01(0.01)	0.04(0.03)	0.01(0.01)	0.11(0.02)	0.17(0.04)
Al_2O_3	21.13(0.18)	20.52(0.28)	20.95(0.31)	20.15(0.14)	20.15(0.26)
FeO	35.73(0.08)	33.95(0.38)	33.89(0.51)	28.95(0.39)	26.66(0.33)
MnO	3.00(0.27)	5.86(0.37)	2.93(0.32)	1.14(0.16)	2.67(0.41)
MgO	2.16(0.12)	2.03(0.12)	3.24(0.07)	2.84(0.17)	2.25(0.11)
CaO	1.44(0.09)	1.27(0.07)	2.04(0.07)	8.97(0.70)	10.38(0.42)
Total	101.19	101.49	101.12	101.28	100.38
Si	3.018	3.030	3.022	3.032	3.024
Ti	0.001	0.003	0.001	0.006	0.010
Al	1.992	1.939	1.963	1.884	1.886
Fe	2.390	2.277	2.254	1.921	1.771
Mn	0.203	0.398	0.197	0.077	0.180
Mg	0.257	0.243	0.384	0.336	0.267
Ca	0.124	0.109	0.174	0.763	0.884
Total	7.985	7.998	7.995	8.019	8.022
X_{Mg}	0.087	0.080	0.128	0.109	0.086
X_{Fe}	0.804	0.752	0.749	0.620	0.571
X_{Ca}	0.042	0.036	0.058	0.246	0.285
X_{Mn}	0.068	0.132	0.066	0.025	0.058

Numbers in parentheses denote 1σ uncertainties in rim compositions established using the approach of Hodges and McKenna (1987).

Table 3b. Biotite rim analysis compositions (11 O basis).

	PELITES			AMPHIBOLITES	
	NB16-1	NB16-4	CC273	NB5-1	NB17-6
SiO_2	35.13(0.07)	35.14(0.41)	35.95(0.26)	35.09(0.73)	36.08(0.13)
TiO_2	1.95(0.14)	2.50(0.43)	1.61(0.09)	1.96(0.51)	2.70(0.06)
Al_2O_3	18.97(0.02)	19.51(0.58)	19.98(0.16)	15.45(0.58)	15.52(0.21)
FeO	24.42(0.46)	22.72(0.72)	19.65(0.37)	23.45(0.92)	20.57(0.18)
MnO	0.08(0.02)	0.30(0.08)	0.21(0.03)	0.11(0.05)	0.08(0.07)
MgO	6.54(0.45)	6.94(0.17)	9.52(0.42)	9.42(0.48)	10.40(0.15)
CaO	0.07(0.06)	0.05(0.03)	0.02(0.01)	0.23(0.17)	0.10(0.03)
Na_2O	0.00(0.00)	0.11(0.05)	0.15(0.07)	0.06(0.03)	0.08(0.01)
K_2O	8.52(0.17)	9.04(0.21)	8.88(0.30)	8.13(0.99)	9.18(0.16)
Total	95.68	96.40	95.97	93.93	94.71
Si	2.712	2.684	2.704	2.763	2.786
Ti	0.113	0.144	0.091	0.116	0.157
Al	1.726	1.756	1.771	1.434	1.412
Fe	1.577	1.451	1.236	1.545	1.329
Mn	0.005	0.019	0.013	0.008	0.005
Mg	0.752	0.789	1.067	1.106	1.197
Ca	0.006	0.004	0.002	0.019	0.008
Na	0.000	0.016	0.022	0.009	0.011
K	0.839	0.881	0.852	0.816	0.904
Total	7.731	7.743	7.757	7.817	7.809
XMg	0.261	0.242	0.370	0.337	0.377
Xfe	0.546	0.444	0.429	0.470	0.419

Numbers in parentheses denote 1σ uncertainties in rim compositions established using the approach of Hodges and McKenna (1987).

Table 3c. Muscovite rim analysis compositions (11 O basis).

	NB16-1	NB16-4	CC273
SiO_2	47.21(0.18)	46.81(0.31)	46.81(0.28)
TiO_2	0.56(0.02)	0.39(0.31)	0.58(0.14)
Al_2O_3	35.99(0.05)	35.25(0.16)	35.48(0.57)
FeO	0.98(0.16)	1.47(0.18)	1.03(0.16)
MnO	0.01(0.02)	0.02(0.03)	0.06(0.02)
MgO	0.26(0.04)	0.58(0.06)	0.64(0.12)
CaO	0.01(0.01)	0.01(0.01)	0.02(0.02)
Na_2O	0.82(0.02)	0.64(0.05)	1.17(0.09)
K_2O	9.72(0.06)	9.91(0.34)	9.25(0.10)
Total	95.58	95.07	95.05
Si	3.107	3.110	3.099
Ti	0.028	0.019	0.029
Al	2.792	2.760	2.768
Fe	0.054	0.082	0.057
Mn	0.001	0.001	0.003
Mg	0.026	0.057	0.063
Ca	0.001	0.001	0.001
Na	0.105	0.082	0.151
K	0.817	0.840	0.782
Total	6.930	6.952	6.954

Numbers in parentheses denote 1σ uncertainties in rim compositions established using the approach of Hodges and McKenna (1987).

Table 3d. Plagioclase rim analysis compositions (8 O basis).

	PELITES			AMPHIBOLITES	
	NB16-1	NB16-4	CC273	NB5-1	NB17-6
SiO_2	63.87(0.46)	65.29(0.19)	62.15(0.35)	44.58(0.17)	44.99(0.26)
Al_2O_3	23.24(0.10)	23.03(0.06)	24.40(0.18)	33.83(0.48)	34.62(0.25)
FeO	0.36(0.05)	0.30(0.07)	0.25(0.08)	0.15(0.08)	0.24(0.04)
MgO	0.03(0.01)	0.04(0.01)	0.03(0.01)	0.02(0.01)	0.03(0.01)
CaO	4.30(0.14)	3.57(0.01)	5.33(0.14)	19.07(0.13)	18.72(0.20)
Na_2O	9.09(0.10)	9.70(0.10)	8.52(0.07)	0.67(0.07)	0.89(0.02)
K_2O	0.10(0.01)	0.12(0.04)	0.06(0.02)	0.03(0.02)	0.01(0.01)
Total	101.00	102.05	100.74	98.35	99.49
Si	2.797	2.824	2.736	2.095	2.088
Al	1.200	1.174	1.266	1.874	1.894
Fe	0.013	0.011	0.009	0.006	0.009
Mg	0.002	0.002	0.002	0.002	0.002
Ca	0.202	0.165	0.252	0.960	0.931
Na	0.775	0.816	0.730	0.061	0.080
K	0.005	0.007	0.003	0.002	0.001
Total	4.994	5.000	4.998	4.999	5.005
X_{an}	0.206	0.167	0.255	0.939	0.921
X_{or}	0.006	0.007	0.004	0.002	0.000
X_{ab}	0.789	0.826	0.741	0.060	0.079

Numbers in parentheses denote 1σ uncertainties in rim compositions established using the approach of Hodges and McKenna (1987).

Table 3e. Amphibole rim analysis compositions (23 O basis).

	NB5-1	NB17-6
SiO_2	43.39(0.19)	43.79(0.51)
TiO_2	0.95(0.04)	0.78(0.08)
Al_2O_3	11.72(0.04)	12.69(0.56)
FeO	20.01(0.14)	19.06(0.29)
MnO	0.18(0.05)	0.32(0.04)
MgO	7.92(0.10)	8.58(0.25)
CaO	11.16(0.19)	11.21(0.07)
Na_2O	0.95(0.02)	0.99(0.06)
K_2O	0.65(0.04)	0.65(0.08)
Total	96.95	98.07
Si	6.602	6.550
Ti	0.109	0.088
Al^{iv}	1.398	1.450
Al^{vi}	0.706	0.798
Al^{total}	2.103	2.237
Fe	2.479	2.384
Mn	0.024	0.041
Mg	1.796	1.912
Ca	1.820	1.796
Na(M4)	0.000	0.000
Na(A)	0.282	0.288
K	0.126	0.124
Total	15.340	15.431
$Fe/_{(Fe+Mg)}$	0.580	0.555

Numbers in parentheses denote 1σ uncertainties in rim compositions established using the approach of Hodges and McKenna (1987).

Table 4: Pelite Thermobarometers

	Reactions	Calibration
(GARB)	$Fe_3Al_2Si_3O_{12} + KMg_3AlSi_3O_{10}(OH)_2 = Mg_3Al_2Si_3O_{12} + KFe_3AlSi_3(OH)_2$ *(Alm + Phl = Pyr + Ann)*	Hodges and McKenna (1987)*
(GASP)	$Ca_3Al_2Si_3O_{12} + 2Al_2SiO_5 + SiO_2 = 3CaAl_2Si_2O_8$ *(Grs + AlSi + Qtz = An)*	McKenna and Hodges (1988)*
(GMAP)	$Fe_3Al_2Si_3O_{12} + Ca_3Al_2Si_3O_{12} + KAl_3Si_3O_{10}(OH)_2 = 3CaAl_2Si_2O_8 + KFe_3AlSi_3O_{10}(OH)_2$ *(Alm + Grs + Ms = An + Ann)*	Berman (1988; 1990)
(GMPP)	$Mg_3Al_2Si_3O_{12} + Ca_3Al_2Si_3O_{12} + KAl_3Si_3O_{10}(OH)_2 = 3CaAl_2Si_2O_8 + KMg_3AlSi_3O_{10}(OH)_2$ *(Pyr + Grs + Ms = Pl + Phl)*	Berman (1988; 1990)

*Calibrations for reactions P1 and P2 were based on least-squared regression treatments of the experimental data of Ferry and Spear (1978) and Hays (1966), Hariya and Kennedy (1968), Goldsmith (1980), Gasparik (1984), Koziol and Newton (1988), respectively. Thermodynamic constants (ΔH, ΔS, and ΔV) for reaction P3 and P4 were calculated using tabulated thermochemical data.

Table 5: Comparative rim thermobarometry- Pelites

	CC273		NB16-4		NB16-1	
	T (K)	P (MPa)	T (K)	P (MPa)	T (K)	P (MPa)
GARB- GASP	950(40)	800(70)	960(50)	870(90)	-	-
GARB- GMPP	950(40)	820(60)	950(40)	750(80)	1000(70)	810(120)
GARB- GMAP	950(40)	800(60)	960(40)	720(80)	1000(70)	780(120)
GASP - GMPP	960(40)	830(60)	730(50)	540(60)	-	-
GMAP- GMPP	960(40)	830(60)	1000(50)	790(90)	1040(80)	850(130)

Reactions correspond to explanation in text. Values in parentheses denote 2σ precision limits derived by propagating analytical uncertainties.

Table 6. Amphibolite Thermobarometers

	Reactions	Calibration
(GH)	$3NaCa_2Fe_4Al_3Si_6O_{22}(OH)_2 + 4Mg_3Al_2Si_3O_{12} = 3NaCa_2Mg_4Al_3Si_6O_{22}(OH)_2 + Fe_3Al_2Si_3O_{12}$ *(Fe-Prg + Pyr = Prg + Alm)*	Graham and Powell (1984)
(HAl)	$NaCa_2Mg_5Si_4(AlSi_3)O_{22}(OH)_2 + 4\ SiO_2 = Ca_2Mg_5Si_8O_{22}(OH)_2 + NaAlSi_3O_8$ *(Ed + Qtz = Tr + Ab)*	Holland and Blundy (1994)
(FePrg)[1,2]	$6CaAl_2Si_2O_8 + 3NaAlSi_3O_8 + 3Ca_2Fe_5Si_8O_{22}(OH)_2 = 3Ca_3Al_2Si_3O_{12} + Fe_3Al_2Si_3O_{12} + 3NaCa_2Fe_4Al_3Si_6O_{22}(OH)_2 + 18SiO_2$ *(An + Ab + Fe-Act = Grs + Alm + Fe-Prg)*	Kohn and Spear (1989)
(MgPrg)[1,2]	$6CaAl_2Si_2O_8 + 3NaAlSi_3O_8 + 3Ca_2Mg_5Si_8O_{22}(OH)_2 = 3Ca_3Al_2Si_3O_{12} + Mg_3Al_2Si_3O_{12} + 3NaCa_2Mg_4Al_3Si_6O_{22}(OH)_2 + 18SiO_2$ *(An + Ab + Tr = Grs + Pyr + Prg)*	Kohn and Spear (1989)
(FeTsc)	$6CaAl_2Si_2O_8 + 3Ca_2Fe_5Si_8O_{22}(OH)_2 = 2Ca_3Al_2Si_3O_{12} + Fe_3Al_2Si_3O_{12} + 3Ca_2Fe_4Al_2Si_7O_{22}(OH)_2 + 18SiO_2$ *(An + Fe-Act = Grs + Alm +Fe-Tsch)*	Kohn and Spear (1990)
(MgTsc)	$6CaAl_2Si_2O_8 + 3Ca_2Mg_5Si_8O_{22}(OH)_2 = 2Ca_3Al_2Si_3O_{12} + Mg_3Al_2Si_3O_{12} + 3Ca_2Mg_4Al_2Si_7O_{22}(OH)_2 + 18SiO_2$ *(An + Tr= Grs + Alm +Tsch)*	Kohn and Spear (1990)

Geobarometers based on reactions A3 and A4 consist of two models (1 and 2).

Table 7. Comparative thermobarometry- Amphibolites

	NB5-1		NB17-6	
	T (K)	P (MPa)	T (K)	P (MPa)
GH - FePrg1	1000(40)	720(60)	960(20)	740(60)
GH - FePrg2	1000(50)	650(70)	960(20)	660(50)
GH - MgPrg1	1000(40)	640(50)	950(20)	630(50)
GH - MgPrg2	1000(50)	620(80)	950(20)	600(50)
GH - FeTsc	1000(40)	580(60)	950(20)	630(40)
GH - MgTsc	1000(50)	530(70)	950(20)	540(30)
	T (K)		T (K)	
HAl	930(50)		870(50)	

Reactions correspond to explanation in text. Values in parentheses denote 2σ precision limits derived by propagating analytical uncertainties. The equilibria were recalibrated incorporating the Elkins and Grove (1990) solution model for plagioclase.

Table 8. Comparative core/matrix thermobarometry- Pelites

	CC273		NB16-4	
	T (K)	P (MPa)	T (K)	P (MPa)
GARB - GASP	920	770	970	930
GARB- GMAP	910	750	960	660
GASP - GMPP	900	750	570	370

Reactions correspond to explanation in text. Values in parentheses denote 2σ precision limits derived by propagating analytical uncertainties.

Table 9. U-Pb Analytical Data and Results

Fractions	Weight	Concentrations		Atomic ratios								Ages (Ma)			
		U	Pb*	$^{206}Pb^{\dagger}/^{204}Pb$	$^{208}Pb^{*}/^{206}Pb$	$^{206}Pb^{\ddagger}/^{238}U$	% err	$^{207}Pb^{\ddagger}/^{235}U$	% err	$^{207}Pb^{\ddagger}/^{206}Pb$	% err	$^{206}Pb/^{238}U$	$^{207}Pb/^{235}U$	$^{207}Pb/^{206}Pb$	Pb
	(mg)	(ppm)	(ppm)												(pg)
NB17-1															
(d-3)+200	0.024	534.7	4.7	169.5	0.305	0.00748	(0.51)	0.04880	(1.32)	0.04734	(1.12)	48.0	48.4	66.5	44
(d-3)+200	0.016	1745.0	15.4	260.7	0.320	0.00749	(0.26)	0.04860	(0.80)	0.04705	(0.70)	48.1	48.2	52.0	59

*Radiogenic Pb. †Measured ratio corrected for fractionation only. Mass fractionation correction of 0.12 ± 0.8%/amu was applied to all Pb analyses. ‡Corrected for fractionation, spike, blank, and initial common Pb. Zircon fractions are designated as nonmagnetic (nm) in terms of degrees tilt on a Frantz magnetic separator, and as +200 in standard mesh size. Decay constants used are $^{238}U = 0.15513 \times 10^{-9}\ yr^{-1}$, and $^{235}U = 0.98485 \times 10^{-9}\ yr^{-1}$ (Steiger and Jäger, 1977). Common Pb corrections were estimated using the method of Stacey and Kramers (1975). Data reduction and error analysis was accomplished using the algorithms of Ludwig (1988) and all errors are reported in percent at the 2σ confidence interval.

FIGURE CAPTIONS

Figure 1. Generalized geologic map of the Bitterroot metamorphic core complex. Rectangles define areas of detailed metamorphic study: BB/GM= Boehls Butte/Goat Mountain; SP = Snow Peak; NB = Northeastern Bitterroot. Map modified from Hyndman *et al.* (1988).

Figure 2. Constraints on peak metamorphic conditions in the Boehls Butte/Goat Mountain (a) and Snow Peak (b) areas. Unlabeled thin curves bound aluminum silicate stability fields after Hemingway *et al.* (1991). Thick light gray curve corresponds to the water-saturated granite solidus (Thompson, 1982). Narrow dark gray curve denotes the nominal water-saturated muscovite breakdown reaction (Thompson and Tracy, 1979; Thompson, 1982), gray dashed line is the approximate upper stability limit for Mg-cordierite (Berman, 1988). Curves labeled (1) and (2) are lower and upper limits of staurolite stability (Berman, 1988).

Figure 3. Photomicrographs illustrating general textures in pelites and amphibolites. Major phases indicated on figure. Plain light images of (a) NB16-4 garnet used in analysis. Plain light image (b) of amphibolite sample NB17-1 illustrating hornblende pseudomorph of garnet surrounded by halo of Qtz + Pl and overgrown by ilmenite and biotite.

Figure 4. Thermobarometric results for pelitic samples. Small filled circles indicate P-T conditions derived through simultaneous solution of GARB and GMPP. All ellipses designate 2σ uncertainties in calculated pressures and temperatures based on analytical imprecision. Curves represent reactions described in Figure 2.

Figure 5. Fe-end-member thermobarometric results for amphibolite samples (a) NB5-1 and (b) NB17-6. Solid ellipse—FeTsc; Shaded ellipse—$FePrg^1$; Dashed ellipse—$FePrg^2$. Curves represent reactions described in Figure 2.

Figure 6. Data from electron microprobe traverse across garnet NB16-4 shown in Figure 3a.

Figure 7. Concordia diagrams for NB17-1. Ages, in Ma, are marked on the concordia curve. Individual analyses are depicted as 2σ error ellipses.

Figure 8. Thermobarometric results for amphibolite samples (dashed lines) and pelites (solid lines) superimposed on P-T constraints from Boehls Butte/Goat Mountain. Curves represent reactions described in Figure 2.

Figure 1

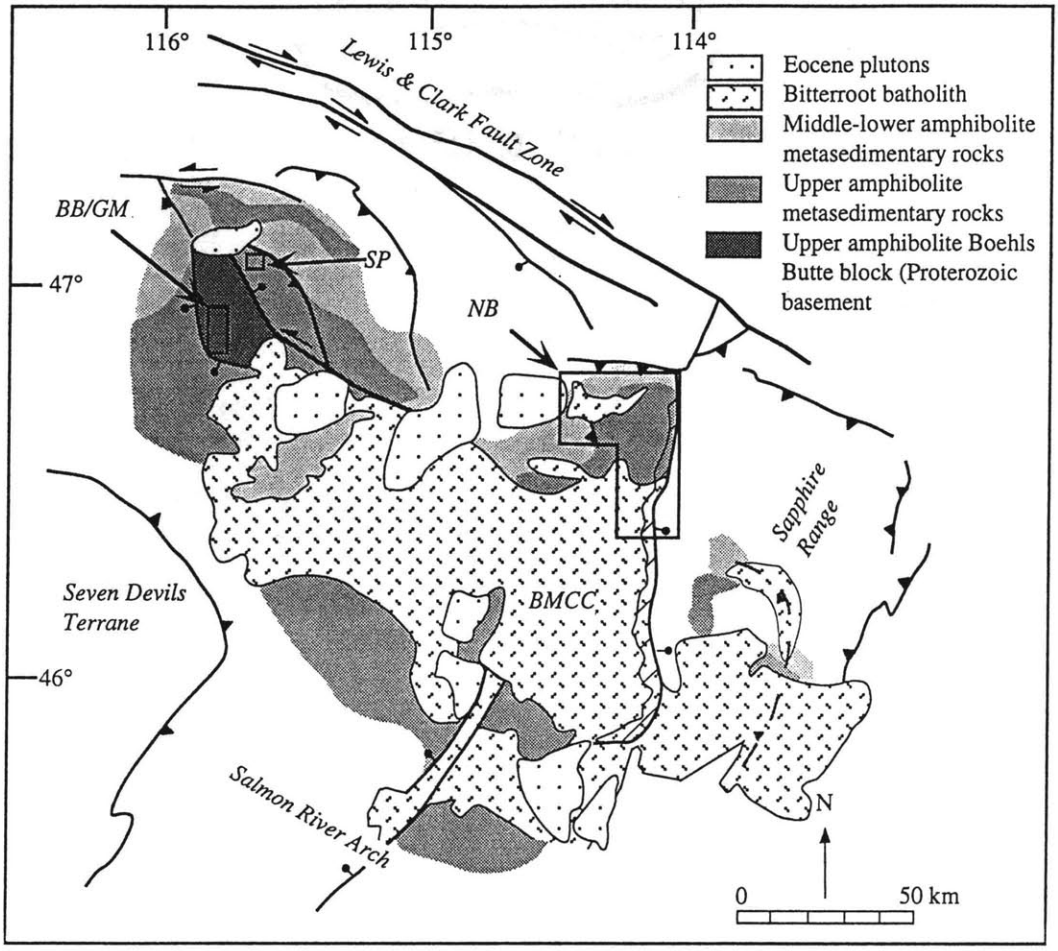
116°
115°
114°
Lewis & Clark Fault Zone
Eocene plutons
Bitterroot batholith
Middle-lower amphibolite metasedimentary rocks
Upper amphibolite metasedimentary rocks
Upper amphibolite Boehls Butte block (Proterozoic basement
BB/GM
SP
47°
NB
Sapphire Range
Seven Devils Terrane
BMCC
46°
Salmon River Arch
N
0
50 km

Figure 2a

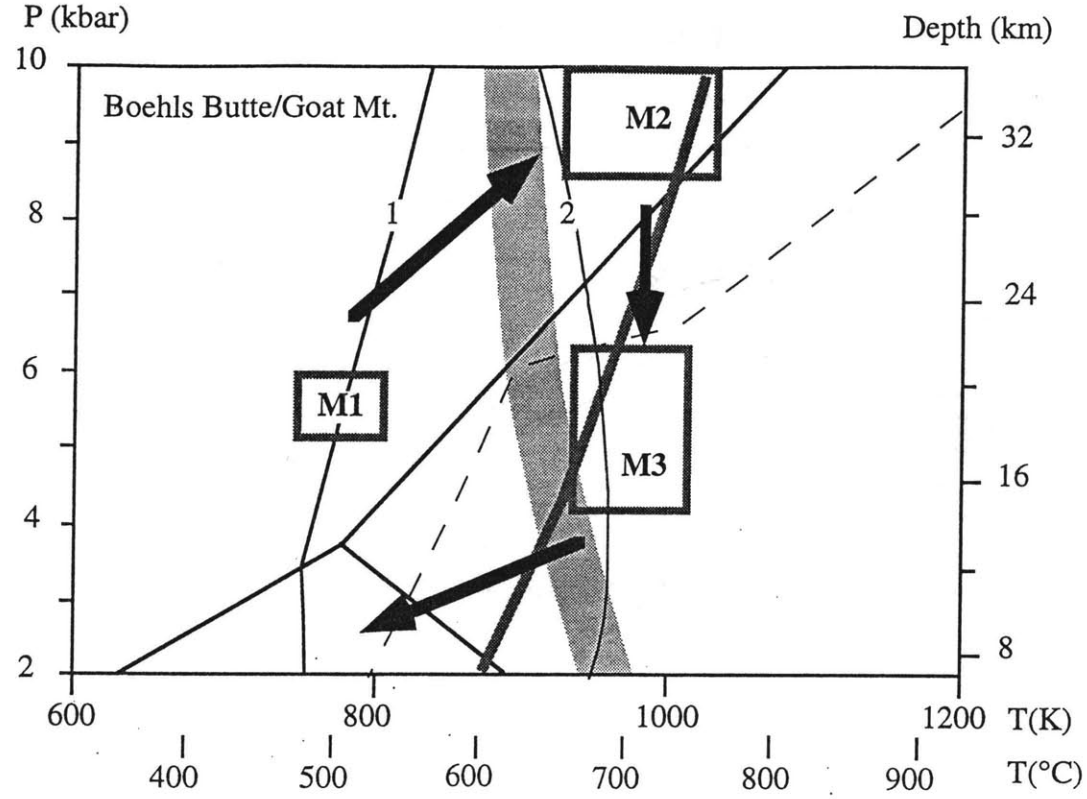

Figure 2b

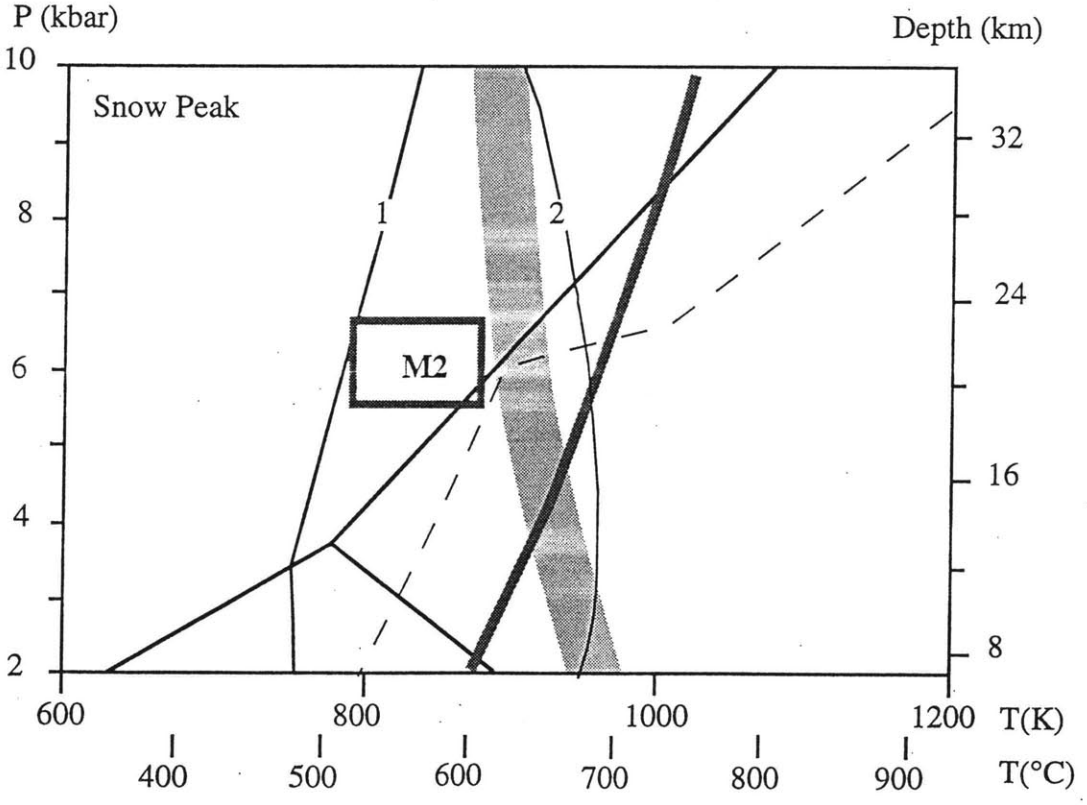

Figure 3a

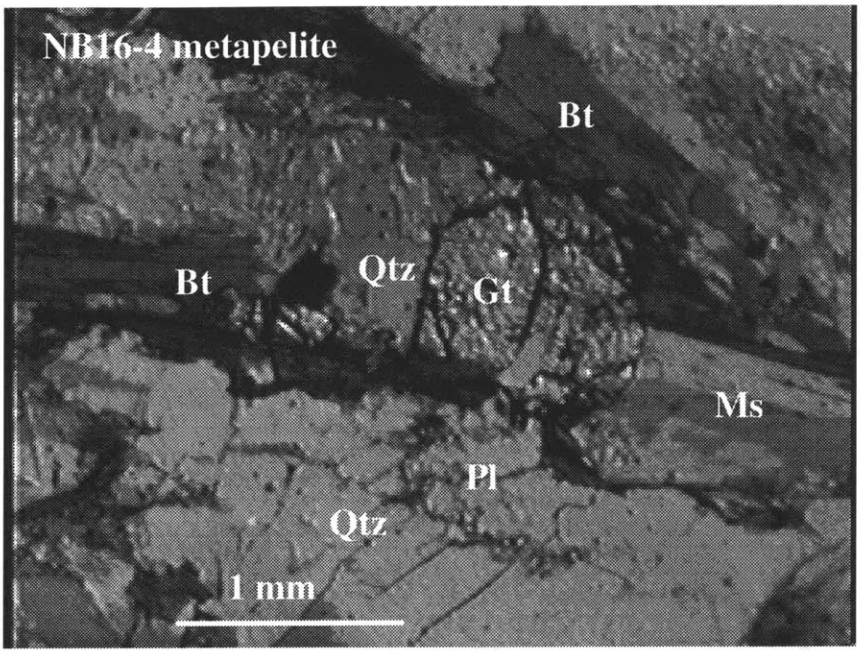

Figure 3b

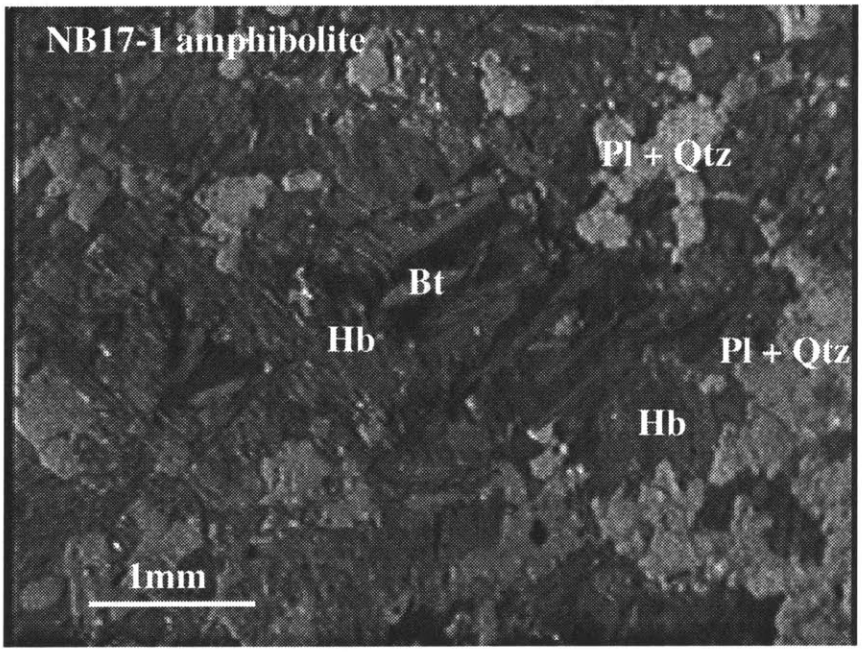

Figure 4

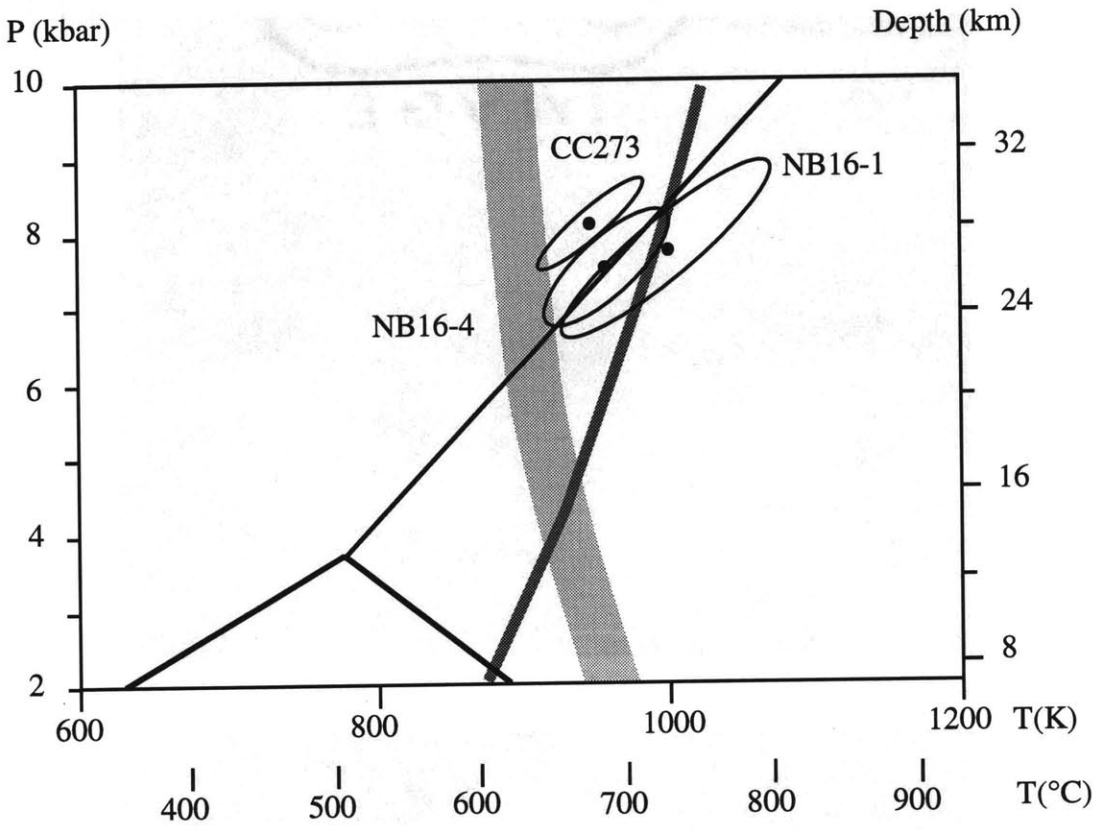
P (kbar)
Depth (km)
10
8
6
4
2
32
24
16
8
CC273
NB16-1
NB16-4
600
800
1000
1200
T(K)
400
500
600
700
800
900
T(°C)

Figure 5a

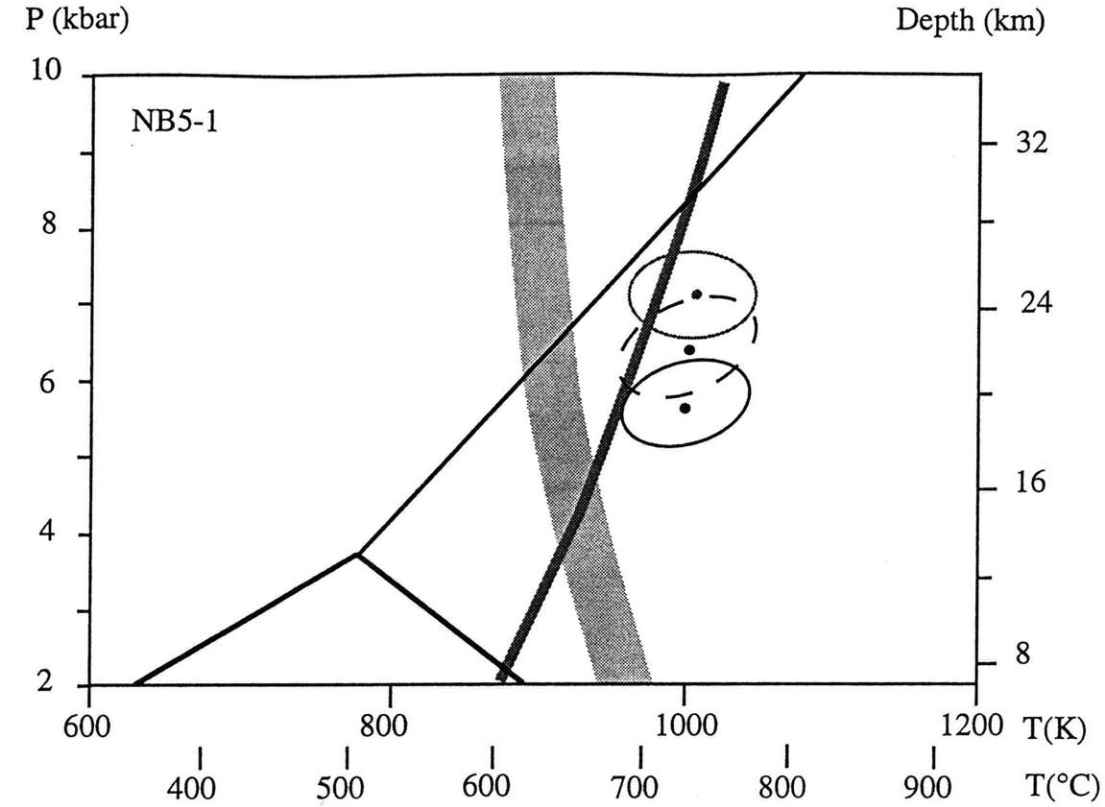

Figure 5b

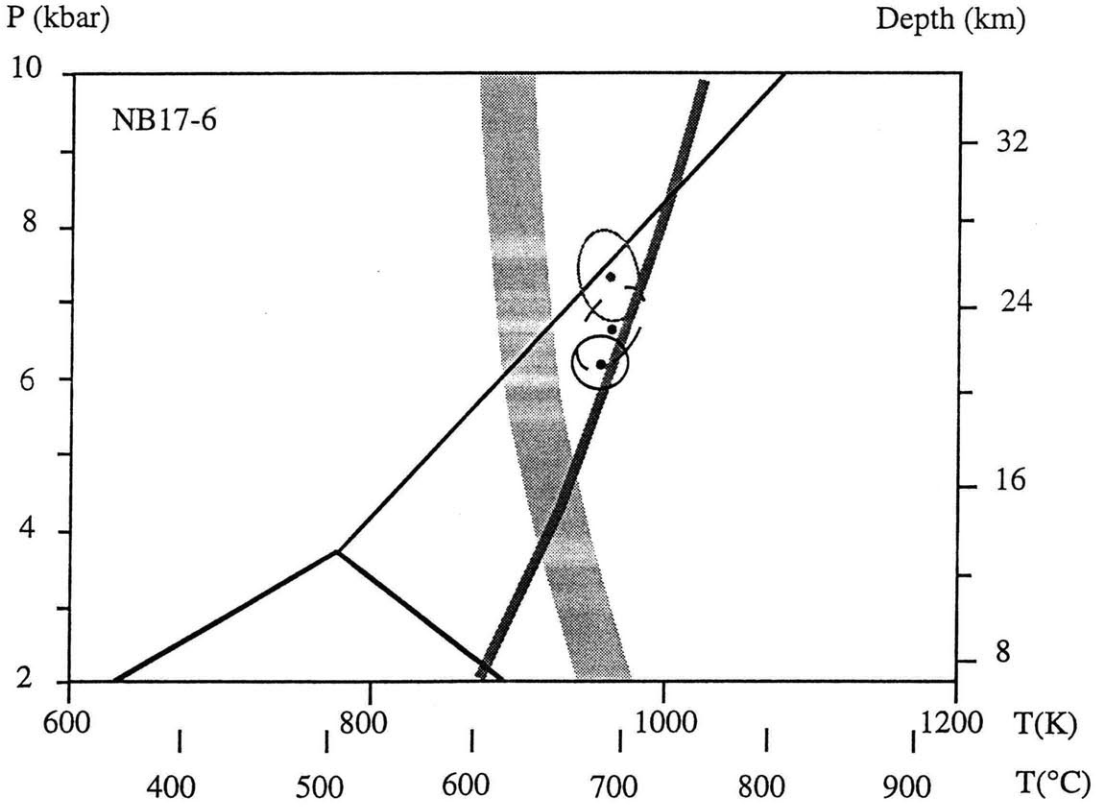

Figure 6

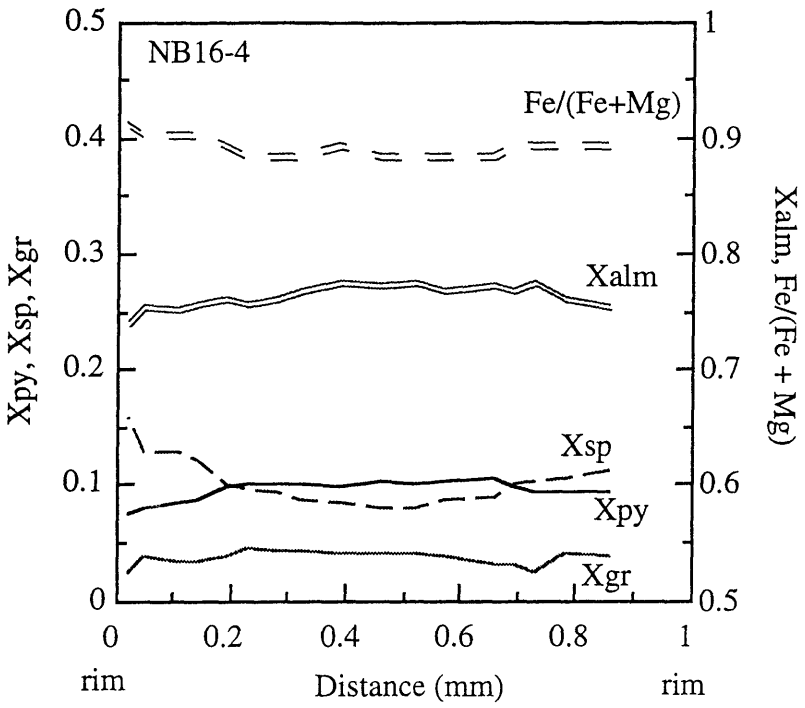
NB16-4
Fe/(Fe+Mg)
Xalm
Xsp
Xpy
Xgr
Xpy, Xsp, Xgr
Xalm, Fe/(Fe + Mg)
0.5
0.4
0.3
0.2
0.1
0
1
0.9
0.8
0.7
0.6
0.5
0
0.2
0.4
0.6
0.8
1
rim
Distance (mm)
rim

Figure 7

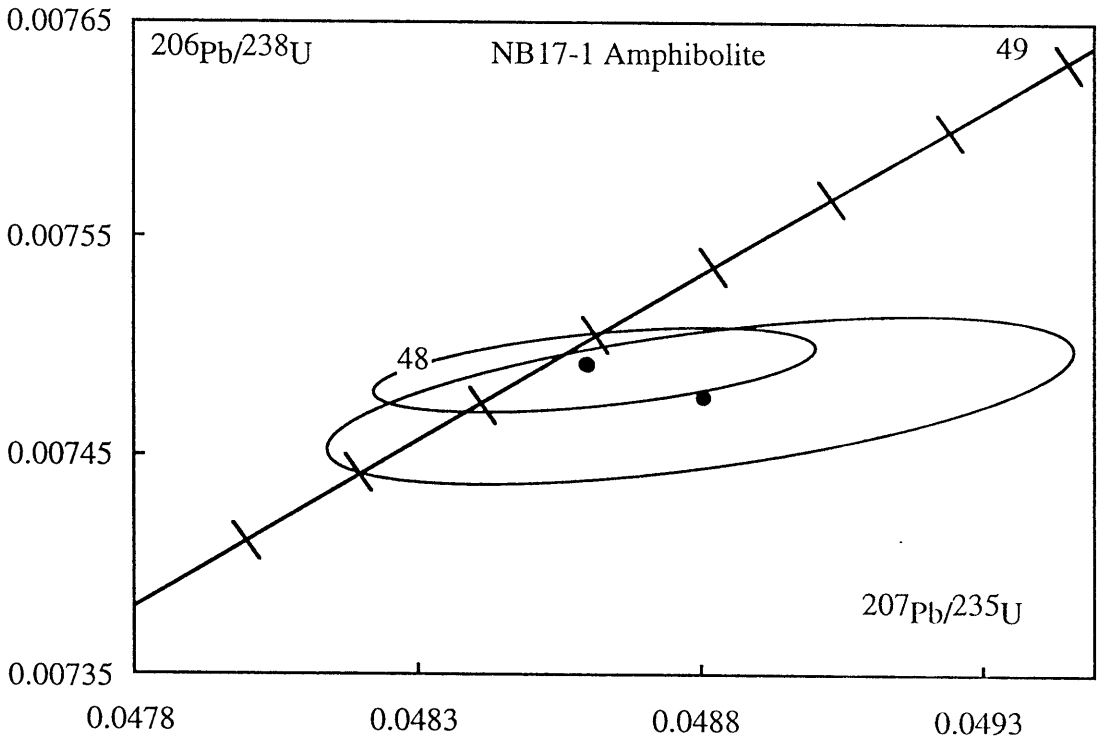
0.00765
0.00755
0.00745
0.00735
206Pb/238U
NB17-1 Amphibolite
49
48
207Pb/235U
0.0478
0.0483
0.0488
0.0493

Figure 8

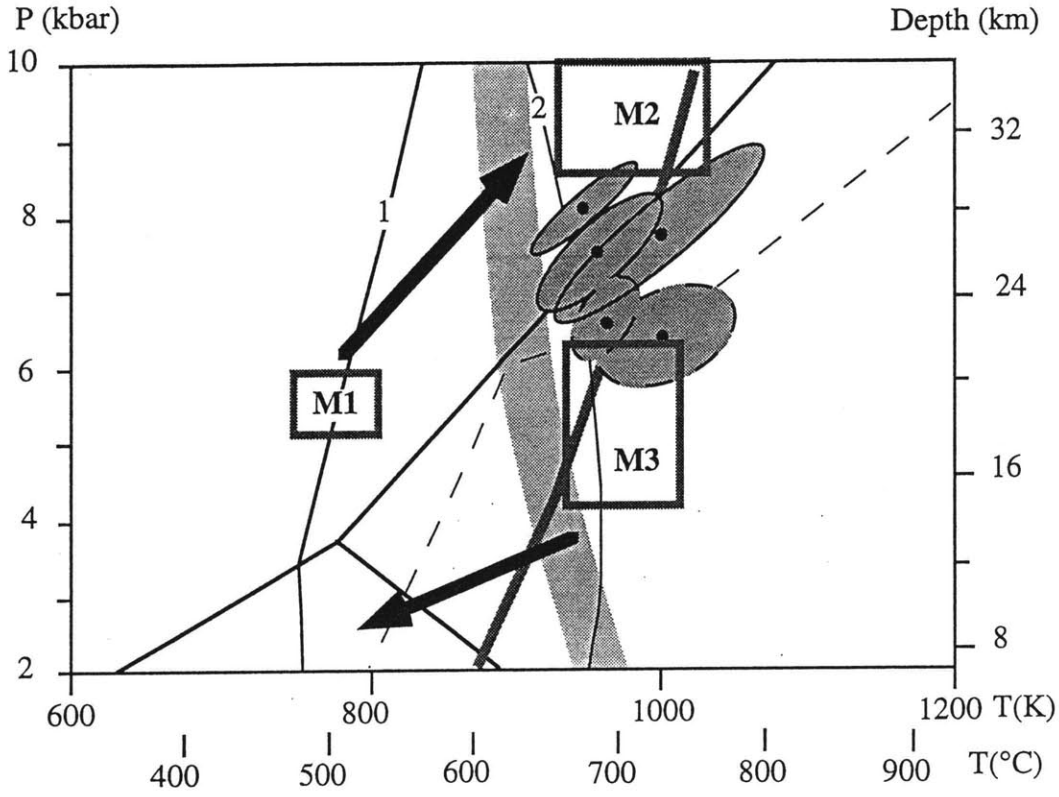
P (kbar)
Depth (km)
10
8
6
4
2
32
24
16
8
1
2
M1
M2
M3
600
800
1000
1200 T(K)
400
500
600
700
800
900 T(°C)

CHAPTER 4

IMPLICATIONS OF MIDDLE EOCENE EPIZONAL PLUTONISM FOR THE UNROOFING HISTORY OF THE BITTERROOT BATHOLITH, IDAHO-MONTANA

ABSTRACT

U-Pb and $^{40}Ar/^{39}Ar$ data from the epizonal Lolo Hot Springs batholith and Whistling Pig pluton in the northwestern and southwestern Bitterroot metamorphic core complex demonstrate that much of the mesozonal Bitterroot batholith and western Bitterroot metamorphic core complex were at shallow levels by ~49 Ma. An U-Pb monazite crystallization age of 55.8 Ma for the mesozonal Skookum Butte stock adjacent to the Lolo Hot Springs batholith demonstrates that ~12 - 18 km of unroofing occurred over a period of ~6 - 7 Ma in the northwestern Bitterroot Range. An eastward progression of older to younger $^{40}Ar/^{39}Ar$ cooling ages in the northern Bitterroot Range suggests that this unroofing event may have begun as early as 55.6 Ma, following crystallization of the Skookum Butte stock, and that it reflects progressive unroofing accommodated by the core-bounding Bitterroot mylonite. The geochronologic data demonstrate that the western BMCC reached shallow depths (~1.5 km) while the eastern BMCC remained at mesozonal structural levels. The geochronologic data require multiple extensional mechanisms, or more likely, a significant component of rotation about a north-south trending axis associated with extension on the Bitterroot mylonite zone.

INTRODUCTION

Most research concerning the Cenozoic unroofing history of the Bitterroot metamorphic core complex (BMCC) has focused on its eastern margin, where dramatic exposures of the Bitterroot mylonite zone attest to an important phase of Middle Eocene extension (Figure 1). However, the BMCC is an extremely large feature, exposing Cretaceous-Middle Eocene rocks of the Bitterroot batholith and their Precambrian host rocks over an area of ~5000 km^2, and more general questions regarding the unroofing of the footwall remain unanswered. For example, when and how did the Bitterroot batholith as a whole reach shallow structural levels? Was denudation of the metamorphic/igneous core accommodated entirely by movement on the Bitterroot mylonite zone and related structures, or did these structures unroof only the eastern side?

A suite of epizonal plutons along the western and southern margins of the BMCC provide some of the answers to such questions. These shallow-level granitic bodies intruded Bitterroot batholith and Precambrian metamorphic rocks that were at depths of at least 20 km prior to denudation during core complex development. Thus, the crystallization ages of the epizonal plutons provide an important constraint on the minimum age of BMCC footwall unroofing in areas far-removed from the trace of the Bitterroot mylonite zone. In this paper, we present new geochronologic constraints for the ages of two epizonal plutons- the Lolo Hot Springs batholith and the Whistling Pig pluton - that are located in the extreme northern and southern portions of the Bitterroot batholith (Figure 1). These data confirm that the epizonal plutons are coeval and suggest that much of the Bitterroot batholith was unroofed in Middle Eocene time. $^{40}Ar/^{39}Ar$ cooling ages for rocks in the northwestern BMCC, when combined with published $^{40}Ar/^{39}Ar$ data from the northeastern BMCC, are consistent with unroofing

of the eastern half of the Bitterroot batholith by movement on the Bitterroot mylonite zone.

REGIONAL SETTING

The BMCC is located in a region that is bounded on the north by the Lewis and Clark fault zone and on the south by the Salmon River Arch (Figure 1; Armstrong, 1975). Footwall rocks of the BMCC consist primarily of granites and granodiorites of the Bitterroot batholith and metamorphosed Proterozoic Belt Supergroup units and pre-Belt crystalline basement (Wehrenberg, 1972; Chase, 1973; Hyndman *et al.*, 1988). The eastern and southeastern margins of the BMCC are defined by the extensional Bitterroot mylonite zone (Garmezy, 1983). Mylonitic fabrics in this shear zone are cut by high-angle normal faults associated with post-mylonitic brittle extension (House, unpublished mapping; Chase *et al.*, 1983; Hyndman and Myers, 1988). Published data bracket the age of this detachment between 48 and 46.4 Ma (Chase *et al.*, 1983; Hodges and Applegate, 1993).

The Bitterroot batholith is the northern lobe of the laterally extensive Idaho batholith (Armstrong, 1975). Rather than a single magmatic phase, the Bitterroot batholith represents multiple magmatic episodes that range from ~125 - 48 Ma (McDowell and Kulp, 1969; Armstrong, 1976; Armstrong *et al.*, 1977). The earliest phases are tonalites and quartz diorites that have been dated at ~100 - 80 Ma (Toth, 1987). Laterally extensive mesozonal granodiorite and granite plutons make up the majority of the Bitterroot batholith, and range in age from ~66 - 57 Ma (Toth, 1987). The youngest of the main-stage plutons are ~52 - 48 Ma (Chase *et al.*, 1978; Bickford *et al.*, 1981; Chase *et al.*, 1983).

The main phase of mesozonal plutonism was followed by emplacement of a suite of granitoids associated with the Challis magmatic episode. Textural evidence indicates a shallow level of emplacement for these plutons (~1.5 km; Rehn and Lund,

1981). These plutons intrude main-stage granites and granodiorites, as well as lower- to upper-amphibolite facies metasedimentary rocks originating at mid-crustal levels. Stratigraphic arguments call for emplacement of the main-stage plutons in the northern portion of the Bitterroot batholith at minimum depths of ~17 - 20 km (Hyndman, 1980; Hyndman, 1981) and quantitative thermobarometric data from rocks in the northeastern border zone suggest that metasedimentary country rocks of the Bitterroot batholith were metamorphosed at depths as great as 28 km (House, Chapter 3). Mineral assemblages in migmatites on the northeastern and southwestern margins further suggest crystallization at depths of ~21 - 25 km (Hyndman *et al.*, 1988). We conclude that much of the Bitterroot batholith was emplaced at depths of at least 20 km and possibly as great as 28 km, requiring a considerable amount of unroofing (~20 km) prior to intrusion of the epizonal plutons.

Epizonal granitoids are in close proximity to the mesozonal Bitterroot batholith in several locations, providing an opportunity to determine the age and magnitude of unroofing throughout the batholith. On the northern margins of the Bitterroot batholith, the epizonal Lolo Hot Springs batholith is adjacent to the mesozonal Skookum Butte stock, and in the south, the Whistling Pig pluton, one of the best-studied epizonal plutons, intrudes main-stage granodiorites of the Bitterroot batholith (Figure 1). In order to constrain the age and magnitude of unroofing in the Bitterroot batholith and resolve the role of the Bitterroot mylonite in bringing the Bitterroot batholith to higher structural levels, we collected a suite of samples for U-Pb and $^{40}Ar/^{39}Ar$ geochronology from Skookum Butte stock, the Lolo Hot Springs batholith, and the surrounding country rocks in the northwestern BMCC, as well as the Whistling Pig pluton in the southern Bitterroot batholith (Table 1). Crystallization ages of the epizonal plutons provide lower-limits on unroofing throughout the Bitterroot batholith, and comparison of these crystallization ages with those for the mesozonal Skookum Butte stock bracket the interval over which this unroofing occurred.

GEOLOGY OF THE NORTHWESTERN BMCC

Country rocks in the northwestern BMCC consists primarily of units of the Wallace Formation and the Ravalli Group and their metamorphosed equivalents; metamorphosed Prichard Formation is also present as pelitic schists and gneisses (Figure 2; Nold, 1974). Metamorphic grade ranges from upper-amphibolite facies in the east to greenschist and lower-amphibolite facies on the western and northern margins of the BMCC (House, unpublished mapping; Nold, 1974). A west-dipping, north-northeast striking mylonite zone—the Spruce Creek mylonite—separates footwall pelitic schists and gneisses from overlying calc-silicates (House, Chapter 5; Ferguson, 1972; Lewis *et al.*, 1992). Shear zone rocks consist of quartzite and calc-silicate gneisses, tonalites, migmatites, and pelites; numerous pegmatites cross-cut the shear zone (House, Chapter 5). The east-vergent Spruce Creek mylonite is ~0.25 km wide and is most-likely an exhumed thrust correlative with similar structures described to the north at Boehls Butte and to the east in the Sapphire range (House, Chapter 5; Lang and Rice, 1985; Skipp, 1987). Broad constraints on the age of the Spruce Creek mylonite are ~100 - 80 Ma, based on the inferred age of tonalites within the shear zone (Toth, 1987).

The Skookum Butte stock is one of several medium to coarse-grained granodiorite plutons associated with the Bitterroot batholith that intrude the metamorphic rocks in the northwestern BMCC (Ferguson, 1972; Nold, 1974). On the northern margins of the stock, hornblende hornfels facies contact metamorphism is evident where the pluton intrudes lower-amphibolite facies Ravalli Group and Wallace Formation metasediments (Ferguson, 1972; Nold, 1974; House, unpublished mapping). The southern and eastern margins of the stock, where it intrudes upper-amphibolite facies pelites, and quartzite and calc-silicate gneisses, are migmatitic (House, unpublished mapping). Foliation in the migmatite parallels the margins of the stock, and granite lenses in the migmatite are similar to granite in the stock, suggesting that

the migmatite was generated in metasedimentary rocks during emplacement of the Skookum Butte stock. These contact relationships call for emplacement of the Skookum Butte stock at moderate depths of ~350-500 MPa (~12 - 18 km) and relatively high temperatures (~825 - 900 K; Spear, 1993). Cross-cutting relationships and textural evidence suggest that the Skookum Butte stock predates unroofing (Nold, 1974). Ferguson (1972) obtained sphene and apatite fission-track ages of 82 and 39 Ma for the Skookum Butte stock, which he interpreted in terms of Cretaceous intrusion and an Eocene thermal resetting or unroofing event.

EPIZONAL PLUTONS

The Lolo Hot Springs batholith and the Whistling Pig pluton are part of the suite of epizonal plutons in the western and southern BMCC. The Lolo Hot Springs batholith intrudes lower- to middle-amphibolite facies metasedimentary rocks in the northwestern BMCC that are correlative to the Wallace Formation and the Ravalli Group (Figure 2). The Whistling Pig pluton intrudes main-phase granitoids of the southern Bitterroot batholith. The plutons are generally unfoliated, suggesting post-tectonic emplacement. Contacts with surrounding metasediments are sharp and characterized by chilled margins; in the Lolo Hot Springs batholith, these chilled margins are ~30 - 60 m-wide (Nold, 1974). Miarolitic cavities are abundant in both plutons and range from ~5 mm to 1 cm in size. They commonly contain euhedral crystals of smoky quartz, plagioclase, and K-feldspar (Figure 3). Minerals visible in outcrop are quartz, potassium feldspar, and plagioclase, with trace amounts of biotite. In thin section, quartz is the dominant mineral (~45%) followed by orthoclase perthite (35%), and plagioclase (15%). Biotite comprises ~3 - 5% of the rock and is often in association with an opaque phase that is most likely an Fe-oxide. Hydrothermal effects from these plutons extend ~2 km into host rocks and they demonstrate considerable evidence for retrograde alteration (Toth, 1987).

ANALYTICAL METHODS

U-Pb Analyses

U-Pb isotopic data were acquired in the radiogenic isotope lab at the Massachusetts Institute of Technology. Zircon and monazite were separated with the use of standard techniques of crushing, Wilfley table, magnetic separation, and heavy liquids. Zircon and monazite were selected on the basis of size, color, and lack of inclusions. Selected zircon was air-abraded (Krogh, 1982) to remove the outer portion of the grains which are prone to Pb-loss and acid-washed in warm 4N HNO_3 for 15 minutes before dissolution in HF + HNO_3. Monazites were rinsed in acetone prior to dissolution. The zircon and monazite were spiked with a mixed ^{205}U - ^{233}U - ^{235}U spike before dissolution in Teflon bombs at 220 °C and 240 °C, respectively, for 48 hours. Lead and uranium were separated using standard anion exchange chemistry. Total procedural blanks during the course of these analyses were 3.5 ± 2 pg for Pb and 1 ± 1 pg for U. Details of the mass spectrometry are presented in Bowring *et al* (1993) and in Table 2. Errors in the $^{206}Pb/^{238}U$, $^{207}Pb/^{235}U$, and $^{207}Pb/^{206}Pb$ were estimated using the method of (Ludwig, 1988), and all age uncertainties are quoted at the two sigma level (Table 2). Initial common Pb compositions for all samples were estimated using the method of Stacey and Kramers (1975) and the estimated age of the sample.

Argon Analyses

Pure mineral separates were obtained by standard magnetic and heavy - liquid methods. Following separation, hornblendes were subjected to an ultrasonic purifier in order to remove composite grains. Samples for furnace and laser analysis were selected from the 180-200 μm sieve fractions for most samples; B85 K-feldspar was hand-picked from the 250 μm fraction. The separates were washed in water, acetone, and ethanol prior to packaging in individual aluminum foil packets for neutron irradiation. Samples were irradiated in position 5C of the McMaster University reactor for 7 hours

with Cd shielding. Corrections for interfering reactions on Ca, K, and Cl were based on analyses of CaF_2, K_2SO_4, and KCl included in the irradiation package. Fast neutron flux was monitored by using MMhb-1 hornblende (520.4 Ma; Samson and Alexander, 1987) and Fish Canyon sanidine (27.8 Ma; Cebula *et al.*, 1986). Irradiated samples were analyzed at the Cambridge Laboratory for Argon Isotopic Research at MIT. Gas was extracted using either a double-vacuum resistance furnace or a 10 W Ar-ion laser, and analyzed using a MAP 215-50 mass spectrometer. Laser blanks were measured after alternate unknowns. During the course of these analyses, laser blanks for M/e 40 and 36 (moles) were 3×10^{-16} and 5×10^{-18}, respectively. Over the 800 - 1500 K range that includes most incremental heating analyses, M/e 40 and 36 blanks (moles) ranged from 5×10^{-14} and 2×10^{-17}, to 9×10^{-15} and 1×10^{-16}, respectively, for B85 K-feldspar. M/e 40 and 36 blanks for the remaining analyses ranged from 2×10^{-15} and 9×10^{-17} at 800 K to 7×10^{-15} and 3×10^{-18} at 1500 K. A more detailed discussion of laboratory procedures is presented in Hodges *et al.* (1994).

All measurements were corrected for system blanks, neutron-induced interferences, and mass fractionation prior to age calculations and statistical analysis. Apparent ages were calculated using an assumed initial $^{40}Ar/^{36}Ar$ ratio of 295.5 and decay constants recommended by Steiger and Jäger (1977). Age uncertainties (calculated by propagating errors in isotopic measurements, corrections, and J) are reported at the 2 σ confidence level (Table 3, Table 4). Nominal closure temperatures commonly applied to hornblende, muscovite, biotite, and K-feldspar were adopted for this study (800 ± 50, 650 ± 50, 620 ± 50 K, and 425 K, respectively; McDougall and Harrison, 1988).

Microprobe analyses for K-bearing minerals were obtained using the JEOL 733 electron microprobe at the Massachusetts Institute of Technology. Compositional data with nominal uncertainties are presented in Table 5.

GEOCHRONOLOGIC RESULTS

Skookum Butte stock and associated migmatite

Six multigrain fractions of zircon from the Skookum Butte stock (NB12-11) consisting of ~20 - 30 small euhedral zircons with no optical evidence for inherited cores were analyzed. Three fractions yield a poorly defined discordia with a lower-intercept of 47 ± 2 Ma (Figure 4a, Table 2). One fraction was nearly concordant, with a $^{206}Pb/^{238}U$ age of 47.7 Ma and a $^{207}Pb/^{206}Pb$ age of 57.8 Ma. The upper-intercept of this chord is 1570 Ma, consistent with an inherited component of Belt Supergroup age.

EM20 is from the migmatite that is marginal to the Skookum Butte stock. Two single monazite crystals from this migmatite were analyzed. Both fractions are reversely discordant, yielding $^{207}Pb/^{235}U$ ages that are lower than those indicated by $^{206}Pb/^{238}U$ (Figure 4b, Table 2). Reversed discordance in monazite is not unusual and is caused by Th-disequilibrium which is apparent in monazite because of its high Th/U ratio (Schärer, 1984; Parrish, 1990). This is particularly problematic in young monazites (< 200 Ma), therefore the $^{207}Pb/^{235}U$ is considered the best estimate for the crystallization age. The least-discordant fraction yields a $^{207}Pb/^{235}U$ age of 55.8 ± 0.1 Ma, suggesting crystallization of the migmatite at this time.

Furnace step-heating of biotite (Mg/(Mg + Fe) = 0.420) from the Skookum Butte stock (NB12-11) resulted in a plateau age of 50.6 ± 0.3 Ma, corresponding to 100% of the gas released (Figure 4c). Most of the $^{39}Ar_K$ was released in the 1350 K step, which yielded a model age of 50.3 ± 1.0 Ma (Table 4.1). Examination of the data using an inverse isotope correlation diagram (Roddick, 1988) reveals a linear array (Figure 4d). Regression analysis including all of the increments yields an age of 50.2 ± 1.0 Ma with a near-atmospheric initial $^{40}Ar/^{36}Ar$ value of 320 ± 50. The mean-squared weighted deviation (MSWD) of this fit is 1.2, very close to the expected value of 1 (Wendt and Carl, 1991). However, the data are highly radiogenic and tend to cluster

near the x-axis. One exception, corresponding to the 900 K increment, appears to control the isochron. To test the extent to which the least radiogenic increment (900 K) controlled the fit, we regressed all the data except this increment. The resulting age (50.1 ± 1.0 Ma) and initial $^{40}Ar/^{36}Ar$ (330 ± 70) are within uncertainty of the results of the regression using all points, suggesting that the isochron is not controlled by the 900 K increment. The isochron age is statistically indistinguishable from the plateau age, suggesting that the cooling age for this biotite is 50.2 ± 1.0 Ma

K-feldspar obtained from the Skookum Butte stock is a K-Na binary solid solution with $X_{Or} = 0.904$ (Table 5.4). The release spectrum for this sample is characterized by two apparent plateaus, with model ages increasing with higher temperature (Figure 4e, Table 4.2). Increments 750 K- 1150 K have model ages of 50.5-52.6 Ma over 40% of the total $^{39}Ar_K$ and the remaining release steps yield higher model ages of 55.1 - 59.5 Ma. The apparent high-temperature and low-temperature plateaus suggest the presence of two distinct diffusion domains in the sample (Lovera *et al.*, 1991). Because the $^{40}Ar/^{39}Ar$ closure temperatures for the least retentive domains in K-feldspars are generally lower than the closure temperature for biotite, we would expect model ages for the low-temperature domain to be younger than the biotite age. This is not the case for this sample; the model ages for both plateaus are higher than the cooling age for biotite from the same sample suggesting that the domains have unusually high closure temperatures (greater than that of biotite) or that ^{40}Ar excess may be trapped in retentive diffusion sites in both domains (Foster *et al.*, 1990).

When plotted in an isotope correlation diagram, the high-temperature increments define a linear array that is distinctive from that defined by the low-temperature increments (Figure 4f). Linear regression of the two arrays results in slightly different intercept ages (52.4 ± 2.0 Ma and 55.9 ± 2.8 Ma, respectively) and very different initial argon compositions. The low-temperature segment defines a mixing line between a radiogenic component and a non-radiogenic component that is

indistinguishable from modern atmosphere. The high-temperature increments yield a more complex mixing line between a dominantly radiogenic component and a trapped component with excess ^{40}Ar. The isochron age of the low-temperature steps is slightly higher but within 2σ uncertainty of the biotite cooling age.

Lolo Hot Springs batholith

Multiple morphologically and chemically distinct populations of zircons were identified in the Lolo Hot Springs batholith (NB11-1, Figure 5). One population consists of small, elongate, euhedral zircons that are clear and demonstrate no evidence for inherited cores (Figure 5a). These zircons occur as inclusions in biotite aggregates and are surrounded by a wide halo of radiation-damage to the biotite. Five multigrain fractions of this population, each consisting of 20 - 40 grains, were analyzed (Figure 6, Table 2). One fraction is concordant, with $^{206}Pb/^{238}U$ age of 48.7 ± 0.3 Ma. The remainder of the fractions have a considerable inherited component despite the apparent absence of visible cores. All five fractions form a poorly defined discordia with an upper-intercept of 1500 ± 300 Ma and a lower-intercept of 48 ± 6 Ma, consistent with mixing between an inherited Proterozoic (Belt Supergroup?) component and a younger magmatic component of Eocene age.

A second zircon population from the Lolo Hot Springs batholith consists of euhedral bipyramidal zircons that are extremely metamict (Figure 5a, b) and tend to occur in more magnetic fractions. These zircons are readily apparent in thin section as euhedral grains occurring in fractures and at grain boundaries, as well as adjacent to biotite clusters (Figure 5b). This population is characterized by extremely high U-concentrations ranging from 3250 - 34913 ppm, compared to values of 303 - 773 ppm for the first population (Table 2). The high U-content is most likely the cause of the metamict nature of the zircons and is a characteristic of hydrothermal zircons. Multigrain fractions consisting of 4 - 20 grains were analyzed. One fraction is

concordant with an age of 40.2 ± 0.2 Ma. The remaining fractions are nearly concordant, with $^{206}Pb/^{238}U$ ages of ~ 34 - 44 Ma (Figure 6). The nine fractions define a linear array subparallel to concordia.

Whistling Pig pluton

Zircon, hornblende, biotite, and K-feldspar were obtained from the Whistling Pig pluton (B85) for U-Pb and $^{40}Ar/^{39}Ar$ analysis. Amphibole is classified as "ferro-edenitic hornblende" (Leake, 1978) and biotite is very Fe-rich (Mg/(Mg+Fe) = 0.09). K-feldspar is a binary K-Na solution with $X_{Or} = 0.894$.

One multi-grain fraction of clear, euhedral zircons was analyzed from the Whistling Pig pluton. This fraction is nearly concordant, with a $^{206}Pb/^{238}U$ age of 48.8 Ma and a $^{207}Pb/^{235}U$ age of 48.9 Ma (Figure 7a).

Results of six hornblende laser-fusion analyses are shown on Figure 7b. Individual ages range from 46.0 - 56.2 Ma with a mean model age of 50.7 ± 7.5 Ma (Table 4.3). An isochron consisting of all of the points yields an intercept age of 48.3 ± 6.2 Ma and a near-atmospheric initial $^{40}Ar/^{36}Ar$ value of 330 ± 110.

Laser step-heating of biotite from the Whistling Pig pluton resulted in a slightly convex-upward release spectrum with no plateau (Figure 7c). Model ages ranged from 42.6 - 50.9 Ma (Table 4.4). When the step-heating data are plotted on an isotope correlation diagram with results of two laser-fusion analyses (Table 4.5), the data define a linear array corresponding to an intercept age of 48.6 ± 0.8 Ma and an unusually low initial $^{40}Ar/^{36}Ar$ value of 230 ± 60 (Figure 7d).

Furnace step-heating of K-feldspar from sample B85 yielded a flat release spectrum with only one apparent domain (Figure 7e, Table 4.6). Ten of the twenty increments, consisting of 64% of the total $^{39}Ar_K$, define a plateau age of 47.6 ± 0.3 Ma. When plotted on an inverse-isotope correlation diagram, the data define a single linear array (Figure 7f). Regression of increments 11-20 resulted in an intercept age of 47.8

± 0.6 Ma and an initial $^{40}Ar/^{36}Ar$ value (300 ± 30) that is close to present-day atmosphere.

Country rocks of the northwestern BMCC - Spruce Creek mylonite zone

A suite of samples collected for $^{40}Ar/^{39}Ar$ analysis from the country rocks south of the Skookum Butte stock are part of the Spruce Creek mylonite zone, with the exception of EM3b. Samples EM3b, EM3c, and EM3d are a suite of samples from the same outcrop, whereas EM6 is from ~1 km to the north, near the Skookum Butte stock.

EM3b pegmatite

Muscovite and K-feldspar were obtained from an undeformed granite pegmatite that cross-cuts the Spruce creek mylonite zone. This sample is dominantly quartz, plagioclase, and K-feldspar, with lesser amounts of muscovite. Muscovite shows little deviation from end-member muscovite, with $(Fe_{TOTAL} + Mg)/Al^{VI} = 0.18$, $Si^{IV}/(Si^{IV}+Al^{IV}) = 0.79$, and Na/(Na+K) = .0.006 (Table 5.2). K-feldspar is essentially a binary K-Na solid solution, with $X_{Or} = 0.882$ (Table 5.4).

The release spectrum for muscovite is relatively flat and eight of the ten increments yielded model ages of 48.9 - 49.7 Ma (Figure 8a, Table 4.7). The 1200 K-1350 K increments, corresponding to 56% of the total $^{39}Ar_K$, define a plateau age of 49.4 ± 0.6 Ma. The data define a linear array on the inverse isotope correlation diagram; regression of all of the increments yields an intercept age of 48.7 ± 0.6 Ma with a value for $(^{40}Ar/^{36}Ar)_o$ of 360 ± 50 (Figure 8b).

The K-feldspar release spectrum for this sample is characterized by two apparent plateaus (Figure 8c). The first increment at 725 K, yields an abnormally high model age of 79.1 Ma. This feature is probably due to excess ^{40}Ar contamination concentrated in weakly retentive cation sites or fluid inclusions (McDougall and Harrison, 1988). Increments 750 K - 1000 K define the first plateau, with model ages ranging from 48.5 - 52.8 Ma (Table 4.8). Later, high-temperature increments yield

model ages of 53 - 61.6 Ma. As illustrated by the NB12-11 K-feldspar, the data are suggestive of three-component mixing (Figure 8d). Linear regression of the two arrays results in similar intercept ages and very different initial argon values: 53.3 ± 1.0 Ma and 330 ± 10 for the low-temperature array; 53.5 ± 1.1 Ma and 720 ± 80 Ma for the high-temperature array. The low-temperature array defines a mixing line between a radiogenic component and a component that is statistically indistinguishable from modern atmosphere, whereas the high-temperature array demonstrates mixing between a radiogenic component and an excess ^{40}Ar component. Because the extent to which this excess argon component effects the low-temperature points cannot be determined with certainty, isochron ages must be considered overestimates of the cooling age. A more likely maximum age for the sample can be determined on the basis of linear regression of the points defining the upper-limit of the field of data. The 900 K increment, the most radiogenic point with the highest $^{39}Ar/^{40}Ar$ ratio, yields a model age of 47.8 Ma when forced through the modern atmospheric $^{40}Ar/^{36}Ar$ value. This maximum age is consistent with the muscovite age and suggests that this sample cooled through K-feldspar closure at ~47.8 Ma.

EM3c granite

Sample EM3c is from a deformed granitic layer that is concordant with the Spruce Creek mylonite. Quartz and plagioclase feldspar are the most abundant constituents (50% and 30%, respectively), and biotite makes up the rest (~20%). Biotite (Mg/(Mg + Fe) = 0.391) was separated for $^{40}Ar/^{39}Ar$ analysis (Table 5.3). The release spectrum is relatively well-behaved, and all ten increments define a plateau age of 49.9 ± 0.3 Ma (Figure 9a, Table 4.9). When examined on an inverse isotope correlation diagram, the data define a linear array with an intercept age of 49.3 ± 1.0 Ma and a near-atmospheric initial value of 300 ± 20 (Figure 9b). These data suggest cooling through biotite closure at 49.3 ± 1.0 Ma.

EM3d diorite boudin

EM3d is a diorite boudin from within the quartzite gneiss layer in the Spruce Creek mylonite. Major phases in this sample are plagioclase (40%), quartz (25%), biotite (15%), and hornblende (10%). Microprobe analysis demonstrates that amphibole from this sample is "ferropargasite" (Leake, 1978) and biotite is Mg-rich (Mg/(Mg + Fe) = 0.592) (Table 5.1, Table 5.3).

Incremental heating of hornblende from this sample yielded a relatively flat release spectrum with model ages generally falling between 67 - 74 Ma (Figure 10a). Most of the K-derived argon ($^{39}Ar_K$) was released over two steps corresponding to 1275 and 1300 K (Table 4.10). These steps have model ages of 69.3 and 69.1 Ma, respectively. There is minimal scatter in the data when plotted on an inverse isotope correlation diagram (Figure 10b). An isochron age of 55.6 ± 2.0 Ma based on eight of the ten increments is highly sensitive to outliers and provides no constraint on the initial argon composition (1780 ± 3200). An isochron age has little meaning for these highly clustered data; the low $^{36}Ar/^{40}Ar$ values and consistent $^{39}Ar/^{40}Ar$ values effectively pin the intercept age of the sample. Because the data provide no constraint on the magnitude of excess ^{40}Ar contamination, the intercept age is a maximum limit for the cooling age for this sample.

The biotite release spectrum for EM3d is flat; nine of the ten increments define a plateau age of 55.6 ± 0.9 Ma over 94% of the $^{39}Ar_K$.(Figure 10c, Table 4.11) On an inverse isotope correlation diagram the data cluster near the x-axis with the exception of the 900 K increment (Figure 10d). This step has a lower model age (51.4 Ma) than the rest of the steps and a has a low radiogenic component ($^{40}Ar^*$ = 60.1). An isochron including all of the points corresponds to an intercept age of 55.5 ± 2.1 Ma and has an upper-intercept indicating a near-atmospheric initial $^{40}Ar/^{36}Ar$ value of 270 ± 30. The 900 K increment controls the isochron and forces it through this initial value. Omitting the first point from the regression removes this effect and yields an intercept age of 53.8

± 2.0 Ma and an initial value (570 ± 400) that is much higher than present-day atmosphere and poorly constrained. Because the data cluster at one point there is little control on the composition of the non-radiogenic argon component, therefore the effects of excess argon on the apparent age are difficult to quantify. The intercept age calculated by omitting the 900 K increment is statistically indistinguishable from that obtained by regression of all of the points and is considered a maximum limit for the biotite cooling age of this sample.

EM6 amphibolite

Sample EM6 is an amphibolite pod that is within the quartzite and calc-silicate gneiss layer of the Spruce Creek mylonite. Relatively coarse-grained hornblende (~ 1 mm in length) classified as "edenitic hornblende" (Leake, 1978) parallels the foliation and comprises ~70% of the sample (Table 5.1). Fe-rich biotite is a minor component of the amphibolite (Table 5.3).

Hornblende step-heating yields model ages ranging from 67.3-60.1 Ma with the exception of the anomalously old first-increment (91.1 Ma; Figure 11a, Table 4.12). The 1100 K - 1240 K increments yield a plateau age of 65.0 ± 1.0 Ma over 75% of the $^{39}Ar_K$ released. On an inverse isotope correlation diagram, a regression excluding the 1000 K increment yields an isochron with an intercept age 62.7 ± 2.5 Ma and an initial value of 650 ± 400 (Figure 11b). The $^{39}Ar/^{40}Ar$ value corresponding to this apparent age (0.0412) is very close to that of hornblende EM3d from a diorite boudin in the same structural position, (0.0466). This isochron is pinned by a cluster of data points that provide little control on the actual $^{39}Ar/^{40}Ar$ intercept. Therefore, the similarity in intercept values suggests that, within the level of uncertainty of the data, the EM6 hornblende data are consistent with the 55.6 Ma hornblende isochron age from sample EM3d and that the calculated isochron age of this sample is a maximum limit for the cooling age.

As in the other samples, the release data for EM6 biotite define a flat spectrum with model ages ranging from 52.1 - 56.3 Ma (Figure 11c, Table 4.13). A plateau consisting of the 1000 K-1550 K increments consists of 82% of the $^{39}Ar_K$ released and corresponds to an apparent age of 55.0 ± 0.7 Ma (Figure 11d). The data define a linear array on the inverse isotope composition diagram with an intercept age of 54.2 ± 0.6 Ma and an initial $^{40}Ar/^{36}Ar$ value (320 ± 60) that is similar to present-day atmosphere. As in previous samples, biotite data all contain very low $^{36}Ar/^{40}Ar$ values and cluster near the $^{39}Ar/^{40}Ar$ axis, causing the initial $^{40}Ar/^{36}Ar$ value to be highly sensitive to outliers. Excluding the outlying 900 K increment from the regression yields an intercept age of 53.8 ± 2.0 Ma and an initial $^{40}Ar/^{36}Ar$ value of 570 ± 400. Without the 900 K increment, the isochron is pinned at $^{39}Ar/^{40}Ar$ values corresponding to 53.8 Ma but there is no control on the initial value. Therefore, the effects of any excess ^{40}Ar on the isochron age is not resolvable, and the intercept age should be considered a maximum estimate of the cooling age.

DISCUSSION

The U-Pb data from the Skookum Butte stock and the associated migmatite are inconsistent with published sphene fission track ages of 82 Ma (Ferguson, 1972), but are consistent with a growing number of published Eocene crystallization ages for the northern Bitterroot batholith (e.g., Bickford *et al.*, 1981; Chase *et al.*, 1983; Toth, 1987). The U-Pb zircon data can be interpreted to reflect the effects of three components: (1) an inherited 1570 Ma component; (2) a component related to the crystallization of the pluton; and (3) the effects of post-crystallization Pb-loss. The nearly concordant zircon crystallization age of 47.7 Ma is ~2 - 3 m.y. younger than K-feldspar and biotite cooling ages from this pluton, suggesting that the zircon data represent the effects of post-crystallization Pb-loss. Because of their resistance to Pb-loss, monazite crystallization ages from the migmatite associated with the Skookum

Butte stock represent the best estimate of the crystallization age of this granitoid (55.8 ± 0.1 Ma).

We interpret the Lolo Hot Springs U-Pb data to represent the effects of three distinct populations of zircons: (1) a primary magmatic population reflecting the Lolo Hot Springs batholith; (2) a magmatic population containing an inherited component with an isotopic signature indicating mixing between Proterozoic and Eocene components; and (3) a hydrothermal population indicative of post-crystallization hydrothermal activity. The primary magmatic zircons clearly indicate that the Lolo Hot Springs batholith crystallized at 48.7 ± 0.3 Ma and the mixing-line defined by the primary + inherited fractions is consistent with a 48.7 Ma lower-intercept. The hydrothermal zircon data represent zircon growth following crystallization of the Lolo Hot Springs batholith at 48.7 Ma.

Hornblende, biotite, and K-feldspar $^{40}Ar/^{39}Ar$ cooling ages from the Whistling Pig pluton in the southern BMCC are consistent with the nearly concordant $^{206}Pb/^{238}U$ age of 48.8 Ma. The data suggest that the Whistling Pig pluton cooled rapidly following crystallization at 48.8 Ma. The statistical agreement of the crystallization ages of these two epizonal plutons demonstrates that much of the Bitterroot batholith was at shallow levels by ~48.8 - 48.7 Ma. The data also indicate that ~12 - 18 km of unroofing occurred between crystallization of the Skookum Butte stock at 55.8 Ma and emplacement of epizonal granites at 48.8 - 48.7 Ma.

$^{40}Ar/^{39}Ar$ data from the northwestern BMCC record evidence for cooling beginning ~55.6 Ma, shortly after crystallization of the Skookum Butte stock. Hornblende $^{40}Ar/^{39}Ar$ cooling ages from the diorite boudin and amphibolite pod (EM3d and EM6) in the Spruce Creek mylonite are consistent with cooling through hornblende closure temperature (~800 K) at 55.6 Ma. Biotite and muscovite ages of 48.7 - 50.2 Ma are statistically indistinguishable and record continued cooling at the time of emplacement of the epizonal plutons. Biotites from the diorite and amphibolite

from the Spruce Creek mylonite yield anomalously old apparent ages that suggest that excess ^{40}Ar contamination is a factor in the shear zone. This shear zone may have acted as a channel for fluid migration during deformation and the excess ^{40}Ar component may have been introduced via fractures or dislocations developed in the minerals during shearing. Excess ^{40}Ar contamination is also a considerable problem in the K-feldspars, again resulting in anomalously old apparent ages. The excess component affecting the biotites and K-feldspars may have been introduced at low temperatures and may be related to fracturing and fluid migration during continued unroofing at lower temperatures and shallower depths.

The $^{40}Ar/^{39}Ar$ data from the northwestern BMCC are consistent with published data from the northeastern BMCC and range from older to younger cooling ages from west to east across the northern metamorphic core that may reflect progressive unroofing of the Bitterroot batholith (House and Hodges, 1994). Zircon crystallization ages for epizonal plutons demonstrate that much of the Bitterroot batholith, including the western BMCC, was at shallow levels by ~48.8 - 48.7 Ma, whereas mesozonal plutons crystallized in footwall rocks in the eastern BMCC as late as 48 Ma (Bickford *et al.*, 1981; Chase *et al.* 1983). The geochronologic data require that the eastern and western margins of the BMCC were at very different structural levels at 49 - 48 Ma, and can be explained in one of two ways. First, it is possible that the Bitterroot mylonite zone was not the only extensional structure effecting the BMCC. An earlier structure may have accommodated denudation of the western BMCC prior to development of the Bitterroot mylonite zone, and may have been subsequently eroded or tectonically excised by later extensional faulting.

CONCLUSIONS

U-Pb and $^{40}Ar/^{39}Ar$ data from post-tectonic epizonal plutonic rocks in the northwestern and southwestern BMCC demonstrate that much of the western Bitterroot

batholith was at shallow levels by ~49 - 48 Ma. U-Pb monazite crystallization ages for the mesozonal Skookum Butte stock suggest that at least 12 - 18 km of overburden was removed following crystallization of the granitoid at 55.8 Ma. $^{40}Ar/^{39}Ar$ cooling ages confirm that this unroofing event was associated with extension on the Bitterroot mylonite zone and suggest that this cooling event may have begun shortly after emplacement of the Skookum Butte stock, refining the upper limits on the age of extension in the Bitterroot mylonite zone. The date demonstrate that progressive unroofing of the BMCC was accompanied by a considerable component of rotation about a north-south axis, resulting in emplacement of epizonal plutons in the western Bitterroot batholith, while the eastern limits of the batholith remained at mesozonal levels.

REFERENCES

Armstrong, R. L., 1975, Precambrian (1500 m.y. old) rocks of central Idaho-The Salmon River arch and its role in Cordilleran sedimentation and tectonics: American Journal of Science, v. 275-A, p. 437-467.

Armstrong, R. L., 1976, The geochronometry of Idaho: Isochron/West, v. 15, p. 1-33.

Armstrong, R. L., Taubeneck, W. H., and Hales, P. O., 1977, Rb-Sr and K-Ar geochronometry of Mesozoic granitic rocks and their Sr isotopic composition, Oregon, Washington, and Idaho: Geological Society of America Bulletin, v. 88, p. 397-411.

Bickford, M. E., Chase, R. B., Nelson, B. K., Schuster, R. D., and Arruda, E. C., 1981, U-Pb studies of zircon cores and overgrowths, and monazite: Implications for age and petrogenesis of the northeastern Idaho batholith: Journal of Geology, v. 89, p. 433-457.

Bowring, S. A., Grotzinger, J. P., Isachsen, C. E., Knoll, A. H., Pelechaty, S. M., and Kolosov, P., 1993, Calibrating rates of early Cambrian evolution: Science, v. 261, p. 1293-1298.

Cebula, G. T., Kunk, M. J., Mehnert, H. H., Naeser, C. W., Obradovich, J. D., and Sutter, J. F., 1986, The Fish Canyon Tuff, a potential standard for the 40Ar-39Ar and fission-track methods: Terra Cognita, v. 6, p. 139-140.

Chase, R. B., 1973, Petrology of the northeastern border zone of the Idaho batholith, Bitterroot Range, Montana: Montana Bureau of Mines and Geology Memoir, v. 43, p. 1-28.

Chase, R. B., Bickford, M. E., and Arruda, E. C., 1983, Tectonic implications of Tertiary intrusion and shearing within the Bitterroot dome, northeastern Idaho batholith: Journal of Geology, v. 91, p. 462-470.

Chase, R. B., Bickford, M. E., and Tripp, S. E., 1978, Rb-Sr and U-Pb isotopic studies of the northeastern Idaho Batholith and border zone: Geological Society of America Bulletin, v. 89, p. 1325-1334.

Ferguson, J. A., 1972, Fission track and K-Ar dates on the northeastern border zone of the Idaho batholith [M.S.]: University of Montana.

Foster, D. A., Harrison, T. M., Copeland, P., and Heizler, M. T., 1990, Effects of excess Ar on K-feldspar age spectra in the presence of large diffusion domains and plagioclase inclusions: Geochimica et Cosmochimica Acta, v. 54, p. 1699-1708.

Garmezy, L., 1983, Geology and geochronology of the southeast border of the Bitterroot dome: Implications for the structural evolution of the mylonitic carapace [Ph.D.]: The Pennsylvania State University.

Hodges, K. V. and Applegate, J. D. R. A., 1993, Age of Tertiary extension in the Bitterroot metamorphic core complex, Montana and Idaho: Geology, v. 21, p. 161-164.

Hodges, K. V., Hames, W. E., Olszewski, W. J., Burchfiel, B. C., Royden, L. H., and Chen, Z., 1994, Thermobarometric and $^{40}Ar/^{39}Ar$ geochronologic constraints on Eohimalayan metamorphism in southern Tibet: Contributions to Mineralogy and Petrology, v.117, p. 151-163.

House, M. A. and Hodges, K. V., 1994, Limits on the tectonic significance of rapid cooling events in extensional setting: Insights from the Bitterroot metamorphic core complex, Idaho-Montana: Geology, v. 22, p. 1007-1010.

House, M. A., Isachsen, C. E., Hodges, K. V., and Bowring, S. A., 1993, Geochronologic evidence for a complex, post-extensional thermal structure in the Bitterroot dome metamorphic core complex, MT: Geological Society of America Abstracts with Programs, v. 25, p. A411.

Hyndman, D. W., 1980, Bitterroot dome - Sapphire tectonic block, an example of a plutonic-core gneiss-dome complex with its detached suprastructure, *in* Crittenden, M. D., Coney, P. J., and Davis, G. H., ed., Cordilleran Metamorphic Core Complexes: Boulder, CO, Geological Society of America Memoir 153, p. 427-443.

Hyndman, D. W., 1981, Controls on source and depth of emplacement of granitic magma: Geology, v. 9, p. 244-249.

Hyndman, D. W., Alt, D., and Sears, J. W., 1988, Post-Archean metamorphic and tectonic evolution of western Montana and northern Idaho, *in* Ernst, W. G., ed., Metamorphism and Crustal Evolution of the Western United States: Englewood Cliffs, NJ, Prentice Hall, p. 332-361.

Krogh, T. E., 1982, Improved accuracy of U-Pb ages by the creation of more concordant systems using an air abrasion technique: Geochimica et Cosmochimica Acta, v. 46, p. 637-649.

Leake, B. E., 1978, Nomenclature of amphiboles: American Mineralogist, v. 63, p. 1023-1052.

Lovera, O. M., Richter, F. M., and Harrison, T. M., 1991, Diffusion domains determined by ^{39}Ar released during step heating: Journal of Geophysical Research, v. 96, p. 2057-2069.

Ludwig, K. R., 1988, ISOPLOT for MS-DOS: a plotting and regression program for radiogenic-isotope data, for IBM-PC compatible computers: U.S. Geological Survey Open File Report 88-557.

McDougall, I. and Harrison, T. M., 1988, Geochronology and Thermochronology by the $^{40}Ar/^{39}Ar$ Method: New York, Oxford University Press, 212 p.

McDowell, F. W. and Kulp, J. L., 1969, Potassium-Argon dating of the Idaho batholith: Geological Society of America Bulletin, v. 80, p. 2379-2382.

Nold, J. L., 1974, Geology of the northeastern border zone of the Idaho batholith, Montana and Idaho: Northwest Geology, v. 3, p. 47-52.

Parrish, R., 1990, U-Pb dating of monazite and its application to geological problems: Canadian Journal of Earth Sciences, v. 27, p. 1431-1450.

Rehn, W. and Lund, K., 1981, Eocene extensional plutonism in the Idaho batholith region: Geological Society of America Abstracts with Programs., v. 13, p. 536.

Roddick, J. C., 1988, The assessment of errors on $^{40}Ar/^{39}Ar$ dating: Geologic Survey of Canada Paper 88-2, p. 3-8.

Samson, S. D. and Alexander, E. C., 1987, Calibration of the interlaboratory $^{40}Ar/^{39}Ar$ dating standard, MMhb-1: Chemical Geology, v. 66, p. 27-34.

Schärer, U., 1984, The effect of initial ^{230}Th disequilibrium on young U-Pb ages: the Makalu case, Himalaya: Earth and Planetary Science Letters, v. 67, p. 191-204.

Spear, F. S., 1993, Metamorphic phase equilibria and pressure-temperature-time paths: Washington, D.C., Mineralogical Society of America, 799 p.

Stacey, J. S. and Kramers, J. D., 1975, Approximation of terrestrial isotope evolution by a two-stage model: Earth and Planetary Science Letters, v. 26, p. 207-221.

Steiger, R. H. and Jäger, E., 1977, Subcommission on geochronology: convention on the use of decay constants in geo- and cosmochronology: Earth and Planetary Science Letters, v. 36, p. 359-362.

Toth, M. I., 1987, Petrology and Origin of the Bitterroot Lobe of the Idaho batholith: U.S. Geologic Survey Professional Paper, v. 1436, p. 9-37.

Wehrenberg, J. P., 1972, Geology of the Lolo Peak area, northern Bitterroot Range, Montana: Northwest Geology, v. 1, p. 25-32.

Wendt, I. and Carl, C., 1991, The statistical distribution of the mean squared weighted deviation: Chemical Geology, v. 86, p. 275-285.

Table 1. Sample Locations

Sample	Latitude	Longitude
NB12-11	46° 36' 52"	114° 24' 33"
NB11-1	46° 40' 40"	114° 34' 25"
EM3	46° 36' 07"	114° 23' 22"
EM6	46° 36' 55"	114° 23' 38"
EM20	46° 37' 05"	114° 23' 47"
B85	46° 07' 30"	114° 55' 55"

Table 2. U-Pb Analytical Data and Results

Fractions	Weight	Concentrations		Atomic ratios								Ages (Ma)				
		U	Pb^*	$^{206}Pb/^{204}Pb$†	$^{208}Pb^*/^{206}Pb$	$^{206}Pb^‡/^{238}U$	% err	$^{207}Pb^‡/^{235}U$	% err	$^{207}Pb^‡/^{206}Pb$	% err	$^{206}Pb/^{238}U$	$^{207}Pb/^{235}U$	$^{207}Pb/^{206}Pb$	corr. coef.	Pb (pg)
Migmatite (EM20)																
m(10)+100	0.015	5530.8	206.1	519	3.881	0.00874	(0.15)	0.05645	(0.50)	0.046871	(0.45)	56.1	55.8	42.7	0.487	96
m(10)+100	0.015	15777.1	636.9	862	4.271	0.00877	(0.16)	0.05639	(0.38)	0.046651	(0.32)	56.3	55.7	31.4	0.531	160
Skookum Butte stock (NB12-11)																
nm(-3)+200	0.071	488.2	4.6	2004	0.131	0.00931	(0.11)	0.07406	(0.17)	0.05772	(0.13)	59.7	72.5	519.2	0.665	14
nm(-3)+200	0.024	2225.7	20.8	1243	0.126	0.00918	(0.07)	0.07171	(0.15)	0.05663	(0.13)	58.9	70.3	477.2	0.477	29
nm(-3)+200	0.118	984.9	9.0	5491	0.108	0.00916	(0.41)	0.07163	(0.53)	0.05671	(0.33)	58.8	70.2	480.2	0.776	16
nm(-3)+200	0.069	1577.5	11.7	1963	0.225	0.00673	(0.10)	0.05605	(0.14)	0.06038	(0.09)	43.3	55.4	617.1	0.742	27
nm(-3)+200	0.029	3870.6	28.8	1952	0.225	0.00673	(0.10)	0.05602	(0.14)	0.06036	(0.09)	43.2	55.3	616.4	0.741	28
nm(-3)+200	0.030	1073.9	7.8	3374	0.088	0.00744	(0.15)	0 04839	(0.26)	0.04717	(0.21)	47.8	48.0	57.8	0.601	8
Lolo Hot Springs batholith (NB11-1)																
nm(-3)+200	0.054	356.4	4.8	513	0.147	0.01283	(0.12)	0.11967	(0.30)	0.06763	(0.28)	82.2	114.8	857.2	0.387	35
nm(-3)+200	0.048	642.7	6.1	321	0.129	0.00934	(0.23)	0.07557	(0.57)	0.05871	(0.53)	59.9	74.0	556.3	0.401	64
nm(-3)+200	0.031	773.1	6.9	683	0.137	0.00870	(0.26)	0.06362	(0.38)	0.05303	(0.28)	55.9	62.6	330.2	0.686	24
nm(-3)+200	0.054	303.9	2.7	384	0.142	0.00855	(0.37)	0.06352	(0.63)	0.05385	(0.51)	54.9	62.5	365.2	0.602	28
nm(-3)+200	0.044	306.0	2.4	97	0.154	0.00759	(0.50)	0.04909	(2.71)	0.04693	(2.66)	48.7	48.7	45.5	0.189	86
m(6)+200	0.005	24235.4	175.5	120	0.186	0.00682	(0.24)	0.04497	(1.66)	0.04781	(1.66)	43.8	44.7	89.9	0.072	521
m(6)+200	0.006	32228.2	206.9	109	0.118	0.00640	(0.24)	0.04296	(1.82)	0.04869	(1.83)	41.1	42.7	133.0	0.049	880
m(6)+200	0.005	15051.4	102.6	159	0.196	0.00637	(0.20)	0.04239	(1.23)	0.04829	(1.22)	40.9	42.2	114.0	0.114	221
m(6)+200	0.021	34912.8	226.9	62	0.161	0.00625	(0.40)	0.04055	(3.75)	0.04702	(3.76)	40.2	40.4	50.3	0.022	6238
m(6)+200	0.030	12178.1	75.2	232	0.140	0.00604	(0.17)	0.03992	(0.80)	0.04791	(0.79)	38.8	39.7	94.9	0.160	653
m(6)+200	0.047	11770.7	71.8	115	0.174	0.00580	(0.35)	0.03817	(1.76)	0.04769	(1.74)	37.3	38.0	84.0	0.147	2144
m(6)+200	0.044	3442.9	19.8	40	0.135	0.00565	(0.90)	0.03680	(8.05)	0.04722	(8.08)	36.3	36.7	60.4	0.015	2616
m(6)+200	0.041	20187.3	110.4	80	0.139	0.00535	(0.57)	0.03607	(2.69)	0.04887	(2.67)	34.4	36.0	141.8	0.156	4655
m(6)+200	0.054	3250.5	48.7	312	0.164	0.01438	(1.67)	0.09439	(1.78)	0.04762	(0.60)	92.0	91.6	80.2	0.941	551
Whistling Pig pluton (B85)																
nm(-3)+200	0.0100	4193.6	32.2	3067	0.128	0.00760	(0.11)	0.04936	(0.15)	0.04712	(0.10)	48.8	48.9	55.2	0.739	9.7

*Radiogenic Pb. †Measured ratio corrected for fractionation only. Mass fractionation correction of 0.12 ± 0.8%/amu was applied to all Pb analyses. ‡Corrected for fractionation, spike, blank, and initial common Pb. Zircon and monazite fractions are designated as nonmagnetic (nm) and magnetic (m) in terms of degrees tilt on a Frantz magnetic separator, and as +200 or +100 in standard mesh size. Decay constants used are $^{238}U = 0.15513 \times 10^{-9}$ yr^{-1}, and $^{235}U = 0.98485 \times 10^{-9}$ yr^{-1} (Steiger and Jäger, 1977). Common Pb corrections were estimated using the method of Stacey and Kramers (1975). Data reduction and error analysis was accomplished using the algorithms of Ludwig (1988) and all errors are reported in percent at the 2σ confidence interval.

Table 3. Argon Summary

Sample	Rock Type	Mineral	Extraction Method	Plateau Age (Ma)	$^{39}Ar_p$(%)	Isochron Age (Ma)	$^{39}Ar_i$ (%)	Fit	$(^{40}Ar/^{36}Ar)_o$	MSWD
NB12-11	granite	Bt	Furnace	50.6 ± 0.3	100	**50.2 ± 1.0**	100	II	320 ± 50	1.2
NB12-11		Kfs	Furnace	-	-	**52.4± 2.0**	40	II	290 ± 20	2.4
EM3b		Ms	Furnace	49.4 ± 0.6	56	**48.7± 0.6**	100	I	360 ± 50	-
EM3b	pegmatite	Kfs	Furnace	-	-	**53.3 ± 1.0**	25	II	330 ± 10	2.3
EM3c	granite	Bt	Furnace	49.4 ± 0.3	100	**49.3 ± 1.0**	100	II	300 ± 20	0.4
EM3d		Hb	Furnace	-	-	**55.6 ± 2.1**	93	II	1780 ± 3200	1.9
EM3d	diorite	Bt	Furnace	55.6 ± 0.9	94	**53.8 ± 2.0**	94	II	570 ± 400	0.9
EM6		Hb	Furnace	65.0 ± 1.0	75	**62.7± 2.4**	99	II	650 ± 400	0.9
EM6	amphibolite	Bt	Furnace	55.0 ± 0.7	82	**54.2 ± 0.6**	100	I	320 ± 60	-
B85	granite	Hb	Laser	-	-	**48.3± 6.2**	-	I	330 ± 100	-
B85		Bt	Laser			**48.6 ± 0.8**	100	I	230 ± 60	-
B85		Kfs	Furnace	47.6 ± 0.3	64	**47.8 ± 0.6**	90	II	300 ± 30	0.8

For each sample, our interpretation of the best apparent age is shown in bold face. Entries in the "Plateau Age" column were calculated following the method outlined by McDougall and Harrison (1988), and the percentage of the total ^{39}Ar in the smaple that was released in the heating steps included in the plateau are shown in the column labelled"$^{39}Ar_p$". Isochron ages were calculated using fitting algorithms designated in the "Fit" column: I---least-squares linear regression (York, 1966); II--- least-squares linear regression with correlated errors (York, 1969). The column "$^{39}Ar_i$" shows the percentage of total ^{39}Ar in the heating steps used for the regression. The MSWD (mean spared weighted deviation) is shown for Fit II regressions only. All uncertainties are quoted at the 2σ confidence level.

Table 4.1 $^{40}Ar/^{39}Ar$ Furnace Analytical Data for NB12-11 biotite

T(K)	$^{39}Ar/^{40}Ar$	$^{36}Ar/^{40}Ar$	$^{39}Ar(\%)$	$^{40}Ar^{*}(\%)$	K/Ca	Age ($\pm 2\sigma$)
900	0.1093	0.0006	2.9	81.5	98.17	50.4 ± 1.0
950	0.1229	0.0003	9.5	91.5	99.56	50.3 ± 1.0
1000	0.1278	0.0002	17.6	93.7	190.89	49.6 ± 1.0
1050	0.1271	0.0001	24.4	95.8	507.01	50.9 ± 1.0
1100	0.1275	0.0002	29.7	94.4	116.48	50.1 ± 1.0
1150	0.1252	0.0002	34.1	95.4	95.41	51.5 ± 1.0
1200	0.1251	0.0002	39.4	95.3	61.71	51.5 ± 1.0
1250	0.1293	0.0001	51.5	96.9	90.83	50.6 ± 1.0
1350	0.1316	0.0001	90.3	97.9	48.57	50.3 ± 1.0
1550	0.1232	0.0003	100.0	92.2	6.30	50.6 ± 1.0

J value: 0.0038 ± 0.000076. All steps of 5 minutes duration. All steps used in regression. $^{40}Ar^{*}(\%)$—percentage of measured ^{40}Ar derived from natural decay of ^{40}K.

Table 4.2 $^{40}Ar/^{39}Ar$ Furnace Analytical Data for NB12-11 K-feldspar

T(K)	$^{39}Ar/^{40}Ar$	$^{36}Ar/^{40}Ar$	$^{39}Ar(\%)$	$^{40}Ar^{*}(\%)$	K/Ca	Age ($\pm 2\sigma$)
750+	0.0481	0.0002	1.0	93.6	53.49	50.5 ± 1.9
775+	0.0375	0.0008	2.7	75.2	3054.41	52.0 ± 2.0
800+	0.0446	0.0003	4.6	89.8	1426.82	52.3 ± 2.0
825+	0.0492	0.0001	7.0	98.5	1555.40	52.0 ± 2.0
850+	0.0494	0.0001	9.7	97.9	147.22	51.5 ± 1.9
875+	0.0494	0.0001	12.7	98.1	444.19	51.6 ± 1.9
900+	0.0494	0.0001	15.8	98.3	102.31	51.7 ± 2.0
950+	0.0492	0.0001	20.6	98.4	161.28	52.0 ± 2.0
1000+	0.0496	0.0001	26.0	97.8	129.18	51.1 ± 1.9
1050+	0.0494	0.0001	31.1	99.3	0.00	52.2 ± 2.0
1100+	0.0493	0.0001	35.6	99.9	426.96	52.6 ± 2.0
1150+	0.0485	0.0001	40.2	97.8	209.52	52.3 ± 2.0
1200	0.0459	0.0001	56.6	97.6	256.43	55.1 ± 2.1
1250	0.0447	0.0001	58.3	99.5	569.63	57.7 ± 2.2
1300	0.0426	0.0001	62.8	96.0	103.95	58.4 ± 2.2
1350	0.0419	0.0001	76.5	96.3	616.32	59.5 ± 2.2
1550	0.0413	0.0002	100.0	94.8	407.58	59.4 ± 2.2

J value: 0.00146 ± 0.000056. All steps of 10 minutes duration. Steps used in low-temperature regression indicated by (+). $^{40}Ar^{*}(\%)$—percentage of measured ^{40}Ar derived from natural decay of ^{40}K.

Table 4.3 $^{40}Ar/^{39}Ar$ Laser Fusion Analytical Data for B85 hornblende

Subsample	$^{39}Ar/^{40}Ar$	$^{36}Ar/^{40}Ar$	$^{39}Ar_K$	$^{40}Ar^*(\%)$	K/Ca	Age ($\pm 2\sigma$)
1	0.0397	0.0007	14.5	78.7	0.04	56.2 ± 3.4
2	0.0248	0.0020	23.2	40.1	0.02	46.0 ± 2.8
3	0.0448	0.0005	49.5	84.2	0.08	53.3 ± 3.3
4	0.0365	0.0011	64.6	66.3	0.04	51.6 ± 3.1
5	0.0566	0.0004	86.9	87.0	0.11	43.7 ± 2.7
6	0.0335	0.0014	100.0	57.4	0.04	48.7 ± 3.0

J value: 0.00159551, 0.000098. All subsamples used in regression. $^{39}Ar_K$—moles of irradiation-produced ^{39}Ar released during laser fusion. $^{40}Ar^*(\%)$—percentage of measured ^{40}Ar derived from natural decay of ^{40}K.

Table 4.4 $^{40}Ar/^{39}Ar$ Laser Step-Heating Analytical Data for B85 biotite

Increment (Amperes)	$^{39}Ar/^{40}Ar$	$^{36}Ar/^{40}Ar$	$^{39}Ar(\%)$	$^{40}Ar^*(\%)$	K/Ca	Age ($\pm 2\sigma$)
11.5	0.0393	0.0014	4.9	58.9	1.28	42.6 ± 0.8
12.5	0.0513	0.0006	11.9	83.6	3.58	46.3 ± 0.9
13	0.0567	0.0002	19.9	93.1	5.30	46.7 ± 0.9
13.5	0.0503	0.0005	29.0	85.4	3.53	48.2 ± 1.0
14	0.0557	0.0001	41.1	95.8	3.32	48.9 ± 1.0
14.5	0.0557	0.0000	50.2	98.8	13.53	50.3 ± 1.0
15	0.0551	0.0000	59.9	98.8	37.68	50.9 ± 1.0
17	0.0563	0.0001	81.6	96.9	106.03	48.9 ± 1.0

J value: 0.00159551, 0.000098. All steps used in regression. $^{40}Ar^*(\%)$—percentage of measured ^{40}Ar derived from natural decay of ^{40}K.

Table 4.5 $^{40}Ar/^{39}Ar$ Laser Fusion Analytical Data for B85 biotite

Subsample	$^{39}Ar/^{40}Ar$	$^{36}Ar/^{40}Ar$	$^{39}Ar_K$	$^{40}Ar^*(\%)$	K/Ca	Age ($\pm 2\sigma$)
18	0.0547	0.0002	90.1	92.9	43.48	48.2 ± 1.0
20	0.0518	0.0006	100.0	83.1	9.05	45.6 ± 0.9

J value: 0.00159551, 0.000098. All subsamples used in regression. $^{39}Ar_K$—moles of irradiation-produced ^{39}Ar released during laser fusion. $^{40}Ar^*(\%)$—percentage of measured ^{40}Ar derived from natural decay of ^{40}K.

Table 4.6 $^{40}Ar/^{39}Ar$ Furnace Analytical Data for B85 K-feldspar

T(K)	$^{39}Ar/^{40}Ar$	$^{36}Ar/^{40}Ar$	$^{39}Ar(\%)$	$^{40}Ar^{*}(\%)$	K/Ca	Age ($\pm 2\sigma$)
700	0.0025	0.0032	0.7	4.5	41.38	73.3 ± 1.0
725	0.0225	0.0026	1.0	21.9	1075.72	40.1 ± 0.5
750	0.0412	0.0019	1.5	43.0	13.00	43.0 ± 0.5
775	0.0574	0.0017	2.0	50.5	10.70	36.3 ± 0.5
800	0.0648	0.0011	2.7	66.9	31.06	42.4 ± 0.5
825	0.0734	0.0010	3.6	70.9	127.62	39.8 ± 0.5
850	0.0774	0.0007	4.6	80.3	63.07	42.6 ± 0.5
875	0.0780	0.0002	5.9	93.3	41.92	49.1 ± 0.6
900	0.0778	0.0007	7.2	78.3	40.37	41.4 ± 0.5
925	0.0795	0.0003	8.6	90.2	27.99	46.6 ± 0.6
950+	0.0753	0.0004	10.1	87.1	29.68	47.6 ± 0.6
975+	0.0752	0.0004	11.6	87.1	19.71	47.6 ± 0.6
1000+	0.0558	0.0012	15.2	65.3	20.31	48.0 ± 0.6
1050+	0.0781	0.0003	27.6	92.0	29.77	48.4 ± 0.6
1100+	0.0734	0.0005	31.7	85.9	28.14	48.1 ± 0.6
1150+	0.0708	0.0006	36.2	82.5	30.76	47.9 ± 0.6
1200+	0.0727	0.0006	42.6	83.1	40.59	47.0 ± 0.6
1250+	0.0739	0.0005	54.3	86.1	43.34	47.9 ± 0.6
1300+	0.0738	0.0005	72.4	85.8	34.29	47.8 ± 0.6
1350+	0.0753	0.0004	100.0	87.5	28.07	47.8 ± 0.6

J value: 0.002030792 ± 0.000029756 All steps of 10 minutes duration. Steps used in regression indicated by (+).
$^{40}Ar^{*}(\%)$—percentage of measured ^{40}Ar derived from natural decay of ^{40}K.

Table 4.7 $^{40}Ar/^{39}Ar$ Furnace Analytical Data for EM3b muscovite

T(K)	$^{39}Ar/^{40}Ar$	$^{36}Ar/^{40}Ar$	$^{39}Ar(\%)$	$^{40}Ar^{*}(\%)$	K/Ca	Age ($\pm 2\sigma$)
900	0.0886	0.0012	3.4	65.1	45.17	49.7 ± 1.0
950	0.1091	0.0004	4.2	88.7	56.27	54.9 ± 1.1
1000	0.1059	0.0008	6.1	77.5	171.05	49.5 ± 1.0
1050	0.1052	0.0008	10.2	77.6	112.47	49.9 ± 1.0
1100	0.1218	0.0004	27.6	88.1	195.85	48.9 ± 1.3
1150	0.1269	0.0003	39.3	92.0	96.10	49.0 ± 1.0
1200 +	0.1225	0.0003	48.5	90.3	226.57	49.9 ± 1.0
1250 +	0.1229	0.0004	57.5	89.3	238.85	49.2 ± 1.0
1350 +	0.1313	0.0002	95.2	95.4	594.75	49.1 ± 1.0
1550 +	0.0949	0.0009	100.0	73.0	35.02	52.0 ± 1.0

J value: 0.0038 ± 0.000076. All steps of 5 minutes duration. All steps used in regression. $^{40}Ar^{*}(\%)$—percentage of measured ^{40}Ar derived from natural decay of ^{40}K.

Table 4.8 $^{40}Ar/^{39}Ar$ Furnace Analytical Data for EM3b K-feldspar

T(K)	$^{39}Ar/^{40}Ar$	$^{36}Ar/^{40}Ar$	$^{39}Ar(\%)$	$^{40}Ar^{*}(\%)$	K/Ca	Age ($\pm 2\sigma$)
725	0.0089	0.0025	2.1	27.4	49.32	79.1 ± 3.0
750+	0.0452	0.0004	5.6	89.4	27.03	51.4 ± 1.9
775+	0.0308	0.0012	7.2	63.2	20.44	53.3 ± 2.0
800+	0.0394	0.0008	8.9	76.4	17.25	50.3 ± 1.9
825+	0.0468	0.0004	10.6	87.4	19.22	48.5 ± 1.8
850+	0.0485	0.0001	12.4	98.7	17.32	52.8 ± 2.0
875+	0.0492	0.0001	14.5	99.4	30.44	52.5 ± 2.0
900+	0.0493	0.0002	16.8	95.4	33.42	50.2 ± 1.9
950+	0.0497	0.0001	21.6	97.8	50.89	51.1 ± 1.9
1000+	0.0501	0.0001	30.7	98.9	151.57	51.3 ± 1.9
1050	0.0498	0.0001	39.9	98.3	117.60	51.2 ± 1.9
1100	0.0489	0.0001	45.5	99.4	130.83	52.7 ± 2.0
1150	0.0479	0.0001	49.9	97.9	86.71	53.0 ± 2.0
1200	0.0457	0.0001	54.7	97.8	74.69	55.5 ± 2.1
1250	0.0428	0.0001	61.1	95.7	65.89	58.0 ± 2.2
1300	0.0400	0.0003	72.0	92.0	46.53	59.6 ± 2.2
1350	0.0398	0.0003	89.9	91.5	92.10	59.5 ± 2.2
1550	0.0377	0.0003	100.0	89.7	174.29	61.6 ± 2.3

J value: 0.00146 ± 0.000056. All steps of 10 minutes duration. Steps used in regression indicated by (+). $^{40}Ar^{*}(\%)$—percentage of measured ^{40}Ar derived from natural decay of ^{40}K.

Table 4.9 $^{40}Ar/^{39}Ar$ Furnace Analytical Data for EM3c biotite

T(K)	$^{39}Ar/^{40}Ar$	$^{36}Ar/^{40}Ar$	$^{39}Ar(\%)$	$^{40}Ar^*(\%)$	K/Ca	Age ($\pm 2\sigma$)
900	0.1093	0.0007	14.7	80.3	75.55	49.7 ± 1.0
950	0.1131	0.0006	17.8	81.6	86.78	48.8 ± 1.0
1000	0.1217	0.0003	21.8	89.7	103.53	49.9 ± 1.0
1050	0.1241	0.0003	29.5	91.6	55.03	49.9 ± 1.0
1100	0.1209	0.0004	35.0	87.6	38.37	49.0 ± 1.0
1150	0.1173	0.0005	39.4	84.3	40.10	48.6 ± 1.0
1200	0.1175	0.0005	46.1	85.7	43.74	49.4 ± 1.0
1250	0.1263	0.0003	61.5	92.3	104.00	49.5 ± 1.0
1350	0.1296	0.0002	91.2	94.6	52.97	49.4 ± 1.0
1550	0.1146	0.0005	100.0	84.8	7.10	50.0 ± 1.0

J value: 0.0038 ± 0.000076. All steps of 5 minutes duration. All steps used in regression. $^{40}Ar^*(\%)$—percentage of measured ^{40}Ar derived from natural decay of ^{40}K.

Table 4.10 $^{40}Ar/^{39}Ar$ Furnace Analytical Data for EM3d hornblende

T(K)	$^{39}Ar/^{40}Ar$	$^{36}Ar/^{40}Ar$	$^{39}Ar(\%)$	$^{40}Ar^*(\%)$	K/Ca	Age ($\pm 2\sigma$)
1100	0.0285	0.0015	1.5	55.7	0.41	50.7 ± 1.9
1175	0.0268	0.0013	2.2	62.3	0.22	60.1 ± 2.3
1200+	0.0276	0.0008	3.6	76.2	0.20	71.3 ± 2.7
1225+	0.0307	0.0005	6.6	86.5	0.22	72.7 ± 2.7
1250+	0.0330	0.0002	15.0	93.8	0.25	73.3 ± 2.8
1275+	0.0363	0.0002	53.5	94.7	0.28	67.5 ± 2.5
1300+	0.0373	0.0001	69.9	97.2	0.30	67.3 ± 2.5
1325+	0.0326	0.0002	73.7	92.6	0.27	73.2 ± 2.8
1350+	0.0343	0.0001	79.4	97.9	0.28	73.6 ± 2.8
1550+	0.0345	0.0002	100.0	93.2	0.27	69.8 ± 2.6

J value: 0.00146 ± 0.000056. All steps of 5 minutes duration. Steps used in regression indicated by (+). $^{40}Ar^*(\%)$—percentage of measured ^{40}Ar derived from natural decay of ^{40}K.

Table 4.11 $^{40}Ar/^{39}Ar$ Furnace Analytical Data for EM3d biotite

T(K)	$^{39}Ar/^{40}Ar$	$^{36}Ar/^{40}Ar$	$^{39}Ar(\%)$	$^{40}Ar^*(\%)$	K/Ca	Age ($\pm 2\sigma$)
900	0.0304	0.0013	6.3	60.1	41.82	51.4 ± 1.9
950+	0.0432	0.0003	13.7	91.3	53.16	54.8 ± 2.1
1000+	0.0448	0.0002	21.4	95.3	53.73	55.2 ± 2.1
1050+	0.0449	0.0002	28.5	94.8	135.08	54.8 ± 2.1
1100+	0.0443	0.0001	34.5	96.2	49.82	56.3 ± 2.1
1150+	0.0431	0.0002	43.7	94.2	77.95	56.6 ± 2.1
1200+	0.0446	0.0001	58.4	97.3	59.16	56.6 ± 2.1
1250+	0.0456	0.0001	73.9	97.3	23.89	55.3 ± 2.1
1350+	0.0463	0.0001	95.8	97.7	27.52	54.8 ± 2.1
1550+	0.0442	0.0001	100.0	96.3	7.67	56.4 ± 2.1

J value: 0.00146 ± 0.000056. All steps of 5 minutes duration. All steps used in regression. $^{40}Ar^*(\%)$—percentage of measured ^{40}Ar derived from natural decay of ^{40}K.

Table 4.12 $^{40}Ar/^{39}Ar$ Furnace Analytical Data for EM6 hornblende

T(K)	$^{39}Ar/^{40}Ar$	$^{36}Ar/^{40}Ar$	$^{39}Ar(\%)$	$^{40}Ar^{*}(\%)$	K/Ca	Age ($\pm 2\sigma$)
1000	0.0279	0.0001	1.0	99.2	1.17	91.1 ± 3.4
1100+	0.0325	0.0005	1.8	84.4	0.56	67.1 ± 2.5
1150+	0.0365	0.0002	10.1	92.7	0.32	65.6 ± 2.5
1175+	0.0381	0.0002	21.4	92.8	0.29	63.0 ± 2.4
1200+	0.0375	0.0001	40.9	96.1	0.29	66.2 ± 2.5
1220+	0.0388	0.0001	63.8	98.1	0.29	65.4 ± 2.5
1240+	0.0403	0.0001	76.8	98.5	0.30	63.2 ± 2.4
1280+	0.0380	0.0004	78.6	88.7	0.29	60.4 ± 2.3
1300+	0.0379	0.0001	81.8	96.1	0.26	65.6 ± 2.5
1325+	0.0375	0.0001	93.7	97.4	0.25	67.3 ± 2.5
1350+	0.0377	0.0003	99.1	90.9	0.24	62.5 ± 2.4
1400+	0.0364	0.0002	99.8	94.4	0.24	67.0 ± 2.5
1550+	0.0281	0.0012	100.0	65.1	0.23	60.1 ± 2.3

J value: 0.00146 ± 0.000056. All steps of 5 minutes duration. Steps used in regression indicated by (+). $^{40}Ar^{*}(\%)$—percentage of measured ^{40}Ar derived from natural decay of ^{40}K.

Table 4.13 $^{40}Ar/^{39}Ar$ Furnace Analytical Data for EM6 biotite

T(K)	$^{39}Ar/^{40}Ar$	$^{36}Ar/^{40}Ar$	$^{39}Ar(\%)$	$^{40}Ar^{*}(\%)$	K/Ca	Age ($\pm 2\sigma$)
900	0.0379	0.0007	14.9	79.8	310.08	54.6 ± 2.1
950	0.0448	0.0003	18.5	89.9	63.14	52.1 ± 2.0
1000	0.0434	0.0004	23.3	89.0	340.71	53.2 ± 2.0
1050	0.0420	0.0003	28.1	89.9	101.87	55.6 ± 2.1
1100	0.0420	0.0004	32.5	89.3	102.37	55.2 ± 2.1
1150	0.0414	0.0003	38.3	89.8	61.95	56.3 ± 2.1
1200	0.0432	0.0002	49.5	93.4	37.23	56.0 ± 2.1
1250	0.0452	0.0002	65.6	94.7	39.86	54.4 ± 2.1
1350	0.0471	0.0001	97.1	97.6	65.09	53.8 ± 2.0
1550	0.0455	0.0001	100.0	98.4	12.27	56.1 ± 2.1

J value: 0.00146 ± 0.000056. All steps of 5 minutes duration. All steps used in regression. $^{40}Ar^{*}(\%)$—percentage of measured ^{40}Ar derived from natural decay of ^{40}K.

Table 5.1 Hornblende microprobe analyses

	EM6 hornblende	EM3d hornblende	B85 hornblende
MgO	6.96(0.28)	11.42(0.87)	3.90(0.63)
Al_2O_3	13.07(0.26)	10.51(1.37)	7.93(0.34)
SiO_2	39.82(0.75)	44.16(1.62)	41.82(0.46)
CaO	11.25(0.19)	11.88(0.17)	9.97(0.09)
TiO_2	1.22(0.06)	0.65(0.12)	2.10(0.18)
Cr_2O_3	0.09(0.02)	0.07(0.02)	0.05(0.02)
MnO	0.39(0.03)	0.27(0.03)	0.45(0.06)
FeO	22.69(0.28)	16.70(0.94)	28.71(0.89)
Na_2O	1.43(0.05)	1.15(0.19)	2.13(0.08)
K_2O	1.40(0.06)	1.20(0.27)	1.17(0.02)
F	0.49(0.12)	0.73(0.05)	1.43(0.12)
Cl	0.11(0.02)	0.02(0.00)	0.15(0.02)
Total	98.92	98.75	99.80
	Formula Basis 23 Oxygens		
Mg	1.605	2.545	0.924
Al	2.383	1.854	1.487
Si	6.159	6.604	6.654
Ca	1.864	1.903	1.699
Ti	0.142	0.073	0.251
Cr	0.011	0.009	0.006
Mn	0.051	0.035	0.061
Fe	2.935	2.089	3.820
Na	0.429	0.335	0.656
K	0.276	0.229	0.237
F	0.241	0.343	0.722
Cl	0.029	0.006	0.042
Total	16.123	16.022	16.557

Numbers in parentheses denote 1σ uncertainties in compositions.

Table 5.2 Muscovite microprobe analyses

	EM3b muscovite
MgO	1.03(0.09)
Al_2O_3	34.60(0.46)
SiO_2	48.98(1.24)
CaO	0.00(0.00)
TiO	0.14(0.03)
MnO	0.03(0.02)
FeO	4.20(0.22)
Na_2O	0.38(0.07)
K_2O	9.47(1.08)
Total	98.83
Formula Basis 11 Oxygens	
Mg	0.099
Al	2.626
Si	3.156
Ca	0.000
Ti	0.007
Mn	0.002
Fe	0.226
Na	0.047
K	0.779
Total	6.941

Numbers in parentheses denote 1σ uncertainties in compositions.

Table 5.3 Biotite microprobe analyses

	NB12-11 biotite	EM3c biotite	EM3d biotite	EM6 biotite	B85 biotite
MgO	9.44(0.49)	8.00(0.22)	14.42(0.12)	8.73(0.19)	1.84(0.14)
Al_2O_3	15.64(0.19)	17.96(0.30)	15.40(0.14)	16.01(0.14)	12.85(0.35)
SiO_2	36.65(0.52)	35.01(0.37)	38.18(0.53)	36.20(0.21)	34.99(0.30)
CaO	0.04(0.01)	0.03(0.01)	0.02(0.01)	0.06(0.02)	0.09(0.14)
TiO_2	3.56(0.47)	3.38(0.19)	2.23(0.17)	3.10(0.10)	4.12(0.27)
MnO	0.09(0.04)	0.38(0.04)	0.16(0.04)	0.16(0.03)	0.36(0.02)
FeO	23.18(0.15)	22.22(0.65)	17.71(0.37)	25.30(0.31)	33.65(0.33)
Na_2O	0.05(0.04)	0.10(0.03)	0.07(0.03)	0.10(0.02)	0.10(0.06)
K_2O	8.83(0.25)	8.83(0.15)	8.87(0.73)	8.78(0.05)	8.14(0.40)
Cl	0.02(0.01)	0.05(0.01)	0.02(0.02)	0.08(0.01)	0.12(0.01)
F	1.23(0.09)	0.93(0.11)	0.89(0.13)	0.57(0.08)	0.70(0.18)
Total	98.71	96.89	97.97	99.09	96.97
Mg	1.063	0.915	1.585	0.984	0.228
Al	1.393	1.623	1.339	1.427	1.251
Si	2.770	2.685	2.816	2.738	2.822
Ca	0.003	0.002	0.001	0.005	0.008
Ti	0.203	0.195	0.124	0.176	0.243
Mn	0.005	0.025	0.010	0.010	0.024
Fe	1.465	1.425	1.093	1.600	2.320
Na	0.007	0.015	0.010	0.015	0.016
K	0.852	0.862	0.835	0.847	0.810
Cl	0.002	0.007	0.002	0.011	0.016
F	0.293	0.224	0.266	0.135	0.178
Total	8.055	7.977	8.081	7.949	7.915

Numbers in parentheses denote 1σ uncertainties in compositions.

Table 5.4 K-feldspar microprobe analyses

	NB12-11 K-feldspar	EM3b K-feldspar	B85 K-feldspar
Na_2O	0.99(0.07)	1.23(0.12)	1.08(0.31)
MgO	0.07(0.01)	0.04(0.01)	0.01(0.01)
Al_2O_3	19.82(0.20)	19.87(0.15)	18.79(0.11)
SiO_2	66.27(0.49)	66.44(0.85)	67.13(0.85)
CaO	0.00(0.00)	0.00(0.01)	0.04(0.03)
FeO	0.01(0.02)	0.02(0.03)	0.13(0.06)
K_2O	14.13(0.71)	14.06(0.59)	13.76(0.72)
Total	101.29	101.66	100.94
	Formula Basis 8 Oxygens		
Na	0.086	0.107	0.095
Mg	0.005	0.003	0.000
Al	1.052	1.051	0.998
Si	2.984	2.982	3.026
Ca	0.000	0.000	0.002
Fe	0.000	0.001	0.005
K	0.812	0.805	0.792
Total	4.939	4.948	4.918

Numbers in parentheses denote 1σ uncertainties in compositions.

FIGURE CAPTIONS

Figure 1. Regional map of the Bitterroot batholith including features described in text. Box inset shows location of Figure 2. Heavy lines show major faults; strike-slip faults are shown by arrows; thrust faults and normal faults by teeth and barbs on the upper plate, respectively. The Lolo Hot Springs batholith and the Whistling Pig pluton are delineated by (LHS) and (WP). The Skookum Butte stock is indicated by (SB). Map modified from Hyndman *et al*. (1988).

Figure 2. Simplified geologic map of the bedrock geology of the northwestern BMCC with sample locations marked by triangles. Units designated as follows: Kgd—main phase granitoids of the Bitterroot batholith, including the Skookum Butte stock; Kmig—migmatite associated with Kgd; Kt—foliated tonalite; Yw—calc-silicate gneiss of the Middle Proterozoic Wallace Formation; qg—ductily deformed quartzite and calc-silicate gneiss most likely representing intensely deformed equivalents of the Wallace Fm. and the Ravalli Gr.; ps— pelitic schists and gneisses of the Prichard Fm. Approximate limits of the Spruce Creek mylonite zone indicated by hatched region.

Figure 3. Photograph of miarolitic cavity in the Lolo Hot Springs batholith filled with euhedral crystals of smoky quartz. Lens cap for scale.

Figure 4. Geochronologic results for sample the Skookum Butte stock (NB12-11). Concordia diagram for U-Pb zircon analyses (a). For all concordia diagrams, ellipses represent propagated analytical uncertainty at the 2 σ level and numbers along concordia indicate age in Ma; (b) Concordia

diagram for EM20 U-Pb monazite analyses. $^{40}Ar/^{39}Ar$ release spectra and inverse isotope correlation diagrams for biotite (c, d); and K-feldspar (e, f) furnace analyses. For all release spectra, steps included in plateau are shaded. For all inverse isotope correlation diagrams, filled circles are those used in regression analyses; results of these analyses are indicated by the solid line. "Air" represents the $^{36}Ar/^{40}Ar$ ratio of modern atmosphere. In the case of (f), the solid line represents the regression including low-temperature increments (filled) and the dashed gray line represents the high-temperature regression (white).

Figure 5. Photograph of (a) metamict hydrothermal and clear magmatic zircon populations; and (b) photomicrograph of hydrothermal zircon with radiation halo. Scale bar on (a) is 200 μm; (b) is 1.5 mm in long dimension.

Figure 6. Concordia diagram for U-Pb zircon analyses from the Lolo Hot Springs batholith (NB11-1); inset shows scatter in points. Concordant magmatic fraction is indicated by shaded ellipse; hydrothermal fractions are indicated by white ellipses.

Figure 7. Geochronologic results for the Whistling Pig pluton (B85). Concordia diagram for a single U-Pb zircon analysis (a). Isotope correlation diagram for hornblende laser fusion analyses (b). Release spectrum for biotite laser step-heating (c); isotope correlation diagram for biotite laser step heating and fusion analyses (d); Release spectrum and isotope correlation diagram for K-feldspar furnace analyses (e, f).

Figure 8. Geochronologic results for pegmatite sample EM3b. $^{40}Ar/^{39}Ar$ release spectra and inverse isotope correlation diagrams for muscovite (a, b)

and K-feldspar (c, d) furnace analyses. Dashed line in (d) is regression of high-temperature increments.

Figure 9. Geochronologic results for granite sample EM3c. $^{40}Ar/^{39}Ar$ release spectrum and inverse isotope correlation diagram for biotite furnace analyses (a, b).

Figure 10. Geochronologic results for diorite boudin EM3d. $^{40}Ar/^{39}Ar$ release spectra and inverse isotope correlation diagrams for hornblende (a, b) and biotite (c, d) furnace analyses.

Figure 11. Geochronologic results for amphibolite EM6. Release spectra and isotope correlation diagrams for hornblende (a, b) and biotite (c, d) furnace analyses.

Figure 12. Summary of geochronologic constraints on unroofing in the Bitterroot batholith superimposed on published geochronologic data from the eastern BMCC. U-Pb monazite crystallization age of Skookum Butte stock indicated by shaded box. Crystallization age of Lolo Hot Springs batholith and Whistling Pig pluton indicated by white band. Limits on the age of the Bitterroot mylonite, including published uncertainties, indicated by hatched region. $^{40}Ar/^{39}Ar$ data indicated by circles: filled, this paper; open, eastern BMCC (House and Hodges, 1994).

Figure 1

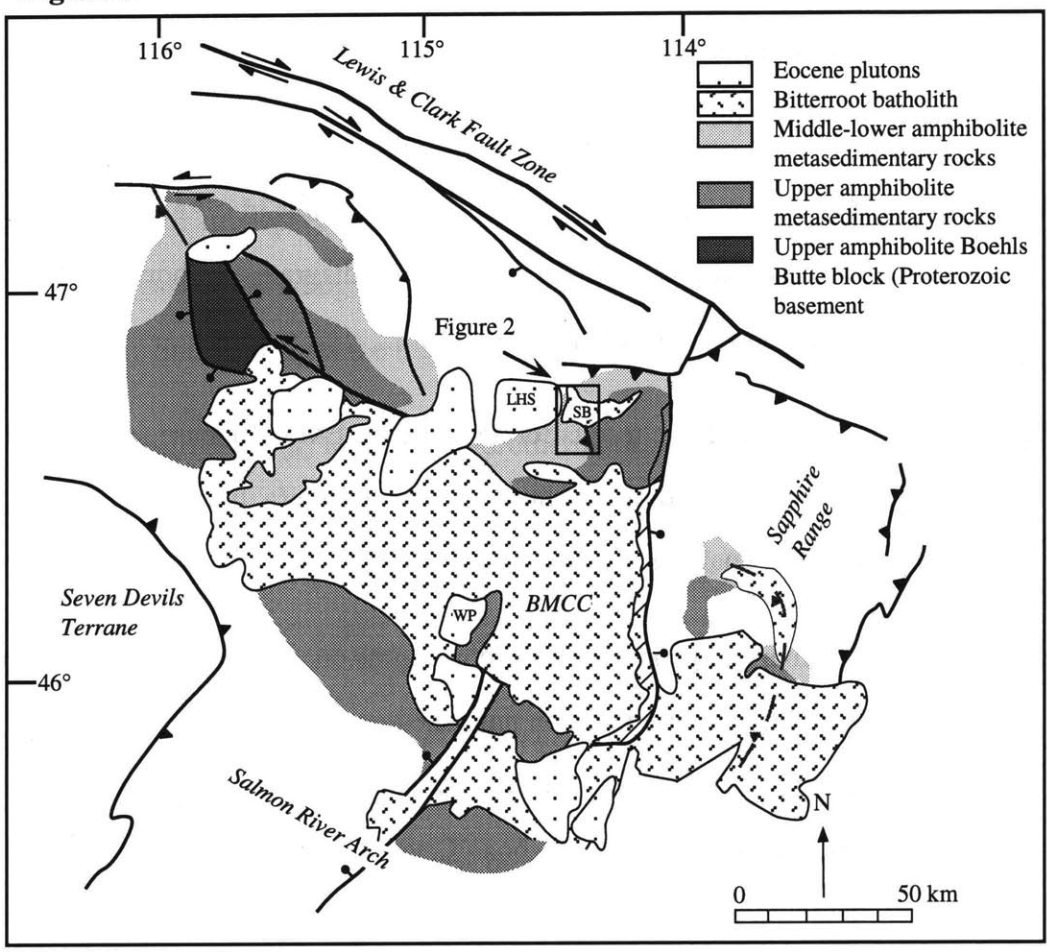
116°
115°
114°
Lewis & Clark Fault Zone
47°
Figure 2
LHS
SB
Sapphire Range
Seven Devils Terrane
WP
BMCC
46°
Salmon River Arch
N
0
50 km
Eocene plutons
Bitterroot batholith
Middle-lower amphibolite metasedimentary rocks
Upper amphibolite metasedimentary rocks
Upper amphibolite Boehls Butte block (Proterozoic basement

Figure 2

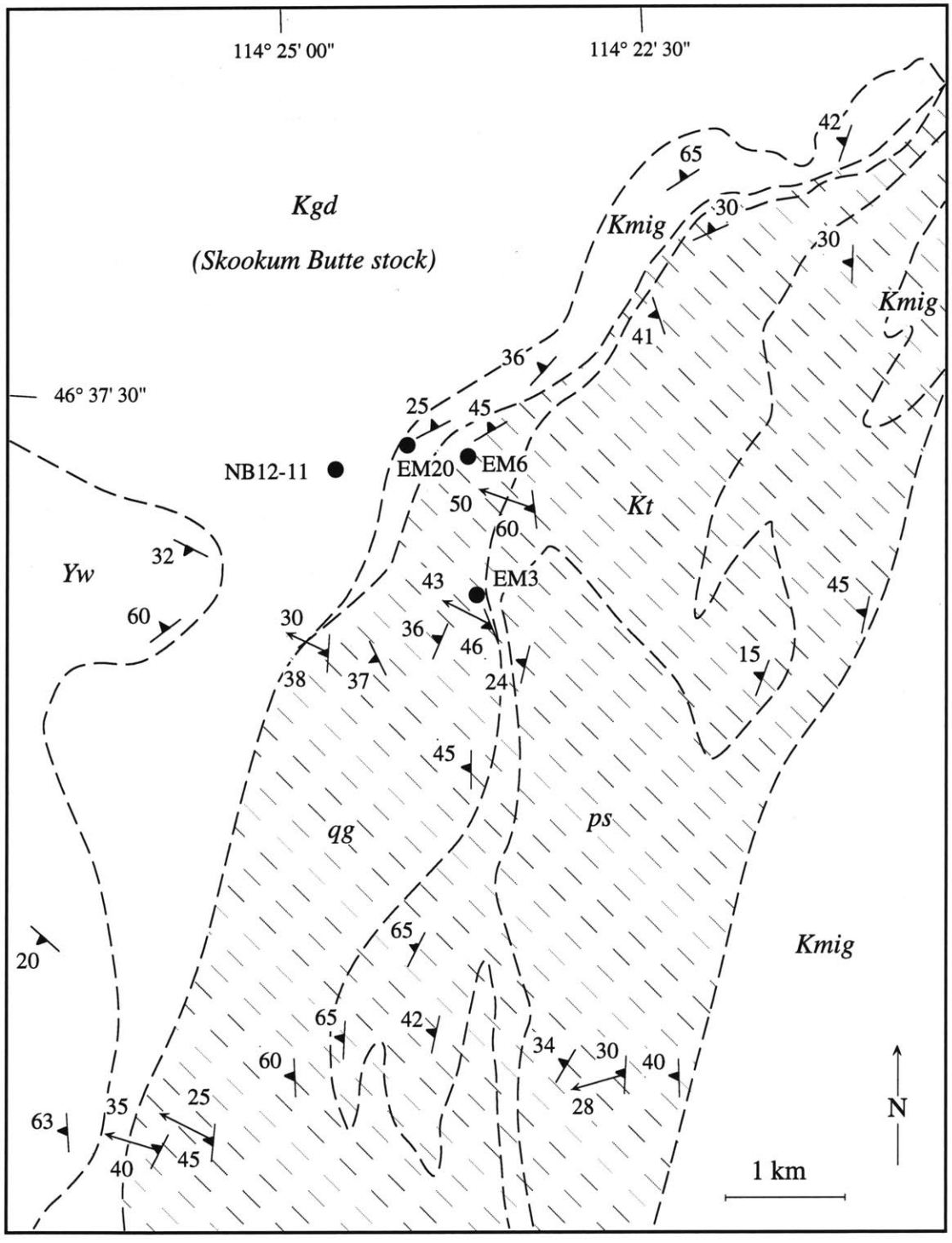
114° 25' 00"
114° 22' 30"
46° 37' 30"
Kgd
(Skookum Butte stock)
Kmig
Kmig
Kmig
Kt
Yw
qg
ps
Kmig
NB12-11
EM20
EM6
EM3
42
65
30
30
41
36
25
45
50
60
32
60
43
45
30
36
46
38
37
24
15
45
65
20
65
42
34
30
40
60
28
63
35
25
40
45
N
1 km

Figure 3

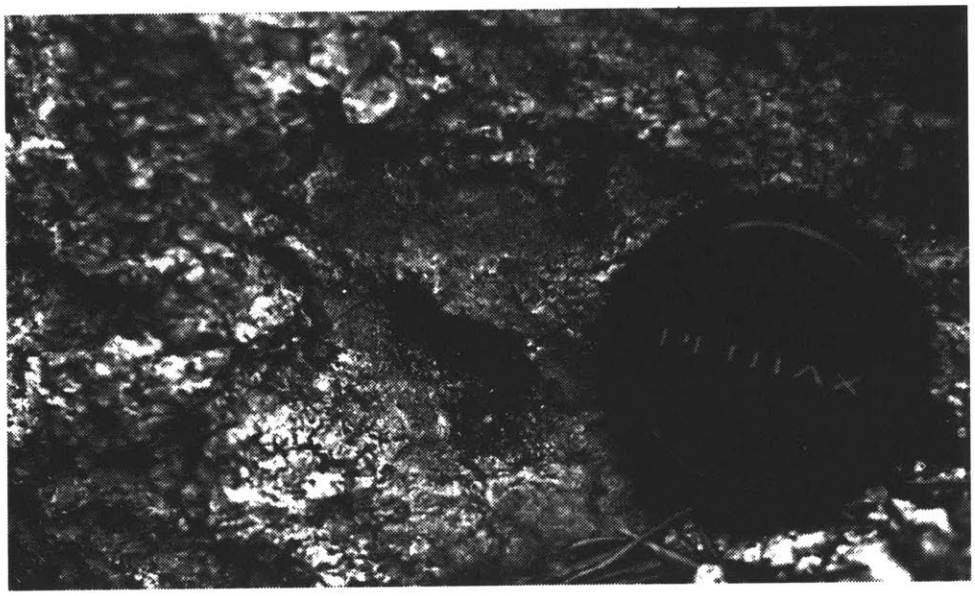

Figure 4a

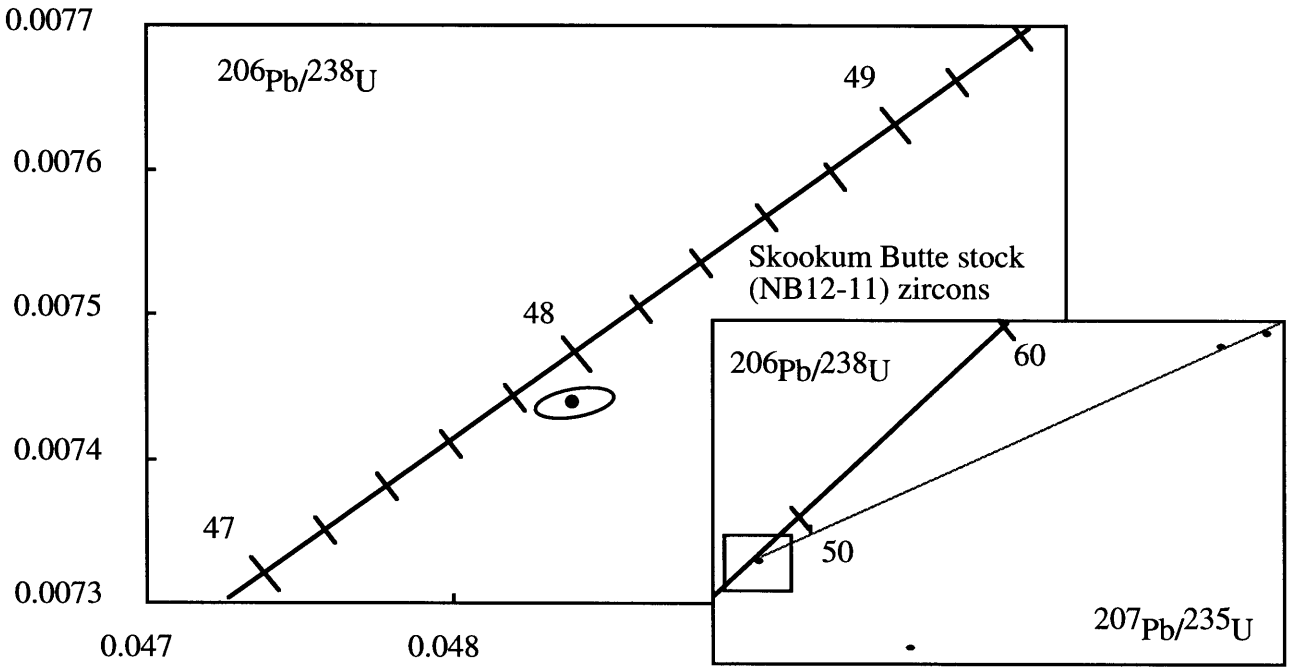
0.0077
0.0076
0.0075
0.0074
0.0073
0.047
0.048
206Pb/238U
47
48
49
Skookum Butte stock
(NB12-11) zircons
206Pb/238U
50
60
207Pb/235U

Figure 4b

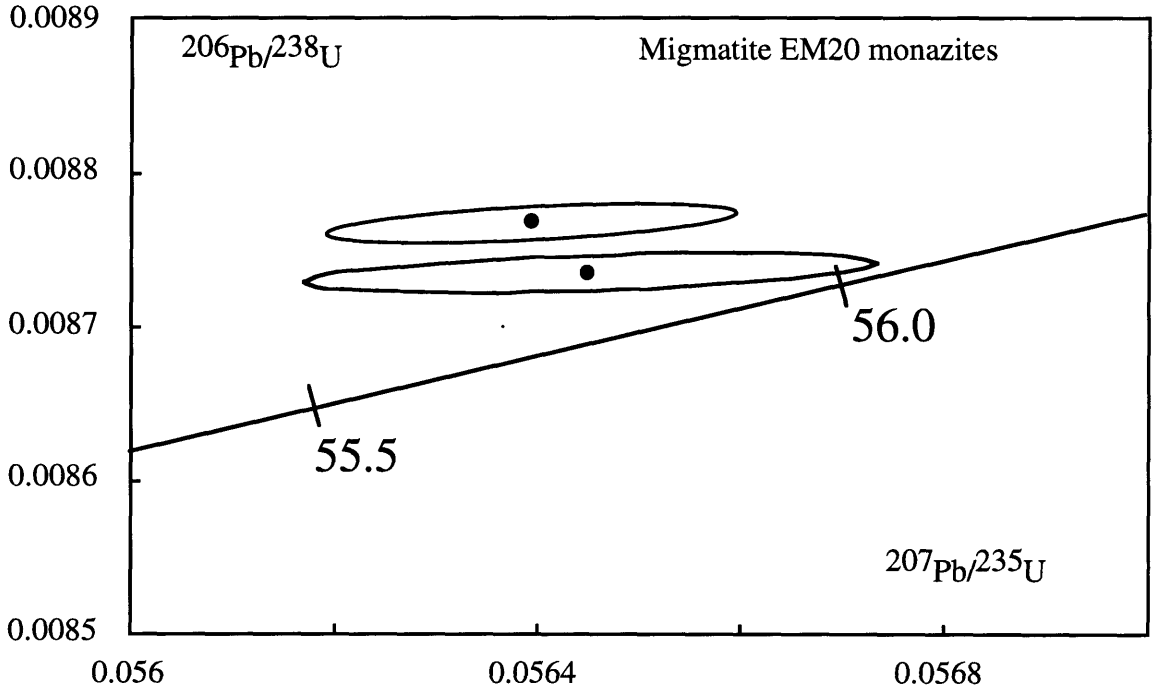
0.0089
0.0088
0.0087
0.0086
0.0085
$^{206}Pb/^{238}U$
Migmatite EM20 monazites
56.0
55.5
$^{207}Pb/^{235}U$
0.056
0.0564
0.0568

Figure 4c

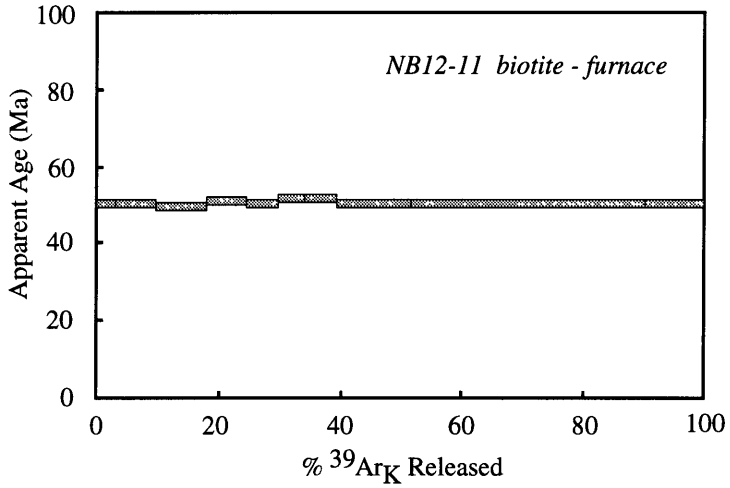

Figure 4d

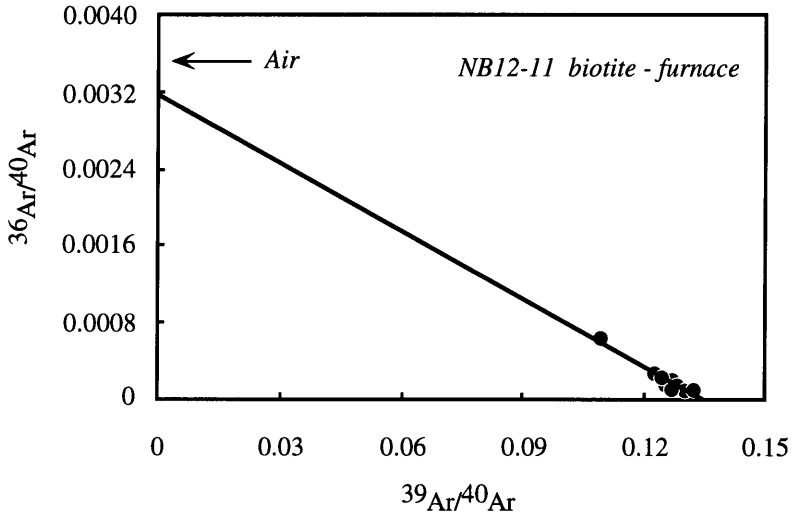

Figure 4e

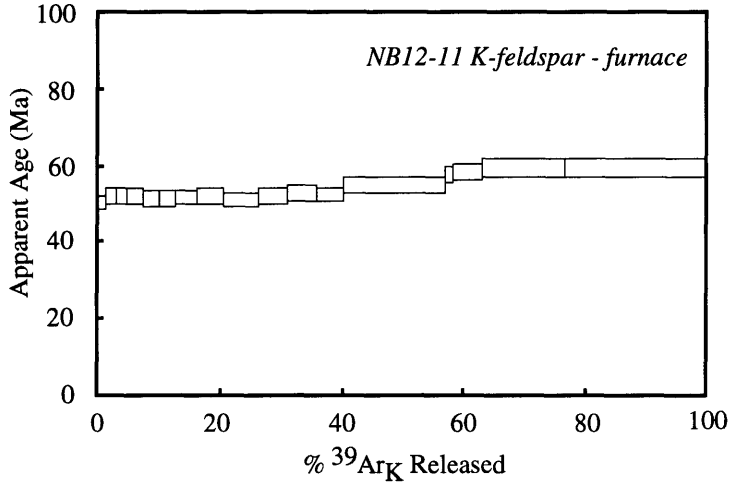

Figure 4f

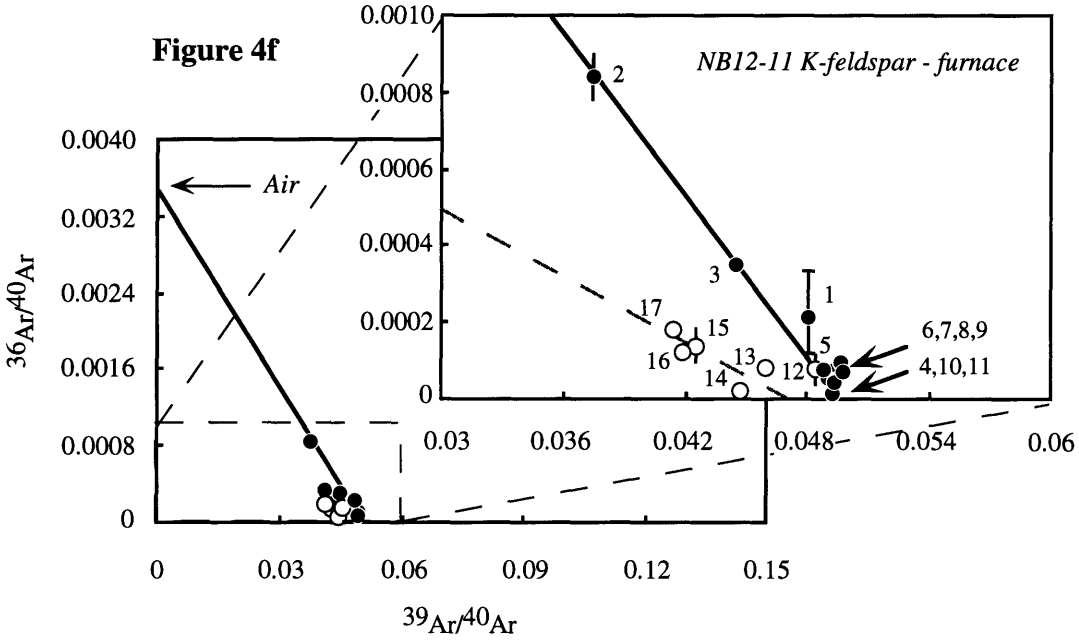

Figure 5a

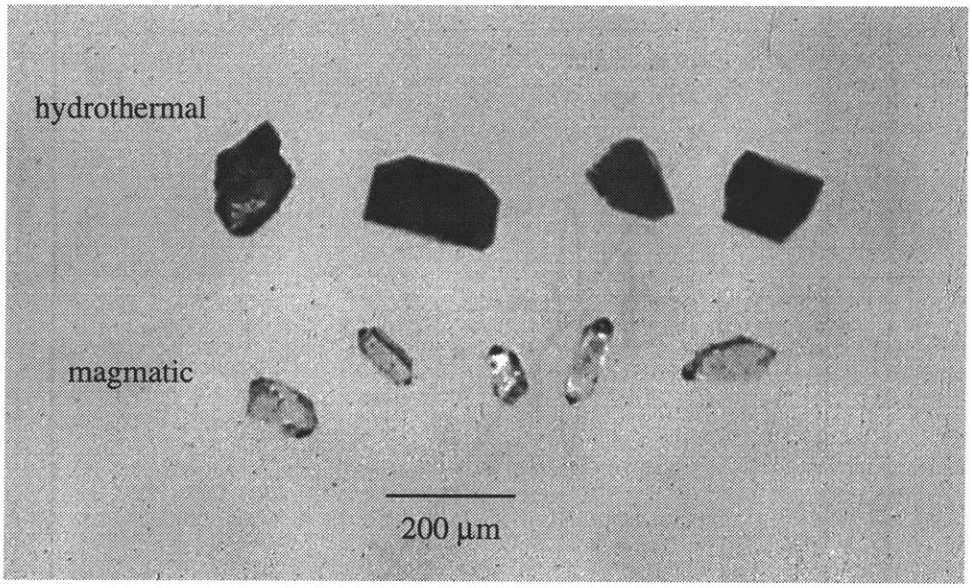

Figure 5b

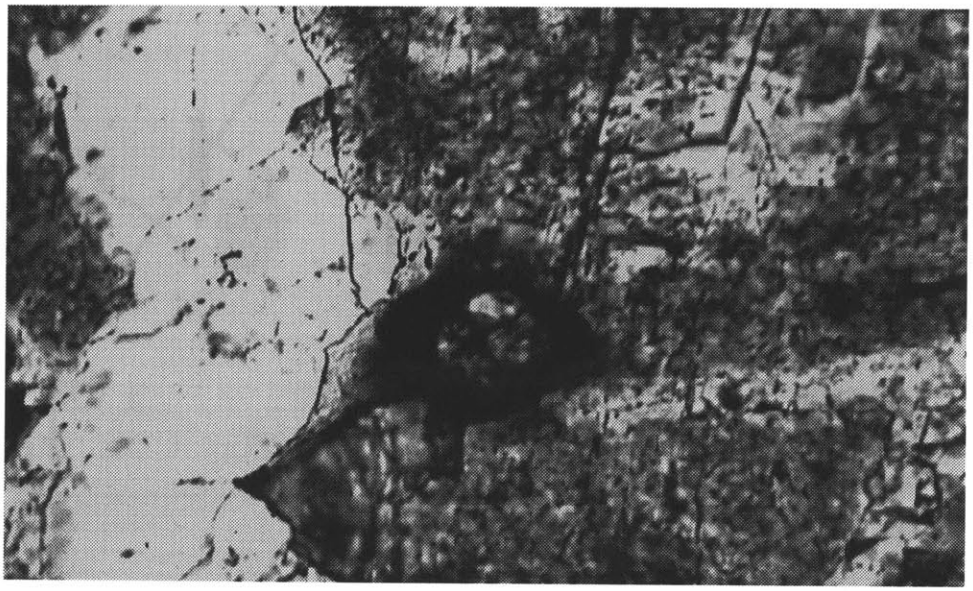

Figure 6

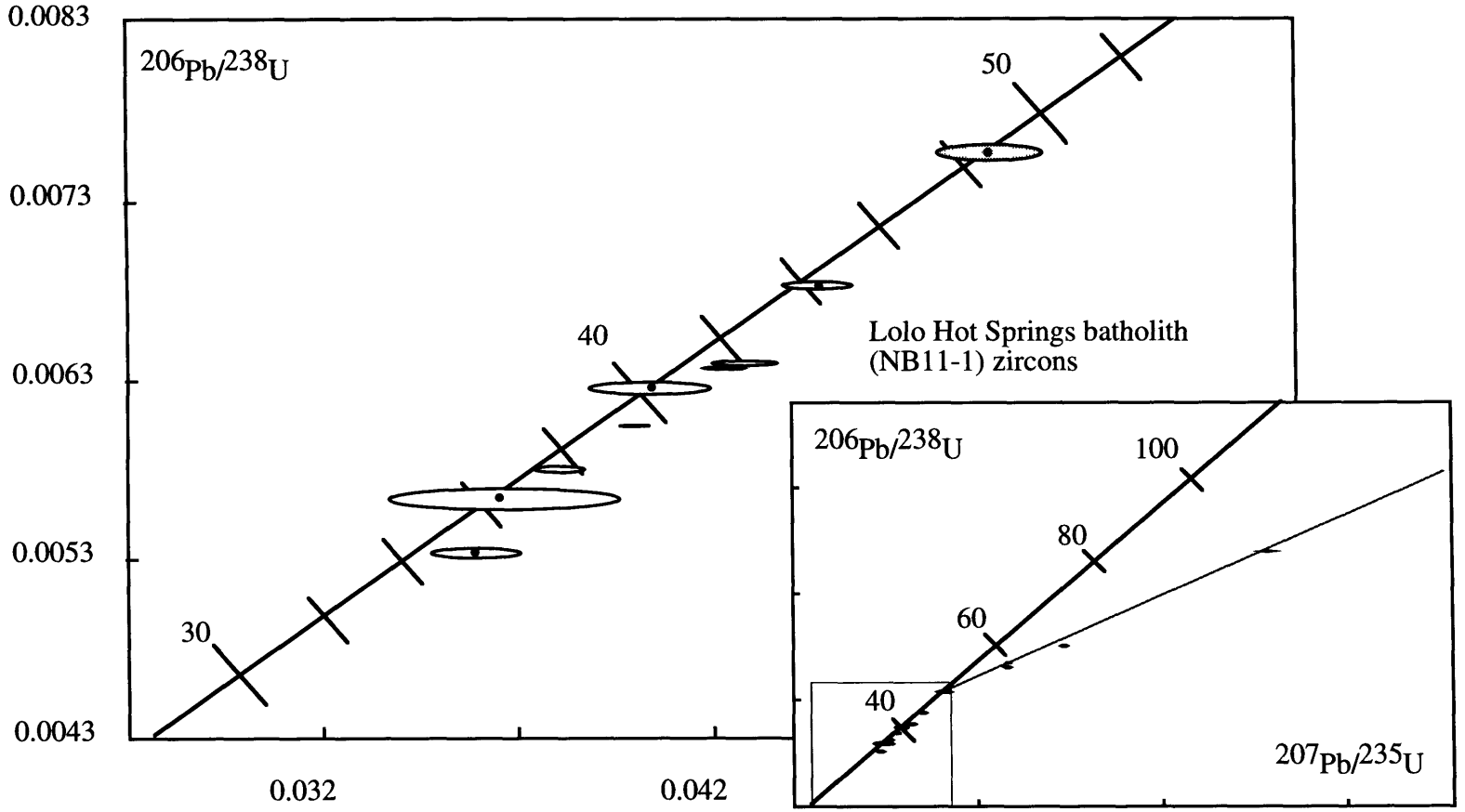
0.0083
0.0073
0.0063
0.0053
0.0043
206Pb/238U
50
40
30
Lolo Hot Springs batholith
(NB11-1) zircons
0.032
0.042
206Pb/238U
100
80
60
40
207Pb/235U

Figure 7a

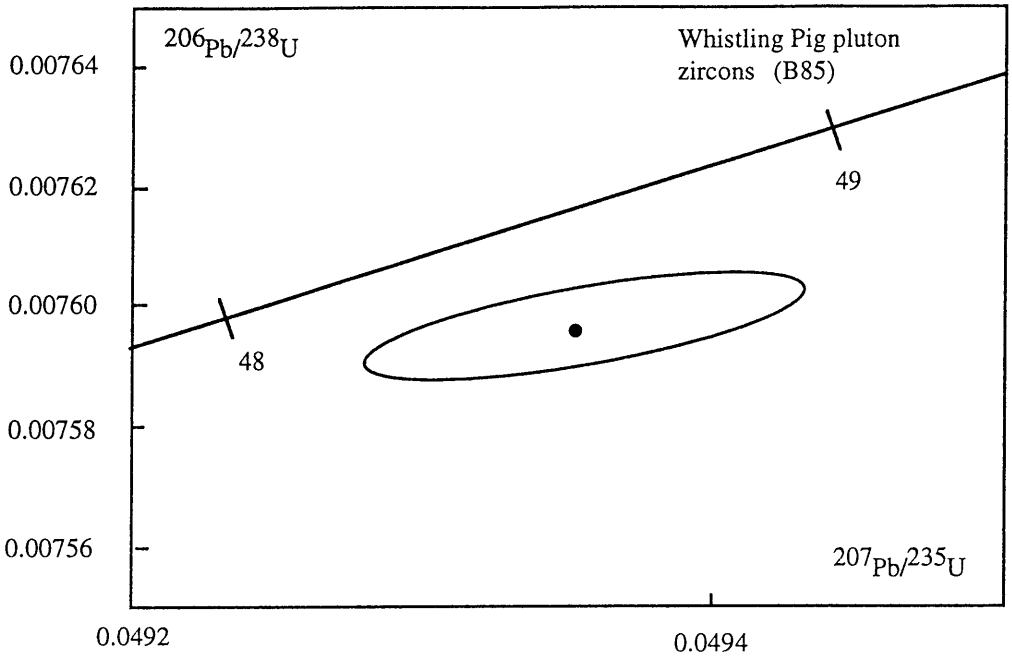
$^{206}Pb/^{238}U$
Whistling Pig pluton
zircons (B85)
0.00764
0.00762
0.00760
0.00758
0.00756
49
48
$^{207}Pb/^{235}U$
0.0492
0.0494

Figure 7b

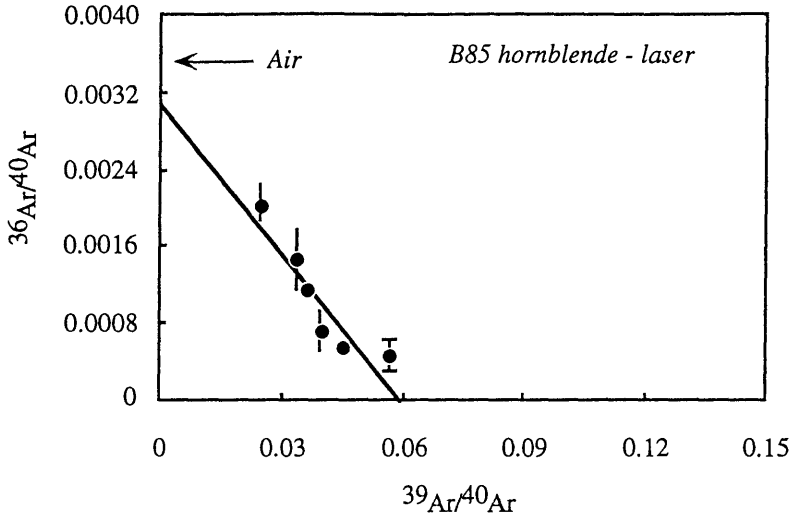
0.0040
0.0032
0.0024
0.0016
0.0008
0
Air
B85 hornblende - laser
$^{36}Ar/^{40}Ar$
0
0.03
0.06
0.09
0.12
0.15
$^{39}Ar/^{40}Ar$

Figure 7c

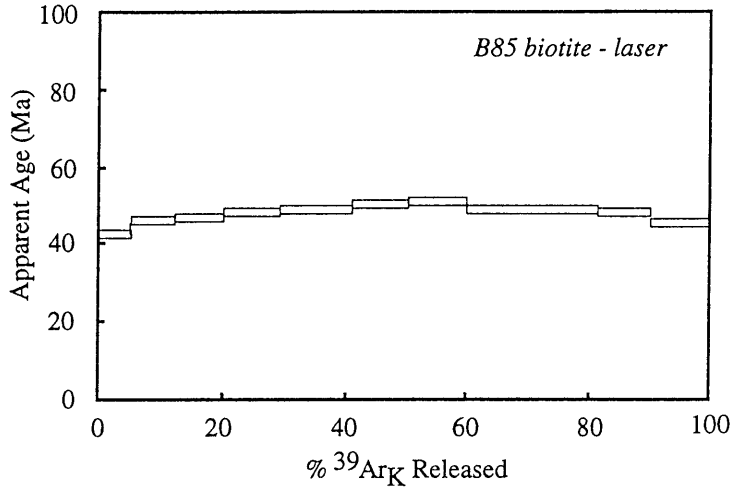

Figure 7d

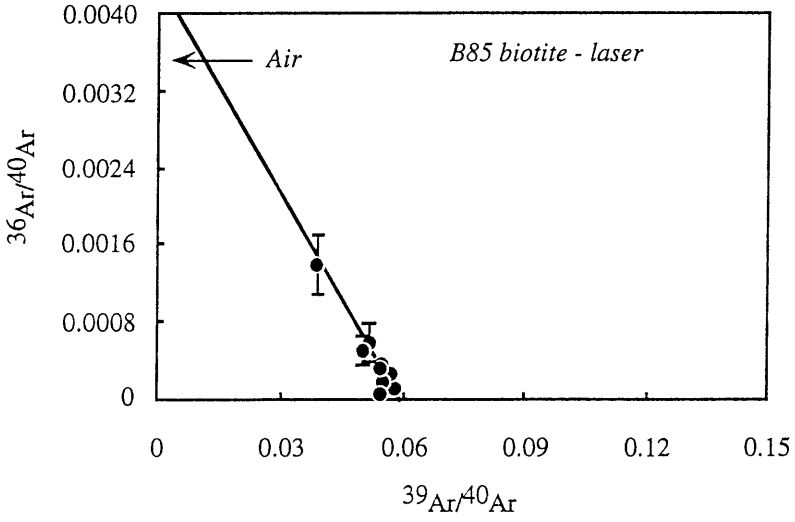

Figure 7e

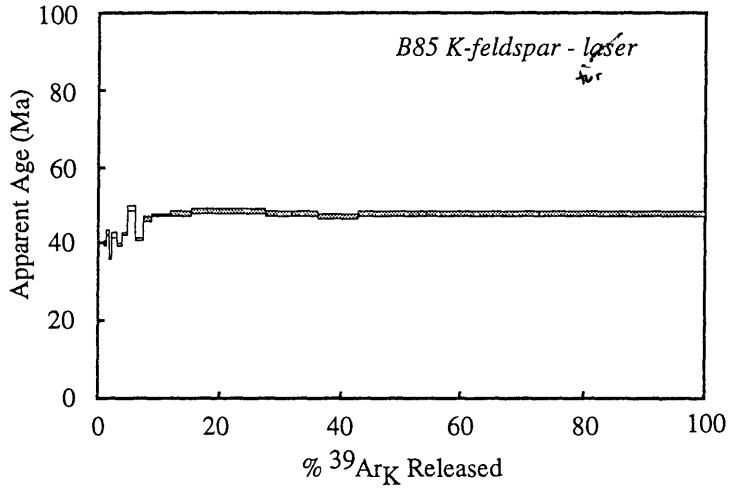

Figure 7f

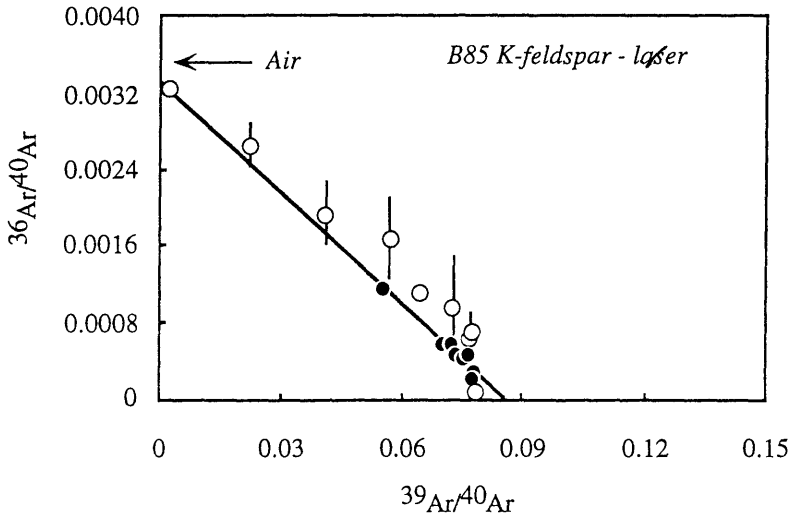

Figure 8a

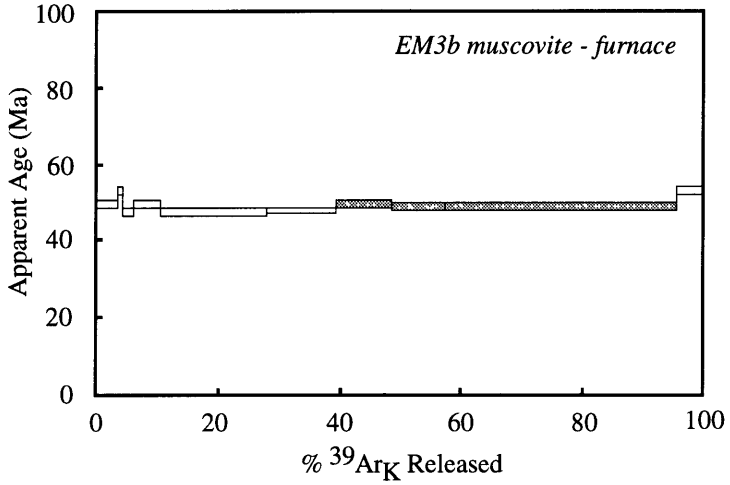

Figure 8b

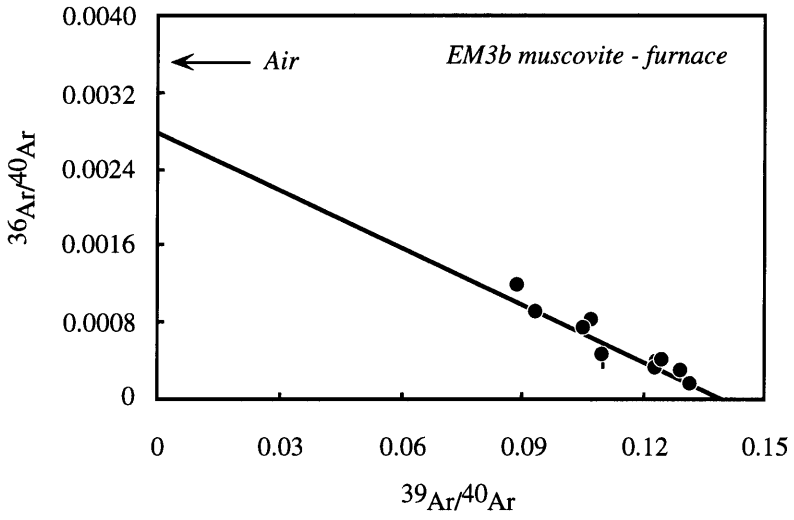

Figure 8c

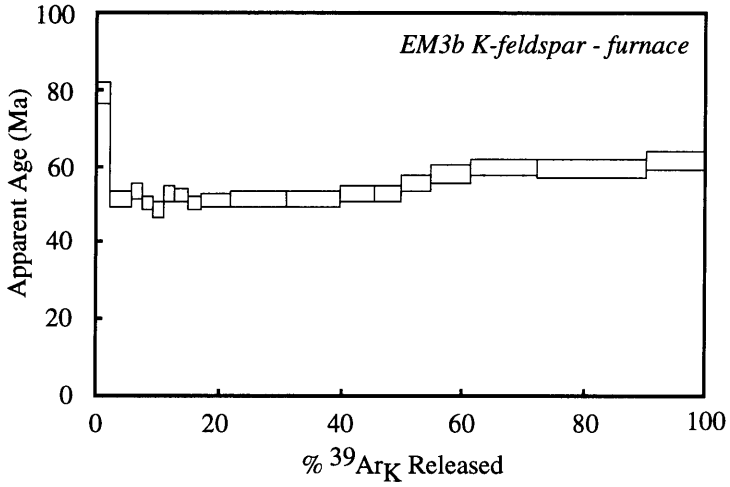

Figure 8d

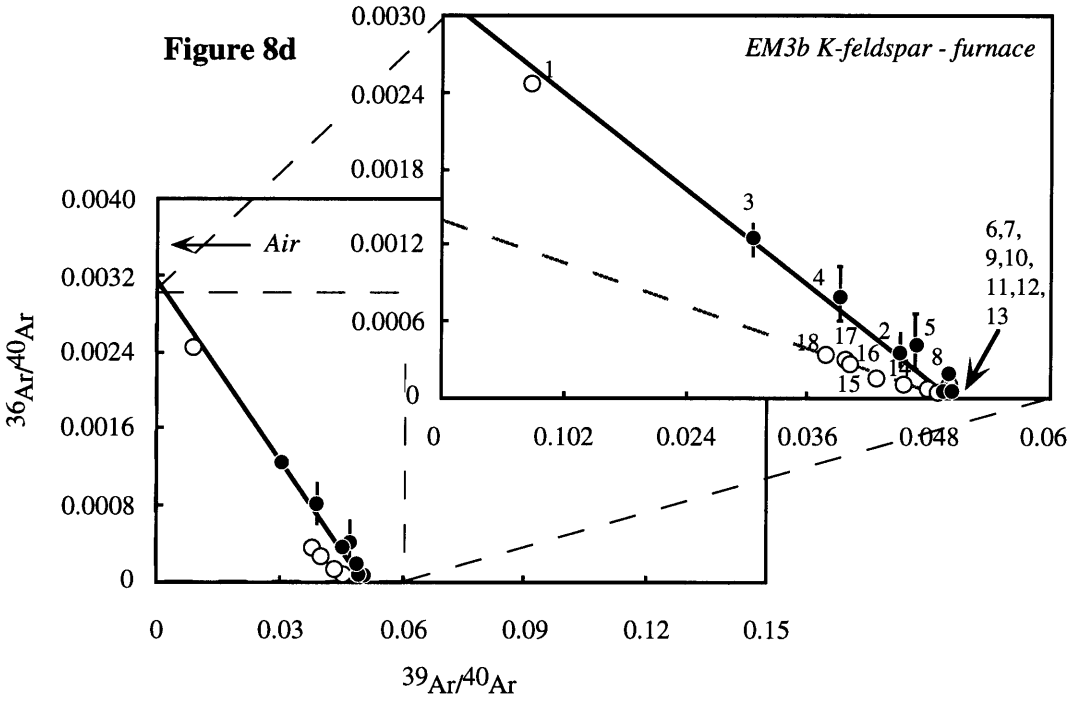

Figure 9a

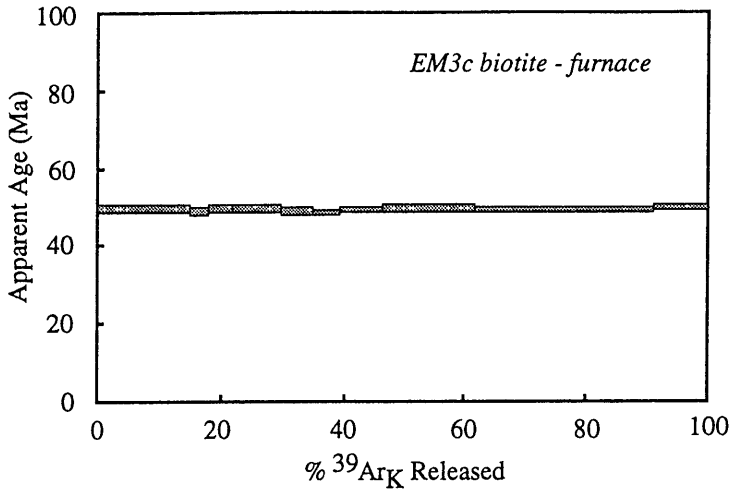

Figure 9b

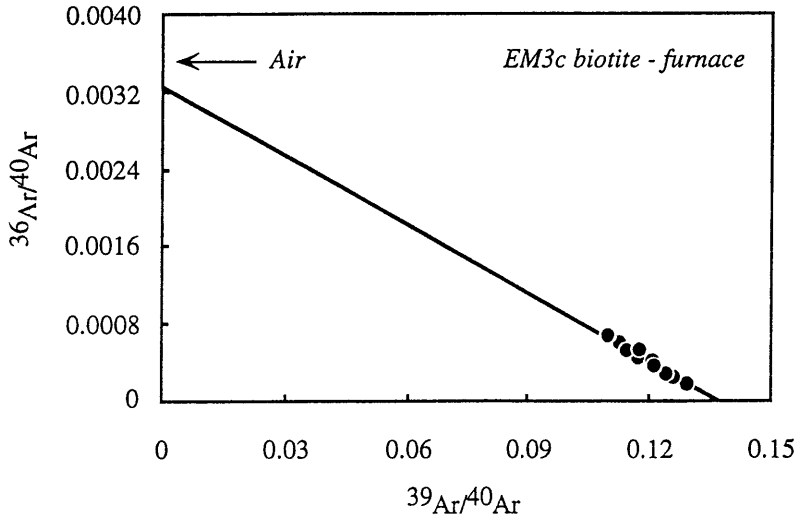

Figure 10a

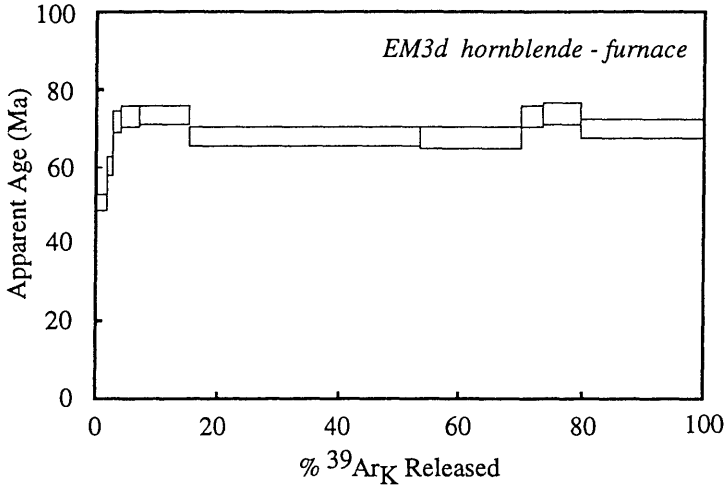

Figure 10b

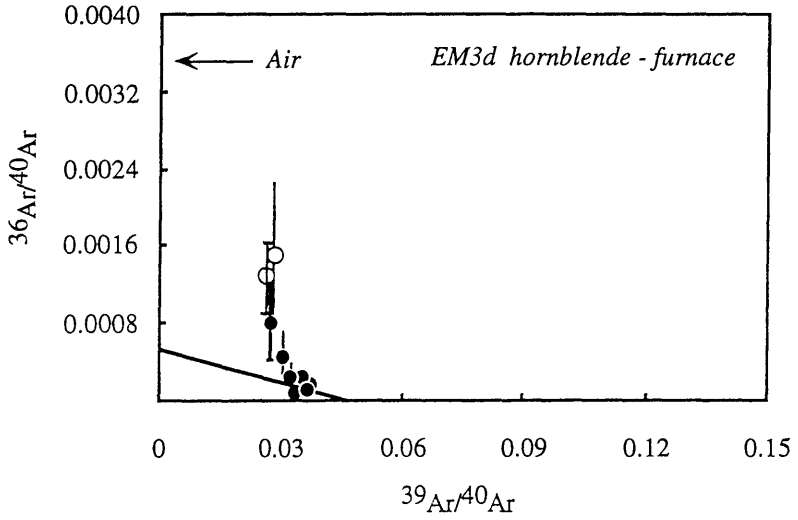

Figure 10c

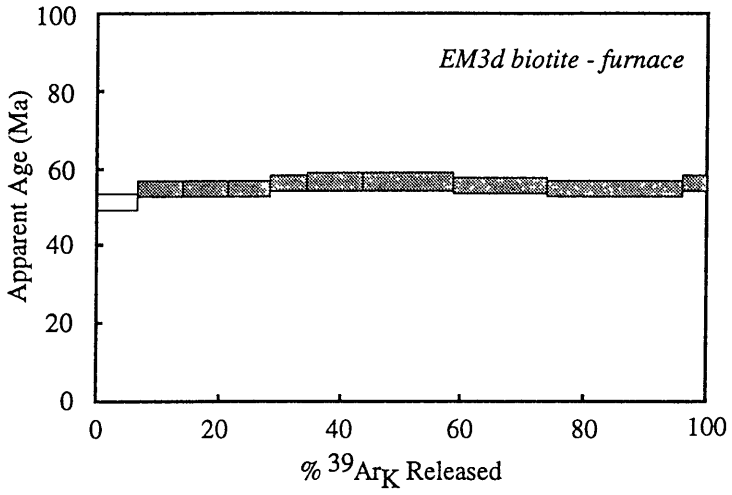

Figure 10d

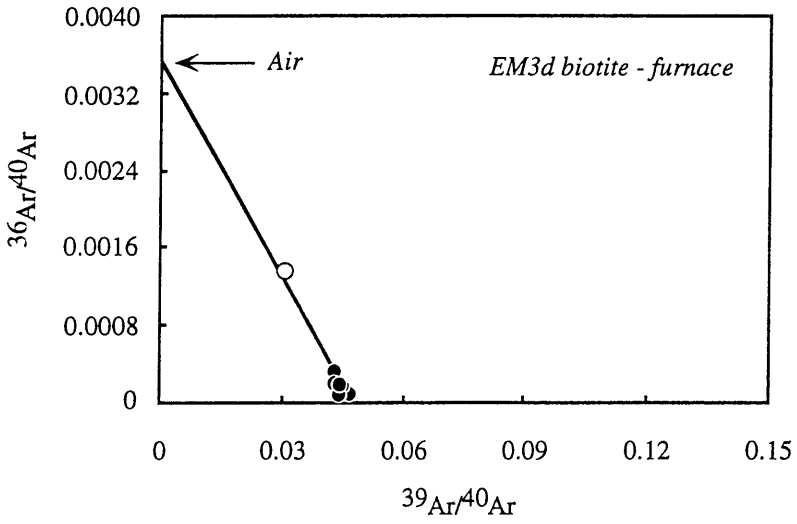

Figure 11a

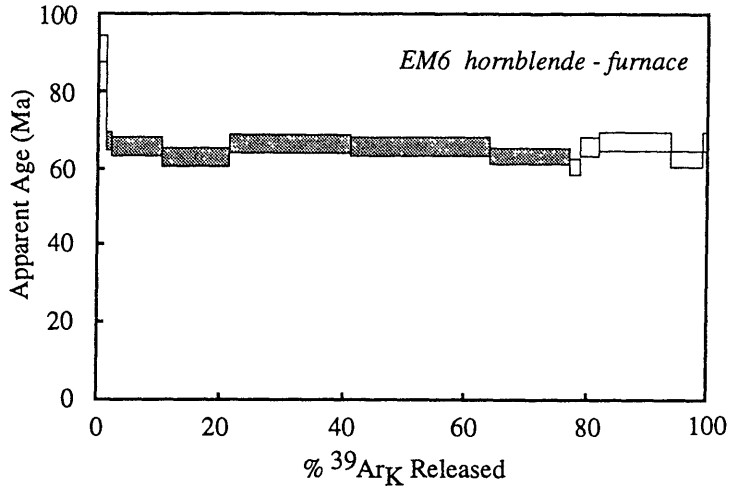

Figure 11b

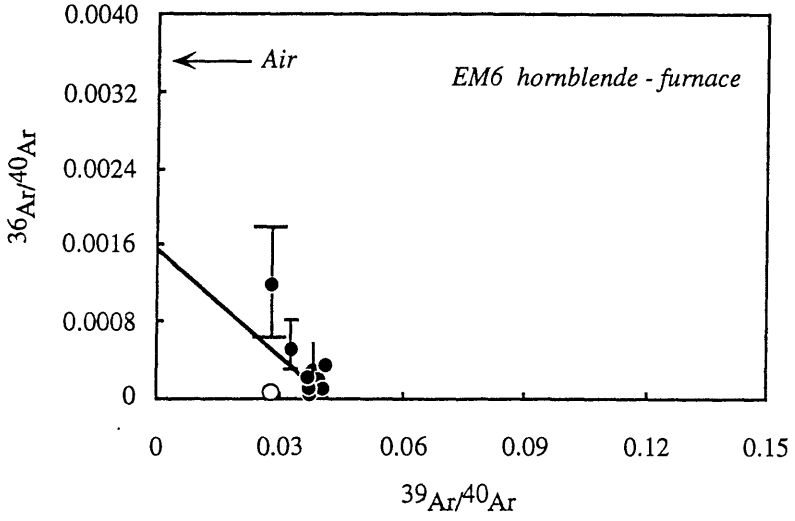

Figure 11c

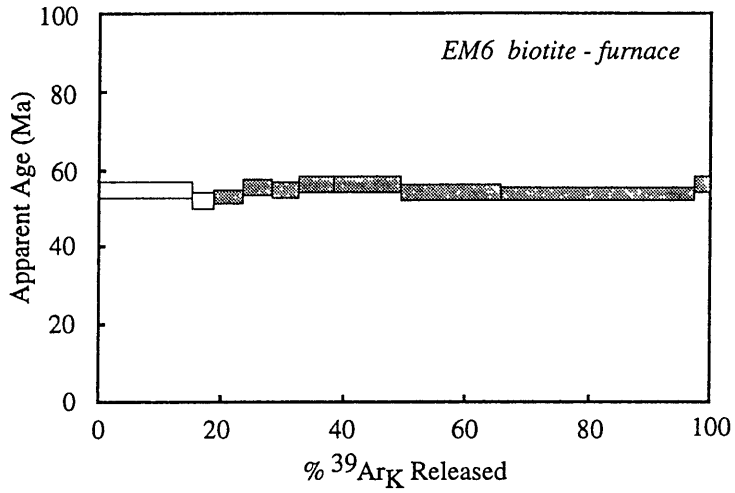

Figure 11d

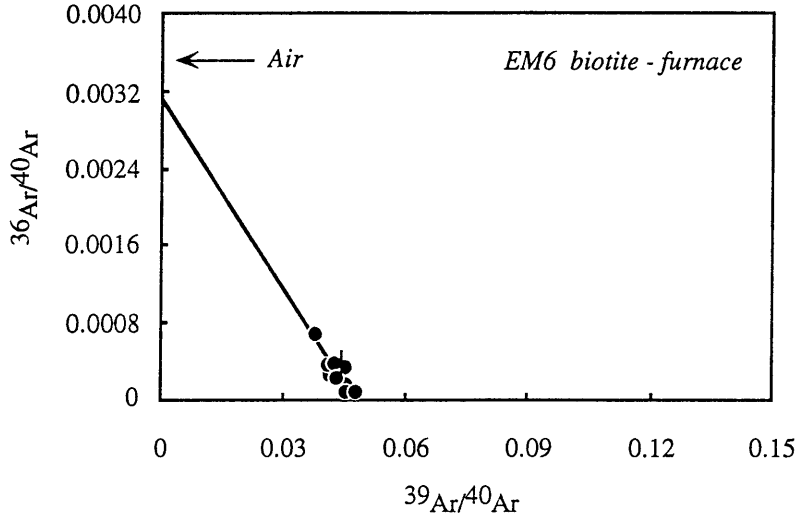

Figure 12

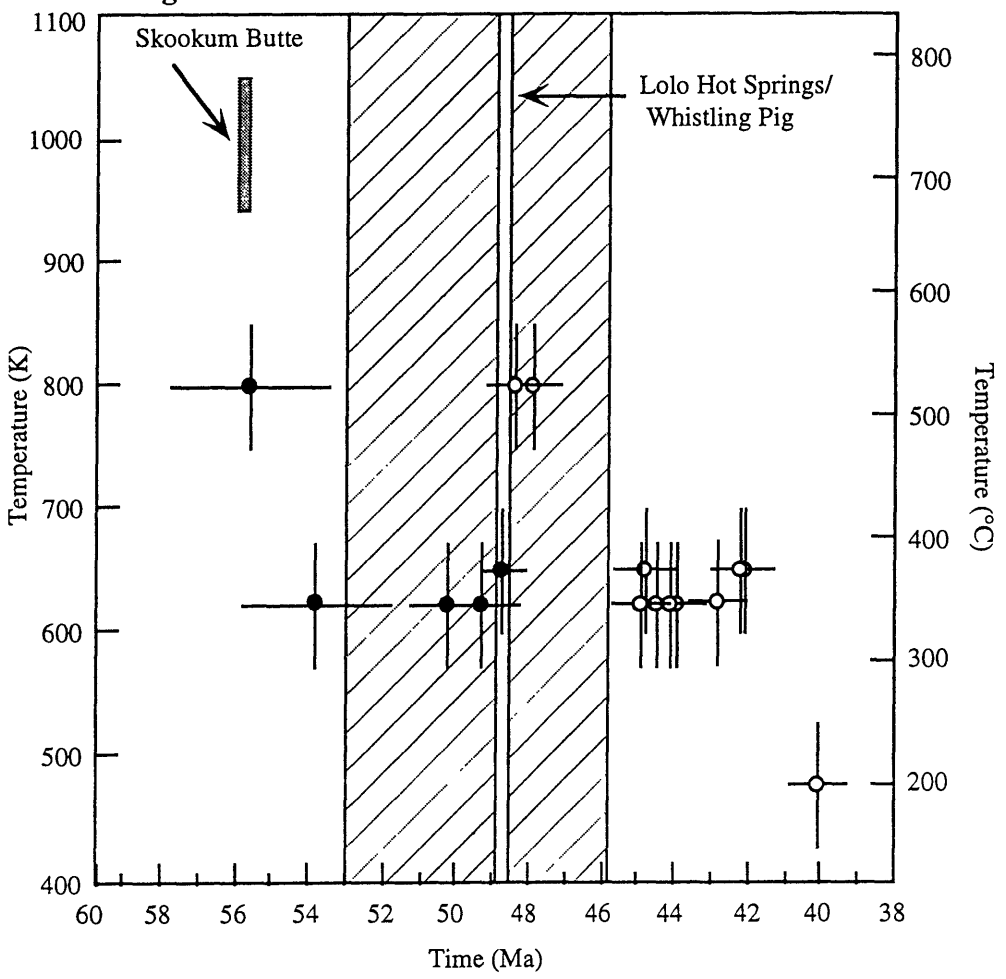
Skookum Butte
Lolo Hot Springs/
Whistling Pig
Temperature (K)
Temperature (°C)
Time (Ma)
1100
1000
900
800
700
600
500
400
800
700
600
500
400
300
200
60
58
56
54
52
50
48
46
44
42
40
38

CHAPTER 5

THE SPRUCE CREEK MYLONITE: AN EXHUMED SPLAY OF A REGIONALLY EXTENSIVE THRUST PLATE IN THE CENTRAL CLEARWATER OROGENIC ZONE

ABSTRACT

Although the Bitterroot metamorphic core complex of western Montana and eastern Idaho occupies a central position within the Cretaceous Clearwater orogenic zone, the correlation of major thrust structures across the complex has proved problematic. In this paper we describe a shallowly west-dipping ductile shear zone in the core complex footwall - the Spruce Creek mylonite zone - that we interpret as an important Cretaceous shortening structure developed at amphibolite facies conditions. The shear zone contains fabrics consistent with east-southeastward displacement of the hanging-wall relative to the footwall, in a thrust sense. Cross-cutting intrusive rocks constrain the minimum age of the shear zone as 55 Ma. We propose that the Spruce Creek structure correlates with similar faults in the Boehls Butte region on the northwestern margin of the Bitterroot batholith. If correct, this interpretation requires a minimum of ~60 km of left-lateral displacement on the intervening Lewis and Clark fault zone prior to the initiation of Tertiary right-lateral motion on this long-lived strike-slip system. Correlation of the Spruce Creek shear zone with elements of the Sapphire thrust system in the Sapphire Range to the east suggests ~50 km of eastward displacement on the Bitterroot mylonite zone and related structures that accommodated tectonic denudation of the Bitterroot metamorphic core complex during Eocene times.

INTRODUCTION

Patterns of Mesozoic thrusting in the central North American Cordillera are complicated by Tertiary extension and magmatism. The Clearwater orogenic zone (Reid and Greenwood, 1968; Reid *et al.*, 1973) of north-central Idaho and western Montana is an example of a region where Tertiary magmatic and extensional activity have made identification of large-scale thrust plates difficult. This region extends from the Lewis and Clark fault zone on the north to the Salmon River Arch in the south; the eastern limits of the terrain extend to the Sapphire Range and the western margin is defined by the Seven Devils terrain (Figure 1; Reid and Greenwood, 1968; Reid *et al.*, 1973). The Bitterroot metamorphic core complex (BMCC), one of the largest such features in the North American Cordillera, occurs within this region, yet no previous workers have mapped major shortening structures within the core complex footwall. Regional structural relationships suggest, however, that a segment of one major Clearwater structure (the Cabin thrust) might occur in this area. In this paper, we suggest that an important shear zone in the northern Bitterroot Range—the Spruce Creek mylonite zone of Lewis *et al.* (1992)—correlates with the Cabin thrust. If this correlation is correct, it has important implications for the magnitude of displacement on the detachments that bound the BMCC, and for the amount of pre-Tertiary, left-lateral movement on the southernmost splays of the Lewis and Clark fault zone.

GENERAL GEOLOGY

The Clearwater orogenic zone is developed in granites and granodiorites of the Bitterroot batholith (Figure 1). These granitoids range in age from ~100 Ma to as young as 48 Ma and intrude Early Proterozoic basement rocks and the overlying Proterozoic Belt Supergroup (Armstrong, 1975; Bickford *et al.*, 1981; Chase *et al.*, 1983; Toth, 1987). East-vergent thrusting in the region is considered to be Cretaceous in age and was followed by a period of Eocene extension, resulting in exposures of

high-grade metamorphic rocks in several locations including the BMCC and at Boehls Butte (Chase *et al.*, 1983; Hietanen, 1984; Grover *et al.*, 1992; House, Chapter 3). Peak metamorphism in these areas occurred at depths of 20 - 30 km. The latest stages of extension are accompanied by Challis magmatic activity.

In this region, the Belt Supergroup reaches a maximum thickness of ~20 km and rests unconformably on ~1,700 Ma crystalline basement (Harrison *et al.*, 1980). Layered anorthosites, commonly inferred to represent basement rocks, are exposed at Boehls Butte; smaller exposures are present in the core of the BMCC (Figure 1; Hietanen, 1963; Berg, 1968; Cheney, 1972; Cheney, 1975). Four major stratigraphic units present in most of the Belt terrain are the Prichard Formation, the Ravalli Group, the Wallace Formation, and the Missoula Group (Harrison *et al.*, 1980). In the Sapphire Range, these units are generally unmetamorphosed. They are metamorphosed at middle- to upper-amphibolite facies conditions and retain little of their original sedimentary features in regions surrounding the Bitterroot batholith (Wallace *et al.*, 1989; Grover *et al.*, 1992).

Metamorphosed Prichard Formation occurs as quartz-muscovite-biotite schists that occasionally contain sillimanite, kyanite, and garnet (Chase, 1973). Metamorphosed Ravalli Group quartzites have minor interlayers of muscovite schist and cross-laminations are locally preserved (Lewis *et al.*, 1992). The Wallace Formation is a calcareous siltite and argillite that is exposed in the Sapphire Range and in the regions north of Boehls Butte (Lewis *et al.*, 1992). The metamorphosed equivalent of the lower and middle members of the Wallace Formation is a highly recrystallized hornblende-diopside-quartz-plagioclase gneiss (Hietanen, 1963; Chase, 1973; Wallace *et al.*, 1989; Lewis *et al.*, 1992). The overlying Missoula Group is present primarily in the Sapphire Range. This unit is a laminated siltite and argillite with subordinate fine-grained quartzite (Wallace *et al.*, 1989). When metamorphosed, the Missoula Group closely resembles the Prichard Formation schists and gneisses.

THRUSTING IN THE CLEARWATER OROGENIC ZONE

East-vergent thrust faulting in the central Clearwater orogenic zone was at one time considered to be genetically related to the development of the BMCC. The core-bounding Bitterroot mylonite zone was thought to be the exhumed root of Late Cretaceous thrusts exposed in the Sapphire Range to the east (Figure 1; Hyndman, 1980). These structures presumably accommodated displacement of hanging-wall rocks (referred to as the Sapphire block) prior to intrusion of the Bitterroot batholith. Subsequent studies demonstrated that the Bitterroot mylonite zone and the Sapphire Range thrusts were of very different ages: the Bitterroot mylonite zone is an Eocene extensional structure (Bickford *et al.*, 1981; Chase *et al.*, 1983; Hodges and Applegate, 1993; House and Hodges, 1994), whereas east-vergent thrusts in the Sapphire Range are constrained by cross-cutting relations to be Cretaceous in age (Desmarais, 1983; Wallace *et al.*, 1989). Thus, while thrusting and extension shared a common direction of movement, they reflect events separated in time by up to 30 Ma.

The Sapphire thrust plate (Wallace *et al.*, 1989) is bounded on the north by the Lewis and Clark line, and the southern and eastern margins are intruded by granites of the Boulder and Bitterroot batholiths (Figure 1). The western margin is cut by the Bitterroot mylonite zone. Wallace *et al.* (1989) determined that the Sapphire thrust sheet is a composite feature, including two major imbricate thrusts carried in the hanging wall of the basal Sapphire thrust fault (Figure 2). They interpreted the observed field relationships, which resulted in the stacking of Wallace Formation, Missoula Group, and Wallace Formation in ascending order, in terms of two phases of deformation: 1) emplacement and folding of early thrust sheets carrying Wallace Formation in their hanging walls; followed by 2) break-back thrusting and imbrication of the earlier thrust sheets. The resulting complex structure is characterized by ~1500 - 4500 m-thick rock packages of a variety of metamorphic grades juxtaposed by low-temperature shear zones. Ages for the two periods of deformation are based on cross-

cutting relationships. Granites and granodiorites of the Sapphire and Bitterroot batholiths that have been dated using K-Ar at 73 Ma and 78 Ma, respectively, cut the thrusts, and place a lower limit on their ages (Desmarais, 1983; Wallace *et al.*, 1989).

Structural mapping north of the BMCC at Boehls Butte has led to the identification of at least two generations of northwest-striking northeast- to east-vergent thrusts (Figure 3; Harrison *et al.*, 1986). The Boehls Butte structures carry Prichard Formation hanging-wall rocks to the east-northeast over Wallace Formation units. Several younger splays cut earlier structures and place Wallace Formation calc-silicate gneisses on pelitic schists of the Prichard Formation (Harrison *et al.*, 1986). These thrusts are associated with a period of regional metamorphism that produced a strong foliation in the rocks (Lang and Rice, 1985). These faults predate emplacement of the Bitterroot batholith and are cut by sinistral and dextral strike-slip faults associated with the Lewis and Clark line and Tertiary high-angle faulting (Harrison *et al.*, 1986).

Geologic mapping and reinterpretation of existing maps in the regions to the north and south of the BMCC led Skipp (1987) to correlate the Boehls Butte and Sapphire thrusts with the Cabin thrust in the Beaverhead Mountains south of the BMCC (Figure 1; Skipp, 1987), which places middle Proterozoic Prichard Formation over Missoula Group rocks. In Skipp's model, the Cabin thrust ramps down-section in the hanging wall to the north, placing Lower Proterozoic basement rocks over Belt rocks. She suggested that the upper-plate of the Cabin thrust is exposed in the footwall of the BMCC. Subsequent Tertiary extension displaced the Cabin thrust down-dip to the east.

While there is considerable evidence for through-going thrust sheets in this region, there is little geologic evidence in the Sapphire Range or the Boehls Butte area to support the Cabin thrust model as it stands. Mapped exposures of basement rocks appear to be in contact with Belt units due to Tertiary normal faulting rather than thrusting (Hietanen, 1963; Hietanen, 1984; Grover *et al.*, 1992). All thrusts currently

mapped in these regions carry Belt rocks in the hanging wall and there is no evidence for basement exposures in the Sapphire thrust plate, as suggested by (Skipp, 1987).

An alternative explanation of the thrust geometry in this region calls for the core rocks of the BMCC to be in the footwall of a regional thrust sheet that we term the Cabin-Sapphire thrust sheet. This thrust plate consists of imbricate sheets of Middle Proterozoic units carried eastward during two distinct periods of thrusting corresponding to those described by Wallace *et al.* (1989). Extensional modification of the overriding thrust plate by the Bitterroot mylonite zone calls for exposure of the Cabin thrust sheet somewhere in the western part of the core complex. A possible candidate for this contact is the Spruce Creek mylonite zone (Lewis *et al.*, 1992) which separates rocks of the Wallace Formation in the hanging wall from metamorphosed equivalents of the Prichard Formation in the footwall (Lewis *et al.*, 1992; House, unpublished mapping).

SPRUCE CREEK MYLONITE

The Spruce Creek mylonite zone is exposed ~20 km west of the Bitterroot mylonite zone in the northwestern BMCC (Plate 1, Figure 4; Ferguson, 1972; Lewis *et al.*, 1992). It is ~2 km wide and strikes north-south and dips moderately to the west (Figure 5a); mineral/stretching lineations developed within the shear zone plunge shallowly westward, with a mean orientation of 32°/271° (Figure 5b). Low topographic relief and the abundance of Quaternary alluvium and dense forests makes detailed mapping of this shear zone difficult (Figure 6). Hanging-wall rocks of the Wallace Formation (Lewis *et al.*, 1992) increase in metamorphic grade toward the shear zone and are characterized by green (diopside and actinolite) and white (plagioclase and quartz) banding (Figure 7a). Diopside is replaced by hornblende near contacts with Bitterroot batholith granitoids. This green and white layering is characteristic of the

lower members of the Wallace Formation in the Boehls Butte region (Harrison *et al.*, 1986; Lewis *et al.*, 1992).

Shear zone rocks are tightly folded quartzofeldspathic and calc-silicate gneisses (qg) and muscovite-biotite-quartz pelitic schists (ps) that locally contain sillimanite (Figure 7; Lewis *et al.*, 1992; House, unpublished mapping). The quartzofeldspathic and calc-silicate gneisses are most likely the metamorphosed equivalents of intermixed Wallace Formation and Ravalli Group. The metapelitic units represent the Prichard Formation and are weakly to strongly mylonitic in the study area (Figure 4). Medium-grained hornblende-biotite tonalites (Kt) intrude the schists and quartzofeldspathic gneisses and exhibit planar features related to the shear zone (Figure 7d). The mylonite zone is cut by granites and granodiorites of the Bitterroot batholith (Kgd) and associated migmatites (Kmig).

Pelites and quartzofeldspathic gneisses in the Spruce Creek mylonite zone are strongly foliated Type II S-C mylonites (Lister and Snoke, 1984). S-planes are defined by shape anisotropy of recrystallized quartz neoblasts and the C-planes are defined by recrystallized mica. Mica fish with the [001] plane sub-parallel to the C-planes are ubiquitous in pelites and are connected by trains of recrystallized mica (Figure 8a - d). In quartzofeldspathic gneisses and tonalites, the mylonitic foliation wraps around rigid porphyroclasts of plagioclase resulting in the development of quartz-filled pressure shadows or "wings" (Figure 8e, f; Hanmer and Passchier, 1991). The geometry of the porphyroclasts and associated "wings" is that of the Greek letter σ, and is suggestive of high recrystallization rates (Passchier and Simpson, 1986; Hanmer and Passchier, 1991). Feldspar augen structures and S-C fabrics in metapelitic rock outcrops are also apparent in thin section (Figure 7c). Asymmetric fold trains are also consistent with east-vergence (Figure 9).

Microstructural features in the shear zone rocks are indicative of deformation at upper-greenschist to lower-amphibolite facies conditions. Fibrolitic sillimanite is often

present in the mica layers (Figure 10). In pelites, quartz neoblasts with long axes parallel to the C-plane are ubiquitous and quartz grain boundaries are serrate; neoblasts display no evidence for undulose extinction. In the quartzofeldspathic gneiss, quartz is extensively recrystallized with a strong grain-shape preferred orientation and lattice preferred orientation. Plagioclase deforms rigidly with fractures orthogonal to the C-plane. K-feldspar is locally surrounded by mortar texture, indicative of grain boundary recrystallization. These textures are suggestive of deformation occurring at temperatures of ~675 - 775 K (Simpson, 1985; Simpson and DePaor, 1991).

Lewis *et al.* (1992) interpreted the Spruce Creek mylonite zone as a westward extension of the Bitterroot mylonite zone that had been folded into its present westward dip by late doming of the range. Although it is true that the transport direction was similar for both structures—at this latitude, stretching lineations in the Bitterroot mylonite zone indicate a 28°/108° transport vector (House, unpublished data)—geochronologic data preclude correlation of the two. The Spruce Creek mylonite zone is intruded by the Skookum Butte stock along its northern margin (Figure 4) and therefore must be older than the 55.8 ± 0.1 Ma U-Pb monazite age of the stock (House, Chapter 4). Deformational fabrics associated with the Bitterroot mylonite zone are developed in granitic rocks with U-Pb zircon crystallization ages as young as 48 Ma (Chase *et al.*, 1983), and $^{40}Ar/^{39}Ar$ data from the eastern Bitterroot Ranges point to a ~48 Ma age for deformation in the range-bounding mylonite zone (Hodges and Applegate, 1993; House and Hodges, 1994). Because the Spruce Creek shear zone predates Eocene extension on the Bitterroot mylonite zone and related structures, and because shear-sense criteria for related fabrics indicate thrust displacement in present coordinates, we suggest that it represents part of the Cabin-Sapphire thrust system and correlates with thrusts mapped at Boehls Butte to the north. Although one argument against a thrust interpretation for the shear zone is that it places younger rocks on older,

such relationships are common in the complex thrust imbricate packages in the Sapphire Range and at Boehls Butte (Harrison *et al.*, 1986; Wallace *et al.*, 1989).

TECTONIC IMPLICATIONS

Correlation of the Spruce Creek mylonite zone with thrusts mapped at Boehls Butte suggests a considerable component of left-lateral motion between the two regions, possibly accommodated by pre-Tertiary motion on a southern splay of the Lewis and Clark fault zone. The Kelly Forks fault is one splay that has been shown to offset thrusts in a left-lateral sense (Hyndman *et al.*, 1988). The northwest-southeast trending fault bounds the southern margin of Boehls Butte and is cut by granites of the Idaho batholith. Projection of this fault through the granitoids places it on the northern margin of the BMCC, north of the Spruce Creek mylonite zone. General map relations call for ~45 - 50 km of left-lateral offset in a northwest-southeast direction between the two regions. This offset may be related to pre-intrusive deformation prior to emplacement of the Bitterroot batholith, or it may reflect the more general effects of changing plate interactions that began prior to batholith emplacement (Harrison *et al.*, 1980).

Many workers have suggested a genetic link between extension and Tertiary right-lateral displacement on the Lewis and Clark fault zone (e.g., Sheriff *et al.*, 1984; Wernicke, 1991) The general strike of the fault zone parallels the extension direction and its splays bound regions that were exhumed by Tertiary unroofing. Many of the right-lateral splays cut thrusts; therefore restoring the thrusts exposed in the Sapphire Range westward to the position of the Spruce Creek mylonite provides an upper-limit on the amount of right-lateral displacement accommodated by the southern Lewis and Clark fault zone as well as the associated extension on the Bitterroot mylonite zone. Restoration of thrusts in the Sapphire Range westward along a trajectory parallel to the mylonitic lineation calls for a maximum of ~50 km of eastward transport. This estimate is consistent with estimates of 60 km of eastward transport estimated by Hyndman

(1980) as well as independent estimates of 35 - 81 km for the magnitude of right-lateral offset (Harrison *et al.*, 1974; Sheriff *et al.*, 1984). Because the projection of the Sapphire thrusts is purely speculative, and there is little control on the exact relationship between these structures and the Spruce Creek mylonite, these estimates are only broad upper-limits.

CONCLUSIONS

Correlation of the east-vergent Spruce Creek mylonite to thrusts exposed to the north and south of the BMCC refines published models for the distribution of major thrust sheets in the central Clearwater orogenic zone. Field relationships and shear sense indicators are consistent with east-vergent motion prior to emplacement of 55 Ma plutons which cut the mylonite zone. We suggest that the Spruce Creek mylonite is a splay of thrusts exposed in the southern Sapphire range and in the vicinity of Boehls Butte (Harrison *et al.*, 1986) and refer to these thrusts as the Cabin-Sapphire thrust plate. Restoration of the pre-extensional configuration of the Cabin-Sapphire thrust provides limits on the amount of left-lateral offset accommodated by early motion on the Lewis and Clark fault zone, as well as broad limits on the magnitude of Tertiary extension and right-lateral motion. Further detailed mapping in these regions should clarify the exact nature of faults such as the Kelly Forks fault, which are crucial to resolving the pre-extensional geometry of major thrust plates in the Clearwater orogenic zone.

REFERENCES

Armstrong, R. L., 1975, Precambrian (1500 m.y. old) rocks of central Idaho-The Salmon River arch and its role in Cordilleran sedimentation and tectonics: American Journal of Science, v. 275-A, p. 437-467.

Berg, R. B., 1968, Petrology of anorthosites of the Bitterroot Range, Montana, in Isachsen, Y. W., ed., Origin of Anorthosite and Related Rocks: Albany, NY, New York State Museum and Science Service Memoir 18, p. 387-398.

Bickford, M. E., Chase, R. B., Nelson, B. K., Schuster, R. D., and Arruda, E. C., 1981, U-Pb studies of zircon cores and overgrowths, and monazite: Implications for age and petrogenesis of the northeastern Idaho batholith: Journal of Geology, v. 89, p. 433-457.

Chase, R. B., 1973, Petrology of the northeastern border zone of the Idaho batholith, Bitterroot Range, Montana: Montana Bureau of Mines and Geology Memoir, v. 43, p. 1-28.

Chase, R. B., Bickford, M. E., and Arruda, E. C., 1983, Tectonic implications of Tertiary intrusion and shearing within the Bitterroot dome, northeastern Idaho batholith: Journal of Geology, v. 91, p. 462-470.

Cheney, J. T., 1972, Petrologic relationships of layered meta-anorthosites and associated rocks, Bass Creek, western Montana [M.A.]: University of Montana.

Cheney, J. T., 1975, Kyanite, sillimanite, phlogopite, cordierite layers in the Bass Creek anorthosites, Bitterroot Range, Montana: Northwest Geology, v. 4, p. 77-82.

Desmarais, N. R., 1983, Geology and geochronology of the Chief Joseph plutonic-metamorphic complex, Idaho-Montana [Ph.D.]: University of Washington.

Ferguson, J. A., 1972, Fission track and K-Ar dates on the northeastern border zone of the Idaho batholith [M.S.]: University of Montana.

Grover, T. W., Rice, J. M., and Carey, J. W., 1992, Petrology of aluminous schist in the Boehls Butte region of northern Idaho: Phase equilibria and P-T evolution: American Journal of Science, v. 292, p. 474-507.

Hanmer, S. and Passchier, C.,1991, Shear-sense indicators: A review: Paper 90-17, Geological Survey of Canada, 72 p.

Harrison, J. E., Griggs, A. B., and Wells, J. D., 1974, Tectonic features of the Precambrian Belt Basin and their influence on post-Belt structures: U.S. Geological Survey Professional Paper 866, 15 p.

Harrison, J. E., Griggs, A. B., and Wells, J. D., 1986, Geologic and structure maps of the Wallace 1°x2° quadrangle, Montana and Idaho, U.S. Geological Survey Miscellaneous Geologic Investigations Map I-1509.

Harrison, J. E., Kleinkopf, M. D., and Wells, J. D., 1980, Phanerozoic thrusting in Proterozoic Belt rocks, northwestern United States: Geology, v. 8, p. 407-411.

Hietanen, A., 1963, Anorthosite and Associated Rocks in the Boehls Butte Quadrangle and Vicinity, Idaho: U.S. Geological Survey Professional Paper 344-B, p. B1-B75.

Hietanen, A., 1984, Geology along the northwest border zone of the Idaho batholith, northern Idaho: U.S. Geological Survey Bulletin, v. 1608, 17 p.

Hodges, K. V. and Applegate, J. D. R. A., 1993, Age of Tertiary extension in the Bitterroot metamorphic core complex, Montana and Idaho: Geology, v. 21, p. 161-164.

House, M. A. and Hodges, K. V., 1994, Limits on the tectonic significance of rapid cooling events in extensional setting: Insights from the Bitterroot metamorphic core complex, Idaho-Montana: Geology, v. 22, p. 1007-1010.

Hyndman, D. W., 1980, Bitterroot dome - Sapphire tectonic block, an example of a plutonic-core gneiss-dome complex with its detached suprastructure, in Crittenden, M. D., Coney, P. J., and Davis, G. H., ed., Cordilleran Metamorphic Core Complexes: Boulder, CO, Geological Society of America Memoir 153, p. 427-443.

Hyndman, D. W., Alt, D., and Sears, J. W., 1988, Post-Archean metamorphic and tectonic evolution of western Montana and northern Idaho, in Ernst, W. G., ed., Metamorphism and Crustal Evolution of the Western United States: Englewood Cliffs, NJ, Prentice Hall, p. 332-361.

Lang, H. M. and Rice, J. M., 1985, Metamorphism of pelitic rocks in the Snow Peak area, northern Idaho: Sequence of events and regional implications: Geological Society of America Bulletin, v. 96, p. 731-736.

Lewis, R. S., Burmeister, R. F., Reynolds, R. W., Bennett, E. H., Myers, P. E., and Reid, R. R., 1992, Geologic map of the Lochsa River area, Northern Idaho: Moscow, Idaho Geological Survey.

Lister, G. S. and Snoke, A. W., 1984, S-C mylonites: Journal of Structural Geology, v. 6, p. 617-638.

Passchier, C. W. and Simpson, C., 1986, Porphyroclast system as kinematic indicators: Journal of Structural Geology, v. 8, p. 831-843.

Reid, R. R. and Greenwood, W. R., 1968, Multiple deformation and associated progressive polymetamorphism in the Beltian rocks north of the Idaho batholith, Idaho: International Geological Conference, p. 74-87.

Reid, R. R., Morrison, D. A., and Greenwood, W. R., 1973, The Clearwater orogenic zone: A relict of Proterozoic orogeny in central and northern Idaho: Belt Symposium, Volume 1, Moscow, Idaho Bureau of Mines and Geology, p. 10-56.

Sheriff, S. D., Sears, J. W., and Moore, J. N., 1984, Montana's Lewis and Clark fault zone: an intracratonic transform fault system: Geological Society of America Abstracts with Programs, 16, p. 653-654.

Simpson, C., 1985, Deformation of granitic rocks across the brittle-ductile transition: Journal of Structural Geology, v. 5, p. 503-511.

Simpson, C. and DePaor, D., 1991, Deformation and kinematics of high strain zones: Geological Society of America Short Course, 116 p.

Skipp, B., 1984, Geologic map and cross sections of the Italian Peak and Italian Peak Middle Roadless area, Beaverhead County, Montana, and Clark and Lemhi counties, Idaho: U.S. Geological Survey Miscellaneous Geologic Field Studies Map MF-1601-B.

Toth, M. I., 1987, Petrology and Origin of the Bitterroot Lobe of the Idaho batholith: U.S. Geological Survey Professional Paper 1436, p. 9-37.

Wallace, C. A., Lidke, D. J., Waters, M. R., and Obradovich, J. D., 1989, Rocks and structure of the southern Sapphire mountains, Granite and Ravalli Counties, western Montana: U.S. Geological Survey Bulletin, v. 1824, 29 p.

Wernicke, B., 1991, Cenozoic extensional tectonics of the U.S. Cordillera, in Burchfiel, B. C., Lipman, P. W., and Zoback, M. L., ed., The Cordilleran Orogen: Conterminus United States: Boulder, CO, Geological Society of America, The Geology of North America, p.553-582.

FIGURE CAPTIONS

Figure 1. Regional map of the Bitterroot metamorphic core complex including features described in the text. Modified from Hyndman *et al.* (1988). Box insets show locations of figures 2 - 4. Heavy lines show faults; strike-slip faults are indicated by arrows; thrust faults and normal faults are indicated by teeth and barbs on the upper plate.

Figure 2. Simplified geologic map and cross-section of the southern Sapphire Range, modified from Wallace *et al.*, (1989). Numbered thrusts indicate relative ages of thrusts.

Figure 3. Simplified geologic map of the Boehls Butte region, modified from Harrison (1986) and Heitanen (1968). Map units: an—pre-Belt basement anorthosites; ps—schists and gneisses of the Prichard Fm.;Yw—Wallace Fm.; Kgd—granitoids associated with the Bitterroot batholith.

Figure 4. Simplified geologic map of the Spruce Creek mylonite. Map units: ps—schists and gneisses of the Prichard Fm.; qg—intensely folded quartzofeldspathic and calc-silicate gneisses; Yw—Wallace Fm.; Kt—foliated diorites and tonalites; Kgd—granitoids associated with the Bitterroot batholith; Kmig—migmatites associated with the Bitterroot batholith. Approximate limits of shear zone indicated by hatched region.

Figure 5. Lower-hemisphere equal area projections of poles to mylonitic foliations and mineral/stretching lineations from the Spruce Creek mylonite (a, b). Contour interval for (a) is 4%/1% area. Mean vector indicated by square.

Figure 6. Photo of the Spruce Creek mylonite looking north from Beaver Ridge, Idaho. Approximate boundaries of map units in Figure 4 indicated by text. Units in foreground of wide line are included in the Spruce Creek mylonite zone.

Figure 7. Photos of major lithologic units associated with the Spruce Creek mylonite. (a) Wallace Fm. calc-silicate gneiss (Yw); (b) intensely folded quartzite and calc-silicate gneiss in shear zone (qg); (c) mylonitic pelitic schist (ps) with asymmetric lenses of felsic material; metamorphic equivalent of the Prichard Fm.; west is to left ; (d) foliated tonalite (Kt). All outcrop photos looking north. Hammer for scale (a, b, c) and lens-cap for scale (d).

Figure 8. Photomicrographs, oriented parallel to the mineral lineation, illustrating S-C relationships in shear zone rocks. Plane and polarized photos of mylonitic schist samples EM4 (a, b) and EM31(c, d). Asymmetric augen from tonalite sample 14-4 (e, f). East is to left; scale bar superimposed on (a-d); (e) and (f) are 4 mm in the long dimension. Lineation plunges ~45°/265.

Figure 9. Photo of east-vergent folds of felsic material in pelitic schist (ps). Looking north. Lens-cap for scale.

Figure 10. Photomicrograph of fibrolite (Sil) parallel to mylonitic foliation in Spruce Creek mylonite zone. East is to left; field of view is 4 mm in the long dimension.

Figure 1

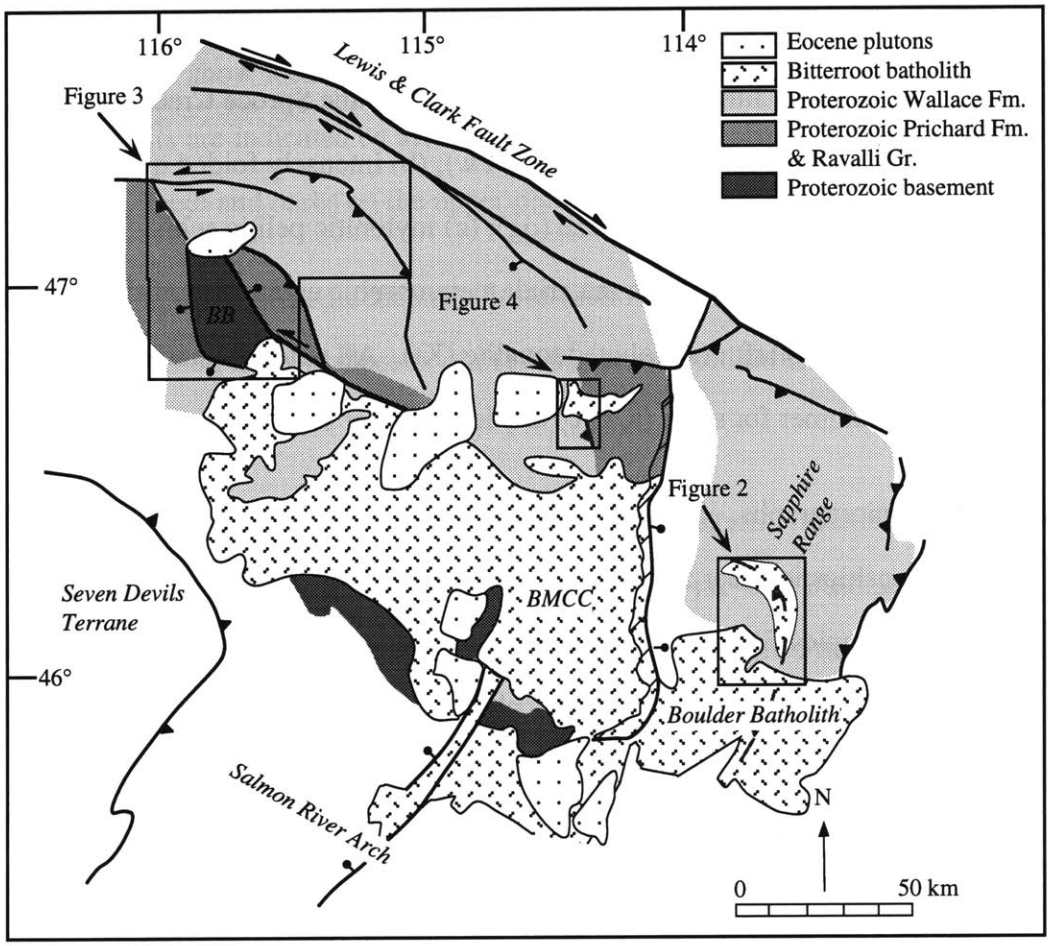
116°
115°
114°
47°
46°
Lewis & Clark Fault Zone
Figure 3
Figure 4
Figure 2
BB
BMCC
Seven Devils Terrane
Saphire Range
Boulder Batholith
Salmon River Arch
Eocene plutons
Bitterroot batholith
Proterozoic Wallace Fm.
Proterozoic Prichard Fm. & Ravalli Gr.
Proterozoic basement
N
0
50 km

Figure 2

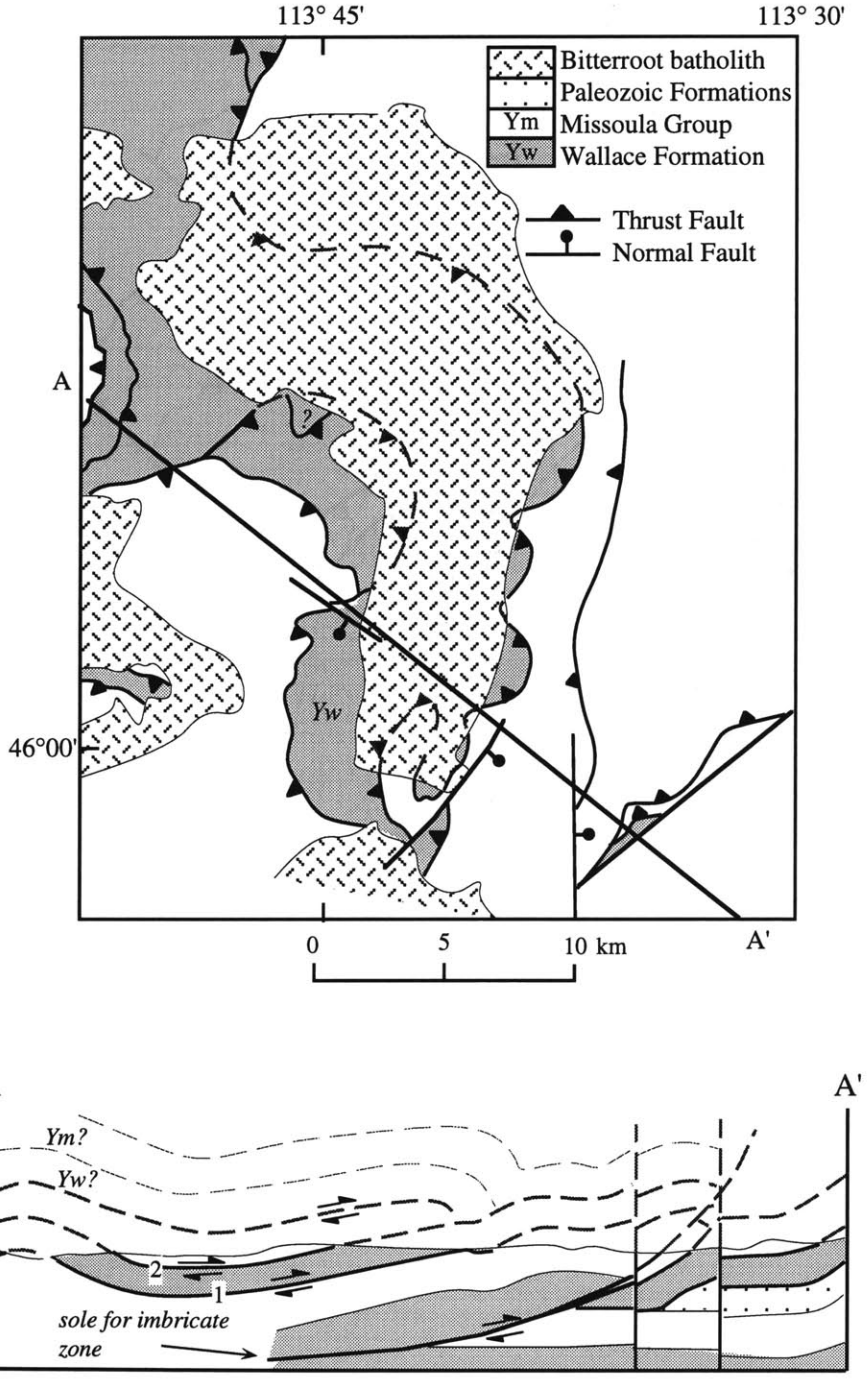
113° 45'
113° 30'
Bitterroot batholith
Paleozoic Formations
Ym Missoula Group
Yw Wallace Formation
Thrust Fault
Normal Fault
A
?
Yw
46°00'
0
5
10 km
A'
A
A'
Ym?
Yw?
2
1
sole for imbricate zone

Figure 3

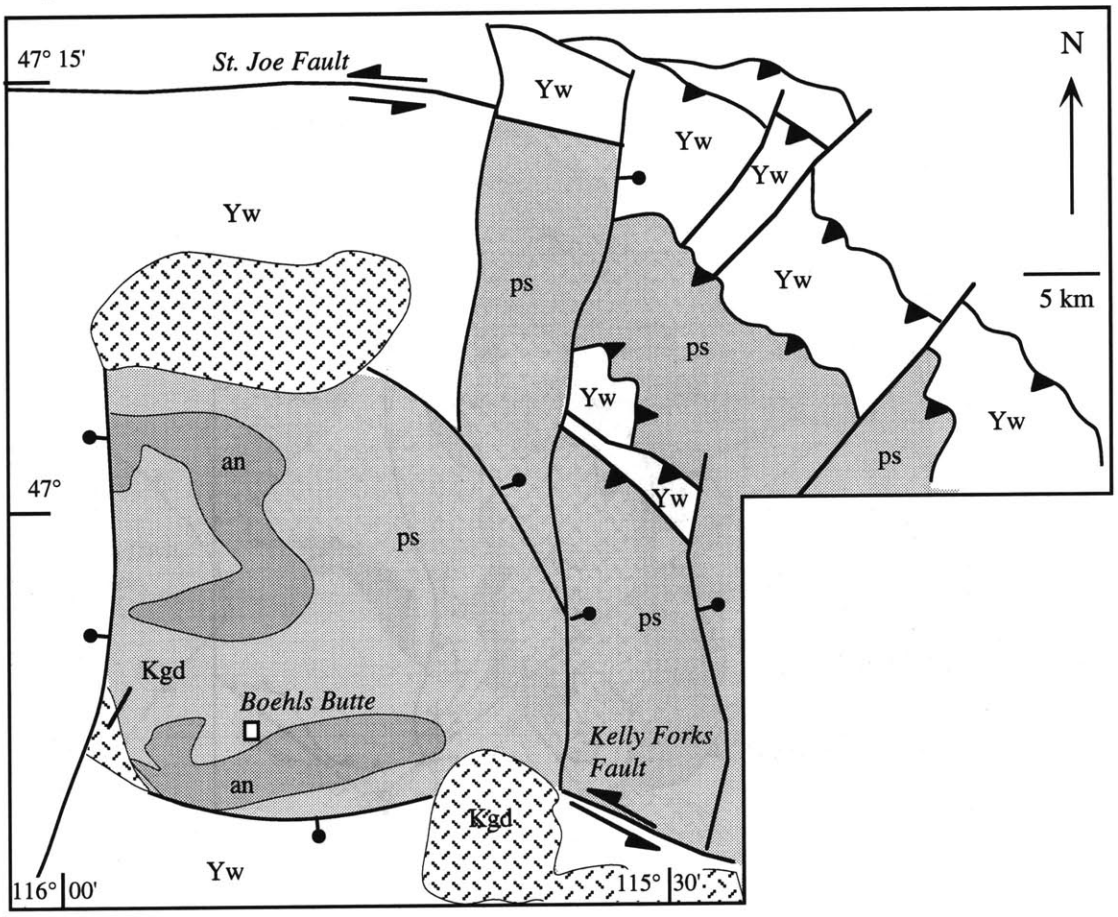
47° 15'
St. Joe Fault
N
5 km
Yw
ps
an
47°
Kgd
Boehls Butte
Kelly Forks
Fault
116° 00'
115° 30'

Figure 4

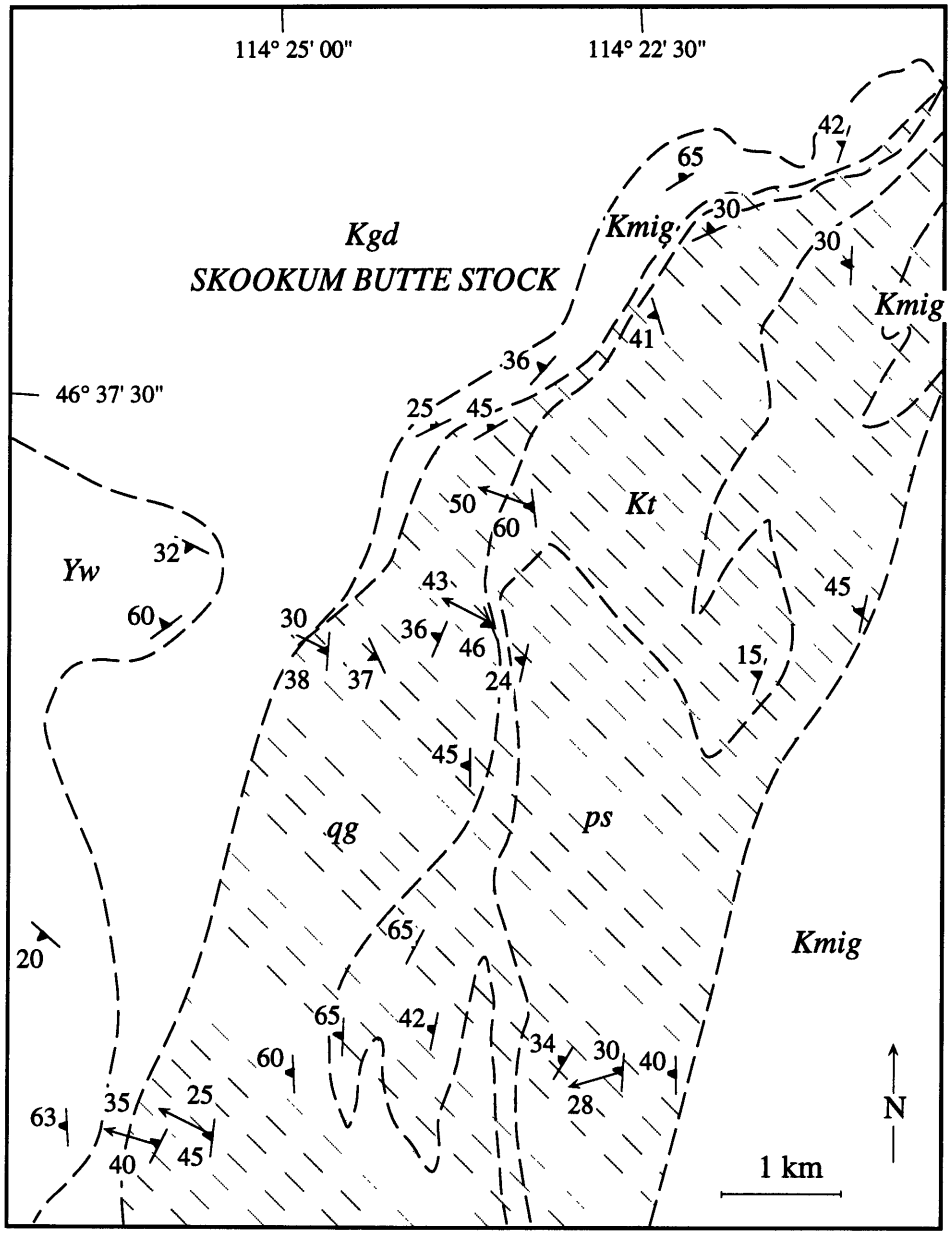
114° 25' 00"
114° 22' 30"
46° 37' 30"
Kgd
SKOOKUM BUTTE STOCK
Kmig
Kmig
Kmig
Kt
Yw
qg
ps
42
65
30
30
41
36
25
45
50
60
32
60
43
30
36
46
38
37
24
45
15
45
20
65
65
42
34
30
40
60
63
35
25
40
45
28
N
1 km

Figure 5a

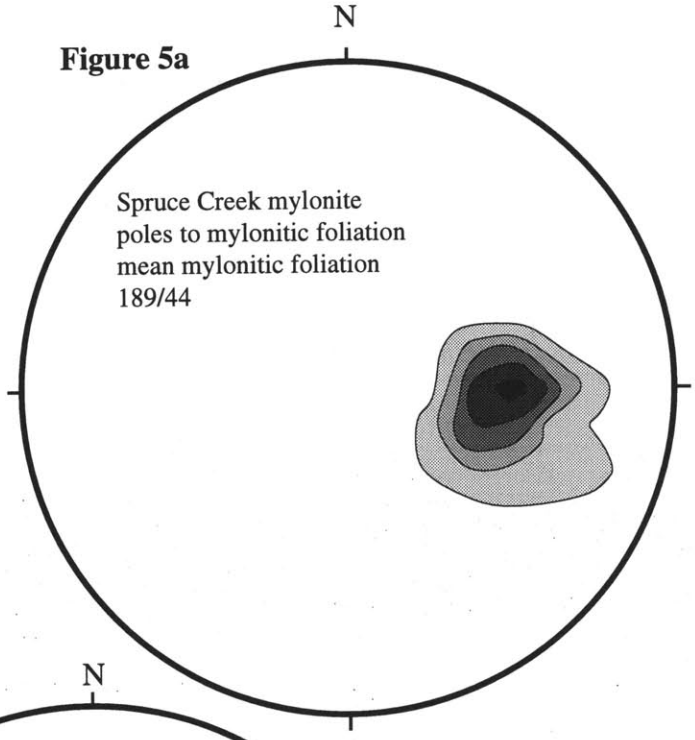

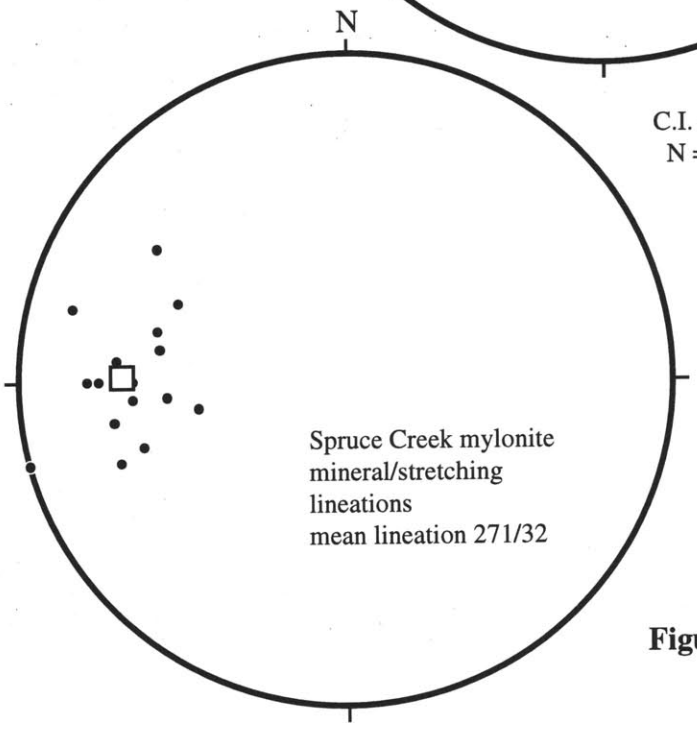

Figure 5b

Figure 6

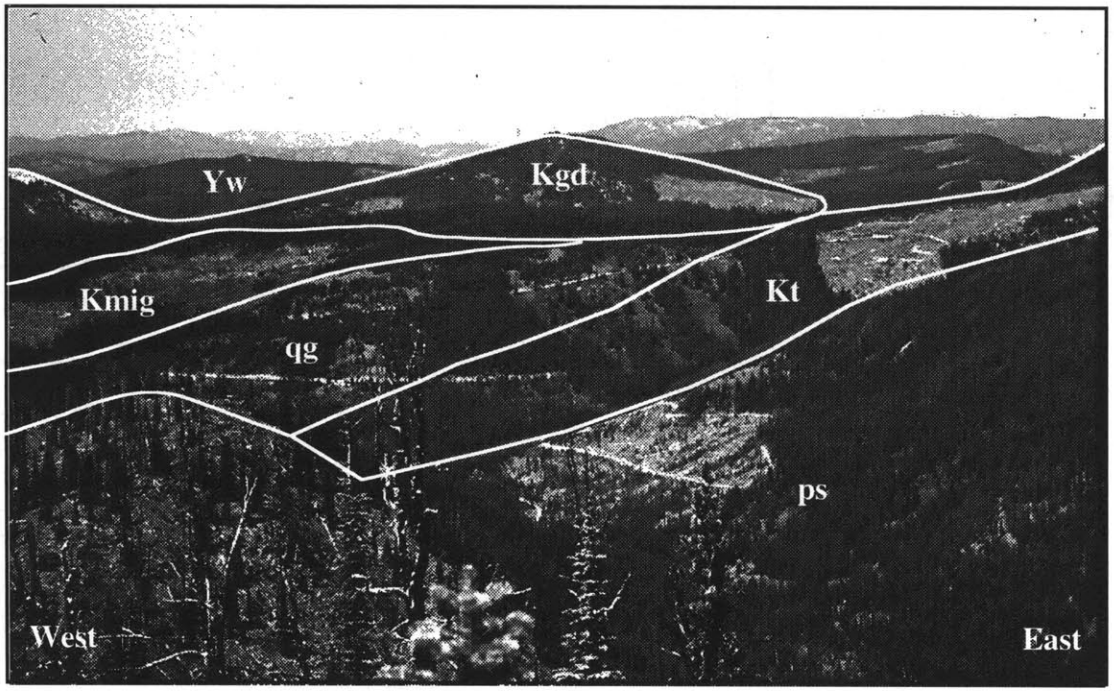

Figure 7a

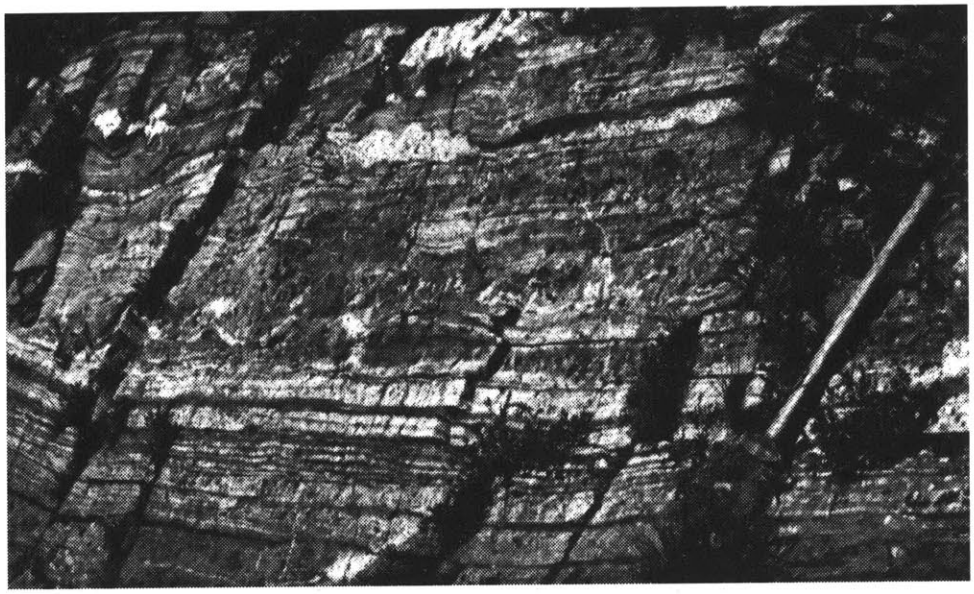

Figure 7b

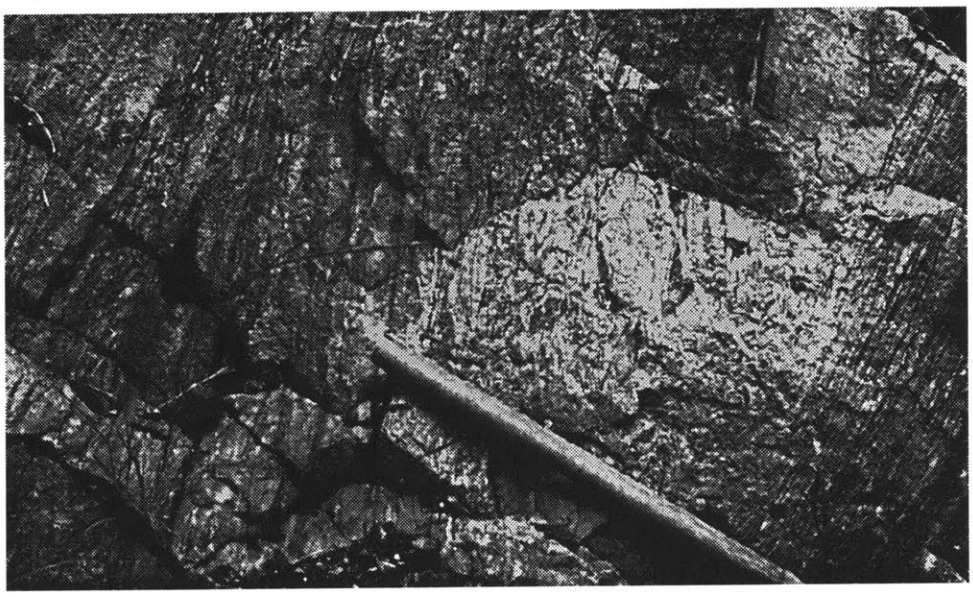

Figure 7c

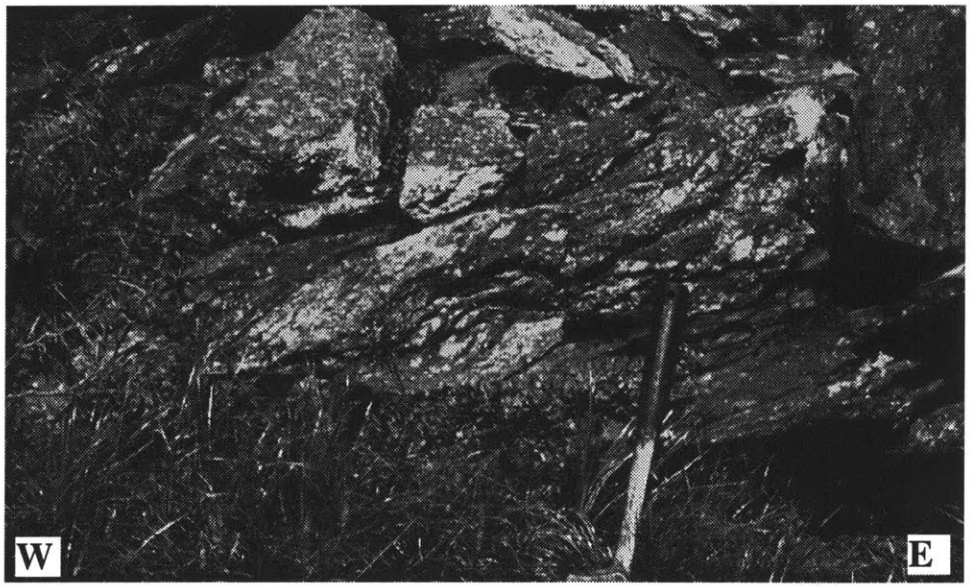

Figure 7d

Figure 8a

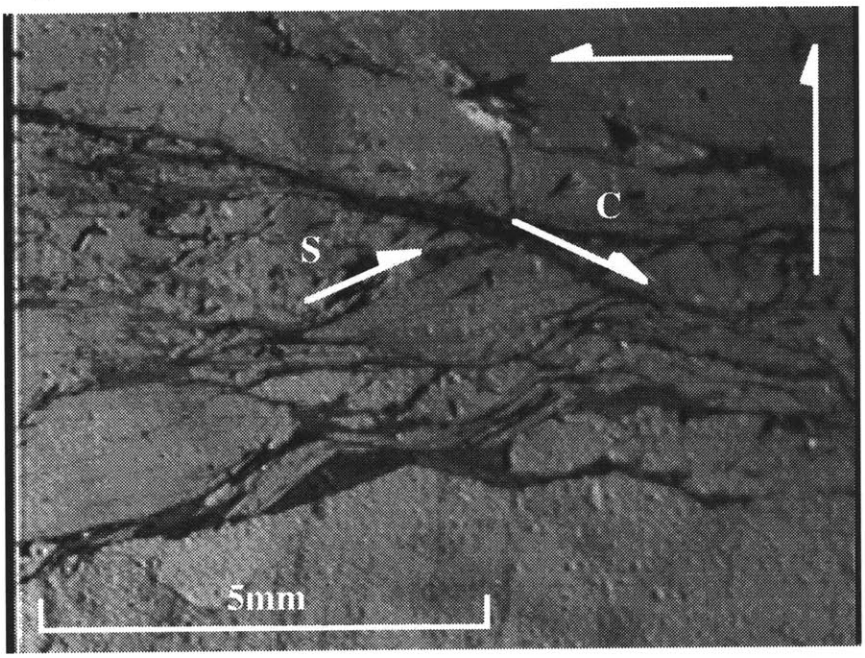

Figure 8b

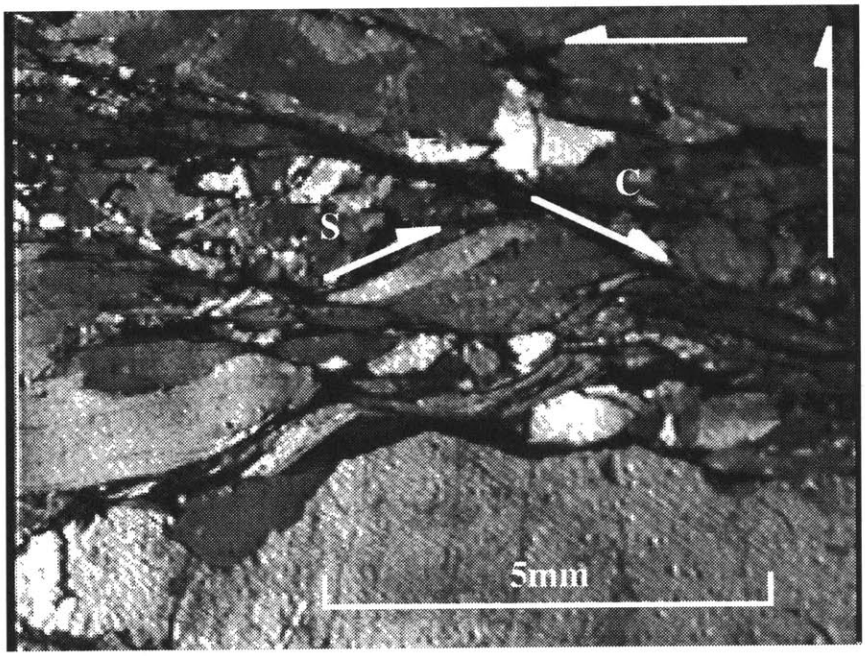

Figure 8c

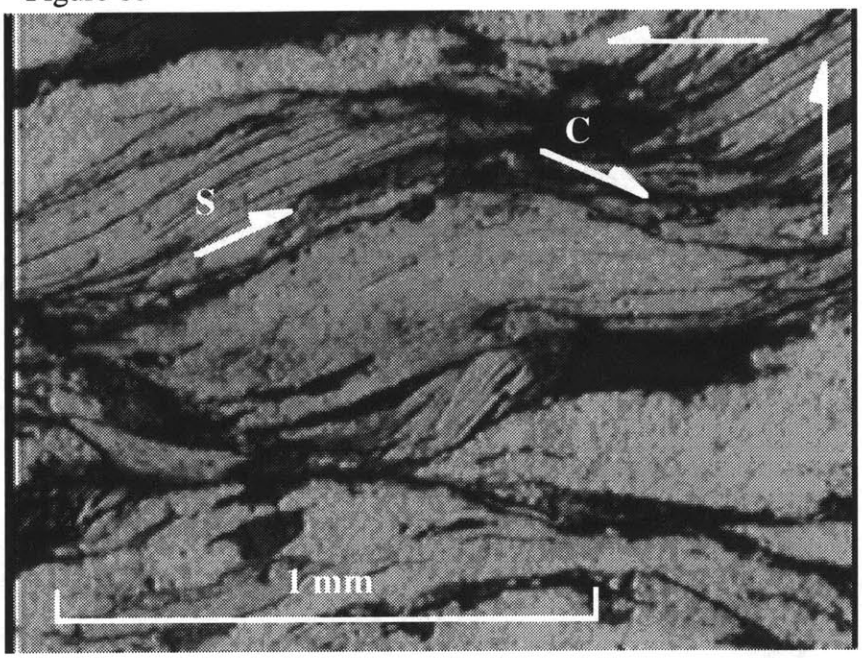

Figure 8d

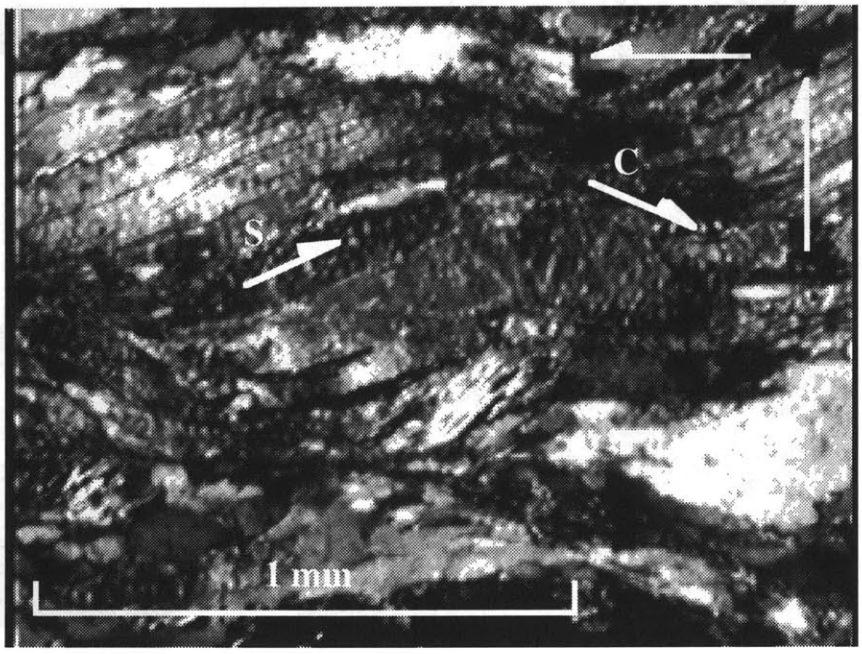

Figure 8e

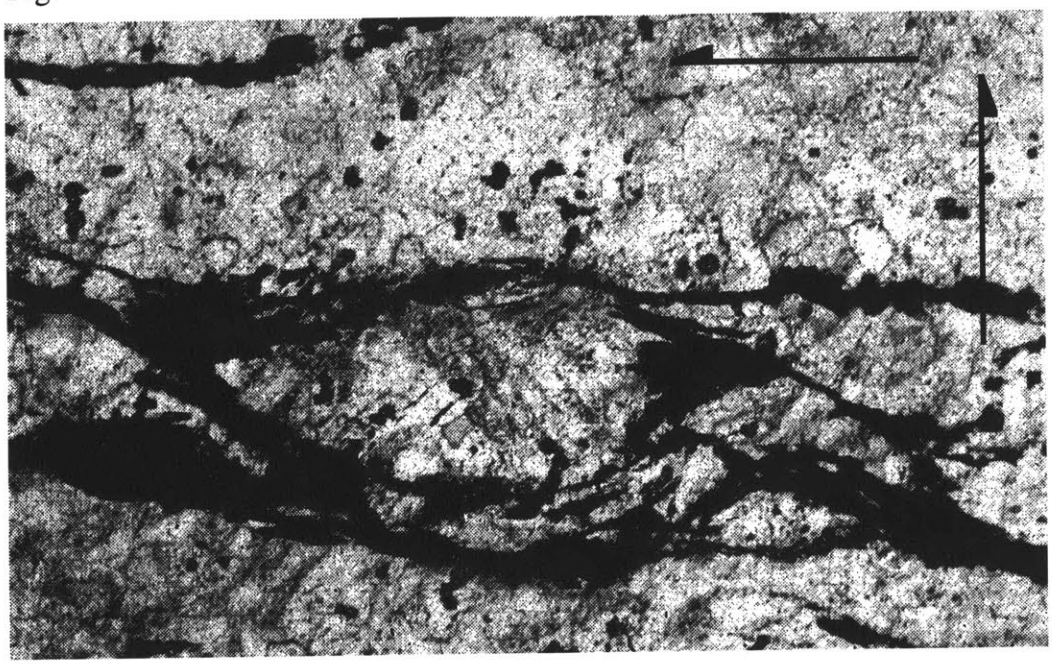

Figure 8f

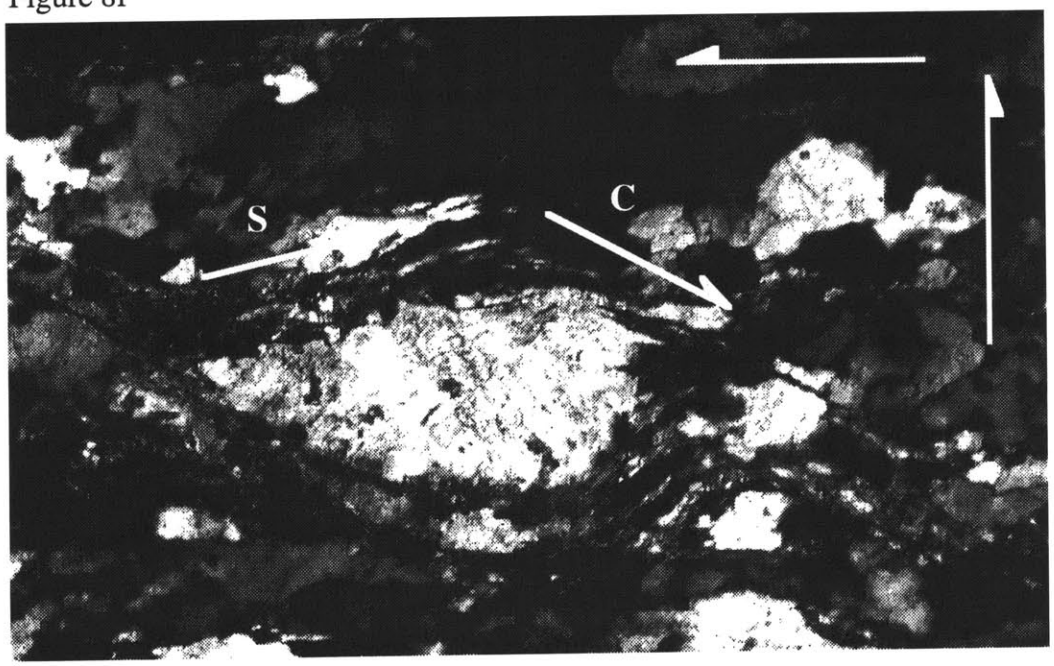

Figure 9

Figure 10

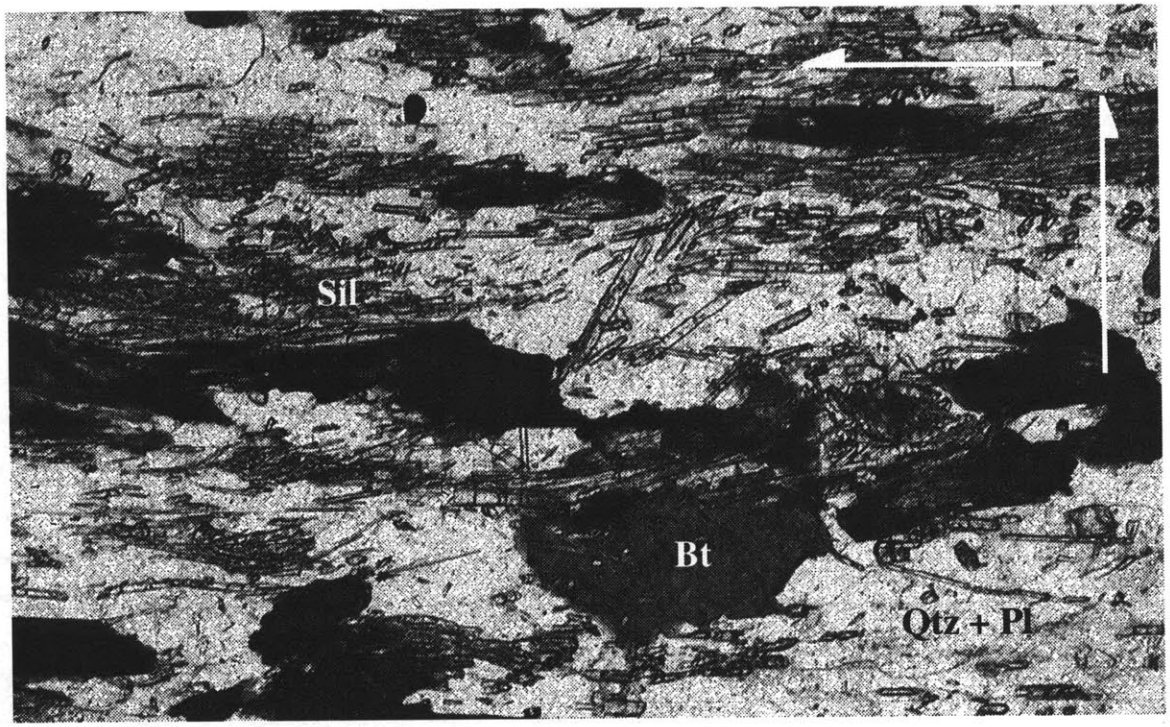

CHAPTER 6

A QUANTITATIVE MODEL OF THE TECTONIC SIGNIFICANCE OF RAPID COOLING EVENTS IN EXTENSIONAL SETTINGS

ABSTRACT

A one-dimensional model of conductive cooling quantifies the thermal response of footwall rocks in metamorphic core complexes to instantaneous extensional unroofing. Our results indicate that footwall cooling documented by $^{40}Ar/^{39}Ar$ cooling ages of muscovite, biotite, and K-feldspar significantly underestimate the age of unroofing. In cases of incomplete tectonic denudation, the times of footwall cooling through the closure temperatures of Ar in muscovite, biotite, and K-feldspar (375, 345, 175°C, respectively) can post-date the age of unroofing by as much as 20 m.y. In cases where the age of the mylonite zone is independently known, comparison of footwall cooling ages can provide a first-order estimate of the magnitude of unroofing accommodated by mylonitic shearing. This model is applied to $^{40}Ar/^{39}Ar$ cooling data from the Bitterroot metamorphic core complex, for which the age of tectonic denudation is independently known. Footwall rocks originating at 25 km depth cooled through the closure temperatures of muscovite and biotite approximately 3 m.y. after mylonitization ceased. These cooling ages can be explained by removal of ~19 km of overburden by extension on the core-bounding Bitterroot mylonite. Subsequent cooling through the closure temperature of K-feldspar is explained by renewed extensional unroofing accommodated by brittle normal faults that cut the earlier mylonitic fabric.

INTRODUCTION

Time-temperature histories based on geochronologic data from extensional terranes commonly indicate a brief interval of rapid cooling (Dokka *et al.*, 1986). Many researchers have attributed rapid cooling of the footwalls of major extensional shear zones to unroofing by movement on the shear zones themselves, inferring that the onset of footwall cooling provides an estimate of the age of the shear zone. The onset of rapid cooling is often equated with the beginning of faulting and footwall denudation (e.g., Davis and Lister, 1988), despite the fact that theoretical models of the time-temperature history of extensional terranes suggest that rapid cooling generally postdates unroofing in such settings (Ruppel *et al.*, 1988). In many cases, the cooling event documented by $^{40}Ar/^{39}Ar$ geochronology is the only constraint on the unroofing event and there is no way to assess the validity of the assumption that rapid cooling is coeval with tectonic denudation.

Published $^{40}Ar/^{39}Ar$ data from the Bitterroot metamorphic core complex, Idaho-Montana document a time lag of several million years between the independently constrained age of tectonic denudation and the times of cooling through mica and K-feldspar Ar closure temperatures (House and Hodges, 1994). Thus, these data thus offer an excellent opportunity to evaluate the relationship between conductive cooling associated with extensional unroofing and the timing of the unroofing. In this paper, we use a simple quantitative model to assess the temporal relationship between rapid cooling of footwall rocks and the timing of tectonic denudation.

TECTONIC DENUDATION IN THE BITTERROOT METAMORPHIC CORE COMPLEX

The Bitterroot metamorphic core complex coincides with the northeastern contact of the Late Mesozoic-Early Tertiary Idaho batholith with Proterozoic Belt Supergroup country rocks (Figure 1; Hyndman, 1980). Quantitative thermobarometry

in footwall rocks indicates peak metamorphic conditions of 725°C and 7.5 - 8.0 kb (~25 - 28 km; House and Bowring, 1994). The Bitterroot mylonite zone is the principal structure responsible for unroofing of core rocks (Figure 1). U-Pb geochronology of footwall rocks and deformed granitoids within the shear zone indicates that mylonitization initiated under high-temperature conditions at 48 ± 1 Ma (Chase *et al.*, 1983; House and Bowring, 1994). Hodges and Applegate (1993) reported a potassium feldspar $^{40}Ar/^{39}Ar$ cooling age of 46.4 ± 0.8 Ma from an undeformed rhyolite dike that crosscuts the Bitterroot mylonite zone, thereby limiting the minimum age for mylonitization. Early ductile deformational features preserved in the shear zone are overprinted by successively lower-temperature fabrics. Post-mylonitic brittle deformational features includes an overlying chlorite breccia and high-angle, east-dipping normal faults that truncate the earlier mylonitic foliation (Chase *et al.*, 1983).

Until recently, rapid cooling documented by $^{40}Ar/^{39}Ar$ data from core rocks in the southern Bitterroot complex was the best indication of the age of tectonic denudation (Garmezy, 1983; Garmezy and Sutter, 1983). Garmezy (1983) and Garmezy and Sutter (1983) assigned a 45.5 - 43.5 Ma age for the mylonite zone on the basis of $^{40}Ar/^{39}Ar$ data. However, the 46.4 Ma dike age reported by Hodges and Applegate (1993) demonstrates that the mylonite zone is significantly older than indicated by footwall cooling. In order to explore this discrepancy further, House and Hodges (1994) obtained $^{40}Ar/^{39}Ar$ cooling ages for hornblende, muscovite, biotite, and K-feldspar for rocks in the northern Bitterroot Range. Hornblende $^{40}Ar/^{39}Ar$ cooling ages for samples collected from within and below the mylonite zone are within the age range of the Bitterroot mylonite, but muscovite, biotite, and potassium feldspar $^{40}Ar/^{39}Ar$ ages of ~45 - 40 Ma define a cooling event that is significantly younger than the Bitterroot mylonite zone. House and Hodges (1994) suggested that post-kinematic cooling documented by $^{40}Ar/^{39}Ar$ data in the northern and southern Bitterroot complex represents thermal re-equilibration of footwall rocks following rapid exhumation or

were the result of renewed brittle extension accommodated by range-bounding high-angle normal faults.

In the next section, we examine whether the apparent discrepancy in ages can be the result of post-tectonic cooling. We do so by modeling the one-dimensional thermal profile of instantaneously unroofed footwall rocks for removal of a range of overburden thicknesses and comparing the results to the $^{40}Ar/^{39}Ar$ data from the northern Bitterroot complex. We then discuss the broader implications of the results for the interpretation of $^{40}Ar/^{39}Ar$ data in extensional settings .

THE METHOD AND MODEL

Rates of extension along detachment faults associated with core complex unroofing are commonly very fast and can approach plate-motion rates (e.g., Davis and Lister, 1988). Because exhumation rates are rapid compared to characteristic conductive cooling times, extension can be treated to first order as instantaneous. For our model, we consider a simple geometry as shown in Figure 2, with a planar, gently dipping fault surface. Although extensional unroofing accommodated by detachment faults involves horizontal and vertical transport of material, the horizontal thermal gradients are generally much smaller than the vertical thermal gradients (Ruppel and Hodges, 1994), therefore we consider only the one-dimensional thermal effects of extension. In the absence of heat production, one-dimensional conductive cooling is governed by the differential equation:

$$\frac{\partial T}{\partial t} = \kappa \frac{\partial^2 T}{\partial z^2} \qquad (1)$$

where T is temperature, t is time, κ is thermal diffusivity (10^{-6} m^2/s), and z is depth (positive downward). We assume a surface boundary condition of 0°C and a linear geotherm, $T = \beta z$. At $t = 0$, we assume instantaneous motion on the fault, such that the

thickness of the hanging wall is reduced from an initial thickness, F_i, to a final thickness, F_f, with a net reduction in thickness of $\Delta F = F_i - F_f$. After faulting, the instantaneous geotherm at $t = 0$ is:

$$T = \beta z \qquad \text{for } z < F_f \tag{2a}$$

$$T = \beta(z + \Delta F) \qquad \text{for } z \geq F_f \tag{2b}$$

The solution to equation 1 that satisfies the these initial boundary conditions is:

$$T = \beta Z_f + \beta\left(\frac{\Delta F}{2}\right)\left[\text{erf}\left(\frac{Z_f - F_f}{2\sqrt{\kappa t}}\right) + \text{erf}\left(\frac{Z_f + F_f}{2\sqrt{\kappa t}}\right)\right] \tag{3}$$

where t is the time elapsed instantaneous unroofing (Figure 2).

APPLICATION TO THE BITTERROOT METAMORPHIC CORE COMPLEX

The significance of this model is best illustrated by its application to the Bitterroot complex. We assumed an initial geotherm of 30°C/km, derived from thermobarometric data from footwall rocks (see above; House and Bowring, 1994). Values used for Z_i are derived from thermobarometric data (25 km), and the position of the rock package below the fault (Z_i-F_i) is determined from field relationships to be ~2 km (House, unpublished mapping; Plate 1). The depth of the rock package after unroofing, Z_f, is treated as unknown (footwall rocks are presently exposed at the surface but it is unclear how much unroofing of the metamorphic core was due to ductile phase of extension and how much resulted from subsequent brittle faulting).

Results for a broad range of values of Z_f are shown in Figure 3, together with $^{40}Ar/^{39}Ar$ data from the northern Bitterroot metamorphic core complex (House and Hodges, 1994). For instantaneous unroofing of footwall rocks at 48 Ma, the

hornblende, muscovite, and biotite cooling ages are best fit by a model calling for ~17 - 20 km of unroofing, leaving footwall rocks at a depth of ~5 - 8 km following mylonitization. (Note that the results are not unique but can be explained by a more complex unroofing history. However, if one assumes a simple single phase of unroofing, the $^{40}Ar/^{39}Ar$ data are well-constrained.)

Continued cooling through the closure temperature of Ar in K-feldspar cannot be explained simply by post-kinematic cooling and suggests a period of renewed extension following ductile extension, most likely accommodated by core-bounding brittle faults that truncate earlier mylonitic fabrics (House and Hodges, 1994). Our results indicate that to first order, post-mylonitic brittle extension must account for removal of ~3 - 8 km of overburden.

IMPLICATIONS FOR INTERPRETATION OF COOLING DATA FROM EXTENSIONAL SETTINGS

The analysis presented in this paper has important implications for interpretation of $^{40}Ar/^{39}Ar$ geochronologic data in extensional settings. The results indicate that the time lag between extension and cooling through mica and feldspar closure temperatures (375 - 175°C) is inversely proportional to the magnitude of unroofing. The model demonstrates that if cooling events documented by $^{40}Ar/^{39}Ar$ geochronology are considered to be coincident with unroofing, then the potential for underestimating the age of extension is considerable. For example, if 15 km of overburden are removed, a rock package originating at 25 km depth will immediately pass through the hornblende closure temperature (525°C), but will not pass through the mica closure temperatures (375 - 345°C) until more than 20 m.y. after unroofing. Alternatively, removal of greater than 23 km of overburden results in closure ages that will more closely approximate the actual age of unroofing. In the case of a steeper geotherm (40°C/ km), the discrepancy between the age of unroofing and cooling through the mica and feldspar

closure temperatures is event greater. In general, the more complete the unroofing, the better the mica and K-feldspar closure temperatures approximate the actual age of the event.

This model considers the effects of conductive cooling only. Incorporating the effects of radioactive heat production would work against conductive cooling, resulting in even greater discrepancies between the age of unroofing and the times at which footwall rocks cool through the closure temperatures of hornblende, biotite, muscovite, and K-feldspar. Likewise, incorporating a steeper geotherm into the model, such as is often indicated by thermobarometry in core complex footwalls (e.g., Silverberg, 1990) also has the effect of increasing the discrepancy between the age of denudation and footwall cooling ages.

CONCLUSIONS

The simple thermal model presented in this paper supports the conclusions by House and Hodges (1994) that periods of rapid cooling documented by $^{40}Ar/^{39}Ar$ data in extensional settings should be considered a minimum constraints on the age of tectonic denudation. In the case of the Bitterroot metamorphic core complex, simple conductive cooling in response to instantaneous extension only partially explains the cooling history of footwall rocks documented by $^{40}Ar/^{39}Ar$ geochronology. A second unroofing event must be invoked, consistent with field evidence for post-mylonitic brittle normal faulting. Our results demonstrate that unless unroofing is complete, mica and feldspar cooling ages will underestimate the age of extension by several million years. Discrepancies between cooling ages and the actual age of denudation can be quite significant in cases when footwall rocks are only partially unroofed by a single extensional event.

REFERENCES

Chase, R. B., Bickford, M. E., and Arruda, E. C., 1983, Tectonic implications of Tertiary intrusion and shearing within the Bitterroot dome, northeastern Idaho batholith: Journal of Geology, v. 91, p. 462-470.

Davis, G. A. and Lister, G. S., 1988, Detachment faulting in continental extension; Perspectives from the Southwestern U.S. Cordillera, *in* Clark, S. P., Burchfiel, B.C., and Suppe, J., ed., Processes in Continental Lithospheric Deformation: Boulder, CO, Geological Society of America, p. 133-159.

Dokka, R. K., Mahaffie, M. J., and Snoke, A. W., 1986, Thermochronologic evidence of major tectonic denudation associated with detachment faulting, northern Ruby Mountains - East Humbolt Range, Nevada: Tectonics, v. 5, p. 995-1006.

Garmezy, L., 1983, Geology and geochronology of the southeast border of the Bitterroot dome: Implications for the structural evolution of the mylonitic carapace [Ph.D.]: The Pennsylvania State University.

Garmezy, L. and Sutter, J. F., 1983, Mylonitization coincident with uplift in an extensional setting, Bitterroot Range, Montana-Idaho: Geological Society of America Abstracts with Programs, v. 15, p. 578.

Hodges, K. V. and Applegate, J. D. R. A., 1993, Age of Tertiary extension in the Bitterroot metamorphic core complex, Montana and Idaho: Geology, v. 21, p. 161-164.

House, M. A. and Bowring, S. A., 1994, New constraints on the relationship between magmatism, metamorphism, and the onset of extensional denudation: An example from the North American Cordillera: Geological Society of America Annual Meeting Abstracts with Programs, v. 26, p. A186.

House, M. A. and Hodges, K. V., 1994, Limits on the tectonic significance of rapid cooling events in extensional setting: Insights from the Bitterroot metamorphic core complex, Idaho-Montana: Geology, v. 22, p. 1007-1010.

Hyndman, D. W., 1980, Bitterroot dome - Sapphire tectonic block, an example of a plutonic-core gneiss-dome complex with its detached suprastructure, *in* Crittenden, M. D., Coney, P. J., and Davis, G. H., ed., Cordilleran Metamorphic Core Complexes: Boulder, CO, Geological Society of America Memoir 153, p. 427-443.

Ruppel, C. and Hodges, K. V., 1994, Pressure-temperature-time paths from two-dimensional thermal models: Prograde, retrograde, and inverted metamorphism: Tectonics, v. 13, p. 17-44.

Ruppel, C., Royden, L., and Hodges, K. V., 1988, Thermal modeling of extensional tectonics: application to pressure-temperature-time histories of metamorphic rocks: Tectonics, v. 7, p. 947-957.

Silverberg, D. S., 1990, The tectonic evolution of the Pioneer metamorphic core complex, south-central Idaho [Ph.D.]: Massachusetts Institute of Technology.

FIGURE CAPTIONS

Figure 1. Simplified geologic map of the Bitterroot metamorphic core complex. Box in inset indicates location of Bitterroot complex. Patterns on map indicate the following units: dark shading: Eocene epizonal plutons; stipple: granitoids associated with the Idaho batholith; white: metamorphosed and unmetamorphosed Belt Supergroup units. Hatched region indicates Bitterroot mylonite zone; Approximate western limit of Bitterroot complex indicated by dashed line. Location of cooling ages reported by House and Hodges (1994) indicated by bold NB.

Figure 2. X-Z and T-Z plots for cooling model discussed in text. (a). Fault geometry prior to instantaneous unroofing (left) and following unroofing (right). A rock package (black dot) is located at an initial depth Z_i, below an incipient fault surface, at depth F_i below the surface. Following unroofing, the hanging wall is reduced by a thickness ΔF, and the rock package and fault surface are now located at depths Z_f and F_f below the surface. (b) Thermal profile before (left) and immediately after (right) instantaneous extension. β is the steady-state linear geotherm (30°C/km). Following extensional unroofing, the original geotherm, β, is maintained in hanging wall ($z < F_f$), and is shifted by an amount $\beta\Delta F$ for depths $z \geq F_f$.

Figure 3. Open circles indicate the hornblende, muscovite, biotite and K-feldspar cooling data (corresponding to temperatures of 575°C, 375°C, 345°C, and 175°C respectively; McDougall and Harrison, 198X) from the Bitterroot metamorphic core complex; uncertainties are discussed in text. The minimum age for ductile shearing, with uncertainties (46.4 ± 0.8

Ma) reported by Hodges and Applegate (1993) is indicated by shaded bar. Z_i is determined by thermobarometric data to be 25 km. Each curve represents a different amount of total unroofing; ΔF is indicated by the number of each curve such that for 5 km, the amount of overburden remaining above the rock package is 20 km.

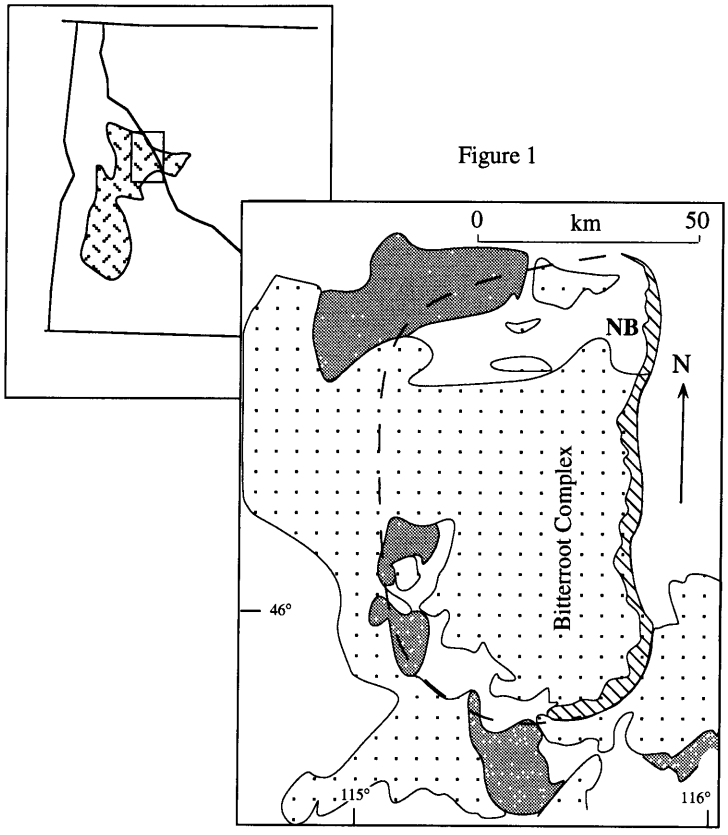

Figure 1

Figure 2a

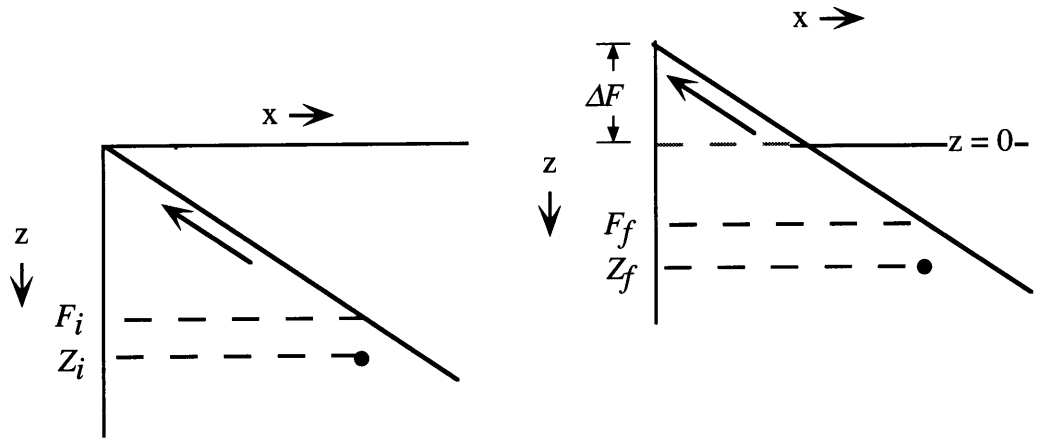

Figure 2b

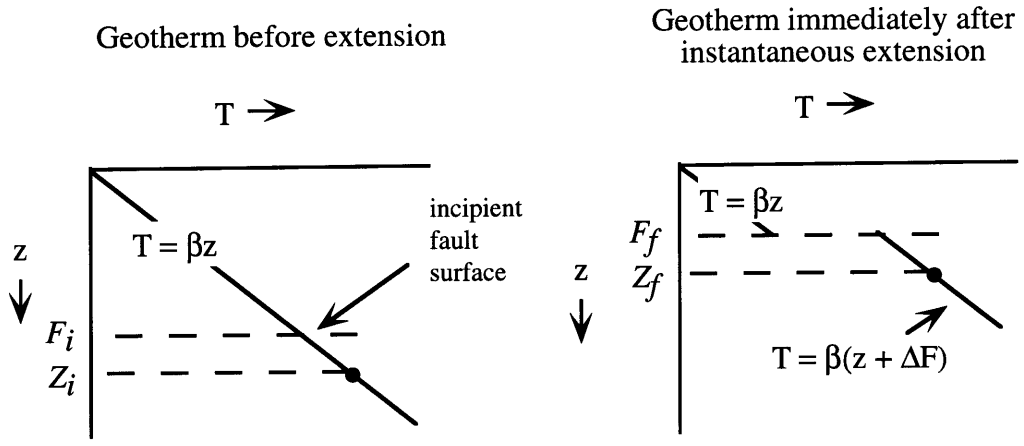

Figure 3

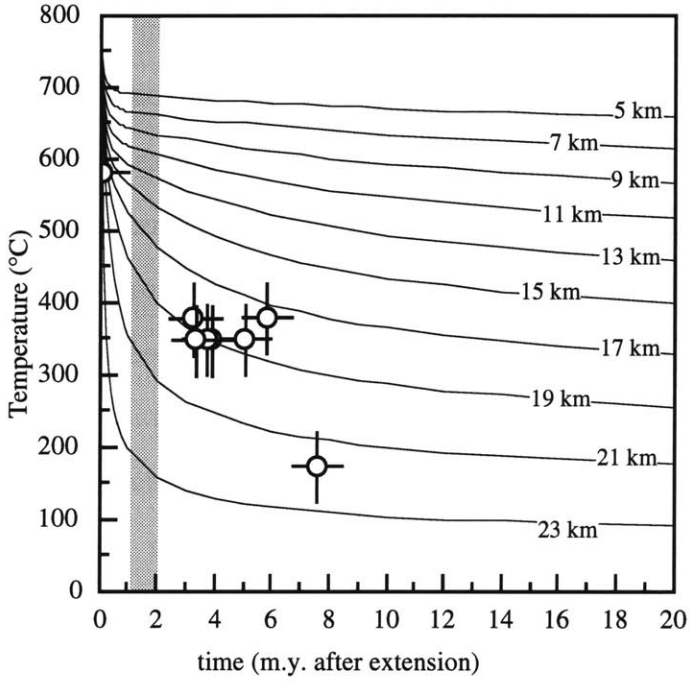
800
700
600
500
400
300
200
100
0
Temperature (°C)
0
2
4
6
8
10
12
14
16
18
20
time (m.y. after extension)
5 km
7 km
9 km
11 km
13 km
15 km
17 km
19 km
21 km
23 km

CHAPTER 7

SUMMARY: IMPLICATIONS OF GEOCHRONOLOGIC AND THERMOBAROMETRIC CONSTRAINTS ON THE THERMAL HISTORY OF THE BITTERROOT METAMORPHIC CORE COMPLEX

INTRODUCTION

Granitic rocks of the Bitterroot batholith and their high-grade metamorphic host-rocks are exposed in the footwall of the Bitterroot metamorphic core complex in western Montana and eastern Idaho. Two metamorphic events are documented in core rocks in the northeastern Bitterroot complex on the basis of textural relations and quantitative thermobarometry. These metamorphic events are correlated with metamorphism described in the Boehls Butte/Goat Mountain and Snow Peak regions to the northwest of the Bitterroot complex. M1 is weakly preserved in the Bitterroot footwall, but it is associated with temperatures of ~775 K and pressures of 500 - 600 MPa to the northwest; textural evidence throughout the northern margin of the Bitterroot batholith suggest that M1 metamorphism accompanied east-vergent thrusting occurring between ~100 - 50 Ma. Upper-amphibolite facies M2 metamorphism in the Bitterroot core complex was associated with granite emplacement during Late Cretaceous-early Tertiary time; M2 mineral isograds are broadly concentric to the northern margins of the Bitterroot batholith. Quantitative thermobarometry in metapelitic rocks in the northeastern Bitterroot footwall indicates that peak metamorphism occurred at temperatures of ~950 - 1000 K and pressures of ~750 - 800 MPa, or depths of ~26 - 28 km. Garnet amphibolite thermobarometry suggests a period of isothermal decompression is associated with the late stages of M2 metamorphism.

This high-temperature decompression is interpreted to represent the early stages of unroofing on the core-bounding Bitterroot mylonite zone. Metamorphic zircon U-Pb crystallization ages from garnet amphibolites from the northeastern Bitterroot complex indicate that peak M2 metamorphic temperatures persisted in this part of the metamorphic core as late as 48 Ma.

$^{40}Ar/^{39}Ar$ and U-Pb geochronology demonstrate that extensional denudation of core rocks initiated shortly after emplacement of mesozonal plutons in the northern Bitterroot Range at 55.8 Ma. Footwall rocks in the northwestern Bitterroot complex cooled through the closure temperatures of hornblende, muscovite, biotite, and K-feldspar (800, 650, 620, and 450 K, respectively) between 55.6 - 48 Ma; cooling continued in the northeastern footwall rocks from 48 - 40 Ma. U-Pb crystallization ages of epizonal plutons in the western portion of the Bitterroot complex demonstrate that western core rocks were at shallow structural levels by ~49 Ma, whereas high-temperature conditions associated with peak metamorphism persisted in footwall rocks in the eastern Bitterroot complex as late as 48 Ma. The geochronologic data suggest that core rocks in the eastern and western portions of the Bitterroot complex were at very different structural levels at ~49 - 48 Ma and can be explained by multiple extensional structures or progressive unroofing by a single feature—the core-bounding Bitterroot mylonite zone.

Northeastern Bitterroot footwall rocks cooled through the closure temperatures of muscovite, biotite, and K-feldspar > 3 m.y. after motion on the Bitterroot mylonite zone ceased. A quantitative model of simple conductive cooling suggests that this time lag represents the thermal re-equilibration of footwall rocks following removal of ~19 km of overburden by extension on the Bitterroot mylonite zone. Continued cooling through the closure temperature of K-feldspar is interpreted to represent renewed extensional unroofing via range-bounding post-mylonitic brittle structures; these high-

angle normal faults may have been responsible for the removal of 3-8 km of overburden.

Geologic data from the northeastern Bitterroot complex demonstrate that the onset of extensional unroofing and footwall cooling closely followed peak metamorphism in core rocks, suggesting that these events are intimately related. Numerous models have been presented in recent years directed at determining the nature of the relationship between this sequence of events. The geochronologic and petrologic constraints on the unroofing history of the Bitterroot metamorphic core complex directly bear on these models. This paper presents brief discussions of the broader implications of the data and expands on points made in the conclusions of the chapters. This summary attempts to place the unroofing history of the Bitterroot metamorphic core complex in a more general context, both in terms of regional geology and regarding general models for core complex development.

STRUCTURAL AND THERMAL SETTING PRIOR TO EXTENSION

Thrusting in the Rocky Mountain Basin and Range

A moderately west-dipping ductile shear zone exposed in the footwall of the Bitterroot metamorphic core complex - the Spruce Creek mylonite zone - is interpreted as a splay of a Cretaceous shortening structure developed at amphibolite facies conditions. The shear zone contains fabrics consistent with east-southeastward displacement of the hanging-wall relative to the footwall, in a thrust sense. We suggest that the Spruce Creek mylonite is a splay of thrusts exposed in the southern Sapphire range and in the vicinity of Boehls Butte (Harrison *et al.*, 1986) and refer to these thrusts as the Cabin-Sapphire thrust plate. These thrusts generally carry Belt Supergroup units and Proterozoic basement rocks eastward over Belt Supergroup units. In the Snow Peak region, to the northwest of the Bitterroot complex, east-vergent thrusting on structures that are most likely correlative with the Spruce Creek mylonite

has been associated with metamorphic conditions of 775 K and 500 - 600 MPa (18 - 21 km; Lang and Rice, 1985). These metamorphic conditions provide a maximum constraint on the thickness of the overriding thrust plate of ~ 18 - 21 km, consistent with published estimates for the thickness of these structures (Glazner and Bartley, 1985).

The Spruce Creek mylonite zone is intruded by the Skookum Butte stock along its northern margin and therefore must be older than the 55.8 ± 0.1 Ma U-Pb monazite age of the stock (House, Chapter 4). Cross-cutting relationships place lower limits of 78 - 73 Ma on correlative thrusts exposed in the southern Sapphire Range (Wallace *et al.*, 1989), indicating that crustal shortening in this region was complete by Late Cretaceous time.

Thermal structure

Thermobarometric data derived from pelitic schists and garnet amphibolites in the Bitterroot core indicate peak temperatures of ~950 - 1000 K at depths of ~750 - 800 MPa (26 - 28 km; Chapter 3). Widespread anatectic melting in core rocks accompanied these conditions (Chase, 1973). Upper-amphibolite facies peak metamorphism in the Bitterroot footwall is part of a larger regional metamorphic event that has also been documented in the Boehls Butte/Goat Mountain region to the northwest (Figure 1; Lang and Rice, 1985; Grover *et al.*, 1992). Mineral isograds associated with this event are roughly parallel to but cut at low angles by the northern margins of the Bitterroot batholith, indicating that the late stages of batholith intrusion were broadly coeval with upper-amphibolite facies regional metamorphism. A 55.8 Ma U-Pb age for a monazite from migmatites in the western Bitterroot complex provides our best estimate of the timing of amphibolite facies metamorphism in this area (Chapter 3). A second stage of zircon growth resulted in metamorphic zircons from footwall rocks in the eastern Bitterroot complex that yield ages of ~48 Ma (Chapter 3). These metamorphic zircons

demonstrate that upper-amphibolite facies metamorphic conditions persisted much later in core rocks of the northeastern complex than in the northwestern footwall.

Peak metamorphic conditions indicated by quantitative thermobarometry in core rocks of the Bitterroot complex are similar to those reported for core complexes elsewhere in the Cordillera (e.g., Parrish *et al.*, 1988; Hodges and Walker, 1990). Crustal shortening has been suggested as a cause for the elevated geotherms documented in P-T data from the footwalls of metamorphic core complexes (Glazner and Bartley, 1985; Liu and Furlong, 1993). Crustal shortening models suggest that the hinterland of the Cordilleran thrust belt reached thicknesses of ~60 km (Coney and Harms, 1984; Wernicke, 1991). However, even with these thicknesses, the high-temperatures indicated by the thermobarometric data and the evidence for accompanying anatectic melting are difficult to explain by simple models (Glazner and Bartley, 1985; Liu and Furlong, 1993). Rather, high rates of radioactive heat production or an alternative heat source are important factors in maintaining elevated geotherms following crustal shortening (Glazner and Bartley, 1985; Liu and Furlong, 1993).

It is clear that advective heating associated with emplacement of the early phases of the Bitterroot batholith played an important role in generating the elevated geotherm documented in Bitterroot core rocks. However, mineral isograds associated with peak metamorphism are cut at low angles by the Bitterroot batholith, indicating that many of the plutons in the batholith may have been the result rather than the cause of upper-amphibolite facies metamorphism. In the Bitterroots, early calc-alkaline plutonic phases that have been attributed to arc-magmatism have been dated at ~100 - 70 Ma and are considerably older than the timing of peak metamorphism as indicated by U-Pb geochronology in the northeastern Bitterroot complex (Toth, 1987).

Thus, crustal shortening and radioactive heat production may also have played a role in achieving peak metamorphic conditions documented in footwall rocks of the

Bitterroot complex. Upper-amphibolite facies metamorphic conditions existed in Bitterroot core rocks at 55.8 Ma (see above), ~20 m.y. after the latest known period of crustal shortening in this region (Wallace *et al.*, 1989). A minimum value for the radioactive heat production that would be required to maintain the elevated geotherm indicated by thermobarometry can be determined by treating the geotherm as steady-state. Assuming that crustal shortening results in a crustal thickness of 60 km (see above), the value for the heat generation that is calculated is well within acceptable ranges for granitic materials (2 $\mu W/m^3$). This moderate value of radioactive heat production is sufficient to maintain the elevated geotherm and to induce anatectic melting in the Bitterroot footwall.

While it is possible that the elevated peak metamorphic geotherm in core rocks could be caused by earlier magmatic activity, it could as easily be explained by crustal shortening. Most likely, the elevated metamorphic geotherm documented in core rocks is the result of a combination of these factors; the relative importance of each remains to be determined.

ONSET OF EXTENSION

Temporal relationships in the northern Bitterroot Range demonstrate that high-temperature conditions were closely followed or coincident with the early stages of unroofing, presumably by the Bitterroot mylonite zone, and post-dates the latest stages of east-vergent thrusting by about 20 m.y. (Chapter 2, 3, 5; Wallace *et al.*, 1989). Crystallization of the mesozonal Skookum Butte stock at 55.8 Ma was closely followed by footwall cooling through the closure temperature of Ar in hornblende (~800 K) at 56.5 Ma in the northwestern Bitterroot complex (Chapter 4). High-temperatures (~1000 K) persisted in core rocks of the northeastern Bitterroot complex until as late as 48 Ma, and were closely followed by cooling through the hornblende closure temperature at ~47.9 Ma (Chapter 2, 3).

Many explanations have been offered for the driving force behind the initiation of extension. These models generally agree that some combination of plate motions, crustal shortening, thermal weakening, and gravitational instability results in extension, but the relative importance of these factors remains the subject of ongoing research (e.g., Coney and Harms, 1984; Glazner and Bartley, 1985). A major question that remains unanswered is how to explain the apparent variations in the temporal relationship between the cessation of compression and the onset of extension along the length of the Cordillera. In the Canadian Cordillera, extension is coeval with the late stages of compression, whereas to the south, extension post-dates compression by ~20 m.y. in the Great Basin, and as much as 70 m.y. farther south (Brown and Journeay, 1987; Wernicke *et al.*, 1987).

Glazner and Bartley (1985) demonstrated that time lags between compression and extension such as those in the Great Basin and in regions to the south can be explained by thermal weakening resulting from crustal shortening. However, their model fails to explain the timing relationships in the Canadian Cordillera. Wernicke *et al.* (1987) and Sonder *et al.* (1987) have argued that forces driving extension could be derived from intraplate stresses in a compressional tectonic regime and that the magnitude of compressional strain and the post-compressional thermal structure determines when extension initiates following compression. They suggest that the lower crust in the Canadian Cordillera may have been partially molten to explain the temporal overlap between the late stages of crustal shortening and the onset of extension in this region (Brown and Journeay, 1987; Sonder *et al.*, 1987).

Geochronologic constraints from the Bitterroot complex demonstrate that extensional unroofing of footwall rocks post-dates published estimates for the age of compression in the Rocky Mountain Basin and Range by ~ 20 m.y. (Wallace *et al.*, 1989) whereas in the Omineca Extended Belt to the north, extension was coeval with the late stage of compression (Brown and Journeay, 1987). The differences in the

temporal relationship between compression and extension in the Omineca Extended Belt and in the Rocky Mountain Basin and Range, as indicated by the Bitterroot data, suggest that the two regions are under very different stress regimes during this time. This period in the tectonic development of the Omineca Extended Belt is associated with considerable strike-slip activity, whereas there is little evidence for transform motion to the south in the Rocky Mountain Basins and Range province (Price, 1979; Price and Carmichael, 1986). These two regions are separated by the Lewis and Clark fault zone, which may have accommodated this variation. Alternatively, the minimum age for compression in the Omineca Extended Belt may be underestimated, and the temporal relationship between compression and extension in the two regions may be more similar than has been suggested.

POST-EXTENSIONAL THERMAL EVOLUTION OF FOOTWALL ROCKS

Rapid cooling events deduced from thermochronologic data are often interpreted to be coincident with the age of extensional denudation in metamorphic core complexes. $^{40}Ar/^{39}Ar$ data for mylonitic and nonmylonitic footwall rocks from the Bitterroot core complex challenge this view. The lower limit on the age of the Bitterroot mylonite zone is constrained by cross-cutting relationships to be 46.4 ± 0.8 Ma (Hodges and Applegate, 1993) and upper-limits range from ~55.6 - 48 Ma. Hornblende $^{40}Ar/^{39}Ar$ cooling ages for samples collected from the mylonite zone are within this age range, consistent with mylonitization at amphibolite facies conditions. However, muscovite, biotite, and potassium feldspar $^{40}Ar/^{39}Ar$ ages of ~45 - 40 Ma for rocks from the same area define a footwall cooling event that is significantly younger than the Bitterroot mylonite zone (House and Hodges, 1994).

A one-dimensional model of conductive cooling applied to the $^{40}Ar/^{39}Ar$ cooling data from the Bitterroot metamorphic core complex quantifies the response of footwall rocks to instantaneous extensional unroofing (Chapter 6). The post-kinematic

cooling ages in the Bitterroot complex can be explained by removal of ~19 km of overburden by extension on the core-bounding Bitterroot mylonite. Subsequent cooling through the closure temperature of K-feldspar (~175°C) at ~40 Ma is explained by renewed extensional unroofing accommodated by brittle normal faults that cut the earlier mylonites. The relationship between footwall cooling and tectonic denudation indicated by the Bitterroot data and the quantitative model suggest that many of the ages that have been cited for extensional denudation in core complexes are actually underestimates of the age of extension and should be re-evaluated.

PROGRESSIVE UNROOFING OF CORE COMPLEXES

U-Pb and $^{40}Ar/^{39}Ar$ data from the epizonal Lolo Hot Springs batholith and Whistling Pig pluton in the northwestern and southwestern Bitterroot metamorphic core complex demonstrate that much of the mesozonal Bitterroot batholith and western Bitterroot metamorphic core complex were at shallow levels by ~49 Ma (Chapter 4). An U-Pb monazite crystallization age of 55.8 Ma for the mesozonal Skookum Butte stock, adjacent to the Lolo Hot Springs batholith, provides an upper-bound for the age of tectonic denudation and demonstrates that ~12 - 18 km of unroofing occurred over a period of ~6 - 7 Ma in the northwestern Bitterroot Range.

While epizonal plutons crystallized in the western Bitterroot complex, the eastern footwall rocks remained at high temperatures (1000 K) and depths on the order of 19 - 26 km (Chapter 3). $^{40}Ar/^{39}Ar$ cooling data from the northern Bitterroot complex become younger in the direction of transport, indicating progressive cooling of core rocks in response to east-directed tectonic denudation (Chapter 2, 3, 4). Cooling ages for hornblende, biotite, muscovite, and K-feldspar in the western footwall rocks range from 55.6 - 48 Ma, and those for the eastern footwall rocks range from 48 - 40 Ma. This progression in $^{40}Ar/^{39}Ar$ cooling ages, combined with geochronologic constraints on the crystallization ages of a suite of epizonal plutons in the western

footwall demonstrate that the western BMCC reached shallow levels (~1.5 km) while the eastern BMCC remained at mesozonal structural levels. These data require multiple extensional mechanisms, or more likely, a significant component of rotation about a sub-horizontal north-south trending axis associated with extension on the Bitterroot mylonite zone.

Models for progressive unroofing of core complexes attempt to explain the domal nature of complexes and the present low-angle geometry of core-bounding detachment faults (Spencer, 1984; Buck, 1988; Wernicke and Axen, 1988). These models predict cooling histories much like that documented in the Bitterroot complex, but it is difficult to distinguish among them based on the Bitterroot data.

REGIONAL IMPLICATIONS

The geochronologic data from the Bitterroot complex resolve the ambiguity of the age of extensional unroofing of this metamorphic terrane. Correlation of the age of extensional denudation of the Bitterroot complex and of compressional structures preserved in core rocks to those elsewhere in the Rocky Mountain Basin and Range and in the Omineca Extended Belt to the north shed some light on the evolution and tectonic significance of the Lewis and Clark fault zone.

Age of extension north of the Snake River Plain

U-Pb and $^{40}Ar/^{39}Ar$ data form the Bitterroot complex demonstrate that extensional unroofing of footwall rocks occurred between ~55.8 - 46.4 Ma, with considerable post-mylonitic footwall cooling (Chapter 2, 4; Hodges and Applegate, 1994). These ages are considerably older than has been previously suggested for the Bitterroot mylonite zone (Garmezy, 1983; Garmezy and Sutter, 1983) and are within uncertainty of those suggested for core complexes in the Omineca Extended Belt of northern Idaho and Washington and southern British Columbia (Orr and Cheney, 1987; Parrish *et al.*, 1988; Harms and Price, 1992). Ar-cooling data and cross-cutting

relationships from footwalls of the Priest River, Valhalla, Kettle, and Okanogan core complexes indicate that extensional unroofing of these complexes occurred during Early to Middle Eocene times (Orr and Cheney, 1987; Parrish *et al.*, 1988; Harms and Price, 1992). Late Eocene K-Feldspar cooling ages reported for the Priest River complex may also be interpreted to indicate post-mylonitic cooling similar to that in the Bitterroots (Fillipone and Yin, 1993; Fillipone and Yin, 1994).

Cooling ages in the Pioneer complex are also consistent with the data from the Bitterroots. Two periods of rapid cooling between 48 - 45 Ma and 36 - 33 Ma have been documented in footwall rocks of the Pioneer complex (Silverberg, 1990). Both cooling events have been attributed to extension on ductile structures. However, the data are also consistent with early ductile unroofing, resulting in footwall cooling between 48 - 45 Ma, followed by renewed brittle or lower-temperature deformation associated with the 36 - 33 Ma cooling ages. Re-evaluation of these cooling ages from the Pioneer complex in the context of new data from the Bitterroot complex suggests that extension in the Rocky Mountain Basin and Range and the Omineca Extended Belt is not diachronous, as has been previously suggested (Wernicke, 1991). Rather it may have occurred everywhere at the same time, suggesting that forces driving this extension were common throughout the whole region.

Role of the Lewis and Clark fault zone

Extensional unroofing in the Omineca Extended Belt has been correlated to dextral motion on splays of the Lewis and Clark fault zone (Parrish *et al.*, 1988; Harms and Price, 1992; Fillipone and Yin, 1993; Fillipone and Yin, 1994). In particular, the Hope fault has been correlated to motion on the Newport fault and the Bitterroot mylonite zone. Published estimates for the age of the Hope fault range from ~52 - 35 Ma. This structure and other dextral faults are truncated by brittle faults bounding the

core complexes of the Omineca Extended Belt (Price and Carmichael, 1986; Harms and Price, 1992).

Correlation of the Spruce Creek mylonite (Lewis *et al.*, 1992), exposed in the footwall of the Bitterroot complex to previously identified thrust plates to the north and southwest provides some limits on the magnitude of the earlier sinistral offset and the amount of horizontal extension accommodated by the Lewis and Clark fault zone and by the Bitterroot mylonite zone, respectively. Correlation of the Spruce Creek mylonite to thrusts exposed at Boehls Butte requires ~45 - 50 km of left-lateral offset early in the pre-Tertiary history of the Lewis and Clark fault zone (Chapter 5). The horizontal component of extension accommodated by the Bitterroot mylonite and associated structures was probably on the order of ~50 km, consistent with previous estimates for this region, as well as for the Omineca Extended Belt (Hyndman, 1980; Harms and Price, 1992). These estimates indicate that there is little variation in the magnitude of extension across the Lewis and Clark fault zone, suggesting that the Lewis and Clark fault zone served as a transfer structure between the offset loci of extension in the Omineca Extended Belt and in the Rocky Mountain Basin and Range to the south.

FUTURE RESEARCH

While a considerable amount of research has been done in the Bitterroot complex, and the Rocky Mountain Basin and Range in general, many ambiguities remain. This dissertation research centered on reconstructing the pressure-temperature-time evolution of the Bitterroot metamorphic core complex, which is just a small part of understanding this region. Two such possibilities for future research are briefly discussed below.

A major source of uncertainty is in the magmatic history of the Bitterroot batholith. This granite mass was originally considered a single batholith, but recent work has demonstrated that it is the result of multiple magmatic events that span a range

of ages (Bickford *et al.*, 1981; Toth, 1987). One reason for this confusion is the paucity of geologic maps that delineate magmatic contacts. A better understanding of the petrology and isotopic characteristics of this extensive composite batholith will be important in determining the cause of elevated geotherms documented in country-rocks and their relation to compressional tectonism.

The Boehls Butte/Goat mountain region to the northwest of the Bitterroot complex is potentially and important link in the correlation of events across the Lewis and Clark fault zone (Doughty and Sheriff, 1992). While extensive metamorphic petrology and some geologic mapping has been done here (Hietanen, 1963; Reid *et al.*, 1981; Grover *et al.*, 1992), there are virtually no constraints on timing relationships, nor has anyone considered the unroofing mechanism for this exposure of lowermost Belt Supergroup/Proterozoic basement rocks. Further study in this metamorphic terrane will shed additional light on the transfer of extension from the Omineca Extended Belt southward across the Lewis and Clark fault zone into the Rocky Mountain Basin and Range.

REFERENCES

Bickford, M. E., Chase, R. B., Nelson, B. K., Schuster, R. D., and Arruda, E. C., 1981, U-Pb studies of zircon cores and overgrowths, and monazite: Implications for age and petrogenesis of the northeastern Idaho batholith: Journal of Geology, v. 89, p. 433-457.

Brown, R. L. and Journeay, J. M., 1987, Tectonic denudation of the Shuswap metamorphic terrain of southeastern British Columbia: Geology, v. 15, p. 142-146.

Buck, W. R., 1988, Flexural rotation of normal faults: Tectonics, v. 7, p. 959-973.

Burchfiel, B. C., Cowan, D. S., and Davis, G. A., 1991, Tectonic overview of the Cordilleran orogen in the western United States, *in* Burchfiel, B. C., ed., The Cordilleran Orogen: Conterminus United States: Boulder, CO, Geological Society of America, p. 407-479.

Chase, R. B., 1973, Petrology of the northeastern border zone of the Idaho batholith, Bitterroot Range, Montana: Montana Bureau of Mines and Geology Memoir, v. 43, p. 1-28.

Chase, R. B., Bickford, M. E., and Arruda, E. C., 1983, Tectonic implications of Tertiary intrusion and shearing within the Bitterroot dome, northeastern Idaho batholith: Journal of Geology, v. 91, p. 462-470.

Coney, P. J. and Harms, T. A., 1984, Cordilleran metamorphic core complexes: Cenozoic extensional relics of Mesozoic compression: Geology, v. 12, p. 550-554.

Doughty, P. T. and Sheriff, S. D., 1992, Paleomagnetic evidence for en echelon extension and crustal rotations in western Montana and Idaho: Tectonics, v. 11, p. 663-671.

Fillipone, J. A. and Yin, A., 1993, Paleogene magmatism and denudation: A mechanism for linking extension across the northern Basin and Range Province: Geological Society of America Cordillera and Rocky Mountain sections Abstracts with Programs, v. 25, p. A37.

Fillipone, J. A. and Yin, A., 1994, Age and regional tectonic implications of Late Cretaceous thrusting and Eocene extension, Cabinet Mountains, northwest Montana and northern Idaho: Geological Society of America Bulletin, v. 106, p. 1017-1032.

Garmezy, L., 1983, Geology and geochronology of the southeast border of the Bitterroot dome: Implications for the structural evolution of the mylonitic carapace [Ph.D.]: The Pennsylvania State University.

Garmezy, L. and Sutter, J. F., 1983, Mylonitization coincident with uplift in an extensional setting, Bitterroot Range, Montana-Idaho: Geological Society of America Abstracts with Programs, v. 15, p. 578.

Glazner, A. F. and Bartley, J. M., 1985, Evolution of lithospheric strength after thrusting: Geology, v. 13, p. 42-45.

Grover, T. W., Rice, J. M., and Carey, J. W., 1992, Petrology of aluminous schist in the Boehls Butte region of northern Idaho: Phase equilibria and P-T evolution: American Journal of Science, v. 292, p. 474-507.

Harms, T. A. and Price, R. A., 1992, The Newport fault: Eocene listric normal faulting, mylonitization, and crustal extension in northeast Washington and northwest Idaho: Geological Society of America Bulletin, v. 104, p. 745-761.

Harrison, J. E., Griggs, A. B., and Wells, J. D., 1986,Geologic and structure maps of the Wallace 1°x2° quadrangle, Montana and Idaho, *in* U.S. Geological Survey Miscellaneous Geologic Investigations Map.

Hietanen, A., 1963, Anorthosite and Associated Rocks in the Boehls Butte Quadrangle and Vicinity, Idaho: U.S. Geological Survey Professional Paper, v. 344-B, p. B1-B75.

Hodges, K. V. and Applegate, J. D. R. A., 1993, Age of Tertiary extension in the Bitterroot metamorphic core complex, Montana and Idaho: Geology, v. 21, p. 161-164.

Hodges, K. V. and Walker, J. D., 1990, Thermobarometric constraints on the unroofing history of a metamorphic core complex, Funeral Mountains, SE California: Journal of Geophysical Research, v. 95, p. 8437-8445.

House, M. A. and Hodges, K. V., 1994, Limits on the tectonic significance of rapid cooling events in extensional setting: Insights from the Bitterroot metamorphic core complex, Idaho-Montana: Geology, v. 22, p. 1007-1010.

Hyndman, D. W., 1980, Bitterroot dome - Sapphire tectonic block, an example of a plutonic-core gneiss-dome complex with its detached suprastructure, *in* Crittenden, M. D., Coney, P. J., and Davis, G. H., ed., Cordilleran Metamorphic Core Complexes: Boulder, CO, Geological Society of America Memoir 153, p. 427-443.

Lang, H. M. and Rice, J. M., 1985, Metamorphism of pelitic rocks in the Snow Peak area, northern Idaho: Sequence of events and regional implications: Geological Society of America Bulletin, v. 96, p. 731-736.

Lewis, R. S., Burmeister, R. F., Reynolds, R. W., Bennett, E. H., Myers, P. E., and Reid, R. R., 1992,Geologic map of the Lochsa River area, Northern Idaho, *in* : Moscow, ID: Idaho Geological Survey.

Liu, M. and Furlong, K. P., 1993, Crustal shortening and Eocene extension in the Southeastern Canadian Cordillera: Some thermal and rheologicial considerations: Tectonics, v. 12, p. 776-786.

Orr, K. E. and Cheney, E. S., 1987, Kettle and Okanogan domes, northeastern Washington and southern British Columbia: Washington Division of Geology and Earth Resources Bulletin 77, v. p. 55-70.

Parrish, R. R., Carr, S. D., and Parkinson, D. L., 1988, Eocene extensional tectonics and geochronology of the southern Omenica Belt, British Columbia and Washington: Tectonics, v. 7, p. 181-212.

Price, R. A., 1979, Intracontinental ductile spreading linking the Fraser River and northern Rocky Mountain Trench transform fault zones, south-central British Columbia and northeast Washington: Geological Society of America Abstracts with Programs, v. 11, p. 499.

Price, R. A. and Carmichael, D. M., 1986, Geometric test for Late Cretaceous-Paleogene intracontinental transform faulting in the Canadian Cordillera: Geology, v. 14, p. 468-471.

Reid, R. R., Greenwood, W. R., and Nord, G. L., 1981, Metamorphic petrology and structure of the St. Joe area, Idaho: Geological Society of America Bulletin. Part II, v. 92, p. 94-205.

Silverberg, D. S., 1990, The tectonic evolution of the Pioneer metamorphic core complex, south-central Idaho [Ph.D.]: Massachusetts Institute of Technology.

Spencer, J. E., 1984, Role of tectonic denudation in warping and uplift of low-angle normal faults: Geology, v. 12, p. 95-98.

Toth, M. I., 1987, Petrology and Origin of the Bitterroot Lobe of the Idaho batholith: U.S. Geological Survey Professional Paper, v. 1436, p. 9-37.

Wallace, C. A., Lidke, D. J., Waters, M. R., and Obradovich, J. D., 1989, Rocks and structure of the southern Sapphire mountains, Granite and Ravalli Counties, western Montana: U.S. Geological Survey Bulletin, v. 1824, p. 29.

Wernicke, B., 1991, Cenozoic extensional tectonics of the U.S. Cordillera, *in* Burchfiel, B. C., Lipman, P. W., and Zoback, M. L., ed., The Cordilleran Orogen: Conterminus United States: Boulder, CO, Geological Society of America, The Geology of North America, p. 553-582.

Wernicke, B. and Axen, G. J., 1988, On the role of isostacy in the evolution of normal fault systems: Geology, v. 16, p. 848-851.

Wernicke, B. P., Christiansen, R. L., England, P. C., and Sonder, L. J., 1987, Tectonomagmatic evolution of Cenozoic extension in the North American Cordillera., *in* Coward, M. P., Dewey, J. F., and Hancock, P. L., ed., Continental Extensional Tectonics: Oxford, Geological Society of London, p. 203-221.

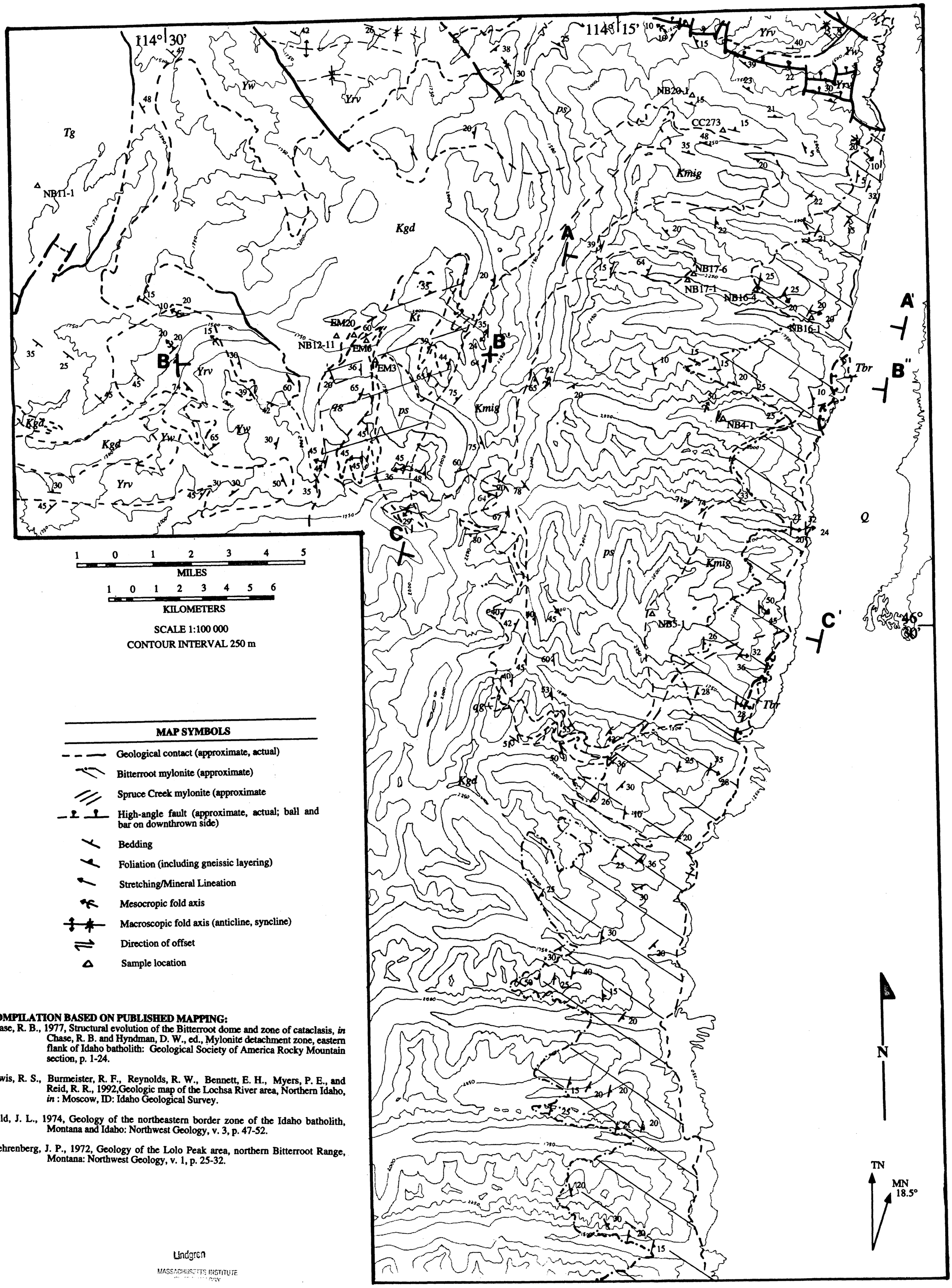

MAP SYMBOLS

- Geological contact (approximate, actual)
- Bitterroot mylonite (approximate)
- Spruce Creek mylonite (approximate
- High-angle fault (approximate, actual; ball and bar on downthrown side)
- Bedding
- Foliation (including gneissic layering)
- Stretching/Mineral Lineation
- Mesocropic fold axis
- Macroscopic fold axis (anticline, syncline)
- Direction of offset
- Sample location

COMPILATION BASED ON PUBLISHED MAPPING:

Chase, R. B., 1977, Structural evolution of the Bitterroot dome and zone of cataclasis, *in* Chase, R. B. and Hyndman, D. W., ed., Mylonite detachment zone, eastern flank of Idaho batholith: Geological Society of America Rocky Mountain section, p. 1-24.

Lewis, R. S., Burmeister, R. F., Reynolds, R. W., Bennett, E. H., Myers, P. E., and Reid, R. R., 1992,Geologic map of the Lochsa River area, Northern Idaho, *in* : Moscow, ID: Idaho Geological Survey.

Nold, J. L., 1974, Geology of the northeastern border zone of the Idaho batholith, Montana and Idaho: Northwest Geology, v. 3, p. 47-52.

Wehrenberg, J. P., 1972, Geology of the Lolo Peak area, northern Bitterroot Range, Montana: Northwest Geology, v. 1, p. 25-32.

PLATE 1. BEDROCK GEOLOGY OF THE NORTHEASTERN BITTERROOT METAMORPHIC CORE COMPLEX, ID-MT.

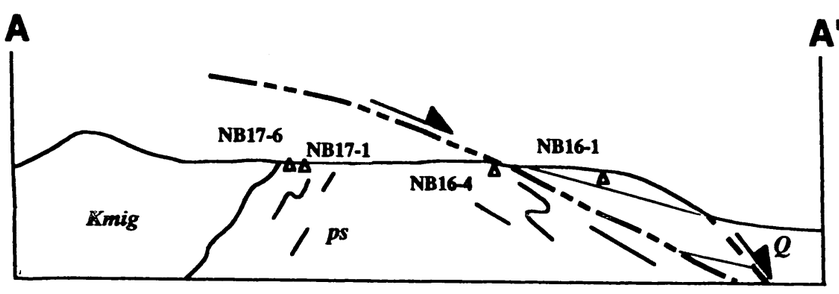

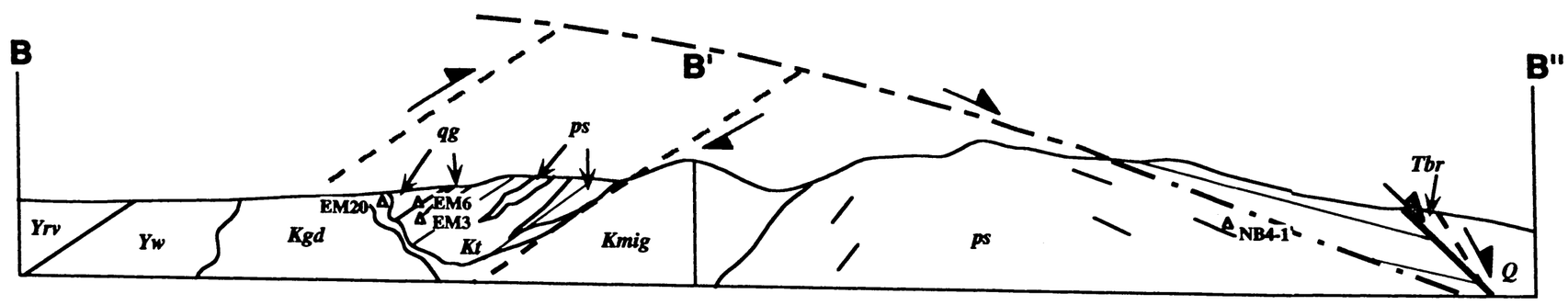

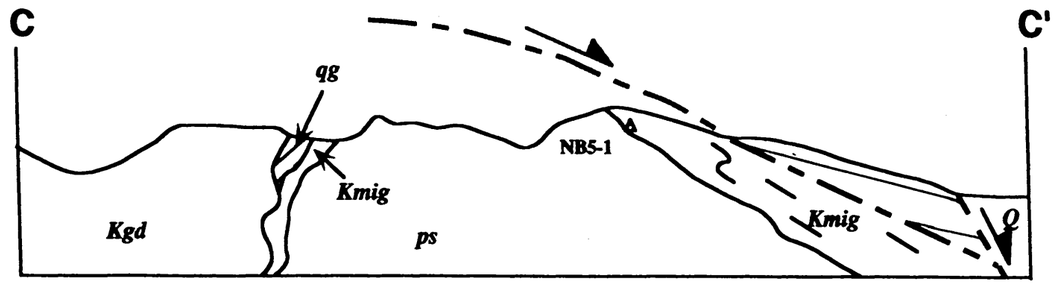

MAP UNITS

SEDIMENTARY AND METAMORPHIC ROCKS

Q **ALLUVIAL, LANDSLIDE, & GLACIAL DEPOSITS** (*Holocene*)-Unconsolidated valley-fill.

Tbr **CHLORITE BRECCIA** - Fault breccia consisting of fragments of Kgd, ps, qg, and Kmig.

Yw **WALLACE FORMATION** (*Middle Proterozoic*)-Gray to brown calcareous siltite and argillite locally containing ripple marks and mud cracks; locally present as banded green and white diopside-plagioclase gneiss.

Yrv **RAVALLI GROUP** (*Middle Proterozoic*)-Light gray, fine- to medium-grained quartzite.

qg **QUARTZITE & CALC-SILICATE GNEISS** - Composite unit of tightly folded and intermixed feldspathic quartzite and calc-silicate gneiss. Includes rocks probably equivalent to parts of Yrv and Yw.

ps **PELITIC SCHIST** - Quartz-muscovite-bioite schist. Locally contains sillimanite ± kyanite and garnet. Most likely equivalent to the Prichard Formation (Middle Proterozoic).

INTRUSIVE ROCKS

Tg **GRANITE** (*Eocene*)-Fine- to coarse-grained hypabyssal granite containing bipyramidal smoky quartz, white to pinkish feldspar, biotite, and sparse amphibolite.

Kmig **MIGMATITE** (*Late Cretaceous?*)-Metamorphic rocks intruded by 30-70% granitic rocks, intermixed at a scale of centimeters to decimeters.

Kgd **BIOTITE GRANODIORITE** (*Late Cretaceous?*)-Medium- to fine-grained biotite granite and granodiorite.

Kt **TONALITE** (*Early Cretaceous?*)-Medium-grained, well-foliated hornblende-biotite tonalite, quartz diorite, and quartz monzodiorite.